# Understanding Li Dendrites in Solid-State Batteries




Dominic Melvin

St Cross College

University of Oxford

Submitted for the degree of *Doctor of Philosophy*

Hilary 2024

# Declaration of Originality

I, Dominic Melvin, declare that this thesis is my own work and has not been submitted to another institution for any other degree or qualification. All contributions from collaborators have been appropriately referenced throughout the work.

This thesis is approximately 36,948 words in length, and so complies with the Departmental word limit for doctoral theses.

Dominic Melvin

Hilary 2024

# Acknowledgements

Firstly, I would like to thank my supervisor Professor Sir Peter Bruce. I am grateful for what has been a challenging yet highly rewarding experience. Thank you for giving me this opportunity and for your mentorship throughout. Additionally, I would like to thank the Faraday Institution for funding my studies, providing resources and equipment, and for organising a valuable training program.

I would like to thank all the members of the Bruce group, both past and present, for their friendship and collaboration over these past years. In particular, I would like to thank Dr Dominic Spencer Jolly for his clear and intelligent guidance throughout my time in Oxford. Your advice has been invaluable when tackling difficult research problems. I would also like to give special thanks to Dr Ziyang Ning and Dr Guanchen Li. Working on the Li dendrite problem together has been incredibly interesting, and I am very grateful to have tackled this subject together which such knowledgeable scientists. I would like to also express my appreciation to the members of both the solid-state subgroup and the SOLBAT project with whom I have had the pleasure of working with; Bingkun Hu, Shengming Zhang, Johann Perera, Bartholomew Payne, Dr Gareth Hartley, Dr Xiangwen Gao, Dr Boyang Liu, Dr Varnika Agarwal, Dr Longlong Wang, Dr Hui Gao, and Dr Junfu Bu. Thank you also to the various professors who have given me additional guidance during my time in Oxford; Professor Patrick Grant, Professor Mauro Pasta, Professor Charles Monroe, and Professor Richard Todd. Furthermore, I would like to thank the team of essential people without whom the research in Rex Richards would not function, namely Miki Bennett, Dr Paul Adamson, Dr Nadia Abdul-Karim and Dr Esther Townsend. A special thanks also to those who helped advise and refine the writing of this thesis; Dr Gregory Rees, Dr Mikkel Juelsholt, Dr Paul Adamson, Dr Dominic Spencer Jolly, Dr Sofia De Sousa Coutinho and Bartholomew Payne.

I would also like to say thank you to all those who contributed to making these years a genuinely enjoyable time in my life. Thank you to Dom, Rob, Greg, Mikkel, Sofia, and Bart for

the lunch time conversations and after work drinks. A special appreciation also to Axel, Marco and Michael, all of whom I am happy to call life-long friends after our time spent living together. To my family, thank you for all the years of love and support. I'd especially like to thank my parents Anita and Roy - you have always supported me, and I owe everything to you both. Finally, I want to express the most heartfelt appreciation to my loving wife Clara. I couldn't have done this without the love and companionship you provide every day. I couldn't have done this without you.

# Abstract

As the requirements placed on rechargeable batteries continue to expand, next-generation technologies beyond today's Li-ion cells are being increasingly sought. Solid-state designs using lithium metal anodes may provide a leap in energy density, but their charging currents have been limited by the formation of Li dendrites which lead to catastrophic cell failure. In this thesis, an examination is made into both the origin of Li dendrites as well as the influence of the solid electrolyte's microstructure and mechanical properties.

Firstly, an investigation is made into underlying processes by which Li dendrites grow within argyrodite-type $Li_6PS_5Cl$ solid electrolytes. Key characteristics are elucidated using *operando* X-ray tomographic imaging, from which a new mechanistic understanding is proposed and modelled using a wide selection of experimentally determined mechanical and microstructural inputs.

Secondly, a range of differently densified $Li_6PS_5Cl$ electrolytes are produced using field-assisted sintering. Following which, an attempt is made to answer the question to what extent realistic changes in the electrolyte's microstructure can affect sustainable Li-anode charging rates.

Finally, the effect of dispersing metastabilised zirconia particles within the microstructure of $Li_6PS_5Cl$ is investigated. The effect on both the fracture toughness and on ionic conductivity is assessed, after which the question as to whether transformation toughening can stabilise propagating dendrite cracks is considered.

# List of Publications

1. **Melvin, D.L.R**.†, Ning, Z.†, Li, G.†, Chen, Y., Bu, J., Spencer-Jolly, D., Liu, J., Hu, B., Gao, X., Perera, J., Gong, C., Pu, S.D., Zhang, S., Liu, B., Hartley, G.O., Bodey, A.J., Todd, R.I., Grant, P.S., Armstrong, D.E.J., Marrow, T.J., Monroe, C.W. & Bruce, P.G. Dendrite initiation and propagation in lithium metal solid-state batteries. *Nature* **618**, 287–293 (2023).
2. **Melvin, D.L.R**.†, Spencer Jolly, D.†, Stephens, I.D.R., Brugge, R.H., Pu, S.D., Bu, J., Ning, Z., Hartley, G.O., Adamson, P., Grant, P.S., Aguadero, A. & Bruce, P.G. Interfaces between Ceramic and Polymer Electrolytes: A Comparison of Oxide and Sulfide Solid Electrolytes for Hybrid Solid-State Batteries. *Inorganics*, **10**, 60 (2022).
3. Ning, Z., Spencer Jolly, D., Li, G., De Meyere, R., Pu, S.D., Chen, Y., Kasemchainan, J., Ihli, J., Gong, C., Liu, B., **Melvin, D.L.R**., Bonnin, A., Magdysyuk, O., Adamson, P., Hartley, G.O., Monroe, C.W., Marrow, T.J. & Bruce, P.G. Visualising Plating-Induced Cracking in Lithium-Anode Solid Electrolyte Cells. *Nat. Mater.*, **20**, 1121-1129 (2021).
4. Zhang, S., Hu, B., Geng, Z., Gao, X., Spencer-Jolly, D., **Melvin, D.L.R**., Ning Z., Li, G., Jenkins, M., Wang, L., Gao, H., Pu, S.D., Marrow, T.J., Monroe, C.W. & Bruce, P.G. Influence of contouring the lithium metal/solid electrolyte interface on the critical current for dendrites. *Energy Environ. Sci.*, **17**, 1448-1456 (2024).
5. Spencer-Jolly, D., Agarwal, V., Doerrer, C., Hu, B., Zhang, S., **Melvin, D.L.R**., Gao, H., Gao, X., Adamson, P., Magdysyuk, O.V., Grant, P.S., House, R.A. & Bruce, P.G. Structural changes in the silver-carbon composite anode interlayer of solid-state batteries. *Joule,* **7**, 503–514 (2023).
6. Spencer Jolly, D., Ning, Z., Hartley, G.O., Liu, B., **Melvin, D.L.R**., Adamson, P., Marrow, T.J. & Bruce, P.G. Temperature Dependence of Voiding in Argyrodite Solid-State Batteries. *ACS Appl. Mater. Interfaces*, **13**, 19, 22708-22716 (2021).
7. Spencer Jolly, D., Perera, J., Pu, S.D., **Melvin, D.L.R.**, Adamson, P. & Bruce, P.G. High critical currents for dendrite penetration and voiding in potassium metal anode solid-state batteries. *J Solid State Electrochem* **26**, 1961–1968 (2022).
8. Liu, B., Pu, S.D., Doerrer, C., Spencer Jolly, D., House, R.A., **Melvin, D.L.R.**, Adamson, P., Grant, P.G., Gao, X. & Bruce, P.G. The effect of volume change and stack pressure on solid-state battery cathodes. *SusMat*, **3**, 721–728 (2023).
9. Pu, S.D., Gong, C., Tang, Y.T., Ning, Z., Liu, J., Zhang, S., Yuan, Y., **Melvin, D.L.R.**, Yang, S., Pi, L., Marie, J.-J., Hu, B., Jenkins, M., Li, Z., Liu, B., Tsang, S.C.E., Marrow, T.J., Reed, R.C., Gao, X., Bruce, P.G. & Robertson, A.W. Achieving Ultrahigh-Rate Planar and Dendrite-Free Zinc Electroplating for Aqueous Zinc Battery Anodes. *Adv. Mater,* **34**, 2202552. (2022).
10. Gong, C.†, Pu, S.C.†, Zhang, S.†, Yuan, Y.†, Ning, Z., Yang, S., Gao, X., Chau, C., Li, Z., Liu, J., Pi, L., Liu, B., Capone, I., Hu, B., **Melvin, D.L.R.**, Pasta, M., Bruce, P.G. & Robertson, A.W. The role of an elastic interphase in suppressing gas evolution and promoting uniform electroplating in sodium metal anodes. *Energy Environ. Sci.*, **16**, 535-545 (2023).

# List of Abbreviations

| | |
|---|---|
| 1D | One Dimensional |
| 2D | Two Dimensional |
| 3D | Three Dimensional |
| AC | Alternating Current |
| ASSB | All-Solid-State Battery |
| BSE | Back-Scattered Electrons |
| CBM | Conduction Band Minimum |
| CCD | Critical Current Density |
| CE | Counter Electrode |
| CL | Condenser Lens |
| CMOS | Complementary Metal Oxide Semiconductor |
| CSZ | 12 mol.% $CeO_2$-$ZrO_2$ |
| DC | Direct Current |
| EDX | Energy-dispersive X-ray Spectroscopy |
| EIS | Electrochemical Impedance Spectroscopy |
| EV | Electric Vehicle |
| FIB | Focused Ion Beam |
| GB | Grain Boundary |
| ISE | Inorganic Solid Electrolyte |
| LEM | Lawn, Evans and Marshall Equation |
| LiPON | Lithium phosphorus oxynitride |
| LISICON | Li Superionic Conductor |
| Li-SSB | Lithium Metal Anode Solid-State Battery |
| LLZO | $Li_7La_3Zr_2O_{12}$ |
| LPS | Lithium thiophosphate |
| LuAG | Lutetium Aluminium Garnet |
| MIEC | Mixed Ionic and Electronic Conducting Interphase |
| MS | Mass Spectrometry |
| NASICON | Na Superionic Conductor |
| OL | Objective Lens |
| PEIS | Potentiostatic Electrochemical Impedance Spectroscopy |
| PFIB | Plasma Focused Ion Beam |
| PVD | Physical Vapour Deposition |
| RE | Reference Electrode |
| SCC | Stress Corrosion Cracking |
| SE | Solid Electrolyte |
| SEI | Solid Electrolyte Interphase |
| SEM | Scanning Electron Microscope/Microscopy |
| SIF | Stress Intensity Factor |
| SIMS | Secondary Ion Mass Spectrometry |
| SSB | Solid-State Battery |
| WE | Working Electrode |
| XCT | X-ray Computed Tomography |
| XRD | X-ray Diffraction |
| ZEBRA | Zeolite Battery Research Africa Project |

# Table of Contents


***Chapter 1 : Introduction*** ***1***

**1.1 Wider Context** **1**

**1.2 Towards lithium metal solid-state batteries** **2**
1.2.1 The lithium-ion battery 2
1.2.2 The lithium metal anode challenge 5
1.2.3 The solid-state battery 7

**1.3 Solid Electrolytes** **9**
1.3.1 A brief history of ceramic electrolytes 9
1.3.2 Solid electrolyte properties: requirements and classes 11
1.3.3 Li-argyrodite sulphide electrolytes 15

**1.4 The Li metal / solid electrolyte interface** **19**
1.4.1 Challenges at the interface 19
1.4.2 Key experimental observations of dendrites 26
1.4.3 Dendrites: Mode 1 35
1.4.4 Dendrites: Mode 2 41
1.4.5 Strategies against dendrites 43

**1.5 Thesis Aims** **50**

***Chapter 2 : Experimental Techniques*** ***53***

**2.1 Aim** **53**

**2.2 Sample Preparation** **53**
2.2.1 Sintering 53
2.2.2 Field Assisted Sintering 54

**2.3 Materials Characterisation** **56**
2.3.1 X-ray Diffraction 56
2.3.2 Scanning Electron Microscopy 59
2.3.3 X-ray computed tomography 64
2.3.4 On-line mass spectrometry 71

**2.4 Electrochemical Techniques** **72**
2.4.1 Potentiostatic Electrochemical Impedance Spectroscopy 72
2.4.2 Galvanostatic Cell Testing 75

**2.5 Mechanical Testing** **77**
2.5.1 Nanoindentation 77
2.5.2 Microcantilever Bending 79

***Chapter 3 : Dendrite initiation and propagation*** ***83***

**3.1 Aim** **83**

**3.2 Introduction** **83**

**3.3 Experimental** **85**
3.3.1 Electrolyte preparation and cell assembly 85
3.3.2 Three-electrode cell cycling 86
3.3.3 *Operando* X-ray computed tomography 86
3.3.4 On-line Mass Spectrometry 87
3.3.5 Plasma FIB-SEM 87
3.3.6 Secondary Ion Mass Spectrometry 88
3.3.7 Nanoindentation: Elastic Modulus, Hardness and Fracture Toughness 88
3.3.8 Microcantilever Bending: Local Fracture Strength 88

**3.4 Results and Discussion ..... 89**
3.4.1 X-ray tomography of dendrite cracks ..... 89
3.4.2 Crack initiation based on pore filling ..... 92
3.4.3 Crack propagation based on wedge-opening ..... 102
3.4.4 When does propagation lead to a short-circuit? ..... 108

**3.5 Conclusions ..... 114**

***Chapter 4 : The Effect of Microstructure on Dendrite Initiation ..... 117***

**4.1 Aim ..... 117**

**4.2 Introduction ..... 117**

**4.3 Methods ..... 119**
4.3.1 Field assisted sintering and electrolyte preparation ..... 119
4.3.2 Three-electrode cells ..... 119
4.3.3 *In-situ* X-ray tomography ..... 120
4.3.4 Plasma FIB-SEM and microstructural analysis ..... 120
4.3.5 Powder X-ray diffraction ..... 121

**4.4 Results and Discussion ..... 121**
4.4.1 Densification of the $Li_6PS_5Cl$ microstructure ..... 121
4.4.2 Effect of $Li_6PS_5Cl$ microstructure on ionic conductivity ..... 125
4.4.3 Determination of the critical current for dendrite initiation ..... 127
4.4.4 The effect of microstructure on dendrite initiation ..... 131

**4.5 Conclusions ..... 136**

***Chapter 5 : Transformation Toughening of $Li_6PS_5Cl$ Solid Electrolytes ..... 138***

**5.1 Aim ..... 138**

**5.2 Introduction ..... 138**

**5.3 Experimental ..... 140**
5.3.1 Electrolyte preparation ..... 140
5.3.2 Potentiostatic electrochemical impedance spectroscopy (PEIS) ..... 141
5.3.3 Three-electrode cells ..... 141
5.3.4 *In-situ* X-ray computed tomography ..... 141
5.3.5 SEM/EDX and Plasma FIB-SEM ..... 142
5.3.6 Nanoindentation: Elastic Modulus, Hardness and Fracture Toughness ..... 142

**5.4 Results and Discussion ..... 143**
5.4.1 Development of $12CeO_2$-$ZrO_2$/$Li_6PS_5Cl$ composites ..... 143
5.4.2 Effect on mechanical properties ..... 147
5.4.3 Effect on ionic conductivity ..... 149
5.4.4 Effect on Li dendrite propagation ..... 152
5.4.5 Feasibility of dendrite crack stabilisation ..... 157

**5.5 Conclusions ..... 157**

***Chapter 6 : Conclusions and outlook ..... 160***

***References ..... 164***

***Appendix ..... 185***

# Chapter 1: Introduction

## 1.1 Wider Context

In the latter part of the 20th century, advances in rechargeable batteries accelerated a digital revolution into a new information age of portable electronics[1,2]. Several decades on, powerful environmental concerns are driving an urgent effort to utilise the leading forms of energy storage to electrify transportation and balance an increasingly renewable electricity grid[3,4]. The prospective applications of rechargeable batteries are therefore broadening, and as their uses diversify, so too are the demands being made of their performance. Cells with the same Li-ion chemistries once optimised for mobile phones are being bundled into large packs to power electric vehicles (EVs), but the simultaneous pursuit of longer ranges, faster charging, extended lifetimes, higher safety, and lower costs is pushing the limits of what can be achieved by engineering alone[5,6]. To meet demands, new chemistries beyond Li-ion such as lithium metal anode cells and solid-state batteries may be required. However, many of these next-generation battery technologies are facing fundamental challenges that must be overcome by research before successful commercialisation can be realised[7,8].

This thesis reports the results of research on the interface between lithium metal anodes and solid ceramic electrolytes for use in solid-state batteries. In particular, the mechanism of Li dendrite failure is explored as well as some potential solutions. As an introduction to this field of study, this chapter aims to summarise the relevant key areas of literature. First, the lithium metal anode solid-state battery is introduced, leading into a detailed discussion of solid electrolytes. Finally, literature on the lithium anode/solid electrolyte interface is surveyed with a special focus on the dendrite problem.

## 1.2 Towards lithium metal solid-state batteries

### 1.2.1 The lithium-ion battery

Batteries are electrochemical energy storage devices capable of acting as a source of direct current, and which, despite a vast array of designs, all consist of some in-series or in-parallel arrangement of galvanic (voltaic) cells*. Within such cells, oxidation and reduction reactions are spatially separate, occurring at two distinct and distant active electrode materials commonly immersed in an ionically conductive, electronically insulative medium known as an electrolyte[9,10]. For either reaction to proceed, the free electrons which are produced must be exchanged through an external circuit connecting one electrode to the other, either liberating or consuming energy in the process. This uncoupling of ionic and electron mobility allows the equilibrium position of the chemical reactions taking place in each electrode, and hence the storage of energy, to be controlled. Among the various cell chemistries, Li-based batteries - because of their higher energy density and design flexibility - have significantly outperformed their competitors[1,11]. Of these, the most successful rechargeable archetype is known as the 'lithium-ion' battery.

* These cells may often be referred to as 'batteries' in the literature and as such this thesis will go on to use the terms somewhat interchangeably.

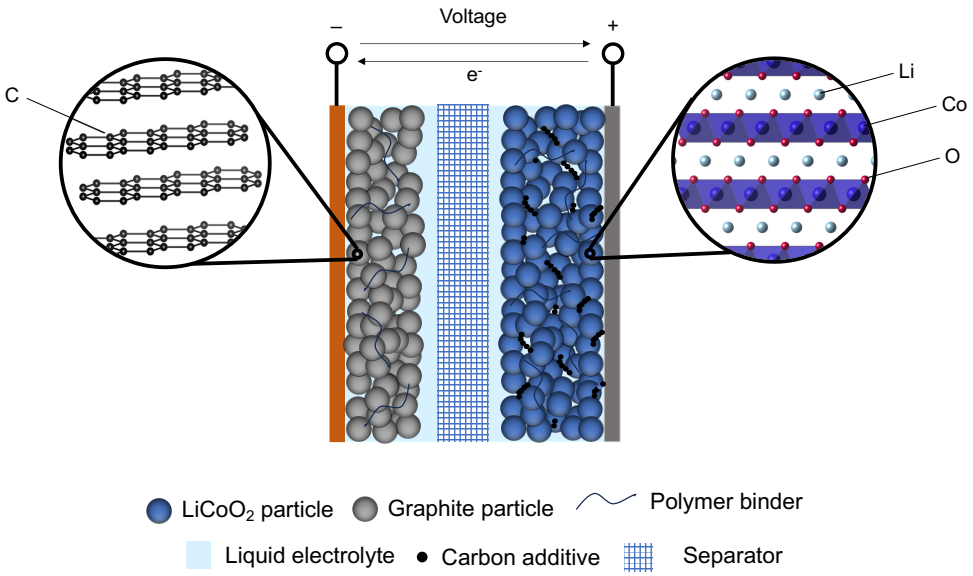



**Figure 1.1:** Schematic of a typical lithium-ion battery, highlighting the key components and the layered atomic structure of intercalation electrodes.

Whilst the term 'lithium-ion' battery can refer to a rather broad range of chemistries in which energy is stored by the movement of Li-ions, most commonly this has meant the type of cells first developed by Goodenough, Whittingham and Yoshino[12–14]. In such designs, inorganic compounds which reversibly intercalate Li-ions act as the active materials for both electrodes, with a layered transition metal oxide typically preferred for the cathode (e.g., $LiCoO_2$) and carbonaceous materials such as graphite preferred for the anode[†]. During the production of the cell, powders of these active materials are cast as part of thin electrode sheets which are then stacked together on either side of a porous polymeric separator. A liquid electrolyte (typically a Li salt dissolved in a non-aqueous solvent) is then injected in so to fully permeate the stack[15]. A schematic of a Li-ion cell is shown in Figure 1.1. As a Li-ion cell is charged, the cathode active material is oxidised and Li-ions migrate across the liquid electrolyte, reducing as they are intercalated into the active anode particles. During discharge, the reverse process takes place, with Li-ions deintercalating from the lithiated carbon anode and intercalating back

[†] Whilst strictly speaking the cathode and anode are defined by where the reductive and oxidative processes occur, within the field of batteries the terms are fixed to what holds true on discharge. Hence the positive and negative electrodes are conventionally referred to as the cathode and anode respectively. For simplicity, this convention will also be used throughout this thesis.

into the layered transition metal oxide active material. It is this mirrored aspect of having two intercalation reactions which has led to their dubbing as 'rocking-chair' type cells.

Lithium-ion batteries are so far the undisputed technology when it comes to electrochemical energy storage[16]. The recent push for vehicle electrification would not be possible without the cost-effective mass production of Li-ion cells in parallel with their yet ever-growing performance[17,18]. However, Li-ion batteries still face numerous challenges which place an upper limit on their performance:

- **Degradation at active material interfaces limits durability**. Reaction between the carbonaceous anode and liquid electrolyte has been a somewhat 'necessary evil' since their first commercialisation, with the reaction forming an inactive resistive layer composed of $Li_2CO_3$, LiF, $Li_2O$ and alkyl carbonates known as the solid electrolyte interphase (SEI)[19,20]. Whilst passivating, the formation of the SEI results in a loss of active Li and a corresponding fade in cell capacity[21]. At the cathode, degradation is particularly problematic at elevated temperatures and when the active material is at a high state-of-charge[22,23]. Degradation at the cathode can even aggravate further SEI formation through the diffusion of transition metal ions across the liquid electrolyte in what is known as 'cross-talk'.[24]
- **Li plating at the anode limits fast charging**. Fast charging Li-ion cells can rapidly accelerate degradation and even trigger degradation mechanisms that are not present under 'normal' operating conditions. Limited Li diffusion through the resistive SEI and through graphite itself can lead to the plating of mossy lithium metal at the anode. This poses serious safety concerns as short-circuiting of the cell can lead to thermal run-away and explosion.[25,26]
- **Application specific safety risks.** Damage to a battery module, for example in the event of a road traffic incident, can result in a mechanical short circuit with risks of fire, explosion, and the release of toxic fumes.[27–29]
- **The active materials have limited energy density**. The energy density of Li-ion batteries has a lower theoretical limit than alternative cell chemistries. Whilst some

increases in cell energy density have been made possible through the discovery of new high-capacity, high-voltage cathode materials, continued improvement may be reliant on increasing anodic capacities beyond the limits of graphite.[17,30]

### 1.2.2 The lithium metal anode challenge

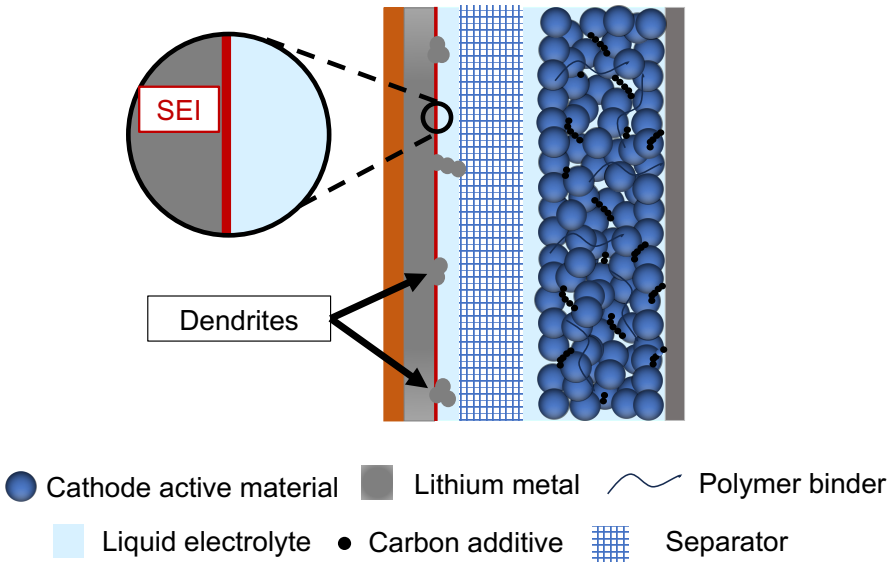



**Figure 1.2:** Schematic demonstrating the common issues faced by lithium anode cells which use liquid electrolytes, namely resistive SEI formation and dendrite growth.

As the most electropositive (−3.04 V versus standard hydrogen electrode) and lightest (equivalent weight $M$ = 6.94 g mol$^{-1}$, and specific gravity $\rho$ = 0.53 g cm$^{-3}$) metal, pure lithium has often been heralded as a 'holy-grail' anode material[31]. Consequently, its use in batteries has been pursued for decades. The first research into lithium batteries was during the 1950s, when it was noticed that Li metal could form an ionically conductive passivation layer when in contact with a number of non-aqueous electrolytes[32,33]. By the 1960s and 70s, the advantage of using Li metal as an anode had been demonstrated with the assembly of primary (non-rechargeable) Li cells[1,32,34,35]. Owing to their high specific capacity and variable discharge rate, these primary cells rapidly found applications as power sources for watches, calculators, and implantable medical devices. If successfully utilised in secondary (rechargeable) cells, the vastly superior anodic specific capacity of Li metal as compared to graphite (3860 mAh/g

compared to 372 mAh/g) would mean a significant improvement in cell energy density as compared to today's Li-ion batteries[30]. Unfortunately, there are still severe unresolved issues faced when using Li metal as a reversible anode:

- **Continuous SEI formation and Li loss leads to severe capacity fade.** Like graphite, a passivating SEI layer forms on the surface of Li metal anodes when placed in contact with liquid electrolytes, but during cycling, both large volume changes and inhomogeneous plating/stripping cause the layer to fracture. This exposes fresh reactive surfaces and enables the formation and detachment of 'dead' Li islands, see Figure 1.2. This continual loss of active Li severely limits the durability of any secondary cells.[36–38]
- **Inhomogeneous Li plating leads to short circuit and safety concerns.** Whilst Li plating will only occur during the fast or overcharging of graphite anodes, the inherent roughening of Li anodes during cycling alone can lead to mossy and dendritic Li growths which can traverse the cell and cause electrical short circuit, see Figure 1.2. Not only does this mean catastrophic failure of the cell, but the heat caused during dendritic shorts can induce runaway reactions and risk explosion.[1,39]

Notable past attempts to successfully produce secondary Li anode batteries include Moli Energy and Exxon in the early 1990s, but safety concerns surrounding their cells were never sufficiently alleviated[40–42]. Current strategies to overcome unacceptable capacity fade and dendritic Li growth generally involve either the use of electrolyte additives[43,44] or expensive high salt concentrations[45,46]. Whilst these strategies have shown some promise at moderate cycling rates, faster charging is still limited, and long cycle lives are yet to be fully realised. Also, even if dendrite failure in such cells can be avoided, the use of Li anodes with liquid electrolytes would likely still require additional cell casing to meet the safety requirements of many desired applications, limiting attainable pack-level energy densities.

### 1.2.3 The solid-state battery

The recent discovery of new types of fast lithium-ion conducting solid electrolytes has triggered a surge of interest in solid-state batteries (SSBs) as one of the more realistic advancements towards a lithium anode secondary cell. The combination of a solid electrolyte and lithium metal anode potentially offers a route to mitigate both the aforementioned issue of continual SEI formation and the dangerous risk of short circuit, Figure 1.3.

When paired with a well-chosen solid electrolyte, degradation at the lithium interface can be minimised or even avoided completely[47,48]. Any reaction that may occur is protected from cross-talk and the solidity of the electrolyte prevents the repeated formation of new unreacted interfaces[30]. As such, capacity fade which results from continuous reaction at the lithium anode interface can be effectively mitigated. Whereas in liquid electrolytes dendritic and mossy Li growth can potentially occur unimpeded across the cell, solid electrolytes can instead act as a dense physical barrier. This being said, it is important to note that solid electrolytes have 'critical current densities' above which Li filaments may penetrate and cause cell failure, albeit with less risk of explosion[49–51]. Whilst low critical currents have so far limited Li-SSB charging times, new interfacial modification strategies coupled with best-in-class materials have enabled critical currents as high as 8.6 mA/cm$^2$.[52]

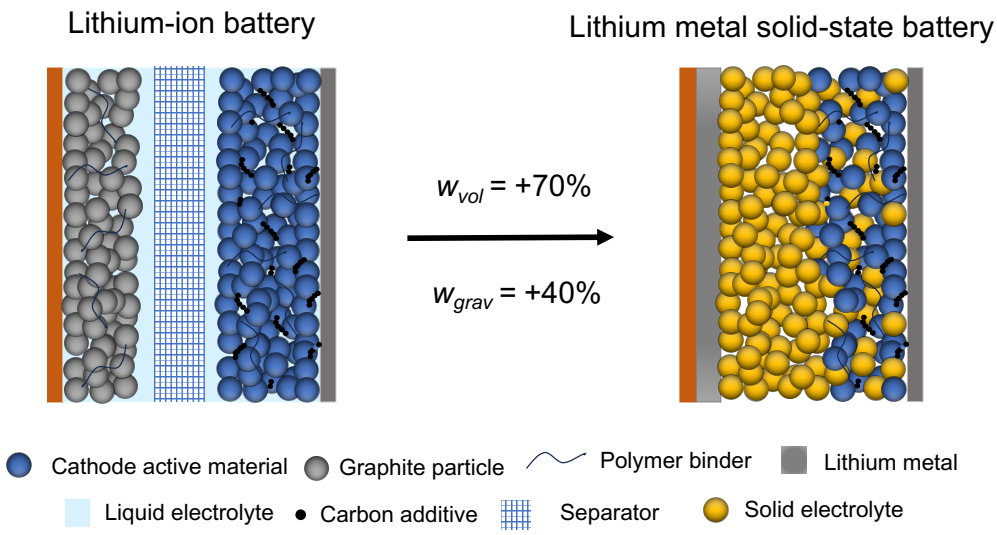



**Figure 1.3:** A schematic demonstrating the potential gains in volumetric and gravimetric energy density when transitioning from a conventional Li-ion battery to a lithium metal solid-state battery. Adapted from Janek *et al.*[30]

Although solid lithium-ion conductors may offer a potential pathway towards reversible lithium anodes, their use as electrolytes poses difficult challenges. For example, processing ceramics into low-cost, highly dense, and highly conductive thin films whilst forming conformal interfaces at both the anode and cathode is a far from trivial feat[53,54]. Liquid electrolytes can be simply injected into the cell, easily wetting the cathode active material to maximise ionic connectivity. In the case of solid electrolytes, electrolyte powders must be mixed into the cathode slurry to form a composite in which ionic pathways are almost inevitably tortuous[55]. Consequently, there is still an active need to design solid electrolytes that offer very high (effective) ionic conductivities in thick and optimised cathode architectures whilst retaining long-term stable and low-resistance interfaces[18]. Whilst some solid electrolytes may have high oxidative stability and thus avoid reacting with cathode active materials, volume changes during cycling can cause contact loss and capacity fade which can only be mitigated through the application of high stack pressures[56]. The design and preparation of solid-state composite cathodes that operate under minimal stack pressure is still an ongoing research challenge.

Whilst the cathode-side problems in all-solid-state batteries demand intense research effort[56,57], this thesis will instead focus on the challenges at the lithium metal anode/solid electrolyte interface. The next section will introduce and discuss the properties of key solid

electrolyte materials (Section 1.3), and the subsequent section (Section 1.4) will narrow down the theory and important literature relating to the metal anode/solid electrolyte interface.

## 1.3 Solid Electrolytes

### 1.3.1 A brief history of ceramic electrolytes

Whilst reports of ionic conduction within ceramics date as early as Michael Faraday[58], discoveries of new ionic conductors were for a long time rare, and for over a century significant advances were limited to Nernst's discovery of zirconia-based oxide ion conductors[59] and Lorenz's discovery of fast $Ag^+$ ion conduction in silver halides[60]. In fact, it wasn't until the 1960s that the first secondary batteries based on ceramic electrolytes were made viable, thanks to the discovery of a new $Na^+$ conductor[61]. Sodium beta alumina, often referred to as $\beta$-$Al_2O_3$, had been discovered embedded in the linings of glass making furnaces[62,63]. Due to its fast ionic conduction, it was possible to develop a new type of battery which was both lightweight and delivered significant power, namely the sodium/sulphur (Na-S) cell. Not only did commercial Na-S cells mark the first viable deviation from the standard use of liquid electrolytes, but their use of molten sodium and sulphur electrodes meant the design specifically relied on the unique aspect of a solid electrolyte to separate the liquid electrodes. Whilst Na-S batteries have been used for stationary energy storage for decades, across other sectors battery designs based on ceramic electrolytes have historically struggled to compete[64,65]. During the 1980s and 90s, liquid electrolyte cells were used to facilitate the portable electronics revolution, with solid electrolytes limited to specialised applications, e.g., glassy LiPON electrolytes in thin-film batteries[66,67]. By the turn of the 21$^{st}$ century, Li-based batteries had become entirely dominant in terms of energy and power density, and ultimately few ceramic fast $Li^+$ conductors were known. It wasn't until the first decade of the 21$^{st}$ century that numerous materials breakthroughs were made, bringing ceramic electrolyte designs back into focus, Table 1.1.

**Table 1.1:** Chronology of ceramic electrolytes.

| | Time | Event |
|---|---|---|
| | 1833[a] | Ionic conduction in $PbF_2$ and $Ag_2S$ (Faraday) |
| | 1897[a] | Oxide ion conduction in $Y_2O_3$ doped $ZrO_2$ (Nernst) |
| | 1920[a] | Ionic conduction in silver halides (e.g., AgI) |
| | 1950[b] | Early attempts at Ag-based ASSBs |
| | 1957[c] | Ionic conduction in $Li_3N$ |
| | 1966[a] | Fast $Na^+$ conduction in $\beta$-Alumina (commercialisation of Na-S secondary cells) |
| | 1970[b] | Development of LiI-based primary cells |
| | 1976[c] | NASICON structure discovered |
| | 1978[c] | LISICON structure discovered |
| | 1985[b] | Development of ZEBRA cells |
| | 1993[c] | LiPON-based thin film ASSBs |
| | 2000[c] | First thio-LISICON sulphides synthesised |
| Age of new fast $Li^+$ conducting ceramics | 2005[c] | Development of Glassy LPS electrolytes |
| | 2007[c] | Fast $Li^+$ conduction in LLZO oxides |
| | 2008[c] | Fast $Li^+$ conducting argyrodite sulphides (e.g., $Li_6PS_5Cl$) |
| | 2011[c] | Thio-LISICON sulphides with comparable conductivity to liquid electrolytes ($Li_{10}GeP_2S_{12}$) |
| | 2012[c] | Fast $Li^+$ conducting anti-perovskite oxides |
| | 2018[d] | Fast $Li^+$ conducting halides (e.g., $Li_3YCl_6$) |

[a]Bruce *et al*.[63] [b]Owens *et al*.[64] [c]Chen *et al*.[68] [d]Nie *et al*.[69]

Since the mid-2000s, newly discovered sulphide electrolytes have demonstrated $Li^+$ conductivities comparable to, or even greater than, that of liquid electrolytes at room temperature[70–72], garnet oxides based on the nominal formula $Li_7La_3Zr_2O_{12}$ (LLZO) have been discovered as part of a small subset of fast conductors stable against Li metal[73,74], and intriguing new lithium halides have demonstrated high oxidative stability[75]. This rapidly expanding repertoire of fast $Li^+$ conducting ceramics has heralded a new wave of interest in the development of high-performance solid-state batteries, and a large amount of research in the last decade has been focused on understanding their interactions with potential electrodes. $Li^+$ ion conducting oxides, halides and sulphides are at the centre of the research movement and so the next section of this thesis will focus on their respective properties, highlighting their merits and drawbacks in the context of 'high-performance' cells.

### 1.3.2 Solid electrolyte properties: requirements and classes

#### 1.3.2.1 Solid electrolyte requirements

To enter consideration as a candidate electrolyte for high-performance solid-state batteries, a material must begin to satisfy the following general criteria:

- **High ionic conductivity at room temperature.** Whilst common liquid electrolytes have total conductivities around $10^{-2}$ S/cm[76] their low transference numbers ($t_{Li+} < 0.5$) mean that this often corresponds at best to several mS/cm of $Li^+$ ion conductivity. Consequently, it has often been suggested that single ion conducting solid electrolytes will require conductivities of just $10^{-3}$ S/cm at room temperature[77]. Whilst this is reasonable for the separator, increased ionic tortuosity within the composite cathode may necessitate conductivities upwards of $10^{-2}$ S/cm to match the performance of liquids[55,78].
- **Low electronic conductivity.** Aside from preventing self-discharge, low electronic conductivity is necessary to reduce internal Li plating and dendrite growth[79]. Because any electron mobility is much greater than the ionic mobility, only a relatively small number of electronic carriers can degrade $t_{Li+}$ to an unacceptable level[63].
- **A low resistance to ion transfer across electrode interfaces.** Generally, interfacial resistance is dictated both by electrochemical stability and mechanical properties. Whilst few fast $Li^+$ ion conductors are stable across entire operating voltage ranges, any resultant degradation layers must be self-passivating, highly conductive and/or very thin[47,48]. Electrolytes which can mechanically deform to enable conformal electrode interfaces are preferred, with elastic deformation ideal for buffering electrode volume changes during cycling[49,80].
- **High critical current densities.** To charge Li anodes at practical rates, a solid separator is needed which does not suffer from Li dendrite penetration during Li plating

at current densities of at least 5 mA/cm$^2$.[54,81] This is often related to both the microstructure and mechanical properties of the material.[82,83]

- **Low cost.** Whilst ease of processibility into dense thin films will be a critical cost consideration, so too will the materials costs. However, it is often difficult to gauge the final price of a material as supply and demand, synthesis and production and other factors are involved. Utilisation of resource-critical elements will likely be a significant cost risk. Consequently, the use of rare earth elements should be avoided, and the density of lithium ions considered, see Figure 1.4.[18]

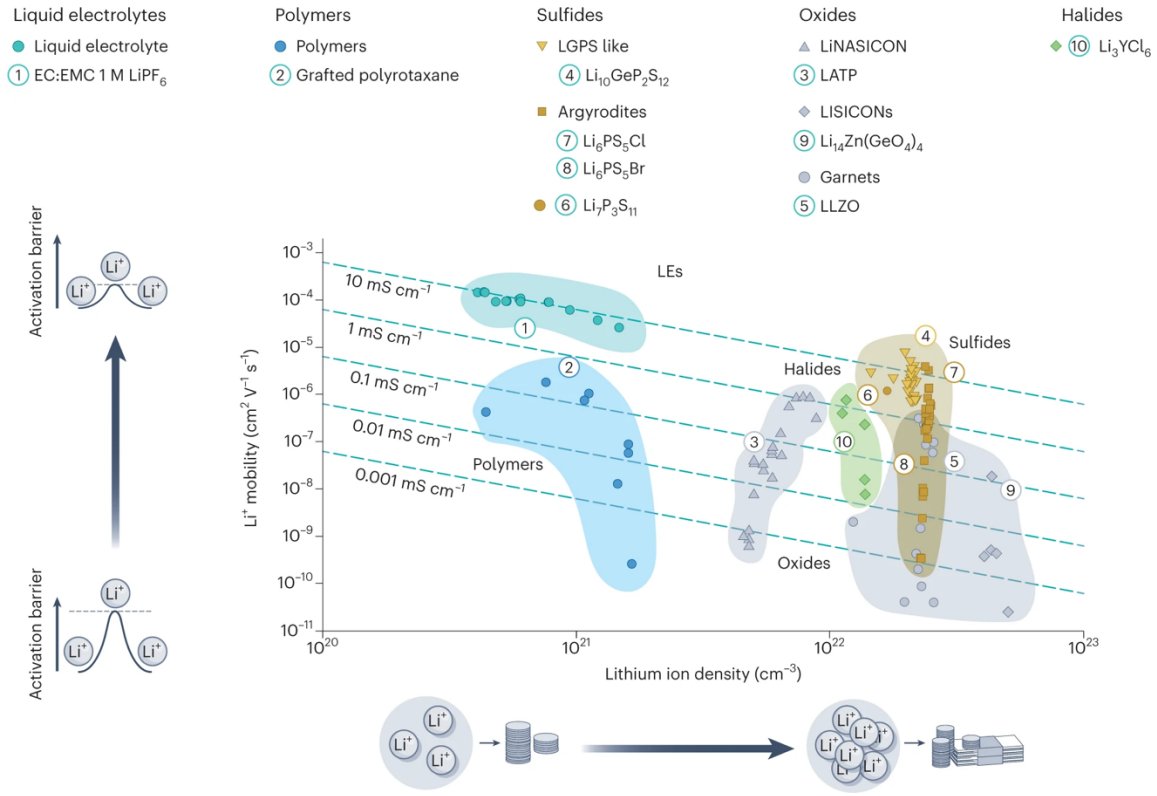



**Figure 1.4:** Figure from Zeier *et al.*[18]. Lithium-ion conductivity as a product of ion mobility, charge (constant, not shown) and ion concentration (as ion carrier density). Solid electrolytes with equal conductivity lie on dotted isoconductivity lines. Reproduced with permission from Springer Nature.

Whilst there is considerable diversity within each, for brevity, ceramic electrolytes used commonly in today's solid-state battery research will be discussed by their materials class.

#### 1.3.2.2 Oxides

Several crystallographic families have produced fast $Li^+$ ion conducting oxides including LISICONs[‡] (e.g., $Li_{14}ZnGe_4O_{16}$), Li-NASICONs[§] (e.g., $Li_{1.5}Al_{0.5}Ge_{1.5}(PO_4)_3$) and perovskites (e.g., $Li_{0.33}La_{0.57}TiO_3$), but their extreme instability with Li metal (due a continuously reactive MIEC[**] interphase) has limited their interest[84–86]. In 2007, a series of garnets based on the nominal formula $Li_7La_3Zr_2O_{12}$ (LLZO) were shown to exhibit faster ionic conduction as well as a rare stability with lithium[73,87]. The avoidance of thick degradation layers when interfacing with lithium anodes, means in principle a low impedance interface can be achieved, yet in practice the formation of a resistive layer of $Li_2CO_3$ and LiOH has proven difficult to avoid[88–90]. The limited reaction of oxide electrolytes under air exposure is far superior to their halide and sulphide counterparts, with this seen as a major benefit to industrial processing. Yet, the high sintering temperatures needed to facilitate even modest $Li^+$ conductivities would be costly if performed at scale. Sintering also poses a serious problem when considering an oxide-based composite cathode, since the limited thermal stability of most cathode active materials rules out the possibility to co-sinter[91,92]. Even if co-sintering were to be achieved, the lower ionic conductivities and the stiff brittle nature of oxides could still limit performance. With this in mind, oxide electrolytes are primarily under consideration as part of hybrid solid-state battery designs in which a separate catholyte is used. Still, these designs are facing a number of issues at their heteroionic interfaces and may have limited safety benefits[93,94].

Overall, oxide electrolytes make up a key materials class of solid electrolytes with opinions split regarding the potential scope of their use in future applications[93,94].

#### 1.3.2.3 Halides

Over the past few years in particular, a host of lithium halide electrolytes have arisen based on the $Li_3M^{3+}Cl_6$ structure, these include $Li_3InCl_6$, $Li_3YCl_6$ and $Li_3ScCl_6$.[95–97] These electrolytes

[‡] LISICON: Li SuperIonic CONductor
[§] NASICON: Na SuperIonic CONductor
[**] MIEC: Mixed ionic and electronic conductor

have gained interest due to their combination of fast ion conduction (which can be maintained across mechanical pressed grain boundaries) and their notably high oxidative stabilities[75,98]. Recent studies have shown promising indications that halide electrolytes could act as effective $Li^+$ pathways within composite cathodes without the need to sinter, and without the need to coat the active cathode material[57,99]. Whilst conductivities would need to be raised to enable their use in thicker electrodes, the avoidance of a resistive degradation layer or coating is a significant advantage.

During their emergence, two key limitations were clear: extreme moisture instability and very poor stability with lithium metal anodes. Whilst halide electrolytes generally do not degrade in the presence of moisture to form toxic gases, their high solubility means little material is recoverable after exposure, so strict and potentially costly procedures would be required for mass production[96,100]. Additionally, newly emerging halides have almost exclusively reacted with lithium metal to form an MIEC interphase which continually grows in thickness over time and during cycling[101]. Consequently, cells interfacing halides with lithium anodes face rising internal resistances as well as unacceptable electronic leakage currents. Interestingly, a recent study reported the discovery of a halide ($Li_{0.388}Ta_{0.238}La_{0.475}Cl_3$) electrolyte demonstrating both high oxidative stability and the formation of a passivating SEI with lithium metal[102]. Whilst these results are yet to be reproduced, the study embodies the hope held by some that further materials discoveries (e.g., new halides) may offer the silver-bullet solution to a single electrolyte all-solid-state battery.

#### 1.3.2.4 Sulphides

Of the new fast $Li^+$ ion conducting electrolytes discovered, the most conductive are sulphide-based with these either being glasses based on $Li_2S$-$P_2S_5$, or crystalline materials based on either the thio-LISICON (e.g., $Li_{10}GeP_2S_{12}$) or argyrodite (e.g., $Li_6PS_5Cl$) structures[70,103,104]. As with halide electrolytes, sulphides are mechanically soft and permit a certain degree of plasticity, allowing them to retain facile ion conduction across mechanically pressed grain

boundaries[105]. Their mechanical properties combined with their high conductivities have made sulphides one of the electrolytes of choice for SSB composite cathode layers, but to sustain high performances, their limited stability requires cathode active materials to be coated so to avoid forming resistive degradation layers[106,107].

During exposure to moisture, sulphide electrolytes degrade and emit toxic $H_2S$ fumes which mandates strict requirements for their preparation. However, large-scale production of sulphide-based electrolytes is still potentially feasible within an acceptable cost using dry rooms[108]. Additionally, many sulphide electrolytes may be synthesised using routes that are potentially ideal for commercial applications (e.g., liquid-phase synthesis from suspension in organic solvents)[109].

Whilst no reported sulphide electrolytes are thermodynamically stable when in contact with lithium metal, several do react to form passivating interphase layers[47,48]. The conductivity and thickness of such layers are important in determining the feasibility of a given electrolyte for lithium anode SSBs. Li-argyrodite sulphide electrolytes, such as $Li_6PS_5Cl$, form exceptionally thin passivating interphases when placed in contact with lithium metal, and they have also demonstrated impressive performances when used in composite cathode layers (with coated active materials)[110,111]. Consequently, these electrolytes currently represent the most practical route a single electrolyte all-solid-state lithium anode cell.

The argyrodite-type $Li_6PS_5Cl$ electrolyte is used as a model solid electrolyte throughout the entirety of this thesis, and hence the next section will cover this family of electrolytes in more detail.

### 1.3.3 Li-argyrodite sulphide electrolytes

The argyrodite structure was originally found in the mineral $Ag_8GeS_6$ with its name loosely translating to "rich in silver" from Greek[112]. Today, its Li-analogues (Li-argyrodites) have attracted serious attention as candidate solid electrolyte materials. Whilst, overall, Li-argyrodites can be seen to follow the general ionic formula $Li^{+}_{12-m-x}(M^{m+}Ch^{2-}_{4})Ch^{2-}_{2-x}X^{-}_{x}$

(where $M$ = P, As, Ge, Si, Sn, Sb; $Ch$ = O, S, Se; $X$ = Cl, Br, I, $BH_4$), the materials of strong interest have been thiophosphates[77]. The simplest of these sulphides are $Li_7PS_6$ ($m$=5, $x$=0) compounds, but whilst high conductivities were measured in the high-temperature cubic phase, these materials crystallise into a low-temperature orthorhombic polymorph and display poor transport properties at room temperature[113]. Fortunately, the high temperature cubic polymorph can be stabilised by the replacement of one or more sulphide anions with a halide anion, resulting in a series of $Li_6PS_5X$ ($X$ = Cl, Br, I) compounds which show significant $Li^+$ transport properties at room temperature[104]. In recent years, the $Li_6PS_5Cl$ ($m$=5, $x$=1) composition has gained specific interest due to its combination of fast Li-ion conductivity and compatibility with lithium anodes.

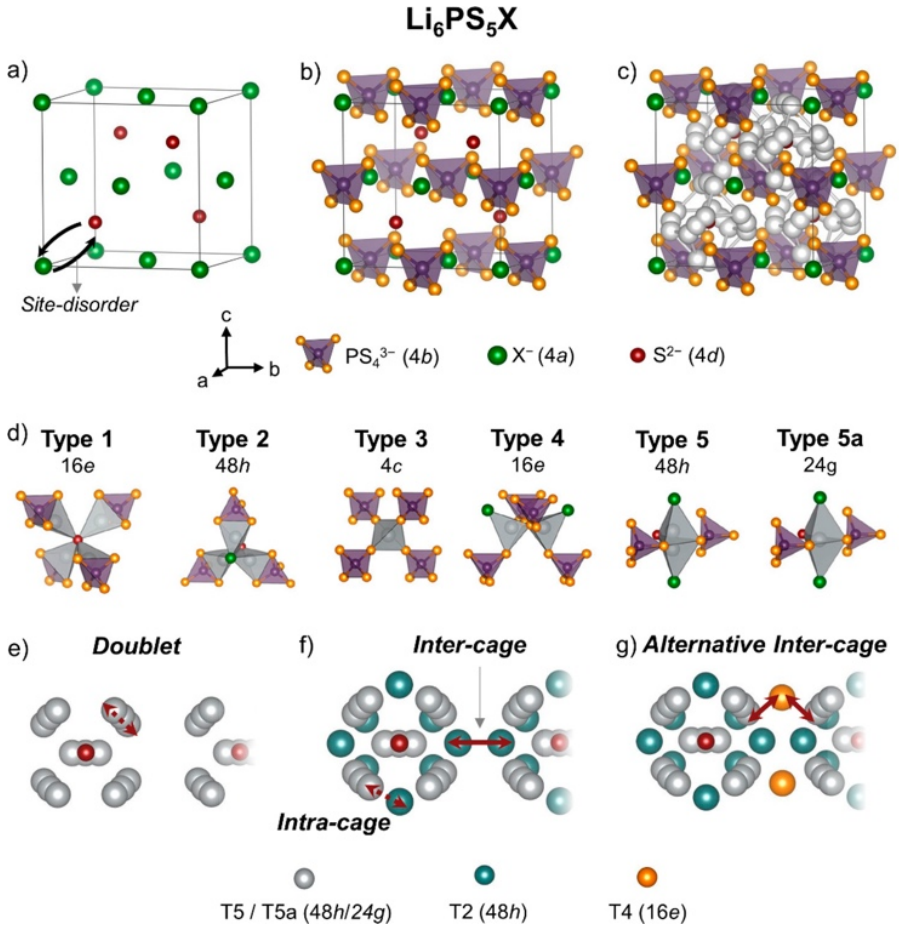



**Figure 1.5:** Figure from Nazar *et al.*[114]. Unit cell of the $Li_6PS_5X$ ($X$ = Cl, Br, I) $F\bar{4}3m$ cubic polymorph. In the ordered configuration, **(a)** $X^-$ anions form a face-centred cubic structure with $S^{2-}$ ions in half of the tetrahedral voids and **(b)** $PS_4^{3-}$ units in the octahedral interstices. Within such an anionic framework, **(c)** $Li^+$ sites form cage-like structures around the free sulphide positions. **(d)** Five different types of tetrahedral voids for potential lithium-ion occupations with their Wyckoff positions. The only possible 48h–48h jump is the doublet process **(e)**, while long-range intra- and intercage jumps **(f)** require lithium migration through 48h sites. In addition to 48h sites, **(g)** alterative

pathways may involve 16e sites for the intercage jump. Reproduced with permission from the American Chemical Society.

Understanding the origin of the high conductivity in the argyrodite-type $Li_6PS_5X$ ($X$ = Cl, Br, I) compounds necessitates an understanding of their structure. The crystallographic arrangement of $Li_6PS_5X$ materials, can be viewed through the framework of an fcc unit cell of halide ($X$) atoms, Figure 1.5a[104,114]. Within this unit cell, $PS_4^{3-}$ tetrahedra occupy the octahedral voids whilst half of the tetrahedral voids are occupied by 'free' $S^{2-}$, Figure 1.5a&b. It is around the 'free' $S^{2-}$ that cages of $Li^+$ sites (24g and 48h) exist in a partially filled arrangement, Figure 1.5c. Across these cage-like Li substructures, three-dimensional ionic conduction pathways exist[77,115]. The conduction pathways that occur throughout this substructure contain three types of jumps:

- **Doublet jumps.** These are between the different 48h and 24g sites within a cage (48h-24g-48h), Figure 1.5e.
- **Intra-cage jumps.** These are between 48h sites within a cage (48h-48h), Figure 1.5f.
- **Inter-cage jumps.** These are from one cage structure to a neighbouring cage (48h-48h), Figure 1.5f. These are the longest and hence the rate-determining-step in terms of long-range ionic conduction. Alternative pathways involving 16e sites have been proposed, but these have not been unequivocally observed, Figure 1.5g.

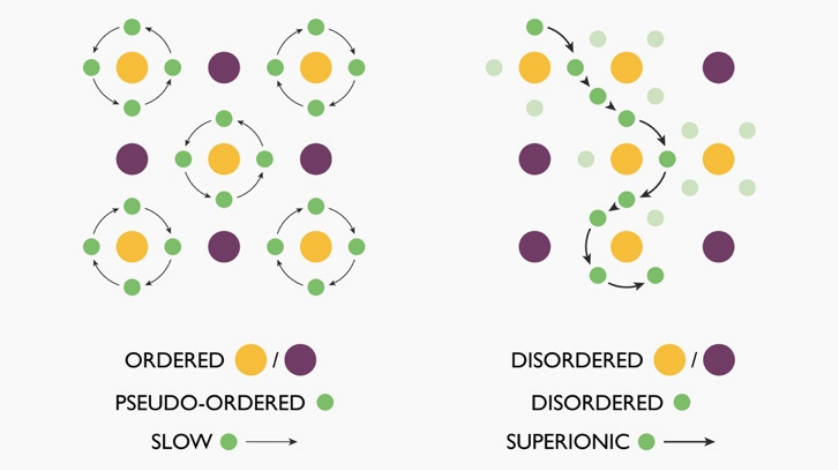



**Figure 1.6:** Figure from Morgan *et al.*[115]. Schematic illustration of how $X^-/S^{2-}$ (yellow/purple) site disorder can lead to fast $Li^+$ (green) conduction. Reproduced with permission from the American Chemical Society.

An important feature of the halide containing argyrodites is their ability to accommodate an intermixing of the halide ($X$) atoms and 'free' $S^{2-}$ between the 4a and 4c sites[77,114]. This $X^-/S^{2-}$ site disorder has been closely correlated to the lowering of jump activation energies and is seen as fundamental to the high observed $Li^+$ ion conductivities, see Figure 1.6. For example, low conductivities are observed in $Li_6PS_5I$ compounds, all of which display high $I^-/S^{2-}$ site ordering[116]. Whereas, doping the $M$ (phosphor) site aliovalently (e.g., $Li_{6+x}P_{1-x}M_xS_5I$) can induce $I^-/S^{2-}$ site disordering giving a range of compounds with conductivities as high as 5 mS/cm at room temperature[117,118]. $X^-/S^{2-}$ site disorder can be affected by varying the halide dopant, e.g., by mixing Cl and Br or simply altering the halide content[119]. The large phase width of $Li_6PS_5Cl$ has recently been exploited to develop a number of halide rich compositions (e.g., $Li_{5.5}PS_5Cl_{1.5}$) in which increased vacancy concentration combined with $Cl^-/S^{2-}$ site disordering lifts conductivities as high as 12 mS/cm[120].

Aside from high ionic conductivity, the interest in Li-argyrodites is also due to a perceived compatibility of $Li_6PS_5Cl$ electrolytes with Li anodes. Whilst the two materials undergo a reaction when placed in contact, the reaction layer that forms is thin and increases in cell resistivity are potentially affordable[121–123]. The reason for this is understood by considering the reaction products. When placed in contact with lithium metal, a host of binary compounds ($Li_2S$, $Li_3P$ and $LiX$ ($X$ = Cl, Br, I)) are formed at the points of contact[121–123]. Due to the electronically insulative nature of these compounds and slow reaction kinetics, this layer essentially forms a thin *in-situ* passivating film no more than a few tens of nanometers in thickness[121]. Such a thin layer results in minimal interfacial strain[124]. Additionally, the reasonable ionic conductivity of the binary compounds means the layer does not severely limit ion transfer across the interface[122]. More on the electrochemical stability of solid electrolytes in contact with lithium metal will be discussed in the next section.

## 1.4 The Li metal / solid electrolyte interface

### 1.4.1 Challenges at the interface

#### 1.4.1.1 Electrochemical stability

Whilst this thesis will primarily focus on morphological degradation during cycling, it is important to hold a full appreciation of any interfacial phenomena which may occur on resting. In particular, the electrochemical stability of the ceramic electrolyte when in contact with lithium metal is of paramount importance when designing a functional interface.

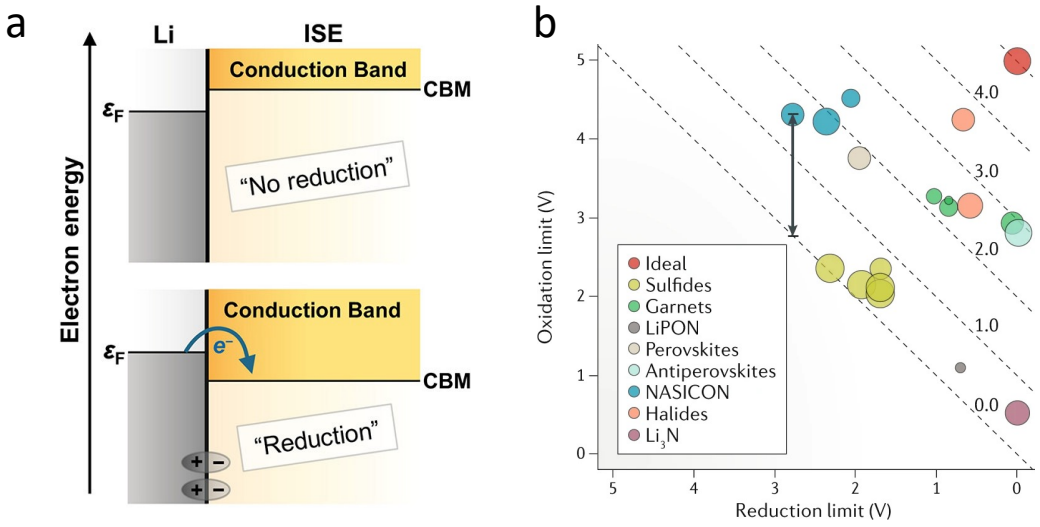



**Figure 1.7: a** Electrochemical stability of a solid electrolyte in contact with lithium metal according to the simplified "band gap approach" assuming that reduction of the electrolyte takes place if its conduction band edge lies below the Fermi level $\varepsilon_F$ of lithium metal. The interface dipole under the assumption of a purely electronic transfer is also indicated. **b** Electrochemical stability windows of common solid electrolytes. Each solid electrolyte is represented by a circle with an area proportional to the order of magnitude of its ionic conductivity (in μS $cm^{-1}$). The stability window is the vertical distance from the centre of the circle to the diagonal line, as illustrated by the arrow. The dashed lines are the contours of the width of the stability window. Adapted from Janek *et al.*[51] and Ceder *et al.*[48] with permission from the American Chemical Society and Springer Nature.

When placed in a cell, the electrolyte's stability with either electrode is determined by its electrochemical stability window, which accounts for both purely chemical potential driven reactions and electric potential-driven instability[63,125]. Under reducing conditions at the anode side, the position of the electrolyte's conduction band minimum (CBM) can be used as an estimate for stability. If the CBM lies below the Fermi level $\varepsilon_F$ of a metallic anode, there will be driving force for electrons to transfer from the metal to the electrolyte, and stability is

unlikely[51,126], see Figure 1.7a. The ideal solid electrolyte candidate is thermodynamically stable when in contact with lithium metal, but almost all the known fast $Li^+$ conducting ceramics react to form some kind of solid electrolyte interphase (SEI) upon contact[48,122], Figure 1.7b. In general, it is useful to distinguish three types of Li/SE interface:

- A nonreactive, thermodynamically stable, or fully kinetically stabilized Li/SE interface, where no solid electrolyte interphase (SEI) forms, Figure 1.8a&d.
- A reactive and unstable Li/SE interface, where a mixed ionic and electronic conducting interphase (MIEC) forms, which results in unwanted progressive growth of the interphase, Figure 1.8b&e.
- A kinetically self-limiting Li/SE interface with the formation of an almost exclusively ion conducting metastable SEI, Figure 1.8c&f.

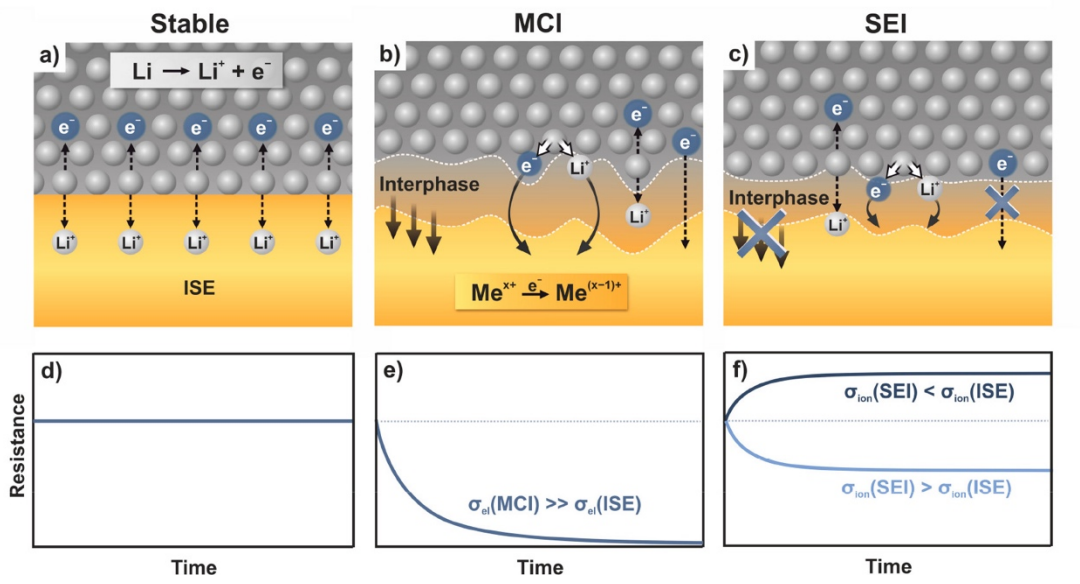



**Figure 1.8:** Figure from Janek *et al.*[51]. Three types of interphase/interface between lithium metal and an inorganic lithium SE: **a** Thermodynamically stable interface, **b** reactive mixed-ionic/electronic conducting interphase MIEC (also known as MCI), and **c** metastable, kinetically stabilized solid electrolyte interphase (SEI) with low partial electronic conductivity. **d–f** Expected time dependent resistance change of the respective interface/interphase type. Reproduced with permission from the American Chemical Society.

As for most liquid electrolyte cells, parabolic growth of the interphase resistance is widely reported for solid-state batteries, which hints towards a simple diffusion-limited growth mechanism whereby the flux $j_{Li}$ of lithium atoms ($Li^+ + e^-$) across the interphase layer can be modelled according to eq. 1.1.[121,127,128]

$$j_{Li} = \frac{\mu_{Li}^{0}(\sigma_{el}\sigma_{Li^+})}{F^2 l_{SEI}(\sigma_{el} + \sigma_{Li^+})} \quad (1.1)$$

with $\sigma_{el}$ = electronic partial conductivity of the interphase, $\sigma_{Li^+}$ = ionic partial conductivity of the interphase, $l_{SEI}$ = thickness of the interphase, and $F$ is Faraday's constant = 96,485 C/mol. Accordingly, changes in the interphase resistance with time strongly depend on the ionic and electronic partial conductivity of the interphase compounds, with an ideal interphase having both high ionic and low electronic conductivity. To have a truly kinetically self-limiting Li/SE interface requires an infinitely low partial electronic conductivity of the SEI. Consequently, every interphase of this kind is in principle an MIEC. However, interphases which are predominantly composed of ion conducting compounds such as $Li_2S$, $Li_3P$, $Li_2O$, $Li_3N$ and LiCl, are generally approximated as SEI-type, and indeed these electrolytes tend to enable better performances in Li-SSBs[121,129].

#### 1.4.1.2 Void formation during Li stripping

At the Li/SE interface, Li ions within the solid electrolyte may exchange readily with lithium atoms in the metal electrode. During the anodic process, a lithium ion passes across the Li/SE interface leaving an electron and a vacant site on the surface of the lithium metal. The ion then goes on to occupy an interfacial vacant site in the solid electrolyte[51]. Due to the incoherent nature of the interface, these vacancies are often treated as if individually injected into the metal anode[130]. For interfacial contact to be maintained, newly injected metal vacancies must be transported away from the interface via diffusion. If vacancy diffusion in the metal is in local equilibrium with the injection rate, the interface can retain its morphological stability in a stable stationary state[††], Figure 1.9. When injection rates exceed that which can be replenished by diffusion, morphological changes occur, manifesting as the formation of void space at the interface and a progressive loss of contact[132]. Due to the limited self-diffusion within Li metal,

[††] Since the relaxation of point defects in the electrolyte is much faster than the relaxation process in the lithium metal, the diffusion of vacancies within lithium metal (the ability of Li atoms to self-transport) is often considered rate-limiting and the relaxation in the ionic conductor is typically neglected.[131]

these morphological degradation processes occur at the rates needed for practical application and so their consideration is important.

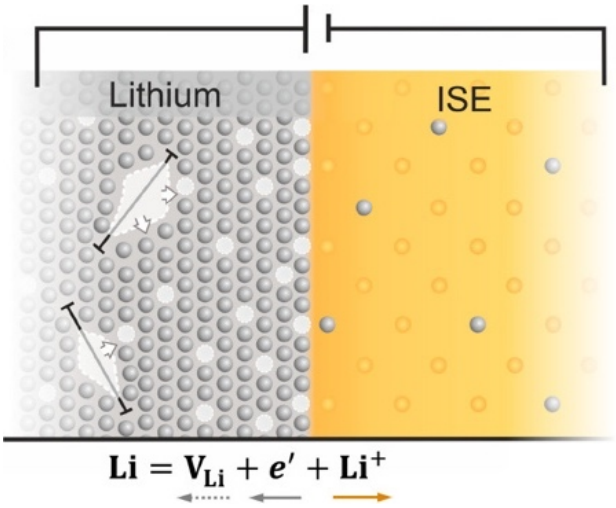



**Figure 1.9:** Figure from Janek *et al.*[51]**.** Simplified schematic showing the microscopic interfacial processes during electrodissolution assuming vacancy driven ionic transport. Occupied lattice sites in the inorganic solid electrolyte (ISE) are shown as grey balls. In lithium metal, dislocations can act as sinks for vacancies increasing the vacancy concentration gradient. Adapted with permission from the American Chemical Society.

Until the 1980s, there were few publications dealing with the anodic dissolution of metals into solids. In early reports, interfacial instability during Li stripping was noted in electrochemical measurements[133,134]. In more recent years, important developments in understanding have followed from studies which combine electrochemical measurements with imaging. Pioneering work from Janek *et al.*[132] performed two-electrode cycling of Li/LLZO symmetric cells in combination with EIS, demonstrating that vacancies can accumulate into larger and larger void clusters during a single stripping process. By performing *ex-situ* SEM imaging before and after the stripping process, the morphological nature of the contact loss was demonstrated for the first time, see Figure 1.10. The dependence of void formation on the current density of stripping was also investigated for cells under no stack pressure, finding that below a critical current (set by the self-diffusion in the Li anode) voids were not observed to form, but that above this current density interfacial contact loss occurred.

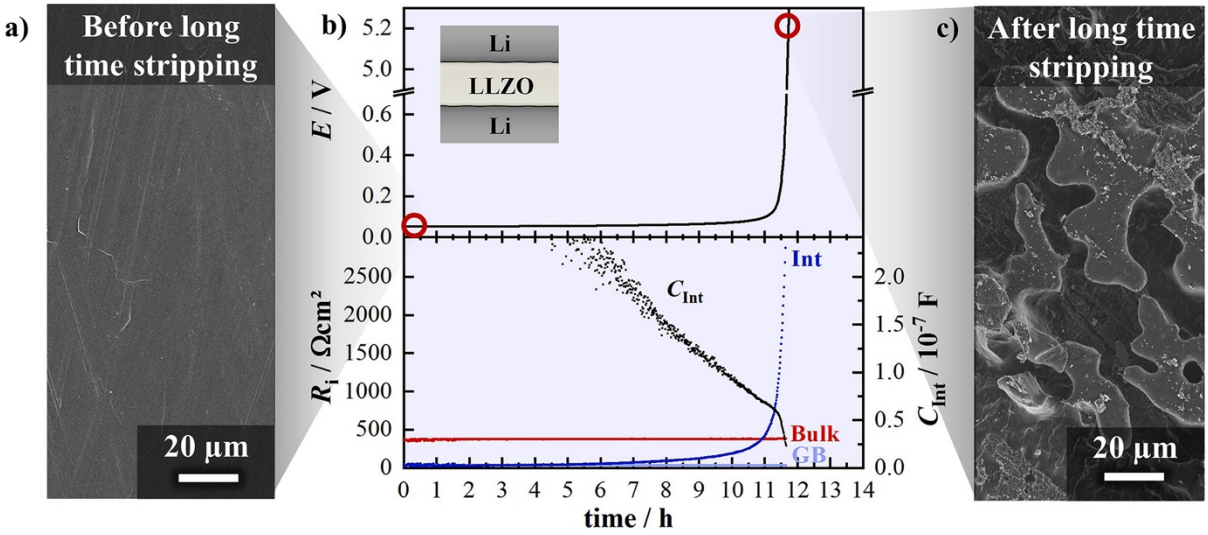



**Figure 1.10:** Figure from Janek *et al.*[132]. **a** Morphology of the lithium metal anode side facing the solid electrolyte before assembling the cell. **b** The voltage profile during stripping (top) as well as the associated changes in bulk and interfacial resistances (with interfacial capacitance) throughout this process (bottom). **c** Morphology of the lithium metal anode after the stripping process, showing void formation at the interface. Reproduced with permission from the American Chemical Society.

Following this, a string of works by Bruce *et al.* considered the development of voids over multiple cycles[135–137]. By combining symmetric Li/$Li_6PS_5Cl$ cycling with *in-situ* XCT imaging, voids formed during initial Li stripping were observed to occlude during subsequent plating only to be uncovered as part of larger contact losses during later cycles, see Figure 1.11. As well, Bruce *et al.* investigated both the temperature and pressure dependence of the void formation[135,137]. With a melting point of only 453 K, Li metal readily undergoes mechanical creep at room temperature and hence even small stack pressures can facilitate the mass transport of Li towards the Li/SE interface. By subjecting cells to higher temperatures and stack pressures, Bruce *et al.* demonstrated that increases in both the mechanical transport mechanisms (e.g., plastic creep flow) and the inherent chemical transport of $Li^+$ vacancies could raise the critical currents under which void formation occurred.

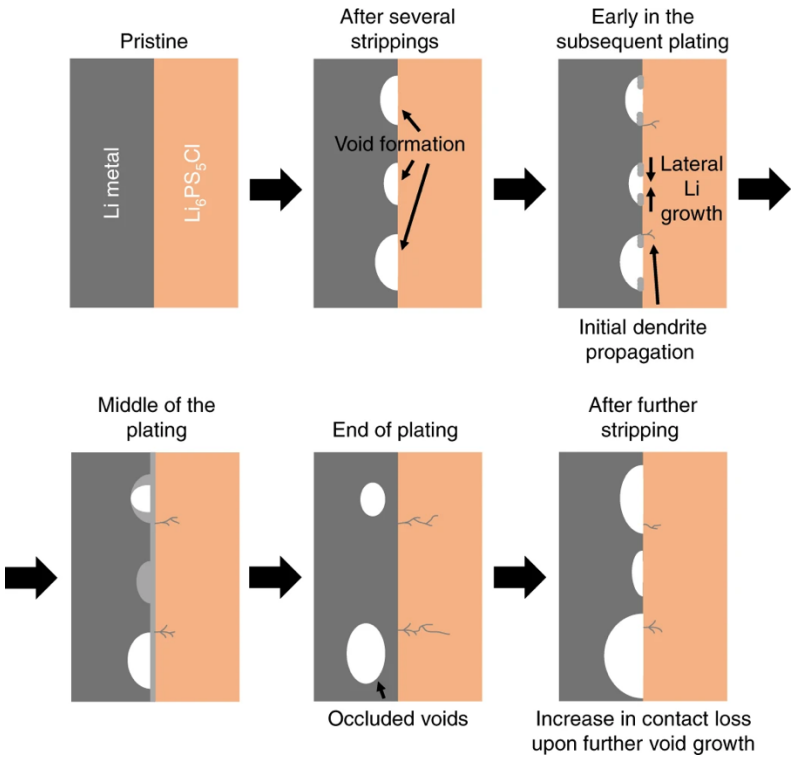



**Figure 1.11:** Figure adapted from Bruce *et al.*[135]. A sequence from pristine to after several strippings and platings of Li metal: voids form on stripping; lateral growth of a thin Li film across the electrolyte surface (nucleating where void edges meet the electrolyte) on subsequent plating results in low plating polarization and formation of occluded voids. Some voids are eliminated on plating, but the occluded voids reopen on subsequent stripping leading to accumulation of voiding and increasing loss of contact with cycling. This increases stripping polarization and results in dendrites on plating. Reproduced with permission from Springer Nature.

An understanding of void formation during Li stripping is crucial when studying Li plating failures. The works of Bruce *et al.* showed that not only will contact loss increase cell overpotentials during cycling, but local current densities at remaining areas of contact will increase[135]. The mechanisms responsible for failure during Li plating, e.g., the formation of Li dendrites, are active only above threshold local current densities. As voiding worsens with cell cycling, the area of contact between the metal anode and solid electrolyte decreases with each cycle, meaning local currents increase until the thresholds for Li dendrite formation are inevitably met, see Figure 1.11. Any study aiming to mechanistically understand Li dendrites on plating must therefore be conscious of void formation during stripping.

#### 1.4.1.3 Dendrite formation during Li plating

Under cathodic load, lithium ions at the surface of the electrolyte are reduced, plating out as lithium atoms at the Li/SE interface. Layer-by-layer deposition is desired, but in practice this is difficult to achieve, especially at high deposition rates. Ultimately, Li/SE interfaces within solid-state cells are far from ideal. Insulating contaminants, flaws in the solid electrolyte, pre-existing porosity in the metal anode and electrode edge-related current enhancement amongst other factors can lead to inhomogeneous Li plating and morphological degradation[51]. During the fast charging of Li-SSBs, short circuits are widely observed. While dielectric breakdown of the ceramic or its grain boundaries at high applied potentials could theoretically lead to cell failure, the short circuits observed experimentally are typically caused by the growth of lithium metal filaments through the solid electrolyte, commonly known as Li dendrites[138,139].

Interestingly, Li dendrites are observed only to penetrate through solid electrolytes above a certain threshold plating current density, termed the 'critical current density' or 'CCD'.[140] Critical current values appear to be dependent on a multitude of factors such as the type of solid electrolyte, its microstructure, its mechanical properties, its electronic conductivity as well as the properties of the metal electrode. Yet so far, under any practical conditions, the measured critical currents of every major candidate solid electrolyte have remained too low for commercial application[138–140]. Whilst significant advances in understanding have been made, there remains a wide range of conflicting ideas surrounding how dendrites occur in ceramic electrolytes[51]. Consequently, the dendrite problem still stands as the foremost barrier to any practical application of Li-SSB designs.

The primary focus of this thesis centres around an investigation of Li dendrites in $Li_6PS_5Cl$ electrolytes, hence the remainder of this introduction will cover the key observations and leading understanding of Li dendrites in ceramic electrolytes, as well as summarising common mitigation strategies.

### 1.4.2 Key experimental observations of dendrites

#### 1.4.2.1 Post-mortem microscopy

Following the discovery of superionic LLZO electrolytes stable with lithium metal, numerous studies were performed aimed at probing the performance of these electrolytes in symmetric Li cells[141–147]. It was during these early works that widespread reports of short circuits resulting from lithium filaments first emerged. At this stage, the characterisation of Li filaments primarily came in the form of post-mortem imaging. Specifically, after peeling away the Li electrodes, cross-sectional images would be collected at ‘dark regions' of the short-circuited LLZO surface, see Figure 1.12a-c. Curiously, despite multiple studies using virtually the same methodology, there was still considerable variation in what was observed. For example, in 2015 Ce-Wen Nan’s research team noted that Li plating had primarily occurred within interconnected subsurface pores, whereas only several months later, imaging by Sakamoto *et al.* showed that Li plating had occurred almost exclusively along the grain boundaries[144,145], Figure 1.12d-i. Around the same time, multiple post-mortem investigations were also made by researchers at Imperial College London which appeared to show Li could even deposit directly within isolated pores[146,147], see Figure 1.12j&k.

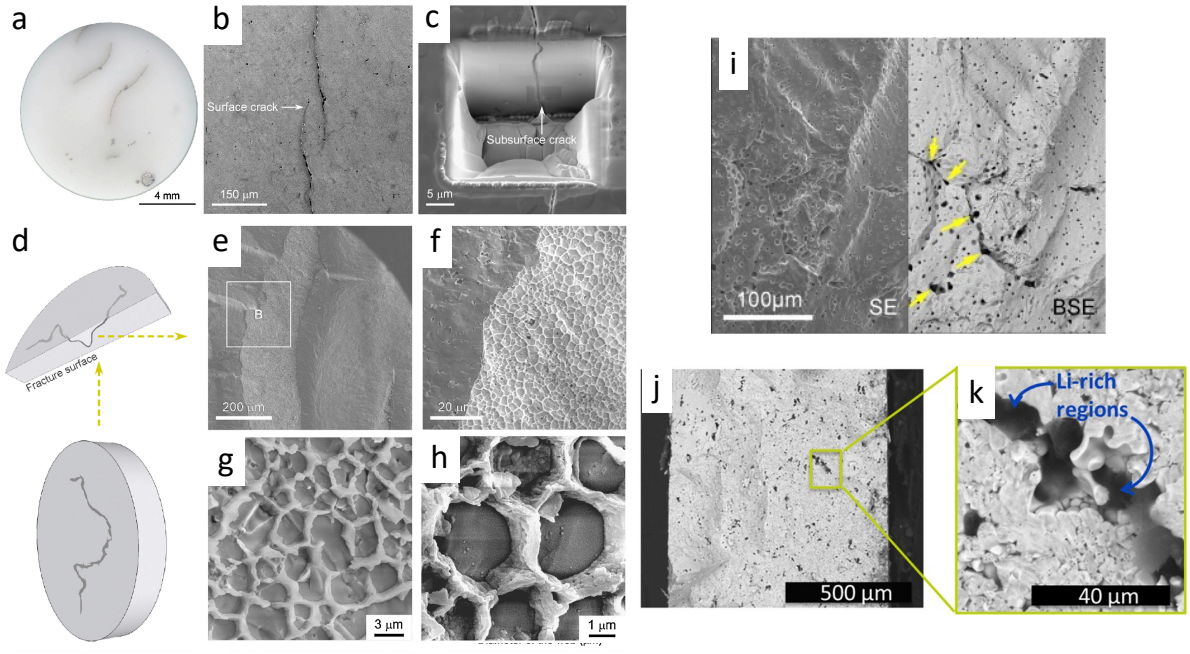



**Figure 1.12: a-h** Reproduced from Sakamoto *et al.*[145]. **a** An optical image of a cycled LLZO pellet showing the appearance of black linear features, believed to be caused by the propagation of metallic Li, **b** SEM image of a polished surface exhibiting fissures on the surface once in contact with a Li electrode, **c** SEM image of a subsurface fissure excavated by FIB. **d** Illustration of a fractured surface through a black linear feature, **e-h** SEM images of fracture surface with progressively higher magnification showing lithium dendrites at grain boundaries. **i** Reproduced from Nan *et al.*[144] and indicates Li plating in interconnected pores. **j** and **k** are reproduced from Kilner *et al.*[146] and indicates Li plating into isolated pores. Adapted with permission from the American Chemical Society and Elsevier.

#### 1.4.2.2 *Operando* microelectrode set-ups

Ultimately, the post-mortem characterisation of dendrites raised more questions than it answered, and serious efforts were made to capture their full development. In 2017, Yet Ming Chiang's research team published a seminal study in which an *operando* microprobe-optical microscopy set-up was used to record incidences of Li penetration into a range of solid electrolytes[148], see Figure 1.13a. This novel set-up took advantage of the translucent nature of highly dense solid electrolytes to image the morphology of newly formed Li dendrites.

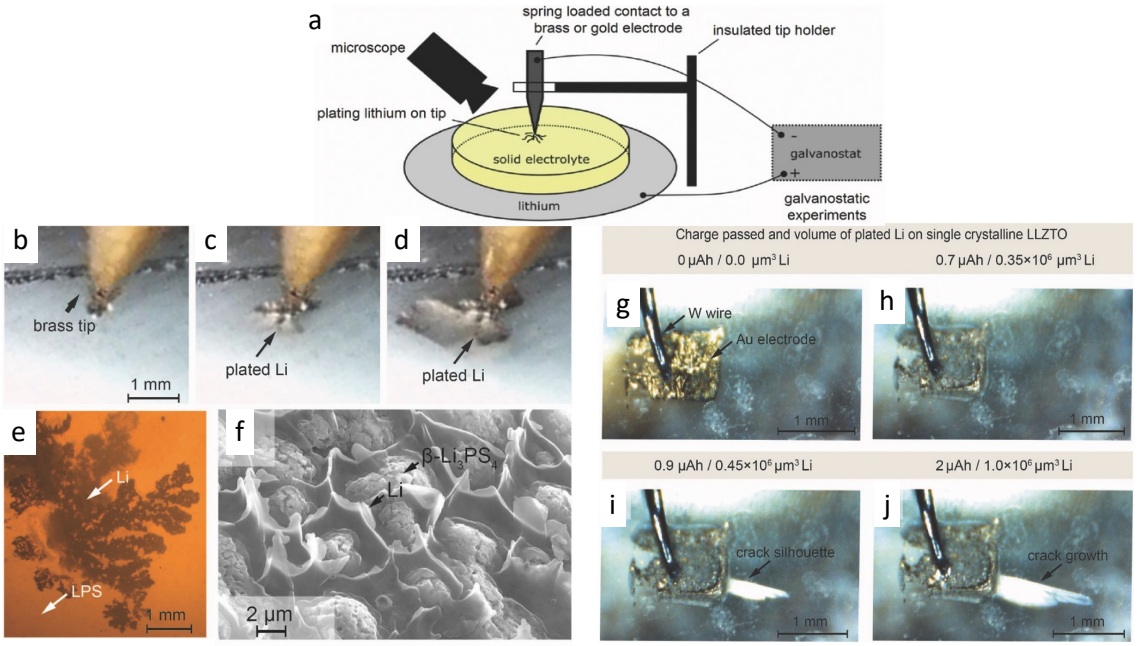



**Figure 1.13:** Adapted from Chiang *et al.*[148]. **a** Schematic of *operando* microprobe-optical microscopy set-up. **b-d** Lithium metal deposition propagates into densely pressed polycrystalline β-$Li_3PS_4$ from a brass tip electrode. **e** Viewed in transmission optical microscopy, the lithium metal network shows a branching pattern. **f** Cellular network of Li on β-$Li_3PS_4$ fracture surface. **g-j** Optical microscopy images of a polished single crystal of LLZTO with sputtered gold electrode during galvanostatic deposition of lithium metal. Uniform plating behaviour appears to take place until a crack is observed to propagate (white silhouette). Reproduced with permission from John Wiley and Sons.

Key observations were made not only on both polycrystalline and single crystalline LLZO-type oxides, but also on relatively understudied sulphide electrolytes such as crystalline $Li_3PS_4$ and glassy LPS. Interestingly, quite different observations were made across the material classes. For example, the *operando* imaging of dendrites within crystalline $Li_3PS_4$ electrolytes revealed a branching cloud-like morphology progressing from the surface, within which further cross-sectional imaging would reveal a cellular pattern of Li metal, Figure 1.13b-f. In contrast, no such observations were made for dendrites in LLZO-type materials, and instead Li ingress was seen to cause rapid fracturing of the electrolyte, producing large and long Li filled cracks[148], Figure 1.13g-j.

Of perhaps the most importance were findings surrounding the sensitivity of dendrite formation to pre-existing surface flaws. For example, the defect-free fracture surface of a glassy LPS electrolyte was shown to withstand high plating currents without any signs of Li ingress. Whereas by scratching the same surface and subjecting it to the same currents, Li dendrites

were shown to fracture deep into the solid electrolyte with minimal plating across the electrolyte surface[148].

Inspired by the work of Yet Ming Chiang's group, numerous studies have since used analogous *operando* microprobe set-ups to observe the development of Li dendrites. In accordance with Chiang *et al.*[148], Janek's research team observed that Li ingress can be avoided at high current densities in defect-free regions of LLZO and $Li_6PS_5Cl$ electrolytes by depositing Li microelectrodes, whereas Li deposition would readily fracture the electrolyte when the electrodes were placed in regions containing grain boundaries, cracks and porosity[149,150], see Figure 1.14. In recent studies by Fincher *et al.* and McConohy *et al.*, the progression and directionality of Li dendrites in LLZO-type electrolytes was shown to be heavily influenced by the application of unidirectional stress[151,152]. As well, McConohy *et al.* demonstrated that dendrite penetration events were stochastic and followed a Weibull distribution[152]. Consequently, these studies have concluded Li dendrites are mechanically driven and propagate primarily through the fracture of the electrolyte.

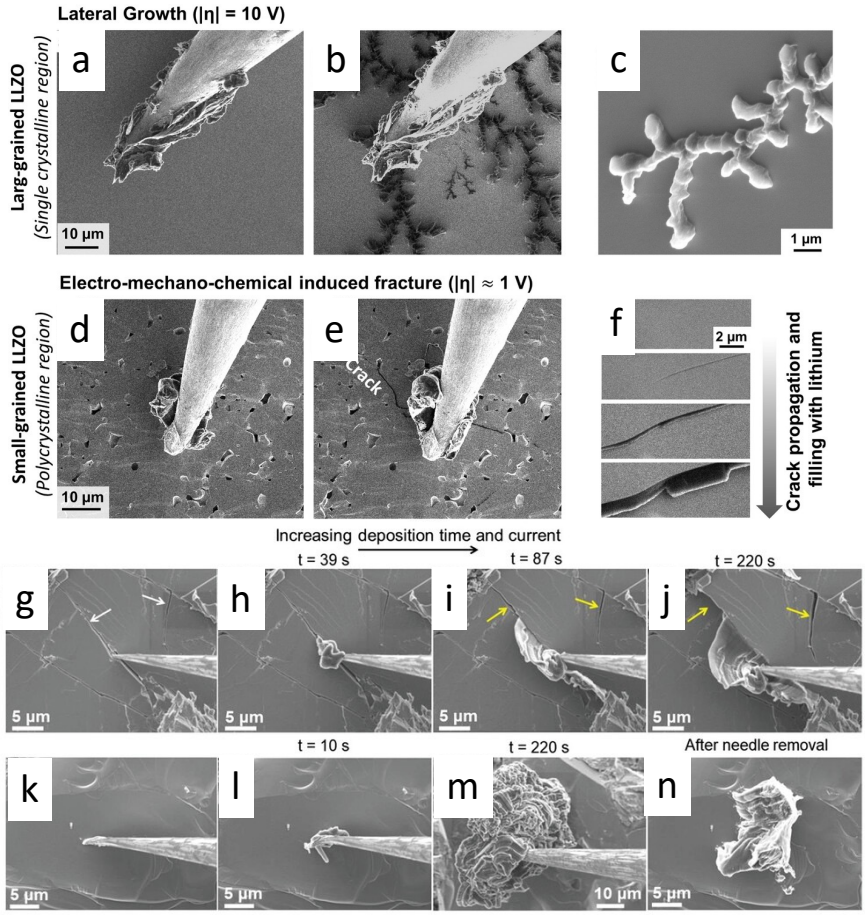



**Figure 1.14:** Figure is reproduced from the SEM-microprobe studies of Krauskopf *et al*.[149] and Singh *et al*.[150] **a-c** shows lateral Li growth at a defect-free surface of LLZO. **d-f** shows crack initiation and Li ingress into an LLZO interface containing defects. **g-j** Li insertion and crack extension in $Li_6PS_5Cl$ at grain boundary/pre-cracked surface. **k-n** Vertical growth of lithium occurs on a flaw-free $Li_6PS_5Cl$ grain surface region. Reproduced with permission from John Wiley and Sons.

Whilst some streams of consistency have been made through the *operando* microscopy of Li dendrites, overall, there still remains a considerable diversity in what has been observed. This is perhaps most evident in the work by Dasgupta *et al.*[153] who performed an impressive series of *operando* video experiments. In this work, Li dendrite penetration was observed in both LLZO-type and glassy LPS electrolytes. Depending on the interface quality and plating/stripping parameters, different crack-like features presented during Li ingress in a somewhat unpredictable manner. Straight, branching and pot-hole-like spallation cracks were all identified in both types of electrolytes[153], see Figure 1.15.

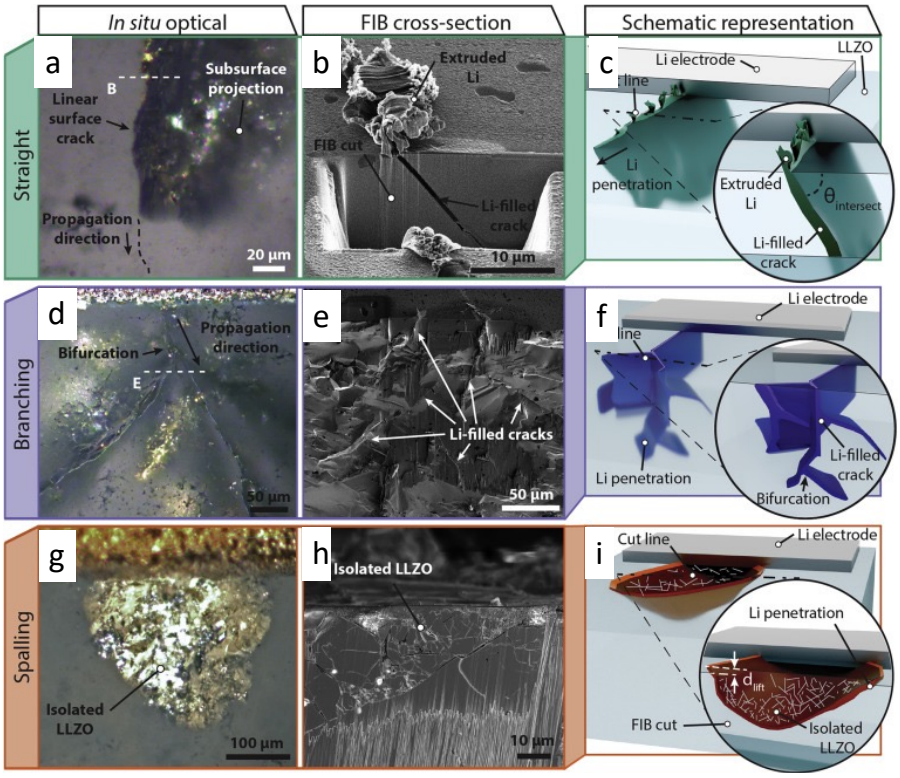



**Figure 1.15:** Reproduced from Dasgupta *et al.*[153]. Optical images (**a, d, g**), SEM images (**b, e, h**), and schematics (**c, f, i**) of straight Li-penetration type (**a–c**), branching type (**d–f**), spalling type (**g–i**). Reproduced with permission from Elsevier.

Perhaps most interestingly, in their LLZO-type electrolytes a fourth type of electrolytic degradation presented, which was named 'diffuse' degradation. Here a diffuse darkening was observed as well as the sporadic formation of dark spots. Post-mortem inspection revealed that the diffuse darkening was due to the formation of a network of very thin structures and that the dark spots resulted from the plating of isolated islands of Li metal[153], see Figure 1.16a-c. These observations were similar in nature to the electrolytic degradation of Na-$\beta$-alumina in Na-S cells. During the 1980s, a progressive darkening of the Na-$\beta$-alumina had been observed within which isolated regions of Na deposition surrounded by microcracks could be identified[154], Figure 1.16d. As well, in more recent years, *operando* neutron depth profiling has been used to demonstrate a homogeneous progression of isolated Li growths in both $Li^+$ conducting oxides and sulphides, indicating this kind of degradation may in fact be possible in a range of electrolyte systems[79], Figure 1.16e.

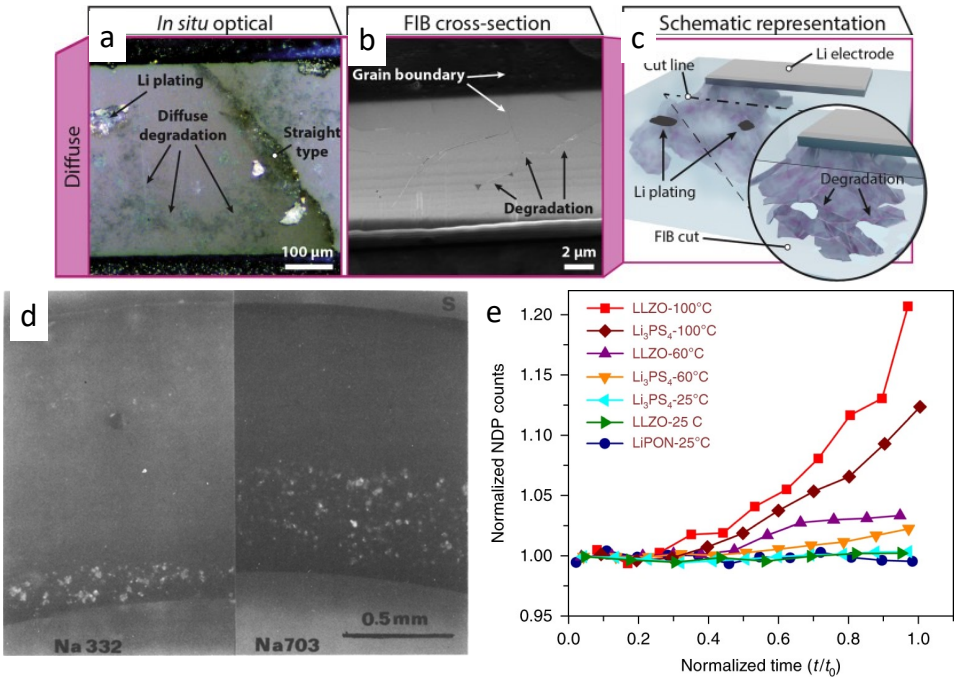



**Figure 1.16:** Optical image (**a**), SEM (**b**) and schematic (**c**) 'diffuse'-type dendrites in LLZO, adapted from Dasgupta *et al.*[153]. **d** Progression of the damage layer in Na-$\beta$-alumina after charging, adapted from De Jonghe *et al.*[154]. **e** Neutron depth profile counts across the bulk electrolyte versus time during Li plating for various electrolytes. The count is correlated to internal Li concentration. Adapted from Han *et al.*[79]. Figure reproduced with permission from both Elsevier and Springer Nature.

Overall, whilst *operando* microprobe set-ups have provided some of the most important insights into Li dendrite failure in ceramic electrolytes, these studies have some inherent limitations. In cells, Li/SE interfaces span orders of magnitude larger areas than in these specialised set-ups, as well as this, the ability to precisely control applied currents and pressures using microprobes is questionable. This raises some doubts surrounding how representative the observations are with regards to what takes place in a real SSB cell. Furthermore, *operando* microprobe set-ups are inherently reliant on the use of highly dense semi-transparent electrolytes to gain any information about the character of propagating dendrites, and consequently the studies are biased towards certain kinds of materials.

#### 1.4.2.3 X-ray tomographic imaging

Faced with the challenges of imaging Li dendrites in more representative *operando* conditions, there has been a rapid development of X-ray computed tomography (XCT) studies. In theory,

XCT imaging can provide both high spatial and temporal three-dimensional imaging of morphological changes within an SSB during its operation. This being said, strict criteria must be met to successfully image Li dendrites in ceramic electrolytes, and technique development is still ongoing several years after the first studies.

Early microtomograms collected of Li dendrites within ceramic electrolytes suffered from an inability to suitably balance ideal imaging conditions with desired cell configurations. In 2018, Hatzell *et al.*[155] used XCT imaging to quantify the volume of cracks present within a short-circuited LLZO material as compared to its pristine state, but strong conclusions regarding Li penetration were inhibited by the high attenuation of the electrolyte which limited the contrast between features. Following this, Pylypenko *et al.*[156] replaced the LLZO electrolyte with an LPS sulphide and lowered their sample diameter so to achieve faster *in-situ* imaging with better contrast, but their poor cell designs meant the imaged samples suffered from having a high number of pre-cracks.

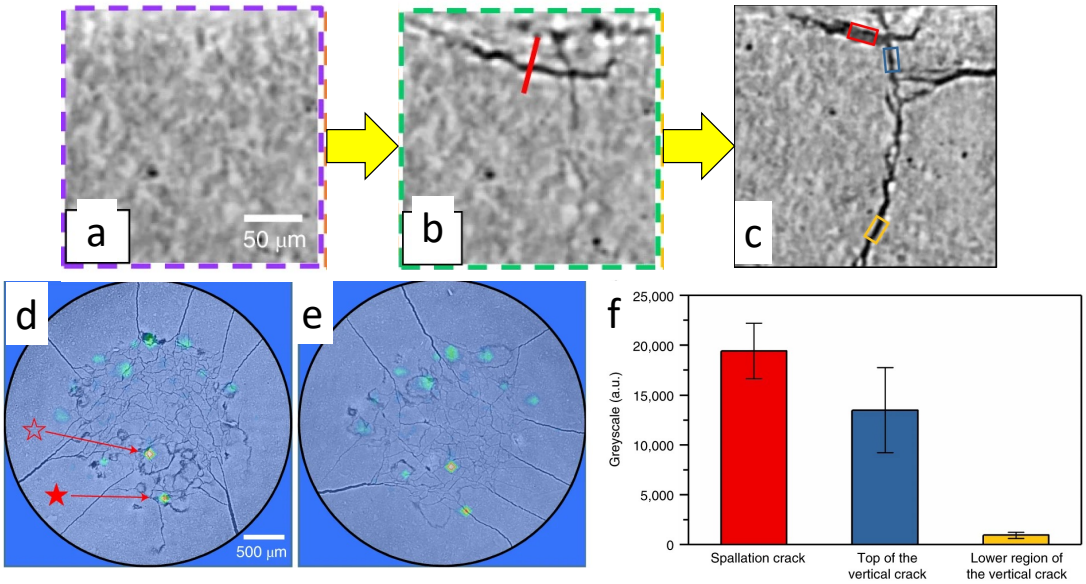



**Figure 1.17:** Adapted from Bruce *et al.*[83]. **a-c** Virtual XCT cross-sections at the Li/$Li_6PS_5Cl$ interface show dendrites first form spallation cracks and then traverse the electrolyte. **d** & **e** XCT image slices from planes in the electrolyte parallel and adjacent to the two electrodes. The locations of the dendrites are revealed using diffraction mapping which is superimposed on the images (highlighted in green and yellow, where green represents low intensity). **f** Greyscale analysis showing the amount of lithium in the regions of the crack identified by the boxes in **c**. The colours in the histogram plot correspond to the colours of the boxes. Reproduced with permission from Springer Nature.

Despite these early difficulties, important insights into the nature of Li dendrites in ceramic electrolytes have been made using XCT imaging. Meng *et al.*[157] captured microtomograms of Li dendrite cracks in $Li_6PS_5Cl$ electrolytes *in-situ* and under representative cell conditions. Their images elucidated that multiple instances of branching crack morphologies may occur simultaneously. In 2021, Bruce *et al.*[83] performed phase contrast XCT imaging on $Li_6PS_5Cl$ electrolytes to reveal a multitude of important characteristics of their Li dendrites. Li dendrites were shown to first induce spallation-type cracking of the electrolyte before causing the rapid propagation of straight cracks which traverse the electrolyte to induce short-circuit, see Figure 1.17a-c. This sequence of spallation and transverse cracking was shown to also occur in $Li_3N$ and Na-$\beta$-alumina electrolytes and has been subsequently shown in LLZO-type electrolytes[158,159]. Multiple dendrite fracture events were seen to occur during Li plating, and these were seen to spatially correlate with the Li electrode edges where currents are locally focused, Figure 1.17d&e. Interestingly, grey-scale analysis of the dendrite cracks imaged using phase-contrast modes provided enough contrast between Li metal and free-space to enable an estimation of the extent of Li filling[83]. Transverse dendrite cracks in $Li_6PS_5Cl$ electrolytes were shown to propagate whilst only partially filled, meaning their progression was not driven by Li deposition at the crack tip as had been previously assumed, Figure 1.17c&f.

#### 1.4.2.4 Outlook

Ultimately, dendrite failure in ceramic electrolytes has proven a difficult characterisation challenge, with important microscopic developments occurring rapidly at buried solid-solid interfaces. Consequently, even though many imaging studies have been conducted, many of these works have had to compromise on their representativeness of real cell conditions. Whilst it is possible to attribute the many observational inconsistencies regarding Li dendrites to phenomenological complexity, the difficulties caused by a lack of possible standardisation must also be appreciated. Cell design, materials selection, microstructural control as well as operating conditions (i.e. applied currents, capacities, temperatures and pressures) are all

lacking in consistency and comparability between studies. As well, whilst the use of different characterisation techniques with contrasting strengths may be important to gain a holistic understanding of Li dendrites, technique requirements have often resulted in a siloing of specific methods being used for certain electrolyte classes rather than broad universal usage. However, as research continues and imaging techniques continue to progress, and as the solid-state battery field continues to mature, better conformity in the observations surrounding Li dendrites may yet develop.

Still, due to the multitude of observations, there still exists a wide range of conflicting ideas surrounding how exactly dendrites occur in ceramic electrolytes. If the dendrite problem is to be overcome, a comprehensive mechanistic understanding is urgently needed. Whilst a number of mechanisms have been proposed, the vast majority do generally apply to one of two dendrite classifications: mode 1-type describing rapidly penetrating dendrites (often propagating by electrolyte fracture) and mode 2-type describing slow internal deposition of metal inside the electrolyte. The following sections will hence discuss the latest models for Li dendrites through the lens of these two categories.

### 1.4.3 Dendrites: Mode 1

#### 1.4.3.1 Li (flow) pressures

Many investigations into the dendrite failure of ceramic electrolytes have demonstrated that the ingress of Li coincides with a progressive fracturing of the ceramic[83,148–150,157]. Following these observations, the big question then becomes how the plating of a soft metal such as Li can induce the fracture of a hard ceramic.

As has been discussed, Li plating at the interface is far from ideal, with inhomogeneity encouraged by the presence of insulating contaminants at the interface and by electrode edge-related current enhancement amongst other factors[51]. The slow self-diffusion within Li metal means any fast redistribution to homogenise newly deposited Li is limited[51,130,160]. Consequently, at practically relevant plating current densities, non-uniform interfacial currents

are expected to cause pile-ups of Li which will result in local mechanical stress build-ups. But whilst this may provide a theoretical basis for stresses to develop within the Li anode during plating, there remains a difficulty in proposing how any pressure in the Li can induce fracture of the electrolyte, since the low yield stress of Li metal and its propensity to undergo creep at ambient temperatures means any stress build-up would be readily accommodated by plastic flow[161,162].

So how then to explain electrolyte fracture which results from Li plating? One proposed answer relies, as almost all explanations of mechanical failure do, on considering the presence of microstructural defects. As Li plating proceeds, it is expected that the surface defects of the electrolyte, such as cracks, will fill first. This is both because the overpotential is low, needing to only overcome surface and interfacial energies, and because the electric field concentration is increased there[148,163]. Consequently, these defects may act as points of non-uniform interfacial currents and experience an enhanced Li flux during plating. If pressure gradients build within a microstructural defect, the constrained flow of Li may be such that significant pressures are then exerted onto the surrounding electrolyte inducing fracture.

The first fracture mechanism of this type was proposed in 1974 by Armstrong *et al.*[164] to explain the sudden failure of Na-$\beta$-alumina electrolytes during the plating of molten Na. In their model, a pre-existing surface crack fully filled with molten Na was treated as a cylindrical pipe in with a hemispherical tip, similar to what is shown in Figure 1.18. Current flow is imposed on the crack tip, meaning pressure gradients can build within. A simple analytical relationship (eq. 1.2) was then derived by comparing the Griffith criterion for crack extension with the Hagen-Poiseuille relationship for the pressure generated by fluid flow through a pipe.

$$\Delta P = \frac{8\eta i V_m l^2}{nFr^3} \tag{1.2}$$

where $\Delta P$ is the Poiseuille pressure, $\eta$ is the coefficient of viscosity of sodium, $i$ is current density, $V_m$ is molar volume, $l$ is the crack length, $r$ is the radius of the crack tip, $n$ is the number of electrons and $F$ is Faraday's constant. From this relationship, a specific current

density (e.g., the CCD) could be predicted to fracture the electrolyte for a given flaw size and fracture strength.

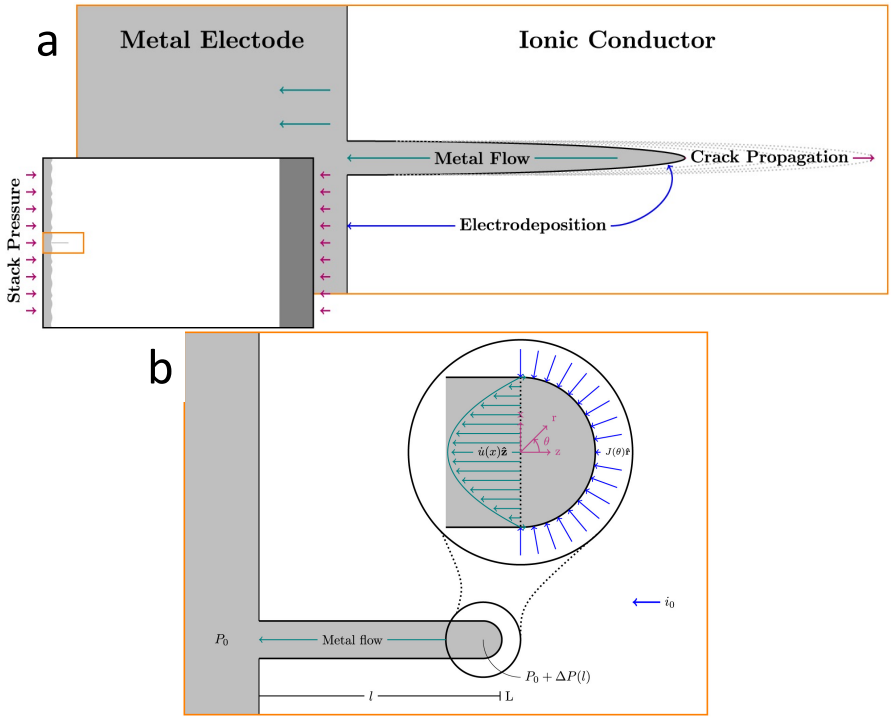



**Figure 1.18:** Figure reproduced from Ceder *et al.*[165]. **a** Theoretical domain representing the local region in a metal electrode and inorganic solid ion conductor interface around a metal filled flaw. The inset shows where the considered domain fits within the total metal electrode and conductor system. **b** Simplified geometry used in semi-analytical derivations. Metal electrode/solid electrolyte interfaces with metal filled planar flaw of length L and tip radius $r_0$, held at stack pressure $P_0$. Reproduced with permission from IOP Publishing.

Interestingly, the values predicted using this simple analytical relationship were several orders of magnitude above the measured CCD values for Na-$\beta$-alumina electrolytes. Several reasons were considered for the over prediction of the model, including: (1) inaccuracies in the input fracture criterion, e.g., due to unconsidered anisotropy[166] (2) the influence of imperfect Na wetting on local currents[167], and (3) the potentially higher viscosity of Na in narrow channels[168]. Whilst many of these uncertainties were to remain unresolved, in the years to follow, several improvements to Armstrong's model were proposed[169–171]. By 1983, a model by Vikar *et al.*[172] enabled CCD predictions within one order of magnitude of experimental data, with the main improvement resulting from considering a three-dimensional Laplace solution for current focussing at the crack tip.

As has been the case since the early models for Na-$\beta$-alumina, a continual challenge faced when proposing any model of dendrite failure is the balancing of predicted driving forces and counterforces so to match experimental observation. In recent years, there has been a revival in the use of mode 1-type models to explain dendrite failure in Li solid electrolytes, during which considerable variation has centred around both the correct mechanical treatment of Li metal and the use of pressure dependent Li deposition kinetics. In 2017, Yet Ming Chiang *et al*.[148] considered a Li filled crack under conditions of limited Li extrusion, meaning newly deposited Li would contribute directly to a hydrostatic stress build up. Hence rather than considering a 'flow' pressure, a hydrostatic stress is related to the molar volume of Li deposited for a given overpotential. As like in Armstrong's model[164], considerations were confined solely to deposition at the crack tip without a strict treatment of wider current focusing effects, and since the model considered the limiting case of no Li extrusion, the mechanical properties of Li were not considered. Following this, mode 1-type models for Li dendrites have been postulated which directly involve Li flow pressures. McMeeking *et al.*[173] considered the 'best-case scenario' of unrestricted Li plasticity during plating by treating Li as an incompressible inviscid fluid, and Ceder *et al.*[165] approximated a pseudo-viscosity for Li in their model by using a Perzyna formulation[174] of strain rate for associated flow, see eq. 1.3. In the last few years, creep tests on Li metal have now made it possible to directly extract an equivalent pseudo-viscosity for Li metal[161,162].

$$\eta = \frac{\sigma_Y}{\sqrt{3}\dot{\bar{\varepsilon}}} \tag{1.3}$$

One of the difficulties posed to models which invoke Li flow stresses are reports made of significant Li hardening at small length scales. McMeeking *et al.*[173] pushed back on reports of microscale Li hardening (some of which claimed yield strengths as high as 95 MPa[175]) by demonstrating that if this were the case within surface flaws, then even flaws under 1 nm would undergo uncontrollable propagation. Ultimately, little is still known about the microstructure of Li within dendrite cracks. Darnbrough *et al*.[176] recently showed that lithium grains are typically large in size (up to 1mm diameter), and its properties are highly related to

the crystal orientation and the manner in which stress is applied. Consequently, variation in measured values is to be expected, and prescribing specific values to dendrites still remains contentious.

Whilst some discussion has centred around Li mechanics, another point of debate has been the influence of pressure on the Li deposition kinetics. Both Bucci *et al.*[177] and McMeeking *et al.*[173] treated interfacial kinetics using a pressure dependent Butler-Volmer equation, whereas no such consideration was made by Chiang *et al*.[148]. Ceder *et al.*[165] considered a boundary traction potential in their model which additionally considered the effect of stress on ionic transport within the electrolyte as well as at the interface. This meant the bulk ionic conductivity of the electrolyte would play a key role in preventing dendrite failure. Whilst these kinds of features can provide significant counterforces to dendrite formation, often bringing CCD predictions closer to experiment, an experimental validation of the magnitude of such pressure effects is still lacking.

Overall, although some parameters are still debated, models which invoke Li flow stresses can explain a large number of key experimental observations such as: (1) lower CCDs in defect populous surfaces[148–150], (2) higher CCDs with increasing temperature and smaller stack pressures[157,160,178,179], and (3) higher CCDs in softer metal SSBs such as Na and K[136,180,181]. Consequently, these kinds of models have gained significant popularity.

#### 1.4.3.2 Alternative fracture mechanisms

Whilst Li flow-type mechanisms for ceramic fracture have attracted significant interest, there have been several alternative explanations worth noting.

In 2020, Harris *et al.*[182] suggested that dendrite failure in LLZO-type electrolytes may involve some level of stress corrosion cracking (SCC), see Figure 1.19a-d. SCC generally occurs when the surface of a material is chemically (usually electrochemically) attacked at a defect or heterogeneity, i.e. a grain boundary[183]. The result is the formation or extension of an incipient crack that can grow if its tip is in a sufficiently high state of tension. Thus, SCC crack

growth occurs under the combined effect of a chemical reaction plus a local tensile stress above some threshold value, but below the level required for fast crack propagation. Similar ideas were proposed previously for Na-$\beta$-alumina electrolytes, in which a stress-assisted dissolution of the electrolyte in molten Na was postulated[169,184]. Ultimately experimental investigations of stress corrosion cracking of beta-alumina showed an absence of electrolyte dissolution as well as little time dependence of strength during exposure to molten Na[185]. Likewise, little direct experimental evidence has yet been ascertained for SCC in LLZO-type electrolytes.

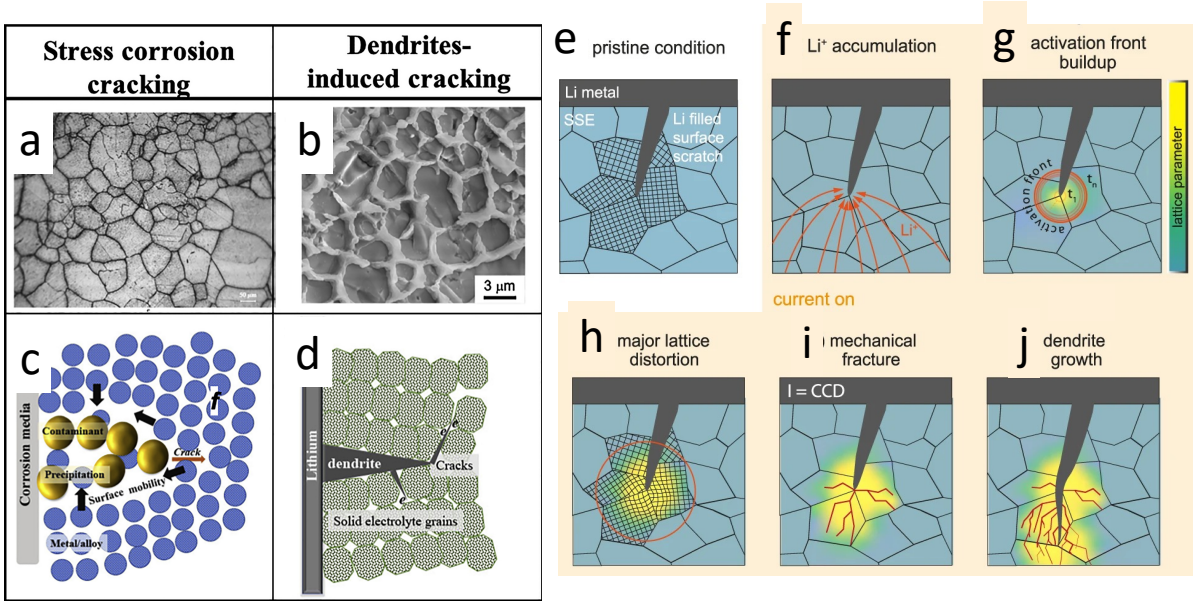



**Figure 1.19: a-d** Comparison between the intergranular cracks caused by SCC and Li intergranular penetration into LLZO, reproduced from Harris *et al.*[182]. **a** & **b** compare surface morphology, and **c** & **d** are schematic comparisons. **e-j** Schematic of electrochemical cracking, reproduced from Rettenwander *et al.*[186] illustrating how local Li-ion concentrations can induce lattice distortions and fracture. Reproduced with permission from both Elsevier and Springer Nature.

In recent years, some mechanisms have been proposed in which fracture originates from stresses within the electrolyte itself rather than being built-up in the lithium. Rettenwander *et al.*[186] proposed a local reduction of the electrolyte in the region surrounding the defect tip, causing the build-up of a Li-activity front. This local stoichiometry change (i.e., additional Li-ions and changed ionic valences due to additional electrons) are proposed to induce a change of the local lattice parameter. Since the bulk electrolyte is unaffected by Li activity changes, there will be an elastic energy build up until a critical Li activity is reached, at which the stress

is relaxed by fracture of the electrolyte, Figure 1.19e-j. Similar considerations have also been made by Li *et al.*[187] but across larger length scales. In their model, large variations in electronic leakage currents may occur across the entire electrolyte thickness, and consequently a narrow transition region may develop within the centre of the electrolyte between the somewhat partially reduced and oxidised interfacial regions. In their view, the eigen-strain mismatch of such a transition region could be significant enough to cause brittle fracture of the electrolyte.

### 1.4.4 Dendrites: Mode 2

Although most observations report some kind of rapid fracture during the Li dendrite failure of ceramic electrolytes, observations in some electrolytes have indicated the possibility of isolated Li deposition[79,153]. The mechanism and potential consequences of this kind of electrolytic degradation should therefore be considered.

Nucleation of lithium at the electrode interface can only occur at the intersections of electronic and ionic pathways. In other words, for $Li^+$ ions to deposit as Li metal, an electron source is required to facilitate their reduction. Therefore, for Li deposition to occur inside the solid electrolyte, some partial electronic conductivity of the electrolyte must be afforded[51]. It is worth noting that experimentally measured electronic partial conductivities on polycrystalline samples can be dominated by grain boundaries or surface regions that often show different electronic conductivities. In particular, experiments have shown reduced band gaps as well as Galvani potential drops at grain boundaries in LLZO-type electrolytes[188,189]. Consequently, many models for dendrite failure in these electrolytes centre around Li deposition at the grain boundaries[190,191].

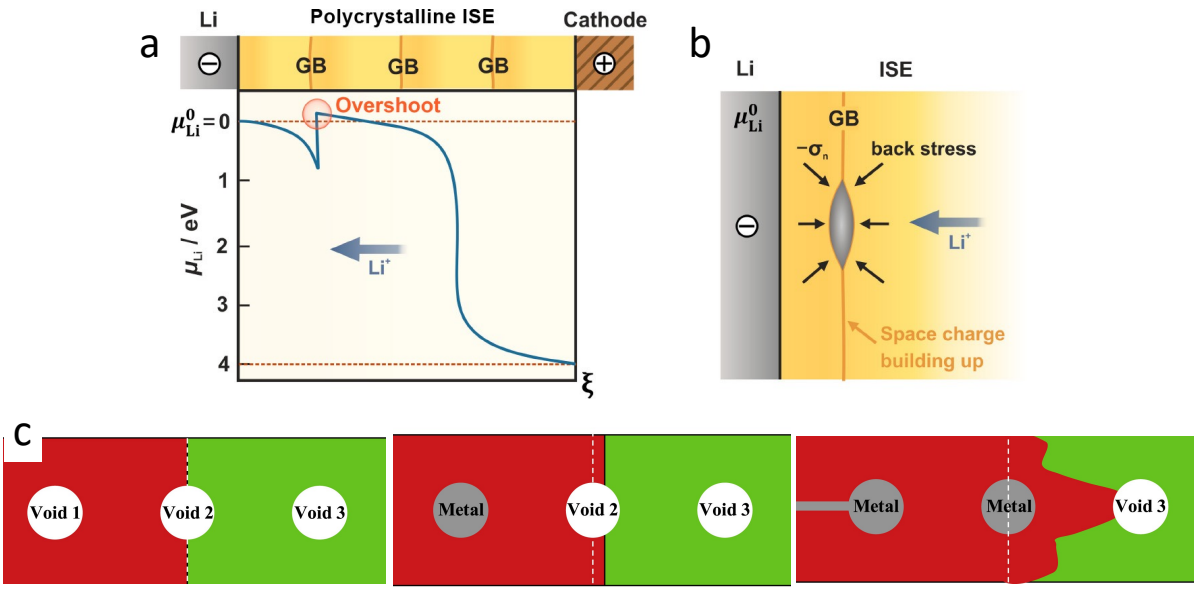



**Figure 1.20: a & b** Reproduced from Janek *et al.*[51]. **a** A qualitative steady state profile of the chemical potential $\mu_{Li}$ during charging of a solid-state battery with an ideal electrolyte with grain boundaries of varying resistivity (the highest resistivity close to the Li anode). Mathematically an overshoot of $\mu_{Li}$ at a position ξ in the electrolyte is possible depending on the boundary conditions. **b** Schematic showing the mechanical compressive traction which must be overcome for lithium nucleation at the grain boundary. **c** Schematic of successive cracking events caused by the filling of isolated voids, reproduced from Ceder *et al.*[192]. Red indicates the regions of the electrolyte which are susceptible to Li plating at each stage. Green indicates "safe" regions. Reproduced with permission from both the American Chemical Society and Elsevier.

Even if some partial electronic conductivity is afforded, for Li to nucleate inside the electrolyte a thermodynamic driving force must still exist. More explicitly, somewhere within the electrolyte the local chemical potential of lithium, $\mu_{Li}$, must be elevated above the standard chemical potential of lithium metal, $\mu_{Li}^0$.[193] Accordingly, several potential mechanisms for how $\mu_{Li}$ might kinetically 'overshoot' inside the electrolyte itself have been proposed. In early work on Na-$\beta$-alumina electrolytes, sufficient $\mu_{Na}$ overshoots were speculated to occur due to local gradients of the transference number inside the electrolyte[194]. Such gradients were a consequence of the progressive reduction of Na-$\beta$-alumina when immersed in molten Na at high temperatures. The reduction introduced oxygen vacancies which were then compensated by electrons.

In more recent lines of thought, chemical potential overshoots have been considered to originate at defects which act as ionic bottlenecks, such as pores and grain boundaries, see Figure 1.20. For example, Raj *et al.*[195] considered Li nucleation at transverse grain boundaries.

In such a case, a mechanical back stress of the solid electrolyte would need to be initially overcome for deposition to take place, Figure 1.20b. In contrast, the overpotential for Li nucleation within isolated porosity has no initial mechanical contribution. Such a situation was recently considered by Ceder *et al.*[192]. They postulated if pores were sufficiently large, further plating may continue after filling, inducing a fracture of the surrounding electrolyte. They went on to consider whether fracture back to the interface could extend the potential front through the electrolyte activating deeper pores, the final result of which could eventually enable a percolating Li pathway through the electrolyte, Figure 1.20c.

Whilst it remains contentious as to whether mode 2-type degradation can be ultimately responsible for short circuit of Li ceramics during plating, if such processes do take place their effects must be considered. In 1983, Kuribayashi *et al.*[196] suggested mode 2-type degradations of Na-$\beta$-alumina may coincide together with mode 1-type failures in a somewhat symbiotic relationship. As such, similar considerations could potentially be made for any Li electrolytes which also demonstrate clear mode 2-type degradation.

### 1.4.5 Strategies against dendrites

The need for fast charging, in for example electric vehicles, means that plating current densities in excess of 5 mA $cm^{-2}$ are desirable[54,140]. The major classes of solid electrolyte under consideration, oxides, sulphides and halides, struggle to achieve lithium plating currents in this range without dendrite penetration, short-circuit and cell failure. Higher critical currents are needed. Given the importance of the dendrite problem, there have been many attempts to resolve it. In general, the pursued strategies have fallen into one of two categories: modification of the Li/SE interface or some modification of the solid electrolyte itself.

#### 1.4.5.1 Interfacial Modification

##### 1.4.5.1.1 Lower and more homogeneous interfacial currents

The formation of dendrites has been closely associated to interfacial regions of inhomogeneous plating which act as sites of enhanced current flow[51,83]. Encouraging homogenous Li plating and preventing local current hotspots may ultimately prove necessary in enabling higher overall rates of charge.

On LLZO-type materials in particular, exposure to moisture can result in the formation of highly resistive carbonates and hydroxides on the electrolyte's surface[89,142]. Work by Sakamoto *et al.*[197] and others have implemented a number of methods to 'clean' the interface. Heat treatments[197], laser cleaning protocols[198] and acid treatments[199] have all proven valid ways of removing interfacial impurities, ensuring high areal resistances do not limit measured critical currents. In a similar spirit, both Janek *et al.*[132] and Bruce *et al.*[135] have shown that high formation pressures can lower interfacial resistances considerably by improving the interfacial contact between Li and the solid electrolyte. Stack pressures can also be maintained so to avoid dynamic contact losses during Li stripping, but it is worth noting that high pressures are widely considered unfeasible for larger format cells during cycling.

Another way to reduce local currents is to increase the total interfacial contact area. Wachsman and co-workers have published numerous SSB designs in which a porous network of solid electrolyte percolates the anode, thus deviating from the standard planar configuration[200,201]. Whilst these designs enable high effective current densities, they have significant drawbacks on cell energy densities. With this in mind, several studies have sought to find a compromised solution by introducing a microscale patterning of the solid electrolyte surface[202–204]. Whilst optimised contouring of the interface can facilitate higher critical currents, any improvement is ultimately limited due to increasing current focussing effects[204].

#### 1.4.5.1.2 Interlayers

One approach in preventing Li dendrites has been to incorporate a thin interlayer between the Li and the electrolyte. Such a layer may act to physically buffer the solid electrolyte from the Li plating process.

Several years ago, Hu *et al.*[205] demonstrated that thin ceramic interlayers such as $Al_2O_3$ can drastically improve the wettability of Li and hence the interfacial resistance of garnet electrolytes. Yet difficulties in avoiding layer damage and maintaining homogenous Li plating limited improvements in CCD. In more recent years, significant improvements in plating critical currents have been made possible by the use of a mixed ionic and electronic conducting (MIEC) interlayer[51,206]. Depositing layers of Li-alloying metals such as Mg, Al, In, Au and Ag allows a buffer alloying layer to first form before Li precipitation[207–210]. The enhanced Li diffusion within these alloy layers as compared to pure Li metal allows for better Li redistribution, homogenising interfacial currents[207], see Figure 1.21a&b. With this being said, large volume changes and reversibility challenges have typically limited longer term cycling performances of pure alloy layers[51,211].

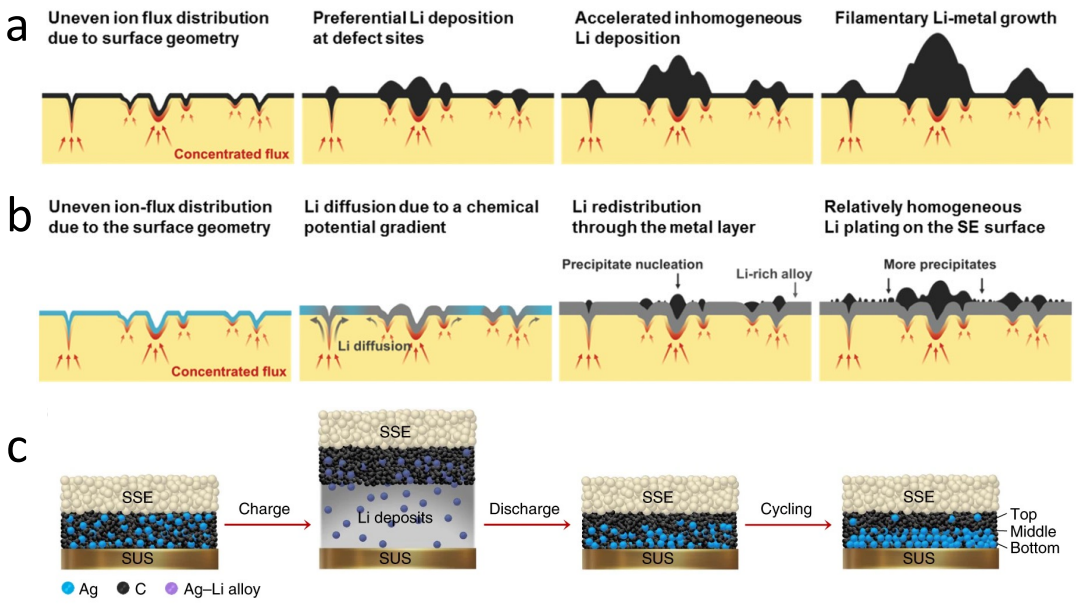



**Figure 1.21: a & b** Reproduced from Kim *et al.*[207] **a** Schematic of inhomogeneous lithium deposition caused by uneven lithium-ion flux at surface morphological fluctuations. **b** lithium redistribution and homogeneous Li nucleation through the gold layer. **c** A schematic of Li plating–stripping on the current collector with an Ag–C nanocomposite layer, reproduced from Lee *et al.*[111]. Reproduced with permission from both John Wiley and Sons and Springer Nature.

Very recently, carbon-based MIEC interlayers have attracted serious attention due to their impressive long term cycling performances at high rates[52,111,212,213]. As well as buffering bulk Li anodes, carbon-based interlayers (often composited with metal nanoparticles) can readily facilitate anodeless cell designs with high energy densities, see Figure 1.21c. Early studies have shown that whether Li is plated away from or at the solid electrolyte interface depends on the applied current density, meaning charging currents still face some limitations despite considerable improvement[212]. Ultimately, very little is known about the exact mechanism of these rather complex interlayers and a large amount of research is still ongoing.

#### 1.4.5.2 Modification of the solid electrolyte

##### 1.4.5.2.1 Mechanical properties

Due to the link between Li dendrite propagation and fracture of the ceramic electrolyte, researchers have sought to improve the fracture resistance of the solid electrolytes to raise critical currents.

One fairly popular idea has been to induce a state of residual compressive stress at the electrolyte surface, either by shot-peening[214] or ion exchange/implantation[215,216], see Figure 1.22a. Residual stresses can enable highly tough ceramics. For example, the significant crack resistance of Gorilla Glass is a result of exchanging smaller sodium atoms near the surface with larger potassium atoms[182]. However, stresses within the electrolyte can significantly diminish ionic transport, consequently no study has so far successfully balanced both electrolyte toughness and conductivity.

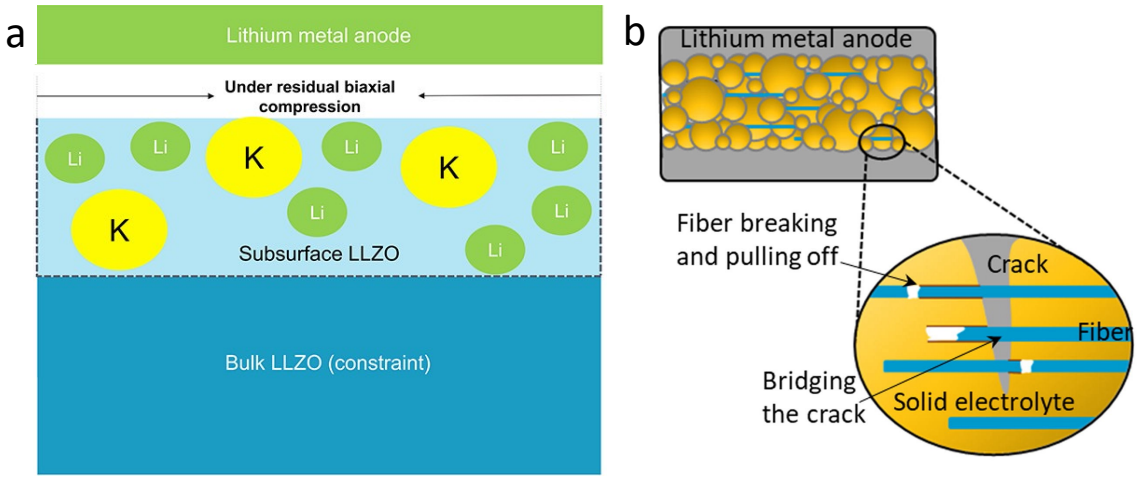



**Figure 1.22:** Schematic illustration of a K ion exchanged LLZO surface, the added compression resists crack growth but also hinders ionic transport, reproduced from Jagad *et al.*[216]. Schematic of a fibre-reinforced solid electrolyte composite with associated toughening mechanisms, reproduced from Janek *et al.*[217]. Figures adapted with permission from the American Chemical Society and Elsevier.

Another route to toughen ceramics is through the incorporation of secondary phases into the microstructure – giving an overall tougher composite material. A number of works have used either platelets[218] (e.g., reduced graphene oxide) or fibres[217,219,220] (e.g., alumina, borosilicate glass or Kevlar) to toughen ceramic electrolytes through mechanisms such as crack-bridging or crack deflection, Figure 1.22b. Whilst many of these studies neglected to relate mechanical improvements to critical plating currents, some studies did report minor improvements[217,219,220]. Still, to date there has been a surprising lack of research dedicated to the mechanical refinement of Li ceramic electrolytes in the context of raising charging currents. During the popular development of Na-$\beta$-alumina electrolytes, dispersed secondary phases were used to transformation toughen the material[221–226]. Specifically, small particles of partially stabilised zirconia were dispersed within the microstructure, with the idea that these particles should undergo a stress-sensitive phase transformation in proximity to the tip of an advancing crack. Whilst this addition of zirconia particles has since become standard for many commercially produced Na-$\beta$-alumina electrolytes, no attempts to induce transformation toughening in $Li^+$ conducting solid electrolytes have so far succeeded[227]. Chapter 5 of this thesis will detail investigations by the author into the effect of transformation toughening $Li_6PS_5Cl$ electrolytes.

#### 1.4.5.2.2 Microstructural control

Whilst a given electrolyte may have some inherent mechanical properties, there can be a drastic variation due to changes in microstructure. As well, microstructural defects are believed to play a direct role in the formation of Li dendrites within ceramics.

In the context of dendrite mitigation, a considerable amount of research has been dedicated to the microstructural control of oxide electrolytes. With regards to porosity, generally studies have sought to minimise pore connectivity, size and total volume[51,155]. Research focused on grain design has been somewhat less consistent. Early works coarsened grains to lower the total number of grain boundaries, whereas more recent studies pursued smaller or even bimodal grain sizes to reduce grain boundary porosity and increase grain boundary complexity[228–233]. Ultimately though, no matter the grain boundary configuration, highly dense garnet electrolytes with best-in-class surface preparation still fail to reach critical plating currents above ~ 1 mA/cm$^2$.[51,140] Studies on single crystals have shown the altogether removal of grain boundaries can help break this barrier, but their dendrite resistance is eventually limited by the presence of surface flaws[186,234]. As well, single crystal garnet films are not seen as a practical solution for mass-produced Li-SSBs. Consequently, a significant amount of research is still focused on solutions for polycrystalline garnets. In particular, a number of different sintering additives have been introduced to coat the grain boundaries, often with an amorphous phase[235–239], see Figure 1.23a. These additives are generally touted to reduce the porosity, increase the strength and or decrease the electronic conductivity of the grain boundaries, but so far, no compound has demonstrated notable CCD improvement.

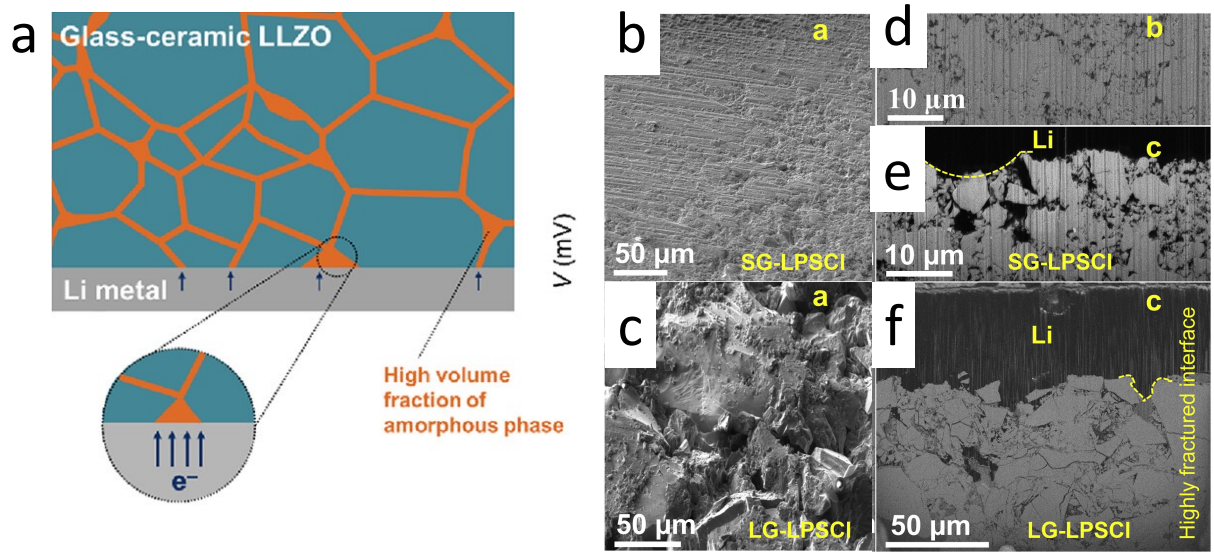



**Figure 1.23: a** A schematic of LLZO electrolyte in which the grain boundaries have been modified with a low electronic conductivity amorphous phase, adapted from Hoinkis *et al.*[239] **b-f** reproduced from Singh *et al.*[82] demonstrating different microstructures of pressed $Li_6PS_5Cl$ electrolytes. **b** & **c** demonstrate varying surface morphologies and **d-f** reveals the internal microstructures. Reproduced with permission from both the American Chemical Society and Elsevier.

As compared to oxides, far less attention has been given to the microstructural optimisation of sulphide electrolytes. In particular, the vast majority of studies involving polycrystalline thiophosphate sulphide electrolytes (e.g., $Li_6PS_5Cl$ and β-LPS), form the electrolyte separator through cold pressing alone[157,240]. Consequently, the reported variation in microstructure has been limited. Recently, Janek and co-workers investigated the effect of particle size in the context of Li dendrite failure within cold pressed $Li_6PS_5Cl$ electrolytes[82]. Whilst they found better surface homogeneity as well as increased crack deflection in electrolytes made with smaller particles, ultimately all electrolytes in the study were highly porous and had limited CCDs, Figure 1.23b-f. In recent years, some studies have implemented sintering procedures to densify thiophosphate sulphides to improve ionic conduction, but to-date no electrolytes of this kind of been reported with high densities (e.g., above 95%)[241,242].

In an attempt to minimise microstructural defects, glassy sulphide electrolytes have fallen under some consideration. As previously mentioned, when using a microprobe imaging set-up, Chiang and co-workers had reported a significant resistance to Li ingress when plating on cleaved, highly dense LPS glass surfaces[148]. Similarly, Ceder *et al.*[243] noted that highly dense LPS glasses could sustain high single plating currents without dendrite formation in Li

symmetric solid-state cells. Whilst these glassy sulphides have demonstrated some promise, other studies have shown high plating currents cannot be maintained during prolonged cycling[244–246]. Whilst glasses may avoid grain boundaries they are ultimately not without flaws. As well, their highly brittle nature can pose difficulties in production and when handling, often leading to macroscopic cracks[247].

## 1.5 Thesis Aims

As has been detailed in this chapter, solid-state batteries have attracted major interest as a route towards reversible lithium metal anodes, but the issues faced at the Li/solid electrolyte interface are far from trivial. Of these, the dendrite problem has proven the most problematic and the most vexing. The aim of this thesis is to better understand this important failure mechanism and to explore strategies with which it may be mitigated.

After a discussion of the experimental methods used in this thesis in Chapter 2, Chapter 3 aims to provide a mechanistic understanding of Li dendrites in $Li_6PS_5Cl$ electrolytes. X-ray tomographic imaging is used capture key developments *in-operando*, with these observations forming the basis for answering the questions: how do Li dendrites first initiate and how do they then propagate?

Following the new mechanistic understandings provided within Chapter 3, Chapters 4 and 5 aim to understand how altering the solid electrolyte's microstructure and mechanical properties may affect Li dendrite failure. In Chapter 4, an investigation is first made into the effect of sintering on the solid electrolyte microstructure, and in particular on the microstructural defects involved in the initiation of Li dendrites. FIB-SEM is used to quantify the cracks and pores within a range of differently sintered $Li_6PS_5Cl$ electrolytes, after which X-ray CT imaging is combined with electrochemical testing to probe changes in Li dendrite morphology and to determine the effect of microstructural change on the critical current for dendrite initiation. In Chapter 5, the effect of adding metastable $CeO_2$-$ZrO_2$ (CSZ) nanoparticles into $Li_6PS_5Cl$ solid electrolytes is explored. Firstly, the mechanical properties

and $Li^+$ conductivities are measured across a range of composites varying in composition. Following this, an investigation is made into the effects on dendrite morphology, with a focus on dendrite propagation.

# Chapter 2: Experimental Techniques

## 2.1 Aim

This chapter serves as an introduction to the sample preparation methodology and experimental characterisation used throughout this thesis. An explanation of the theory behind these practices and techniques is integrated with discussion of practical considerations for their use in solid-state battery research.

## 2.2 Sample Preparation

### 2.2.1 Sintering

Sintering is a process in which particulate material is consolidated during heat treatment and has traditionally been the principal method to produce dense ceramic bodies[248]. The basic idea is to join particles together without necessarily melting them, with temperatures remaining below the melting temperatures of the material. The driving force for sintering is the reduction in the total free energy of the particulate system, $\Delta G$, which is composed of free energy changes of volume, $\Delta G_v$, boundaries, $\Delta G_b$, and surfaces, $\Delta G_s$, see eq. 2.1[249].

$$\Delta G = \Delta G_v + \Delta G_b + \Delta G_s \quad (2.1)$$

In conventional sintering, the dominant term in the free energy reduction is that due to surface area reduction.

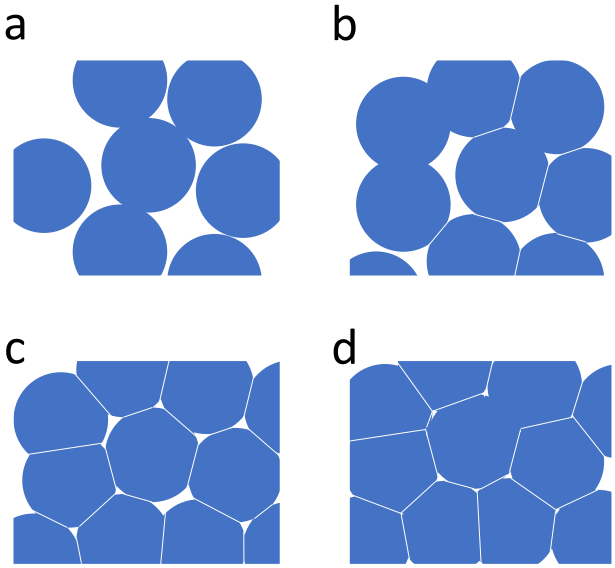



**Figure 2.1:** Development of ceramic microstructure during sintering: **a** Loose powder particles; **b** initial stage; **c** intermediate stage; and **d** final stage. Adapted from Lee *et al.*[250].

The stages of sintering are depicted in Figure 2.1. Before sintering, the ceramic particles are compacted together using pressure to form what is known as a 'green body'. When subject to firing, further re-arrangement of the particles may occur, and at the points of contact, chemical bonds may form producing new grain boundaries. Typically, at the bonded points of contact particles will neck together, which in turn helps to reduce the number of pores and shrink the overall ceramic body[248]. Eventually a small selection of isolated pores will remain which may be eliminated through vacancy diffusion. Therefore, an optimisation of both the size, shape and packing of particles as well as the atmosphere, heating ramp, hold temperatures and hold times are all necessary to optimise the thermodynamic driving forces and active mass transport mechanisms during sintering.

### 2.2.2 Field Assisted Sintering

Field assisted sintering (also commonly known as spark plasma sintering) is a variation of hot pressing whereby the ceramic body is heated under low atmospheric pressure through the application of pulsed electric currents rather than using an external source. As with traditional hot pressing, both the uniaxial powder pressing and the heat treatment are performed simultaneously. This application of pressure during heating directly affects the thermodynamic

sintering driving force and activates pressure driven mass transport mechanisms such as plastic deformation[248]. As a result, both field assisted sintering and traditional hot pressing can enable significant densification at lower temperatures than traditional sintering.

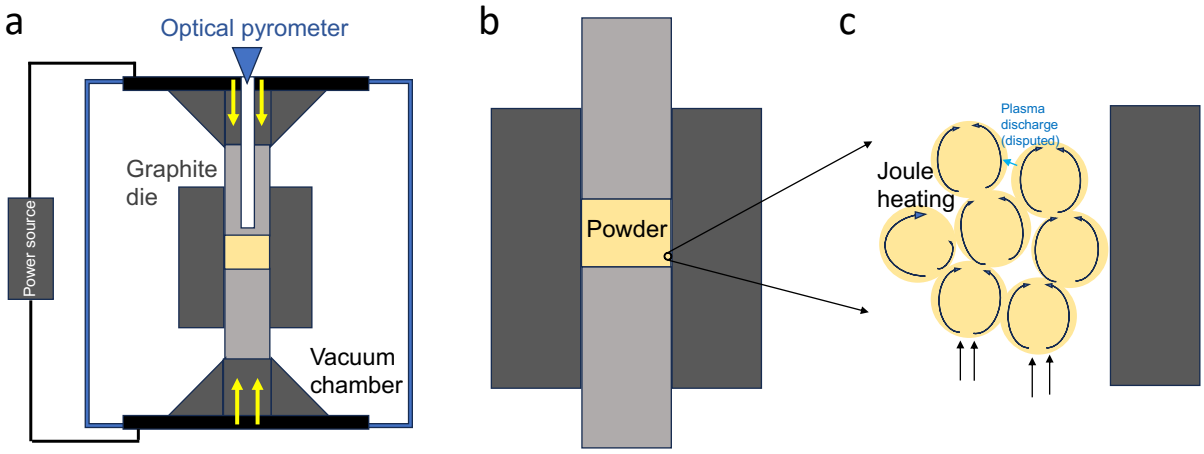



**Figure 2.2: a** Schematic of a field assisted sintering set-up. **b&c** Illustration of the Joule heating and disputed spark plasma discharge mechanisms which contribute to the densification of ceramic powders.

A schematic of a field assisted sintering set-up is given in Figure 2.2a. Powders are typically compressed within a die and loaded between the two pistons. Graphite dies are often preferred due to their affordability, low thermal expansion, good thermal and electrical conductivity as well as good creep resistance. During operation the chamber is put under vacuum and load is applied via the pistons. Pulsed currents are applied to induce heating, monitored either by thermocouples or an optical pyrometer.

The application of a pulsed current which passes both through the electrically conductive die and ceramic body means the powders are heated both from the outside and the inside during field assisted sintering. The rapid heating means field assisted sintering can produce a higher throughput for a lower energy consumption and open new processing windows as compared to hot pressing[251]. A number of mechanisms have been proposed to account for the enhanced sintering abilities of the field assisted sintering process. Of these mechanisms, one commonly put forth, and the one that draws the most controversy, involves the presence of momentary plasma generated between particles (hence the name 'Spark Plasma Sintering')[252]. Regardless of whether dielectric breakdown occurs between particles, mechanisms such as

rapid joule heating and current effects in conducting samples are relatively well established and can explain the mechanism of internal heating[251], see Figure 2.2b&c.

In this thesis, field assisted sintering is used to densify sulphide solid electrolytes. The rapid heating helps to both facilitate the densification as well as avoid significant degradation of the electrolytes.

## 2.3 Materials Characterisation

### 2.3.1 X-ray Diffraction

X-ray diffraction (XRD) is a powerful technique for characterising crystalline structures allowing for the elucidation of atomic positions, lattice parameters and crystallite sizes. Additionally, it can be used to quantify the phase fractions within crystalline mixtures, thereby helping to identify the presence of impurity phases[253].

When an incident beam of X-rays enters a material, some will transmit through, and some will be scattered by the electron density surrounding the atoms. Of these, a certain number will be scattered both coherently and elastically, i.e., without the loss of energy or change in phase. Consequently, the atoms within a material illuminated with X-rays will begin themselves to act as sources of coherently scattered X-rays. In a crystalline solid, most the scattered X-rays will cancel one another through destructive interference, but in a few specific directions constructive interference will occur. For a given family of crystallographic planes[‡‡] the constructively scattered X-rays can be considered to reflect off at an angle identical to the angle of incidence. If the crystal is aligned relative to the incident beam such that the difference in path length of X-rays scattered by a family of planes is equal to an integer number of wavelengths, then significant constructive interference occurs between the reflections of each plane and a peak in intensity is observed in the detected radiation. These conditions are described by Bragg's Law (eq. 2.2)[254].

[‡‡] Crystallographic planes can be grouped into parallel families described by 3 values h, k and l, known as the Miller indices, which are the inverse values of where the planes intercept with the a, b and c axes respectively.

$$n\lambda = 2d_{hkl} \sin\theta \tag{2.2}$$

Where $n$ is an integer, $\lambda$ is the wavelength of radiation, $d_{hkl}$ is the inter-planar spacing for a given (hkl) family, and $\theta$ is the incident angle of the beam relative to the (hkl) plane, see Figure 2.3. Since both the crystal type and unit cell parameters determines the inter-planar spacings, $d_{hkl}$, they are related to the number and position of peaks in the measured diffraction pattern.

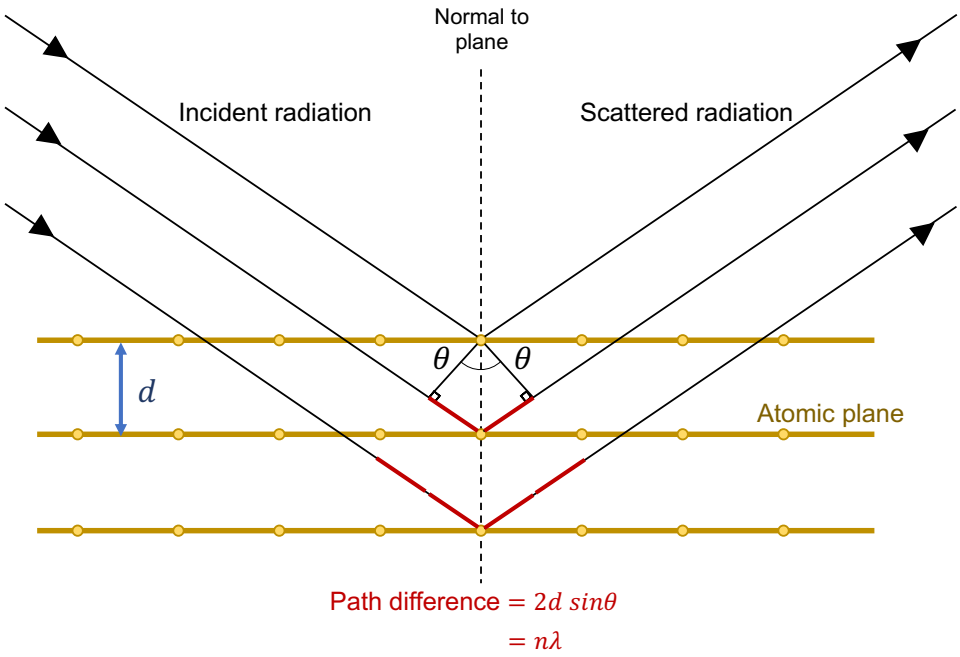



**Figure 2.3:** Schematic illustration of Bragg's Law, e.g., how the $d$ spacing between atomic planes, the diffraction angle and the wavelength of the radiation together influence the interference pattern.

The intensity of the peaks is related to the atomic scattering factor, $f$, which for X-rays is proportional to the electron density around the atom (and hence the atomic number), the Bragg angle, and the wavelength of the incident beam. The sum of contributions from all the constituent atoms in the same (hkl) plane is described by the structure factor $F_{hkl}$, see equation 2.3[253].

$$F_{hkl} = \sum_{j=1}^{N} f_j e^{2\pi i(hx_j + ky_j + lz_j)} \tag{2.3}$$

Where $x_j$, $y_j$ , and $z_j$ are the positional coordinates of the j$^{th}$ atom in the unit cell and $f_j$ is the scattering factor of the j$^{th}$ atom. The intensity of a Bragg reflection in the diffraction pattern is

proportional to the absolute square of the structure factor of the (hkl) family of planes to which it corresponds, see equation 2.4.

$$I_{hkl} \propto |F_{hkl}|^2 \tag{2.4}$$

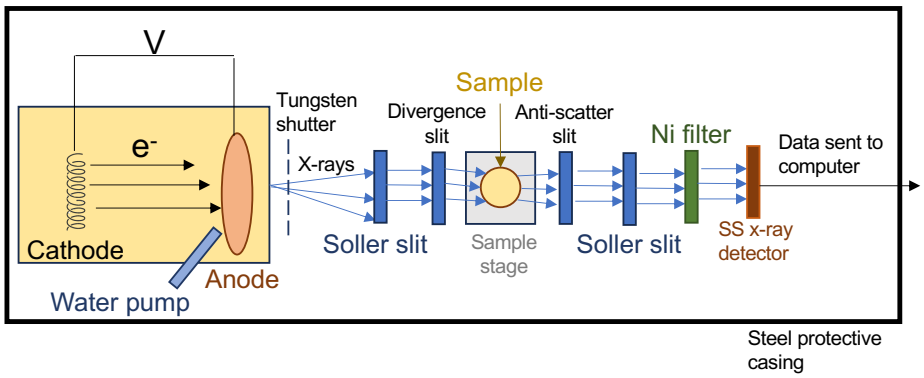



**Figure 2.4:** Schematic of a typical X-ray diffractometer. In this thesis a Rigaku MiniFlex 600 is used to collect XRD patterns, which employs a 600 W Cu X-ray source. The Miniflex is contained within a nitrogen filled glovebox.

Within a typical lab-based X-ray diffractometer, electrons are generated by thermionic emission via a tungsten cathode and accelerated using a high voltage to collide with a copper anode, resulting in the emission of X-rays, see Figure 2.4. Once generated, X-rays are converged through a number of slits. A Soller slit is used to remove horizontal divergence and a divergence slit is used to control the vertical divergence. The focused beam then reaches the sample which is tilted over a number of steps to probe a range of incident angles. Once diffracted the X-rays are shaped through an anti-scatter slit and another Soller slit before passing through a nickel filter. The resultant X-rays can then be considered as collimated (all the X-ray waves are parallel) beam with a narrow range of wavelengths. The intensity of this beam is then measured as a function of angle using a solid-state detector.

When setting the parameters for the diffraction measurements two parameters are particularly important as they affect the resolution and sensitivity of the data. These parameters are the step size and time per step. The step size refers to the difference in angle between each measurement. The smaller the step size the higher the resolution of the data. This is because it ensures that all peaks and features are identified. If the step size is too large peaks may be

missed. Smaller step times can result in the data collection becoming quite time consuming. The time per step is a measure of how long the detector will remain at a particular angle when collecting data. Larger times per step increase the sensitivity of the data as deviations caused by background noise become less significant in the overall spectra (since the number of X-rays collected at each angle is larger). This ensures smaller peaks are not lost.

### 2.3.2 Scanning Electron Microscopy

Electron microscopy techniques can achieve higher resolving powers than their optical counterparts which suffer from the well-known diffraction-limitations of visible light[255]. Consequently, electron microscopy techniques are the method of choice when aiming to obtain high-magnification images of a material's surface topography and composition. Of these, scanning electron microscopy (SEM) is perhaps the simplest and most versatile, in which an electron beam is rastered across relatively large areas with minimal sample preparation required. Various detectors can be coupled inside the SEM chamber meaning a large amount of microanalysis techniques can be used to complement the imaging. In this project focused ion beam (FIB) milling, energy-dispersive X-ray spectroscopy (EDX), secondary ion mass spectrometry (SIMS) and nanoindentation are all combined with secondary electron imaging to characterise solid electrolyte materials.

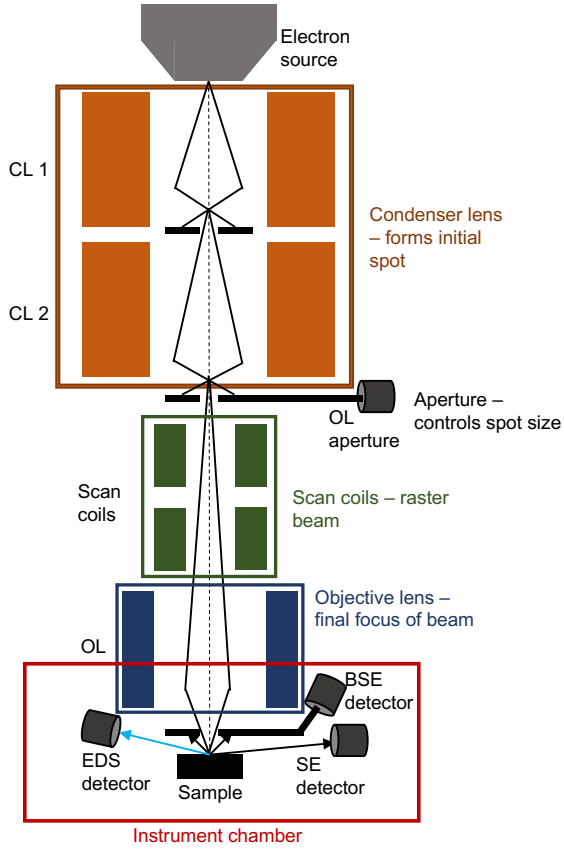



**Figure 2.5:** Schematic of the key components and detectors within a typical scanning electron microscope.

In a typical scanning electron microscope, electrons are generated by a thermionic gun with either tungsten or lanthanum hexaboride sources. The generated electrons are then accelerated through a chamber under ultra-high vacuum (~$10^{-10}$ mbar) whereby a combination of electromagnetic lenses and apertures are used to focus the beam onto the sample, see Figure 2.5. Typically, a set of condenser lenses (CL) will be used to form an initial spot with a later set of objective lenses (OL) used to finalise the focus of the beam. Apertures may be placed after the condenser lenses to fully control the spot size and reduce any aberration effects. In an SEM, scanning coils will be used to raster the electron beam across the sample. When imaging using an SEM, the achievable resolution is highly dependent on the configuration used. Whilst using higher acceleration voltages can lower the wavelength of the electrons and help to improve spatial resolutions, ultimately a collection of electrons is used to yield an image and so the final achievable spot size (affected by diffraction errors and aberrations) is also critical[256]. Higher energy electrons risk beam damage to the sample and

lower spot sizes have an associated signal-to-noise cost and lower depth of field, so the final configuration used is a balance between many considerations.

The accelerated electrons interact with the material in a variety of ways resulting in the emission of electrons and other radiation back out from the same surface with which the probing beam is incident. A schematic illustrating the origin of some of the key emissions is presented in Figure 2.6. Emitted electrons are most commonly captured using either secondary electron (SE) or backscattered electron (BSE) detectors, see Figure 2.5. Secondary electrons are generated by the inelastic scattering of inner core electrons from atoms typically within 5-500 Å of the surface[256]. The efficiency to which secondary electrons can escape is dependent on the surface orientations of the material, with the highest efficiencies typically occurring at sharp edges, see Figure 2.6. As such, the intensity of secondary electron images gives information about the surface topography. Backscattered electrons are beam electrons which have been scattered through high angles by the nuclei of atoms in the first 1-2 microns of the specimen[256]. In addition to topographical information, BSE can also provide compositional information as the intensity of emitted BSE is correlated to the atomic number of the scattering nuclei.

During imaging, fewer electrons escape the sample than are incident. As a result, electronically insulating samples can become locally charged leading to image distortion, uneven brightness, and image drift. Solid electrolytes by design are electronic insulators and so risk charging during imaging. Effective methods to prevent charging effects include coating the sample with a thin film of a metal (e.g., Pt) or imaging using lower acceleration voltages and currents. In this thesis, low voltages and currents were found sufficient to avoid detrimental charging effects.

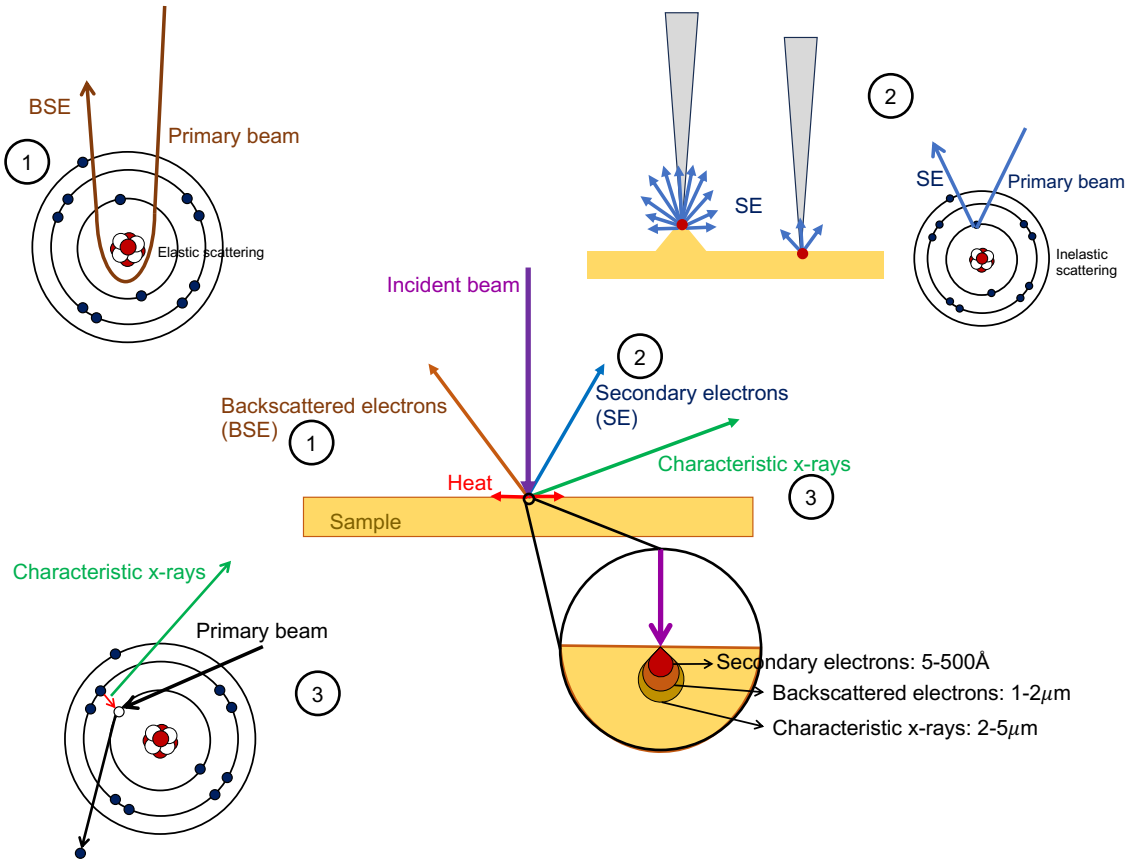



**Figure 2.6:** Schematic illustration of key sample emissions resulting from an incident electron beam, e.g., backscattered electrons (1), secondary electrons (2), and characteristic X-rays (3). The basic mechanistic origins and typical interaction volumes are presented. The relationship between sample topography and secondary electron contrast is also schematically demonstrated (2).

Electron imaging can provide surface information, but in many cases the surface may not fully represent the inner bulk of a material. As well, in solid-state batteries many processes such as dendrite failure initiate within subsurface regions. Sectioning to image regions beneath the surface of the material can thereby provide valuable information. A common sectioning method is to use a focused ion beam (FIB) to mill into the sample by progressively sputtering away material. Typically, a beam of $Ga^+$ or $Xe^+$ ions is focused to mill a trench, the sides of which can be then imaged using the SEM[257]. The process of milling can leave damaged layers on the surface of the specimen which can be tens of nanometers thick. To mitigate beam damage during the work in this thesis, a 5 µm Pt-C layer was pre-deposited on the surface and the milling energy was progressively lowered when approaching the area of interest. Additionally, a Fourier Transform filter was employed to eliminate undesired vertical curtaining

lines, which are common surface artefacts of FIB milling. By milling fiducial markers adjacent to the region of interest, FIB milling can be used to serially section and tomographically image a volume of material. Although destructive, this method can enable the three-dimensional reconstruction of the features imaged in the cross-section.

Aside from electron detectors, the next most common detector installed within SEM chambers is energy-dispersive X-ray spectroscopy detectors. The generation of secondary electrons during electron beam exposure leaves vacant energy levels within the atoms of the sample. The filling of these electron holes by the de-excitation of electrons from higher energy levels in the atom results in the emission of a photon, see Figure 2.6. The energies of the photons are characteristic of the difference between the two energy levels (meaning they are generally in the X-ray frequency range) and are therefore also characteristic of the atomic structure of the emitting element[258]. As a result, the detection of the characteristic X-ray emission spectrum can be used to identify local elemental composition. By rastering the electron beam across the surface, EDX can be used to map the elemental distribution, and combining this with secondary electron imaging, topological information can be superimposed with compositional information. Whilst EDX should still be considered a surface-sensitive technique, the interaction volume may penetrate several microns deep and the mismatch between other imaging methods should be appreciated during analysis[258].

In addition to energy-dispersive X-ray spectroscopy detectors, other chemically sensitive detectors can be mounted within the SEM chamber to give complementary information. One such example is a secondary ion mass spectrometer (SIMS). Although SIMS is a destructive technique it can distinguish even between the isotopes of light elements which cannot be routinely detected using EDX. SIMS essentially involves bombarding a material's surface with a beam of ions (known as the primary beam) and using a mass spectrometer to identify the charged secondary ions which eject from the material as a result of the bombardment[259]. In this thesis, a $Xe^+$ beam focused to approximately 200nm was used for SIMS analysis. Secondary ions were collected and analysed using a quadrupole detector which was tuned to collect the $^7Li^+$ signal. The beam was rastered across the area of interest to generate a 2-

dimensional (2D) map of the distribution of the selected ion signals which could then be overlayed with the corresponding SEM image. This allowed for the identification of lithium metal within subsurface features, something which had been previously inconclusive when using EDX detectors.

### 2.3.3 X-ray computed tomography

X-ray computed tomography (XCT) is a non-destructive imaging technique which can be used to create a three-dimensional map of the internal structure of a material. The precise optics used during XCT can be varied to enable spatial resolutions from tens of microns to several tens of nanometers, with a balance always to be struck between acquisition time, sample size and the field of view[260]. In solid-state batteries, key processes occur at buried interfaces at microscopic length scales and so throughout this thesis specifically 'microtomography' was performed with voxel sizes on the microns length scale.

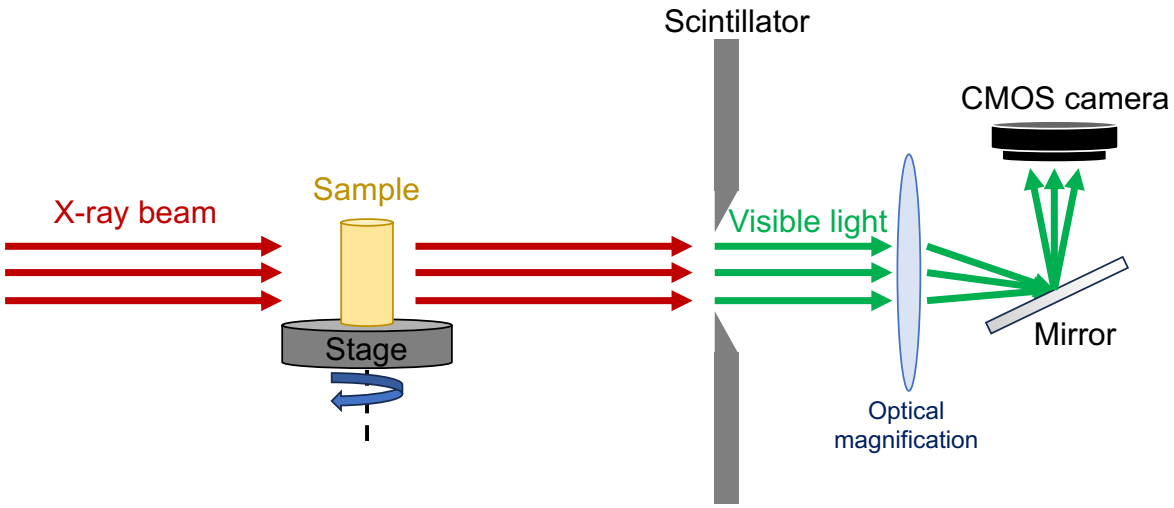



**Figure 2.7:** Illustration of a standard attenuation contrast experimental setup. X-rays penetrate the sample, which is mounted on a rotating stage.

In an X-ray tomography measurement, a collimated (and typically coherent) X-ray beam is directed through a sample, with the transmitted rays collected and converted into visible light using a scintillator, see Figure 2.7. These visible light rays are then optically magnified and imaged using a camera (either a CCD or CMOS detector). At a given angle of rotation, this

process allows for the collection of a two-dimensional projection image. By rotating the sample through 180° and collecting a new projection image at each fraction of a degree, a set of projections can be collected. By feeding these into a (Fourier-based) algorithm, a tomogram can be reconstructed, i.e., a set of virtual cuts through the sample which together contain data for each point in the imaged 3D space[261]. Most X-ray tomography methods provide a 3D map of the X-ray attenuation, as such a more detailed consideration will be made the underlying principle behind these measurements.

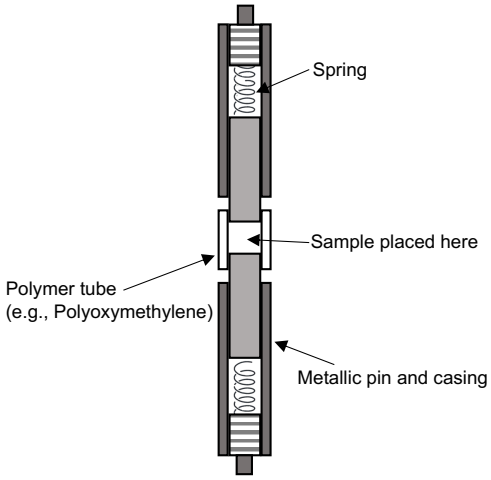



**Figure 2.8:** Simplified schematic of the custom-built XCT tube cell used in this thesis. The cell ensures air-tightness and a constant pressure. During the experiment the cell was connected to a potentiostat via Cu wires connected to the top and bottom. The original cell design was conceived by Ziyang Ning.

In this thesis, *operando* and *in-situ* XCT scans were collected using a custom designed tube cell, a schematic of which is shown in Figure 2.8. The design of the tube cell was such to ensure air-tightness over the course of the experiments (retaining Ar atmosphere) whilst also maintaining a constant stack pressure which could be calibrated prior to the experiment.

#### 2.3.3.1 Attenuation contrast tomography

When X-rays pass through a material, they are partially attenuated, leading to an exponential drop in intensity which can be expressed mathematically using the Beer-Lambert Law, eq. 2.5[262].

$$I(d) = I_0 e^{-\mu d} \tag{2.5}$$

where $I(d)$ is the transmitted intensity for a beam with initial intensity $I_0$ after passing through a material with attenuation coefficient $\mu$ and thickness $d$. In this relationship, the attenuation coefficient, $\mu$, mathematically represents the amount of scattering and absorption events occurring throughout the material. Within a sample, chemical and morphological features mean that the attenuation varies spatially, hence the attenuation coefficient can be treated as a function of position $\mu(x, y, z)$.

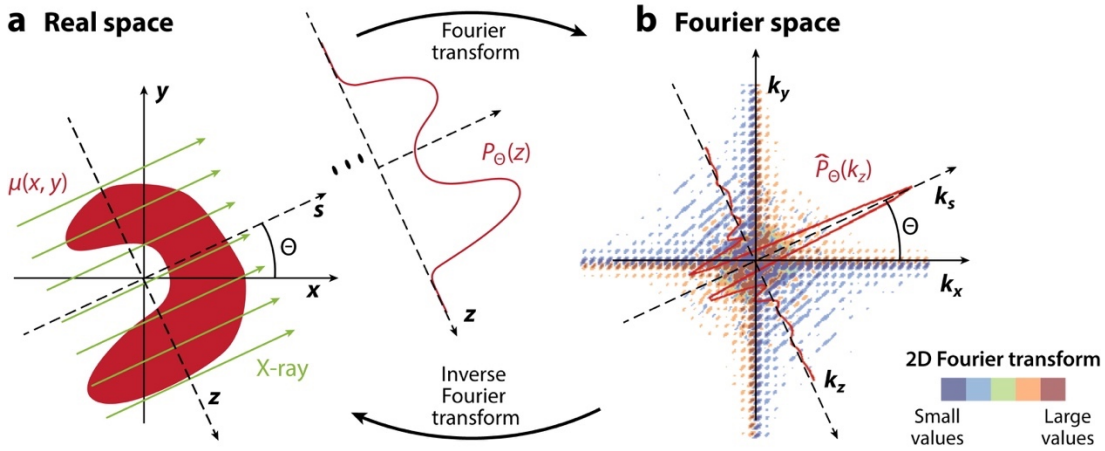



**Figure 2.9:** Figure reproduced from Wood *et al.*[261]. **a** Illustration of a parallel X-ray beam penetrating the sample, which has an attenuation coefficient distribution $\mu(x, y)$ (red) in real space. The corresponding projection $P_\theta(z)$ is acquired at an angle $\theta$. **b** 2D Fourier transform of $\mu(x, y)$ (coloured map) and 1D Fourier transform $\hat{P}_\theta(k_z)$ (red graph) of $P_\theta(z)$ through the origin of the coordinate system orthogonal to the X-ray beam direction. According to the Fourier slice theorem, the set $\{\hat{P}_\theta(k_z)\}_{0\leq\theta<180°}$ is equivalent to $\hat{\mu}(k_x, k_y)$ in polar coordinates. Reproduced with permission from Annual Reviews.

To plot the variation in attenuation in three-dimensions, a series of two-dimensional projections are first captured. Figure 2.9 considers the propagation of a parallel beam of X-rays through an x-y plane in a direction given by $s$, in which a sample is situated with an attenuation coefficient distribution $\mu(x, y)$. At a given angle of incidence on the sample, the X-ray intensity of each position along $z$ is again described using the Beer-Lambert law, see eq. 2.6[§§261].

$$I_\theta(z) = I_0 e^{-\int_{-\infty}^{+\infty} \mu(x,y)\, ds} \tag{2.6}$$

[§§] In this case, $z$ defines a direction orthogonal to the beam path rather than a third cartesian dimension. See also Figure 2.9.

In an XCT experiment, $\frac{I_\theta}{I_0}$ can be determined by taking dark and flat references (projections taken when there is 0% and 100% X-ray transmission, respectively), see eq. 2.7.

$$\frac{I_\theta}{I_0} = \frac{I - I_D}{I_F - I_D} \tag{2.7}$$

Whereby $I$, $I_D$ and $I_F$ are X-ray intensities measured by the detector for the sample, dark reference, and flat reference, respectively. Taking advantage of the Beer-Lambert law, the line integral across $z$ of the attenuation co-efficient $\mu(x, y)$ can be determined using eq. 2.8[261].

$$P_\theta(z) = \int_{-\infty}^{+\infty} \mu(x(\theta, s, z), y\,(\theta, s, z))\, ds = -\ln\left(\frac{I_\theta(z)}{I_0}\right) \tag{2.8}$$

Whereby $P_\theta(z)$ is the projection of $\mu(x, y)$ along the beam path. By repeating this across all multiple angles of incidence (i.e. $0 \leq \theta < 180°$) a set of projections can be collected, $\{P_\theta(z)\}_{0 \leq \theta < 180°}$. According to the Fourier slice theorem, the 1D Fourier transform $\hat{P}_\theta(k_z)$ of a projection $P_\theta(z)$ is equal to the 2D Fourier transform $\hat{\mu}(k_x, k_y)$ of the attenuation coefficient distribution $\mu(x, y)$.[261] Hence, we can directly obtain $\mu(x, y)$ by performing a 1D Fourier transform on the set $\{P_\theta(z)\}_{0 \leq \theta < 180°}$ to obtain the set $\{\hat{P}_\theta(k_z)\}_{0 \leq \theta < 180°}$, and then performing a 2D inverse Fourier transform on that set, see Figure 2.9. After performing this Fourier-based reconstruction, the X-ray attenuation coefficient distribution can then be plotted as normalised grayscale image. By assembling all slices, a virtual 3D model of the sample is generated, in which the greyscale of each voxel represents the X-ray attenuation.

### 2.3.3.1 Experimental considerations

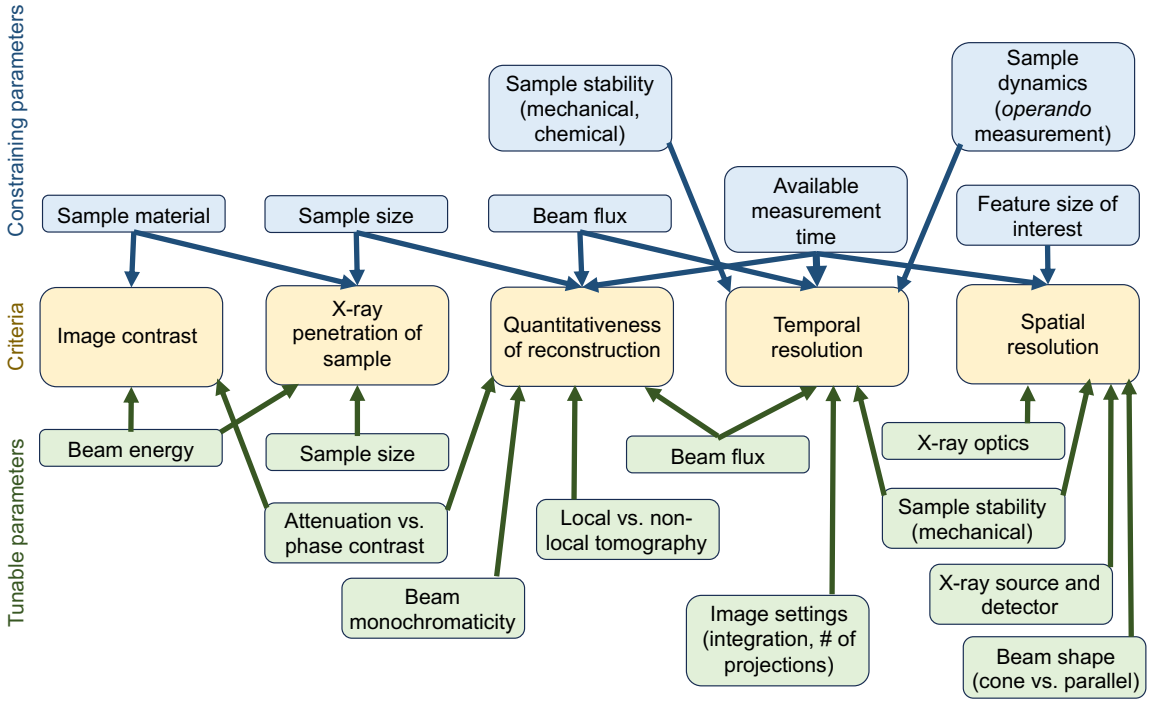



**Figure 2.10:** Chart summarising the most important criteria (yellow boxes) to consider when designing an X-ray tomographic experiment. Whereas some parameters allow for the optimisation of tomographic imaging conditions (green boxes), others constrain the experimental design (blue boxes). Arrows indicate the major interdependencies. Adapted from Wood *et al.*[261].

When designing an XCT experiment, important considerations must be made regarding image contrast, the spatial resolution within scans and the time resolution between scans, as all three determine what features can be analysed and whether developments can be captured dynamically, e.g., under *operando* conditions. A summary is given in Figure 2.10. Temporal resolution is determined by the scan acquisition time which depends on the beam flux, imaging settings (number of projections and integration time), and the properties of the sample itself. In general, high temporal resolution comes at the expense of increased image noise. When considering spatial resolutions, improvements can be made by altering the X-ray optics, but these often limit the flux and hence acquisition times. Alternatively, fast imaging can be retained by adjusting the scintillator and optical microscope, but any improvement then becomes limited by the diffraction limit of visible light. Another important consideration is that due to the finite size of detectors, higher spatial resolution limit set-ups will have restricted field-of-views.

To analyse features of interest, sufficient contrast between the features and the background is needed. This can be optimised by varying the energy of the beam or even altering the type of tomography. For attenuation contrast tomography, photoabsorption is the dominant X-ray–matter interaction, with the attenuation coefficient expressible through eq. 2.9[261,263].

$$\mu = \frac{2h^4c^4}{\lambda}\rho_e\frac{Z^3}{E^4}\left[\frac{1}{m}\right] \tag{2.9}$$

Where $h$ is Planck's constant, $c$ is the speed of light, $\rho_e$ is the electron density of the material, and $Z$ is the atomic number of the material. The contrast between two different materials ($\Delta\mu = \mu_1 - \mu_2$) is hence determined by the heaviness of elements ($\mu \propto Z^3$) and the beam energy ($\mu \propto \frac{1}{E^4}$). When trying to distinguish between low attenuating mediums such as lithium and empty space, alternative tomography methods can be considered, such as phase contrast tomography.

#### 2.3.3.1.1 Phase contrast tomography

Every material has an X-ray complex refractive index $n = 1 - \delta + i\beta$. Whereby the imaginary part $\beta$ describes the change in amplitude and the real part $1 - \delta$ describes the change in wavelength. Changes in attenuation are directly related to the changes in amplitude through $\mu = \frac{4\pi\beta}{\lambda}$ where $\lambda$ is the X-ray wavelength, hence attenuation contrast tomography essentially reconstructs the imaginary part of the complex index of refraction, $\beta$.[261] Changes in $\delta$ across a sample instead result in a phase shift, $\Phi$, see Figure 2.11.

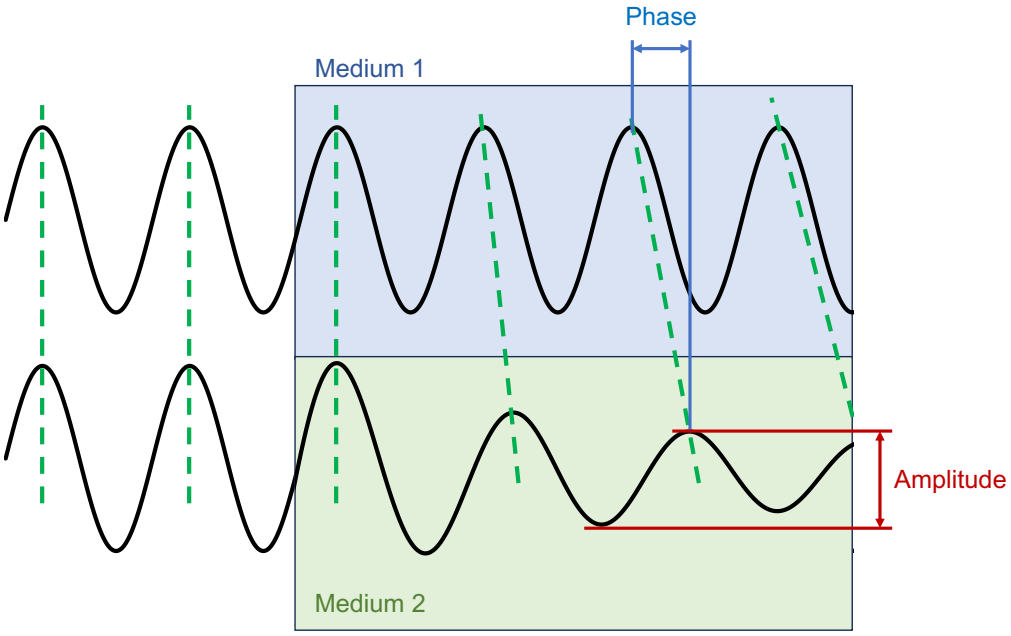



**Figure 2.11:** Illustration of X-ray interaction with a hypothetical sample consisting of two media. Whereas attenuation causes a decrease in beam intensity (the imaginary part of the complex refractive index), refraction causes a deflection of the beam (the real part of the complex refractive index). Adapted from Wood *et al.*[261].

Whilst this phase shift cannot be directly measured, the relative phase shifts between (partially) coherent X-rays that pass through different parts of the sample can cause beam deflections at material interfaces, known as edge enhancements. Using specialised set-ups[***], it is possible to reconstruct the real part of the complex refractive index, $\delta(x,y)$, through the measurement of these interference effects, in a type of tomography known as phase contrast tomography. The magnitude of $\delta$ can be expressed with eq. 2.10[261,263].

$$\delta = \frac{h^2 e^2}{8\pi^2 \epsilon_0 m_e} \rho_e \frac{1}{E^2} \tag{2.10}$$

where $e$ is the elementary charge, $\epsilon_0$ the vacuum permittivity, and $m_e$ the electron mass. $\delta$ is hence independent of atomic number. Consequently, the phase contrast ($\Delta\delta = \delta_1 - \delta_2$) that can be achieved between low attenuation materials, can be orders of magnitude higher than in an attenuation-based measurement.

[***] Whilst specialised set-ups are needed to obtain a quantitative phase contrast map, filtering algorithms such as the one by Paganin *et al.*[264] can qualitatively enhance the contrast of weakly attenuating materials using a standard attenuation contrast experimental set-up.

### 2.3.4 On-line mass spectrometry

Detection of gas consumption and production using mass spectrometry can enable insights into the nature of electrochemical/chemical reactions and or reveal the type and quantity of unknown precursor materials. In this thesis, a chemical reaction was performed so to quantify the amount of Li metal within solid electrolyte samples by means of an on-line gas mass spectrometry set-up. On-line refers to the fact that the mass spectrometer (MS) is connected via a direct pipeline to the reaction chamber. This contrasts with the more common methodology whereby a small gas sample is extracted via a syringe and transported to a distant MS.

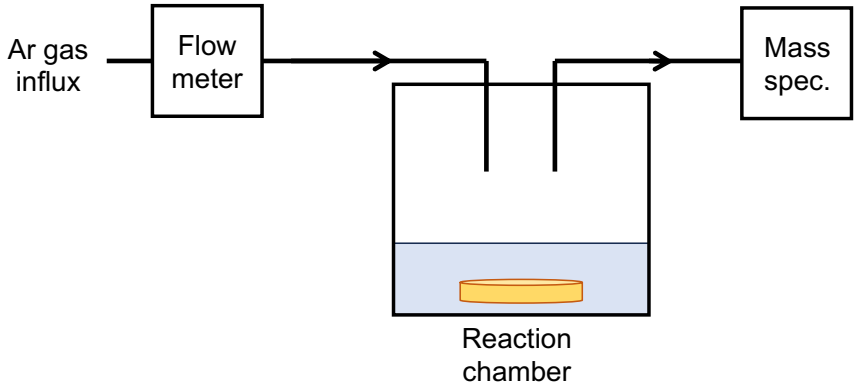



**Figure 2.12:** Schematic illustration of the on-line mass spectrometry set-up used in this thesis.

A basic schematic of the on-line setup in this thesis is presented in Figure 2.12. A carrier gas flow (pure Ar) is passed through a flow meter into the reaction chamber in which gaseous products are generated *in-situ*. These products are then directly delivered via a pipeline to the mass spectrometer for quantitative chemical analysis. The mass spectrometry consists of three basic stages[265]. Firstly, the input gas molecules are ionised using an electron gun within what is known as the ion source chamber. These resultant ionised molecules are then accelerated through a magnetic field whereby slight differences in acceleration can be directly attributed to differing mass-to-charge ratios of the individual ions. These differences are captured by the ion time resolution of the ion detector thereby allowing the type as well as the number of ions to be recorded. Before measurement, the entire set-up is calibrated using known quantities of common gases (e.g., Ar, $O_2$, $CO_2$, $H_2$, $N_2$) accounting for the nonlinearity

and cross-sensitivity of the gas mixture. This calibrated on-line set-up can then be used to precisely quantify the entirety of the gaseous reaction products by simply normalising the detected gases against the carrier gas flow.

## 2.4 Electrochemical Techniques

### 2.4.1 Potentiostatic Electrochemical Impedance Spectroscopy

Impedance spectroscopy is a powerful non-destructive technique which can probe physical processes in electrochemical systems across a wide range of length and time scales. Potentiostatic electrochemical impedance spectroscopy (PEIS) involves using a small perturbation voltage to measure the resultant alternating current response across a range of frequencies. The electrical response of a cell may contain contributions from multiple complex migration and polarisation processes occurring both within the electrolyte and at electrode/electrolyte interfaces[266]. The advantage of an alternating current (AC) method such as PEIS is that, in principle, individual contributions may be separated out. In particular, and in contrast to steady state direct current (DC) measurements, the intra- and inter-crystalline conductivities of polycrystalline electrolytes can be individually determined, and electrolyte conductivities readily measured[267]. As well, by using a small amplitude oscillation (e.g., 5 mV) any perturbation to the system can be minimised, avoiding any irreversible changes.

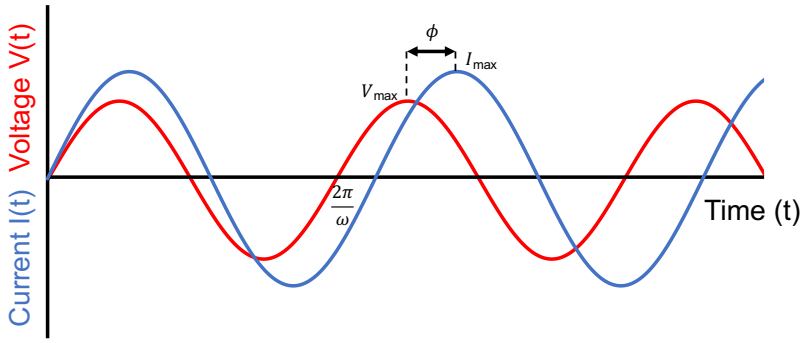



**Figure 2.13:** The relationship between the applied voltage (red curve) and current response (blue curve) during a PEIS experiment.

Whilst fundamentally it is the current response which is measured during EIS, its interpretation is centred around a determination of the system's impedance ($Z(\omega)$). Simply defined,

impedance is the retardation of the flow of charge. By measuring the ability of the system to respond to a change in voltage, we can determine two components to the impedance – a resistive component (energy loss) and a capacitive component (energy storage)[268]. For a given frequency, the maximum magnitude of the current ($I_{max}$) and its temporal lag ($\phi$) from the maximally applied voltage ($V_{max}$)) are both recorded, see Figure 2.13. The total impedance, $Z$, which is the sum of the resistive and capacitive components, follows from Ohm's law $Z = V_{max}/I_{max}$. Together $Z$ and $\phi$ provide polar coordinates for a complex plane. When mapped the resultant graph is referred to as a Nyquist plot. In the Nyquist plot, the abscissa is the real (resistive) impedance, and the ordinate is the imaginary (capacitive) component. By sampling across a range of frequencies (e.g., 0.1 Hz – 1 MHz) the frequency dependence of both the resistive and capacitive impedances can be determined and interpreted, see Figure 2.14.

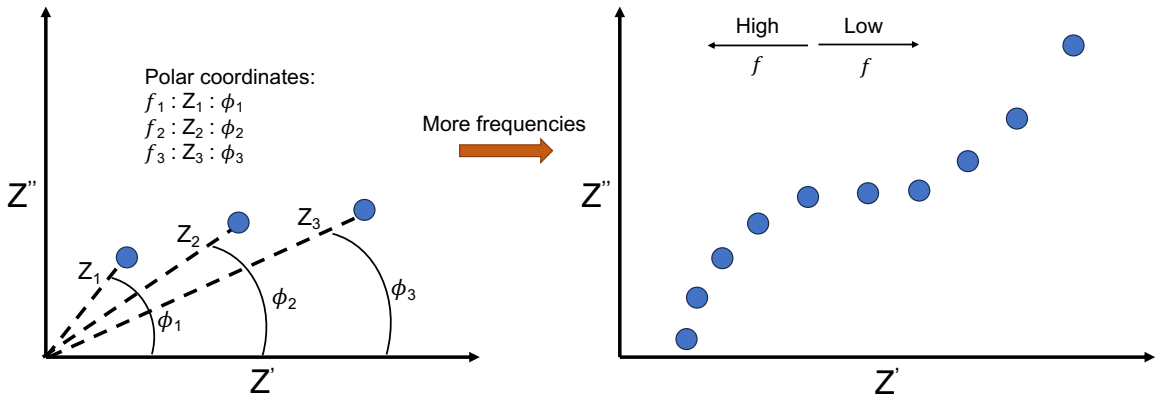



**Figure 2.14:** The data obtained at each frequency ($f$), $\phi$ and $Z(\omega) = V_{max}/I_{max}$ provide the polar coordinates for each point on the Nyquist plot. Higher frequency data points are closer to the origin. Adapted from Browne *et al.*[268].

Electrochemical cells typically exhibit many electrical phenomena, thus to analyse the data it is necessary to consider the physical nature of the cell (whether it contains a polycrystalline or single crystal electrolyte, the existence of any reaction layers etc.) and the electrical behaviour to be expected as a consequence of this. In other words, it is necessary to consider the possible equivalent circuits or networks of electrical components which can represent the cell electrically. Figure 2.15 presents the Nyquist plots for a range of ideal electrical circuits. Ion migration within solid electrolytes and in solid-state cells involves transport across multiple

phases and boundaries (such as bulk crystal, grain boundaries, SEI layers and electrode interfaces) which each induce a combination of resistive and capacitive effects of various characteristic frequencies[267]. As a result, typically a combination of semi-circular features present in the Nyquist plots of solid-state cells.

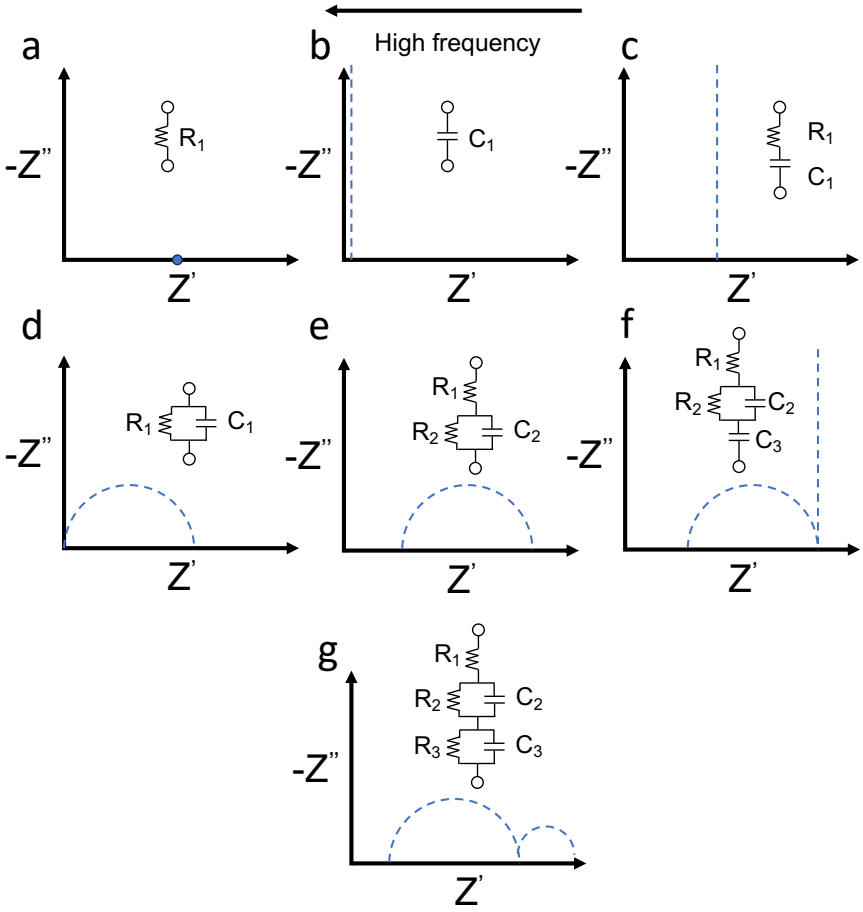



**Figure 2.15:** Nyquist plots for **a** a resistor, **b** a capacitor, **c** a capacitor and a resistor in series, **d** a resistor in parallel with a capacitor (RC component), **e** a resistor in series with an RC component, **f** a resistor in series with an RC component in series with a capacitor, **g** a resistor in series with two RC components.

When using reversible electrodes, such as Li metal in this thesis, the interfacial impedance will present as an overlapping semi-circular feature at low frequencies, as in Figure 2.15g. By using ion blocking electrodes, interfacial impedances will present as a capacitive tail at low frequencies, see Figure 2.15f. In this thesis, EIS is used to determine the conductivity of differently sintered sulphide electrolytes and across a compositional range of solid electrolyte composites. By using blocking electrodes, the contributions resulting purely from the internal impedance of the electrolytes themselves could be more easily isolated.

### 2.4.2 Galvanostatic Cell Testing

Galvanostatic cell testing involves applying a constant current ($I$) between a working and counter electrode whilst the voltage ($V$) is measured relative to reference electrodes. Most commonly the counter and working electrodes themselves may act as the reference electrodes in what is known as a two-electrode set-up, see Figure 2.16a. In battery research, a constant current is typically driven periodically in alternating directions across a cell to simulate charge and discharge cycles[52,111]. Such tests can directly indicate the potential cycle life of a cell. Provided cells are cycled within a well-controlled environment, any change in the voltage needed to drive a constant current through the cell can be interpreted as a change in internal resistance ($R$) within the cell, assuming the validity of Ohm's Law ($V = IR$). Hence voltage profiles may serve as a valuable insight into the extent of any degradation processes occurring during cell operation.

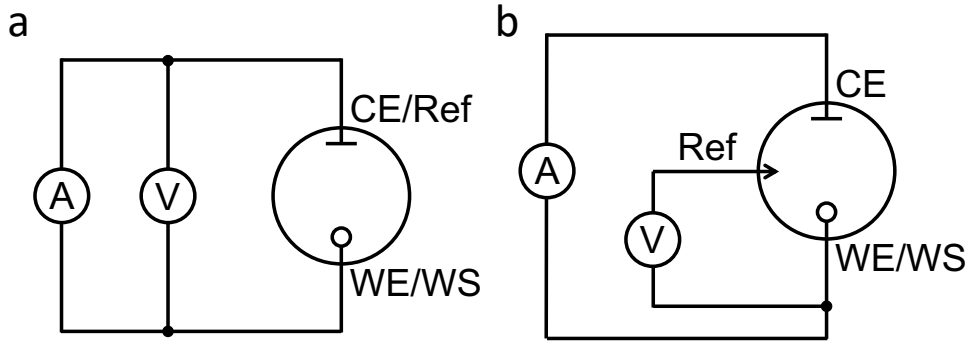



**Figure 2.16:** Diagrams of **a** the two-electrode and **b** the three-electrode set-ups used during the galvanostatic cycling of solid-state cells.

Throughout this thesis, galvanostatic cell testing of Li symmetric cells (Li/SE/Li) has been performed extensively using three-electrode cell set-ups, see Figure 2.16b. By using a three-electrode configuration the voltage changes resulting from one interface can be effectively isolated. This is particularly important when investigating the Li/SE interface, as separate phenomena govern polarisation changes during Li plating and Li stripping, e.g., contact loss and dendrite penetration. When cycling Li symmetric cells with a two-electrode cell configuration, one interface undergoes a Li plating reaction whilst the other undergoes a Li

stripping reaction. Changes in polarisation resulting from each interfacial reaction are thereby difficult to distinguish between.

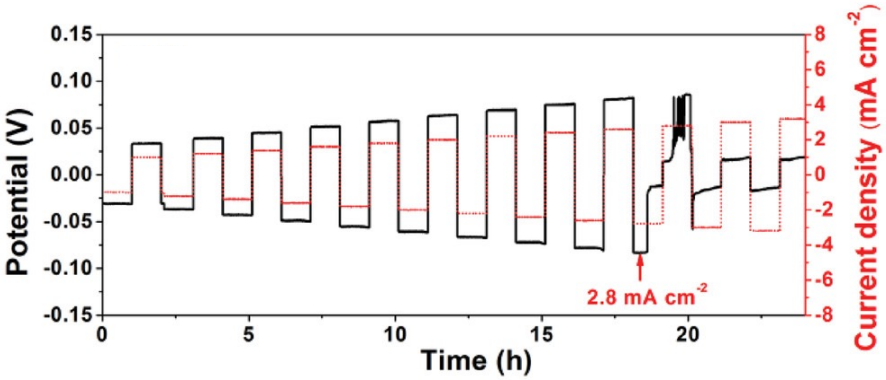



**Figure 2.17:** Figure from Su *et al.*[269]. Typical literature example of a 'rate-test'. Reproduced with permission from Elsevier.

One of the key limitations of solid-state cells is their charge and discharge rates. Several variations of cell cycling exist within the SSB literature which aim at probing maximum charge/discharge rates, with the most common format known as a 'rate-test'[270], see Figure 2.17. These tests often involve a two-electrode set-up whereby the cell is first cycled at low current densities which are sequentially increased until cell failure (generally at the point of short-circuit), at which point a 'critical' current is defined. Unfortunately, this format has suffered from a severe lack of standardisation leading to an unhelpful spread of reported critical currents for identical systems[270]. In this thesis, alternative methods for determining the critical charging currents of solid-state cells are explored. For example, in Chapter 4 single plating experiments are carried out on multiple three-electrode cells with Li electrodes, each at a different current density, with a drop in the plating potential indicating that the critical current for dendrite growth had been exceeded. Carrying out single plating experiments has the advantage that any failures associated with voiding on stripping will not affect the determined critical current, however the method requires that each cell is closely similar and demands high standards of cell reproducibility.

## 2.5 Mechanical Testing

### 2.5.1 Nanoindentation

Nanoindentation is a widely established technique to determine the elastic modulus and hardness of materials without the need for additional imaging. As well, it can be used to estimate the fracture toughness through the incursion of radial cracking in brittle materials. During nanoindentation, a hard diamond tip with known geometry and mechanical properties is driven into a material to induce both elastic and plastic deformation. By measuring both the load and vertical displacement of the tip during indentation, the mechanical properties of the specimen can be extracted.

In 1992, Oliver and Pharr developed a method for extracting the modulus and hardness of materials by analysis of indentation unload curves made at small scales using a Berkovich tip (three-sided pyramid geometry)[271]. Figure 2.18a depicts a load-displacement curve of a typical nanoidentation loading cycle.

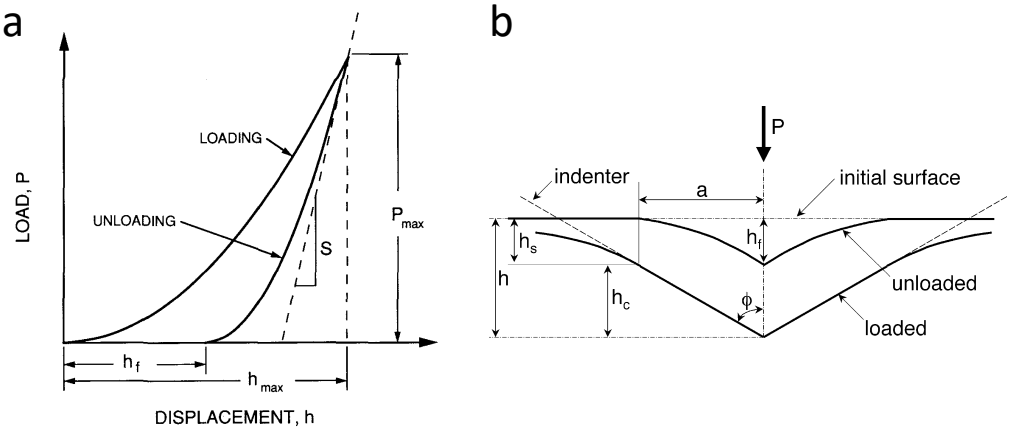



**Figure 2.18:** Figure reproduced from Oliver *et al*.[272]. **a** Schematic illustration of indentation load–displacement data showing important measured parameters. **b** Schematic illustration of the unloading process showing parameters characterising the contact geometry. Reproduced with permission from Springer Nature.

It was found that the indentation hardness of the material could be determined using the contact area of the material during loading, see eq. 2.11[272].

$$H = \frac{P_{max}}{A} \tag{2.11}$$

Whereby, $H$ is the hardness and $P_{max}$ is the maximum applied load. For a Berkovich tip, the contact area, $A$, can be calibrated for a known depth of indentation using a geometrical relationship (eq. 2.12)[272].

$$A = 3\sqrt{3}h_c^2 \tan^2 \phi = 24.494h_c^2 \quad (2.12)$$

Whereby $h_c$ is the depth along which contact is made between the indenter (see Figure 2.18b) and the specimen and $\phi$ is the indenter face angle, which for a Berkovich tip is equal to 65.27°[272].

Measurement of the elastic modulus follows from its relationship to the contact area and the measured unloading stiffness, see equation 2.13[272].

$$S = \beta \frac{2}{\sqrt{\pi}} E_{eff} \sqrt{A} \quad (2.13)$$

Whereby, $S = \frac{\delta P}{\delta h}$, is the elastic unloading stiffness, defined as the slope of the upper portion of the unloading curve during the initial stages of unloading (also called the contact stiffness). $\beta$ is a constant (usually unity) and $E_{eff}$ is the effective elastic modulus takes into account the fact that elastic displacements occur in both the specimen, with Young's modulus $E$ and Poisson's ratio, $\upsilon$, and the indenter, with elastic constants $E_i$ and $\upsilon_i$ (see eq. 2.14)[272].

$$\frac{1}{E_{eff}} = \frac{1-\upsilon^2}{E} + \frac{1-\upsilon_i}{E_i} \quad (2.14)$$

To ensure the inherent properties of the sample are measured with minimal statistical error, in this thesis a range of indents were collected across several locations for varying loads (20 – 400 mN) hence probing a range of displacements. For each region, a mean modulus/hardness is taken by plotting modulus/hardness vs depth, with the values below 0.5 microns discarded to avoid errors from surface roughness. The overall mean value is then determined by fitting a normal distribution to the continuous distribution of mean values and taking the mode (this reduces any skew from anomalous outliers). The standard error is then simply calculated from the variance and the number of tests conducted in each region.

By inducing radial cracking during indentation, nanoindentation can be used to measure the fracture toughness of a material. This is typically achieved by using higher loads and a sharper

tip such as a cube corner tip which gives greater displacement for a given area and load, thereby increasing the likelihood of fracture. In practice, a multitude of indents across several regions are made with the aim to achieve cracking in the sample around each indent. Post testing each indentation site is then imaged using an SEM. If radial cracks were found to be present, then the dimensions of both the indent and surrounding cracks were recorded. The fracture toughness, $K_{1C}$, can then be simply calculated for each cracked indent using the Lawn, Evans, and Marshall equation[273] (eq. 2.15).

$$K_{1C} = \alpha \left(\frac{E}{H}\right)^{1/2} \left(\frac{P}{c^{3/2}}\right) \tag{2.15}$$

Where $E$ is the elastic modulus, $H$ is the hardness, $P$ is the load, $c$ is the total radial crack length and $\alpha$ is a geometric constant for a cube corner tip. The mean value across all indents can then be taken as the final fracture toughness value.

### 2.5.2 Microcantilever Bending

In this thesis, the first initiation of dendrite cracks is considered as a result of the pressurisation of microscopic subsurface pores during Li plating. In such a scenario, fracture is considered to originate through the generation of completely new cracks rather than through the propagation of a critical pre-existing flaw, with the fracture of adjacent grain boundaries the most likely source of weakness. Therefore, a local fracture strength (e.g., grain boundary fracture strength) was considered as a fracture criterion of the solid electrolyte during dendrite initiation. A local fracture strength of the $Li_6PS_5Cl$ solid electrolyte was determined through the mechanical failure of milled microcantilevers.

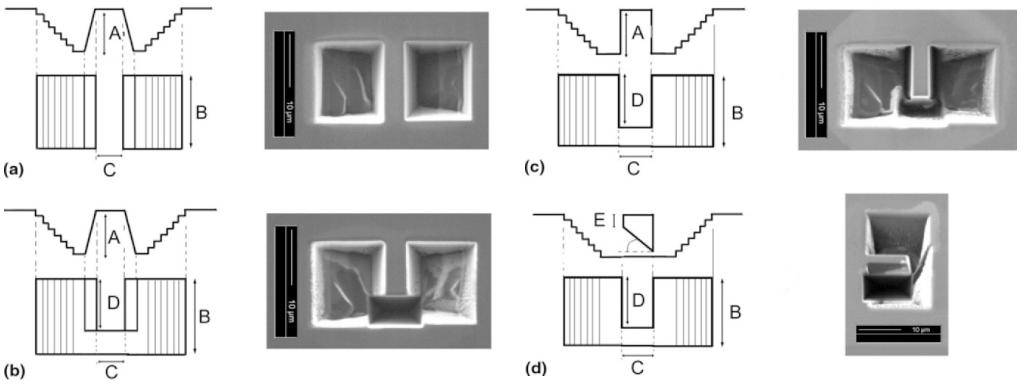



**Figure 2.19:** Figure reproduced from Maio *et al.*[274]. **a-d** the milling stages performed to carve a microcantilever test specimen. Reproduced with permission from Springer Nature.

In this thesis, microcantilevers were manufactured using a focused ion beam milling procedure. The desired cantilever morphology is achieved by first milling a U-shaped trench around the envisaged cantilever (Figure 2.19a&b) and then tilting the sample to perform two undercut milling steps (Figure 2.19c&d). Before milling, grain boundaries were revealed on the surface using ion channelling contrast imaging, cantilevers could then be milled so to include a single grain boundary as its largest pre-existing defect, Figure 2.20.

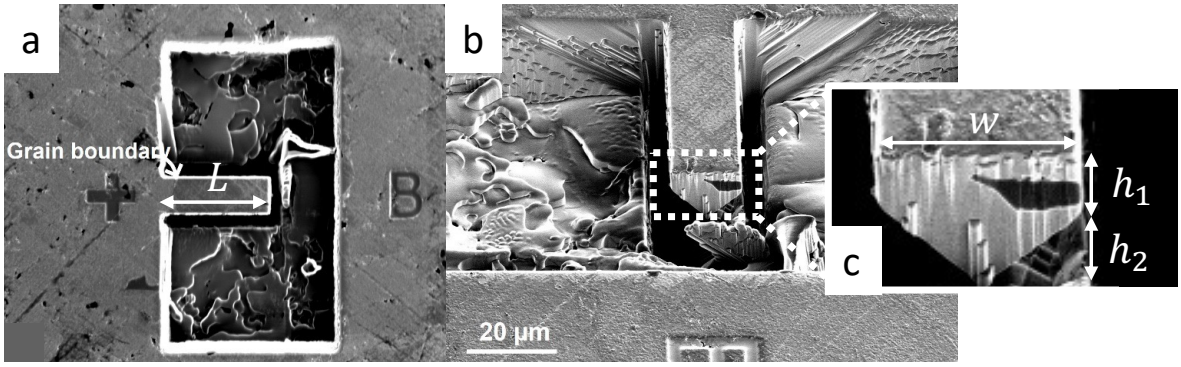



**Figure 2.20: a** Top view ion channelling contrast image of a micro-cantilever with grain boundary and "+" reference points. **b** Side view SEM images of the micro-cantilever demonstrating the cutting geometry. **c** magnified inset of **b** with key microcantilever dimensions labelled.

Once milled, the microcantilevers were subject to mechanical failure through bending tests. A nanoindentor using a cube corner tip was used to apply a load to the free end of the cantilever using a displacement control regime (2.5 nm per second). At the point of fracture, the applied load was recorded. The local fracture strength for each microcantilever was calculated using the following equation for fracture stress[275], $\sigma_c$:

$$\sigma_c = \frac{P_f L_C y}{I} \tag{2.16}$$

Where $P_f$ is the load at the point of fracture, $L_C$ is the distance between the loading point and the crack, $I$ is the second moment of area and $y$ is the vertical distance between the neutral plane and the upper surface. $I$ and $y$ are calculated through measurements of each microcantilevers dimensions imaged using SEM, see Figure 2.20c.

The second moment of area, $I$, is determined using equation 2.17[275].

$$I = \frac{wh_1^3}{12} + \left(y - \frac{h_1}{2}\right)^2 h_1 w + \frac{wh_2^3}{36} + \left(\frac{h_2}{3} + h_1 - y\right)^2 \frac{wh_2}{2} \tag{2.17}$$

The vertical distance between the neutral plane and the upper surface, $y$, is determined using equation 2.18[275].

$$y = \frac{6h_1^2 + 3h_1h_2 + h_2^2}{12h_1 + 3h_2} \tag{2.18}$$

In total, a number of microcantilevers were tested and the mean value taken as the local fracture strength of the solid electrolyte.

# Chapter 3: Dendrite initiation and propagation

## 3.1 Aim

Solid-state batteries with a lithium metal anode and solid ceramic electrolyte (Li-SSBs) could provide a substantial increase in energy density compared to today's Li-ion batteries, yet on charging (lithium plating) at rates of several mA $cm^{-2}$, lithium filaments (known as 'dendrites') penetrate the solid electrolyte, leading to short-circuit and cell failure[30,140,276]. As a result, Li dendrite failure stands as the most significant barrier to any widespread adoption of Li-SSBs[18,138,139]. Progress in mitigating the susceptibility to this failure has been stunted by a lack of mechanistic understanding. This chapter aims to utilise newly advanced *operando* XCT imaging to elucidate novel details of Li dendrite failure in solid electrolytes to develop a comprehensive mechanistic understanding which is consistent with experimental observations. Due to its commercial promise, the sulphide $Li_6PS_5Cl$ ceramic was chosen as a model solid electrolyte for this study.

## 3.2 Introduction

For over a decade, the solid-state battery community has struggled to better understand the mechanism that controls the vexing phenomena of Li metal penetration in solid electrolytes during charging[51,138,140]. All-solid designs had been expected to suppress the dendritic growth of Li that has prevented the use of Li anodes with liquid electrolytes, but the subsequent heralding of new fast Li-ion conducting ceramics across the past 15 years has proven that even stiff solid electrolytes are susceptible to Li metal propagation and short-circuit failure at practical current densities[140,277].

Many of the significant challenges in understanding the underlying processes governing Li dendrite formation in ceramic electrolytes have stemmed from difficulties in characterisation[278,279]. Li dendrites form during cell operation at buried solid-solid interfaces, with key developments occurring at microscopic length scales across short timescales. As a

result, previous attempts to experimentally characterise the formation of Li dendrites have resulted in an incomplete jigsaw of information. Accordingly, there has been a wide range of proposed mechanisms. Whether Li penetrates via purely mechanical fracture or involves electrochemical degradation of the electrolyte, whether Li can deposit directly into isolated defects within the electrolyte, and as to whether grain boundaries, cracks or pores take precedence as points of weakness have all proven matters of contention[51,140].

In 2017, Porz *et al*. used a novel *operando* optical microscopy set-up to demonstrate that Li deposition at high rates induced fracture of the ceramic electrolyte and that the electrolyte's susceptibility to this failure was correlated to the presence and severity of surface flaws[280]. The key question at the heart of the issue then became exactly how a "soft" metal such as lithium could break through a mechanically stiff ceramic. The initial leading consensus took inspiration from earlier work done in the 1980s studying molten Na/Na-β''-Alumina cells, which had proposed Griffith flaws on the surface of the Na-β''-Alumina electrolyte as the points of initiation for short-circuiting cracks during the electrodeposition of Na at high currents[169,171]. Following this, a string of modelling works in more recent years have proposed that Li dendrites in Li-SSBs originate because of Li plating within Li-filled cracks on the surface of the ceramic electrolyte[281–283]. In these models it is proposed that, at sufficient current densities, pressure gradients resulting from preferential Li plating at the tip of the crack can induce pressures capable of extending the crack further into the electrolyte. The extended crack is then proposed to refill and the process to repeat.

In response to the characterisation challenges posed by Li dendrite failure, pioneering work in the past five years has paved the way for the successful application of X-ray computed tomography (XCT) to study Li-SSB failure during *in-situ* and *operando* conditions[284,285]. In 2021, we used X-ray computed tomography (XCT) to image Li dendrite growth *in situ* during the charging of a Li/$Li_6PS_5Cl$/Li cell[286]. The results demonstrated that dendritic cracks propagated whilst only partially filled, which directly contradicted previous models which had relied upon the cracks to be completely filled. Additionally, cracks were seen to spatially

correlate with porosity within the ceramic, raising the question of the role of porosity within the failure process. Further characterisation as well as a new mechanistic understanding has therefore been necessary to explain the origin and development of Li dendrites in a way that adheres to these new observations.

In this chapter, continuous *operando* XCT scanning with vastly improved time resolution is used to follow the development of dendrite cracks during constant-current plating whilst capturing the earliest developments of the cracks. The results suggest two distinct stages of dendritic failure, crack initiation and crack propagation. Initiation is proposed to arise from Li deposition into subsurface pores, by means of microcracks that connect the pores to the surface. By contrast, dendrite propagation occurs by wedge opening, with Li driving the dry crack from the rear, not the tip. Using experimental inputs from XCT, FIB-SEM as well as novel mechanical testing, both the initiation and propagation processes are modelled. The predicted differences in stack pressure dependency between the two processes is then exploited in experimental cells to demonstrate a substantial extension in cycle life in cells despite the initiation of dendritic cracks. The results both verify the mechanistic understanding whilst also pointing the way to future directions to mitigate dendrite failure in Li-SSBs.

## 3.3 Experimental

### 3.3.1 Electrolyte preparation and cell assembly

All procedures were performed inside an Ar-filled glove box ($O_2$ and $H_2O$ levels < 1 ppm). $Li_6PS_5Cl$ solid electrolyte powder was purchased from *MSE Supplies* and pressed into a disc using a 5-mm-diameter stainless steel die set under a uniaxial pressure of 400 MPa. The disc was then transferred to a furnace and heat treated at 300 °C for 20 min (10°C per min heating and cooling rate). The sintered electrolyte disc was then cooled to room temperature and used for cell assembly.

### 3.3.2 Three-electrode cell cycling

For a three-electrode cell, two disc-shaped lithium electrodes of 1 mm diameter were pressed onto the same side of the electrolyte disc as the working and reference electrodes. The working and reference electrode were separated by a 1 mm-wide polymer insulating tape mask. A 5 mm lithium disc was pressed onto the other side as the counter electrode. The assembly was then placed into a pouch cell with stainless steel current collectors and sealed under vacuum (~ $10^{-3}$ bar). For prolonged cell cycling in section 3.4.4.2, cells were cycled galvanostatically with a capacity on each half-cycle of 0.5 mAh/cm$^2$. While the plating current on the working electrode was 4 mA/cm$^2$, a current density of 0.05 mA/cm$^2$ was used on stripping to ensure no void formation at the WE/SE interface. All galvanostatic measurements were performed using a Gamry Interface 1010 potentiostat.

### 3.3.3 *Operando* X-ray computed tomography

X-ray tomograms were recorded at the I13-2 beamline at the Diamond Light Source. A pink beam with beam energy ranging from 8 keV to 30 keV was employed to maximise the X-ray beam flux and so improve the time resolution. Projections were collected with a PCO Edge 5.5 sCMOS camera combined with an optical microscope with a 4x magnification, resulting in a pixel size of 1.625 μm and a field of view of 4.7 × 4.4 mm$^2$. A 500-μm-thick LuAG scintillator was used to convert X-rays to visible light. The exposure time was set to 100 ms. For each tomogram, 1801 equiangularly distributed projections were taken over 180º as well as 50 dark and 50 flat references before and after the *operando* experiment. X-ray tomograms were obtained at the pristine state and were then collected continuously during galvanostatic plating with a current density of 3 mA/cm$^2$ and a capacity of 3 mAh/cm$^2$. For the *operando* XCT characterisation in section 3.4.1, metallic lithium 100 μm thick was punched into 2-mm-diameter disc-shaped lithium electrodes and pressed onto both sides of the $Li_6PS_5Cl$ disc. The cell was then assembled into a customised tube-cell, which maintained airtightness and a stack pressure of 7 MPa on the beamline. The 7 MPa of pressure was applied using a

constantly applied spring force which was measured and calibrated using a transducer, see Chapter 2 for further details.

### 3.3.4 On-line Mass Spectrometry

On-line mass spectrometry measurements were conducted on a range of pristine and Li-plated $Li_6PS_5Cl$ electrolytes. If subject to galvanostatic cycling, the cells were disassembled, and the lithium electrodes removed from the $Li_6PS_5Cl$ discs in an Ar-filled glovebox. For pristine samples, Li electrodes were attached symmetrically to a $Li_6PS_5Cl$ disc, allowing it to rest without electrochemical testing, after which the electrodes were removed following the same procedure. After removal of the Li, the solid electrolyte discs to be tested were transferred into a sealed vial along with a magnetic stirrer. The vials were then connected into the on-line mass spectrometry set-up upon which an Ar flow was established to remove excess gas from within the vial, after which 100% Ar flow could be detected. An excess amount of degassed aqueous LiOH solution was then injected into the vial, slowly dissolving the $Li_6PS_5Cl$ electrolyte and reacting with any Li metal inside the electrolyte evolving $H_2$. $H_2$ gas is not released during the reaction of the $Li_6PS_5Cl$ electrolyte itself[108]. The released $H_2$ was detected and quantified by the mass spectrometer (Prima BT, Thermo Fisher Scientific) as a percentage of the total gas flow. The carrier gas flow rate ($r$) was controlled at 1 mL/min by a digital flow meter (Bronkhorst), so the detected amount of target gas in moles ($n$) can be calculated by the following equation:

$$n = \int \frac{rP}{V_m} dt \tag{3.1}$$

Where $V_m$ is the molar volume of gas (24.79 L $mol^{-1}$ at 25 °C) and $P$ is the percentage of the target gas in the carrier gas stream. Similar set-ups and procedures have been used to quantify metallic Li previously[287,288].

### 3.3.5 Plasma FIB-SEM

A 5 mm pristine $Li_6PS_5Cl$ disc was transferred into the chamber of the PFIB-SEM (Thermo Fisher Helios G4 Plasma-FIB Dualbeam) for FIB milling with an iLoad vacuum sample transfer

system without exposure to air. The freshly milled cross-section was then imaged with SEM to visualise the pores and micro-cracks in proximity to the interface.

### 3.3.6 Secondary Ion Mass Spectrometry

A 5 mm $Li_6PS_5Cl$ disc which had undergone a single plating at 0.05 $mA.cm^{-2}$ for 5 $mAh.cm^{-2}$ was imaged using the PFIB-SEM procedure above. Secondary ion mass spectrometry (SIMS) analysis was performed on the cross-section using a Hidden Analytical EQS quadrupole SIMS detector. A focused beam of $Xe^+$ was used for SIMS analysis. The quadrupole detector was tuned to collect the $^7Li^+$ signal.

### 3.3.7 Nanoindentation: Elastic Modulus, Hardness and Fracture Toughness

*In-situ* nanoindentation and microcantilever bending (Hysitron PI 88) were performed within a TESCAN scanning electron microscope. Samples were transferred to the SEM within an airtight transfer container. Indentation modulus and hardness were measured using the Oliver-Pharr method[289] on multiple indents made with a Berkovich tip. For the determination of fracture toughness, a cube corner tip was used to cause fracture of the electrolyte and measurement of the resulting radial crack length. More details can be found in section 2.5.1.

### 3.3.8 Microcantilever Bending: Local Fracture Strength

Microcantilevers were produced using a Thermo Scientific Helios G4 Plasma FIB DualBeam (or PFIB) system combined with an iLoad vacuum sample transfer system. The preparation of microcantilevers using the FIB milling method is described in detail in previous work[290]. Loading was performed using a cube corner tip, in a displacement-controlled regime, at a rate of 2.5 nm per second until fracture occurred. The grain boundary strength, $\sigma_c$, for each microcantilever was calculated using the following equation for the tensile surface stress:

$$\sigma_c = \frac{P_f L_C y}{I} \tag{3.2}$$

Where $P_f$ is the load at the point of fracture, $L_C$ is the distance between the loading point and crack, $I$ is the second moment of area and $y$ is the vertical distance between the neutral plane

and the upper surface. $I$ and $y$ were calculated for a pentagonal beam as shown by Chen *et al.*[291]. More details can be found in section 2.5.2.

## 3.4 Results and Discussion

### 3.4.1 X-ray tomography of dendrite cracks

To follow the development of Li dendrites through the solid electrolyte continuous *operando* XCT scans were performed during constant-current plating with significantly improved time-resolution as compared to previous works[278,279,284–286]. A two-electrode Li/$Li_6PS_5Cl$/Li cell was assembled as described in section 3.3, then subjected to a constant applied current while XCT scans were collected every 220 seconds, Figure 3.1. The cell was subject to a 3.0 mA $cm^{-2}$ plating current density for a capacity of 3.0 mAh $cm^{-2}$ under 7 MPa stack pressure. A relatively high current density was chosen to be in excess of the critical current for dendrite formation under the conditions used.

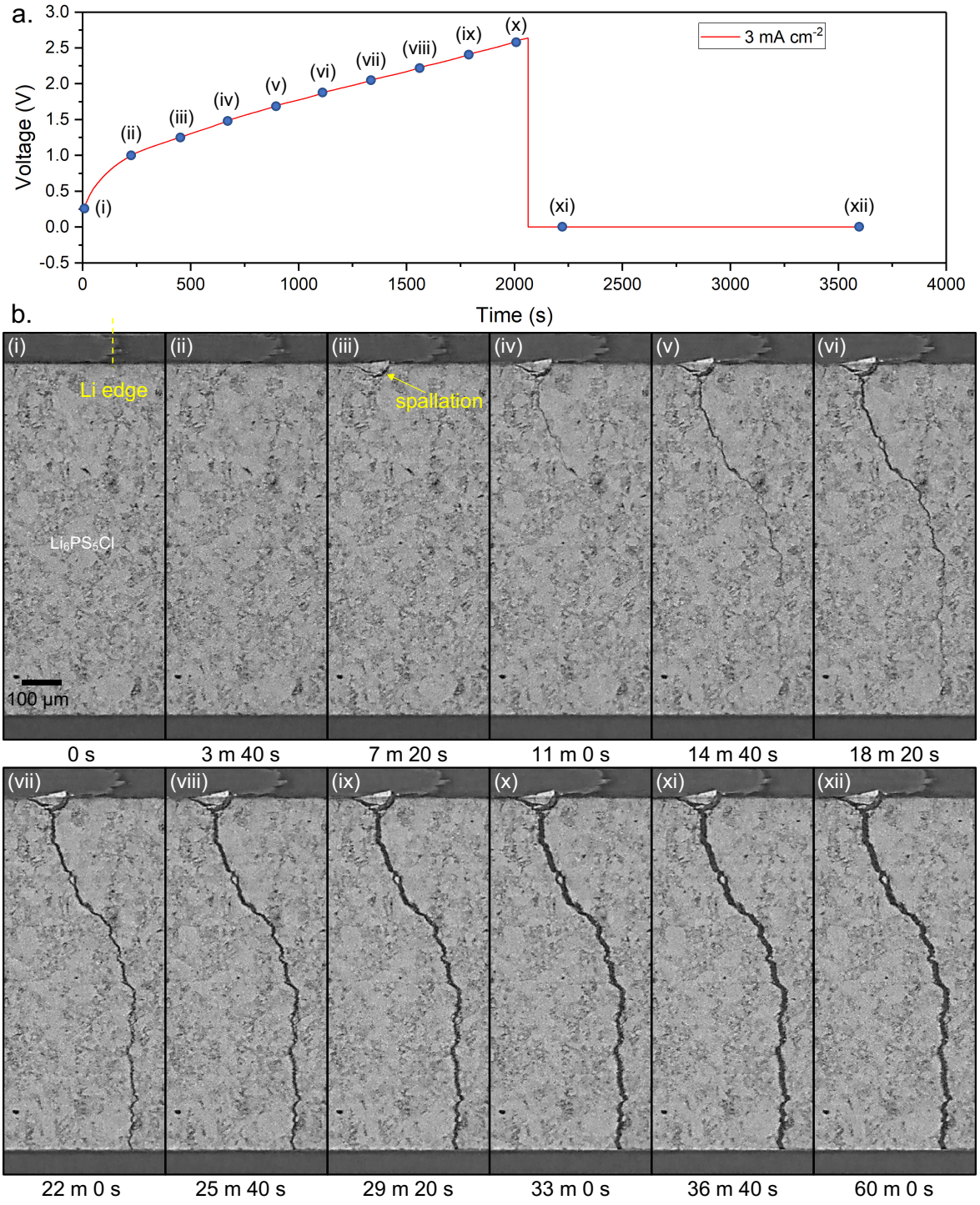



**Figure 3.1: a.** Voltage versus time for a Li/$Li_6PS_5Cl$/Li cell, plated at a current density of 3 mA/cm$^2$ to a capacity of 3 mAh/cm$^2$ under 7 MPa stack pressure. The points indicate times at which XCT scans, shown in **b(i)–(xii)**, terminated. **b.** *Operando* XCT virtual cross-sectional image slices reveal the growth of a crack through an initially pristine electrolyte. A dendrite initiates at the lithium-plating (top) surface **(i)-(iii)**, forming a transverse crack that propagates until the cell short circuits **(iv)-(xii)**. Adapted from[292].

Figure 3.1 presents the *operando* XCT virtual cross-sections collected during plating and demonstrates the development of a dendrite crack from initiation through propagation to

complete short-circuit. Lithium is stripped from the bottom electrode and plated onto the top electrode. After 7 minutes of plating, a pot-hole like crack (referred to as a 'spallation' crack) is seen to form at the lithium edge. These observations are consistent with our previous work whereby spallation cracks were seen to form at the edge of the electrode due to the current flux enhancement[286]. After further plating a straight crack develops from the base of the spallation crack and propagates directly towards the stripped Li electrode (known as a 'transverse' crack). Although the initiation of the dendrite crack was visible after only 7 minutes of Li plating, the complete propagation across the solid electrolyte took 22 minutes and the short-circuit of the cell did not occur until after 34 minutes of plating. This delay between complete crack propagation and short-circuit is in close accord with our previous work in which the key observation was made that the dendrite crack propagates ahead of the Li dendrite, that is to say the crack propagates whilst only partially filled (as a 'dry' crack).

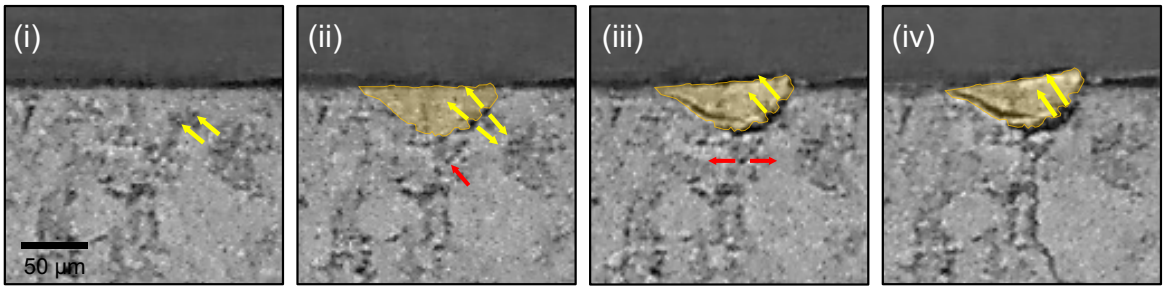



**Figure 3.2**: Magnified images of the region near the plated electrode in Figure 3.1b; pristine **(i)** and after successive plating **(ii)-(iv)**, showing the formation of the spallation and transverse crack. Yellow arrows indicate pores associated with forming the spallation, and red arrows indicate pores associated with the propagation of the transverse crack. The spalled-out solid electrolyte is shaded in yellow to illustrate its movement.

The unprecedented time resolution of these XCT studies enabled close examination of the crack initiation for the first time. Images (i) to (iv) in Figure 3.2 reveal the earliest morphological changes of the solid electrolyte, capturing multiple stages in the initiation of both the spallation crack and then the transverse crack. In Figure 3.2 (iii), a spallation crack initiates and fully cracks back to the interface, leaving a spalled-out piece of argyrodite detached from the bulk electrolyte. The image before detachment, Figure 3.2 (ii), shows that the fracture pathway of

the spallation connects pre-existing pores within the electrolyte (two are indicated by yellow arrows). Comparing Figure 3.2 (i) & (ii) indicates that the pre-existing pores enlarge as plating proceeds, suggesting that they are being filled with Li. Similarly, expanding pre-existing pores can also be identified prior to the initiation of the transverse crack along its fracture pathway, marked by red arrows in Figure 3.2 (iii).

Overall, the XCT results suggest that there are two distinct stages of dendrite failure, crack initiation and crack propagation.

### 3.4.2 Crack initiation based on pore filling

The expansion of pre-existing sub-surface pores immediately prior to the fracture of the solid electrolyte in Figure 3.2 suggests that dendrite cracks initiate because of their filling with Li metal. As Li plating proceeds at the Li/solid electrolyte interface, it is expected that defects connected to the surface of the electrolyte will fill first, both because the overpotential is low, needing to only overcome surface and interfacial energies, and because the electric field concentration is increased near sharp conductor tips penetrating the electrolyte[293]. However, little experimental evidence had previously been collected to demonstrate the potential extent of any Li filling. Further characterisation was therefore necessary to understand whether sub-surface pores within the electrolyte can indeed fill completely with Li metal to any significant extent.

#### 3.4.2.1 Does Li fill pores during plating?

Evidencing the extent of Li ingress within microscopic near-surface defects before fracture poses a serious characterisation challenge. Whilst grey-scale analysis of phase-contrast X-ray tomographs has proven capable of distinguishing the extent of Li filling in large propagating cracks, the low electron density of Li metal means distinguishing it from empty space in smaller microstructural features is inconsistent and unreliable. *Ex-situ* methods such as SEM-EDX are also limited in the identification Li metal, as its characteristic X-rays are so low in energy that they are often undetectable. To overcome these challenges, a combination of plasma FIB-

SEM imaging and secondary ion mass spectrometry (SIMS) was used to both identify and image near-surface porosity and detect the presence of any Li metal.

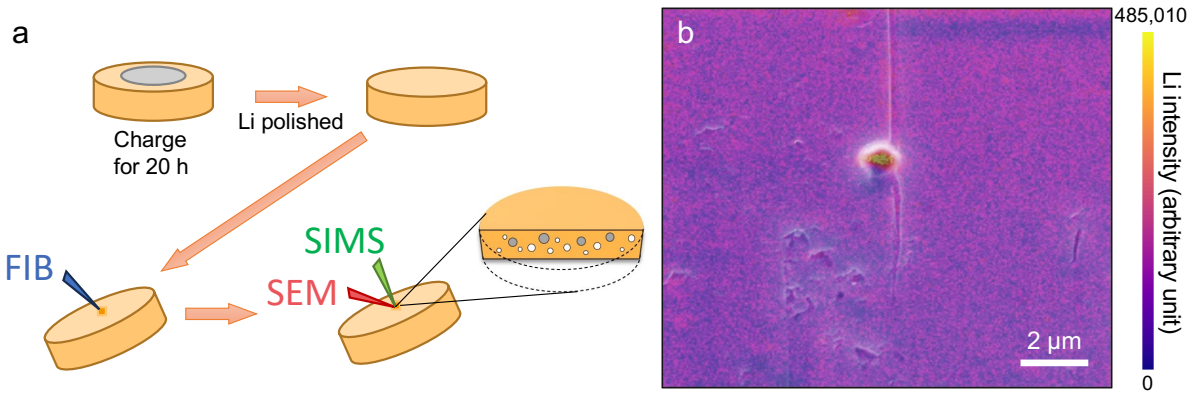



**Figure 3.3**: **a** A schematic illustrating the steps of the characterisation. A symmetric Li/$Li_6PS_5Cl$/Li cell is subjected to a charge at a low current of 0.05 mA $cm^{-2}$ for 20 hours. The Li electrodes are then removed, and FIB milling is used to create a trench in the near-surface region of the solid electrolyte. The trench is then imaged using SEM and its composition spatially mapped using SIMS. **b** FIB-SEM image of a subsurface pore within a $Li_6PS_5Cl$ electrolyte disc after plating. The corresponding $Li^+$ SIMS mapping is overlayed demonstrating the presence of Li metal in the subsurface pore. The SIMS mapping was performed with assistance from Junfu Bu.

To better understand whether Li metal would fill Li defects before any crack formation, imaging was performed on a $Li_6PS_5Cl$ solid electrolyte which had undergone Li plating at a low current density below the critical current for dendrites. This allowed for *ex-situ* characterisation which could determine the existence and extent of Li within the electrolyte before any fracture. FIB-SEM was used to locate and image sub-surface pores in the near-surface regions of the $Li_6PS_5Cl$ electrolyte disc after plating. To then determine whether Li is present within the pore, SIMS was performed on the same fibbed interface on which the pore was imaged. The corresponding $Li^+$ intensity map is overlaid onto the secondary electron micrograph in Figure 3.3 and demonstrates a significant spike in $Li^+$ intensity, suggesting the presence of pure Li metal within the pore.

In addition to SIMS analysis of individual sub-surface pores, it is possible to detect small amounts of Li metal by measuring hydrogen gas formation during controlled exposure to aqueous solution. By etching a $Li_6PS_5Cl$ solid electrolyte which had undergone Li plating (at the same low current density) it was possible to determine whether sub-surface Li deposition

had occurred across the entire interfacial region, thereby complementing, and verifying the generality of the SEM-SIMS results shown in Figure 3.3. Figure 3.4b shows the detection of $H_2$ in the gas phase during the etching of $Li_6PS_5Cl$ solid electrolyte discs with excess LiOH solution. No Li is detected in the pristine sample whereas there was detection of hydrogen gas in sample which has been charged at 0.05 mA/cm$^2$ for 2 mAh/cm$^2$. This indication of the presence of Li metal occurs after an initial delay during which the very outer surface of the electrolyte is etched, hence these results re-affirm the presence of Li metal in sub-surface regions of the electrolyte after plating.

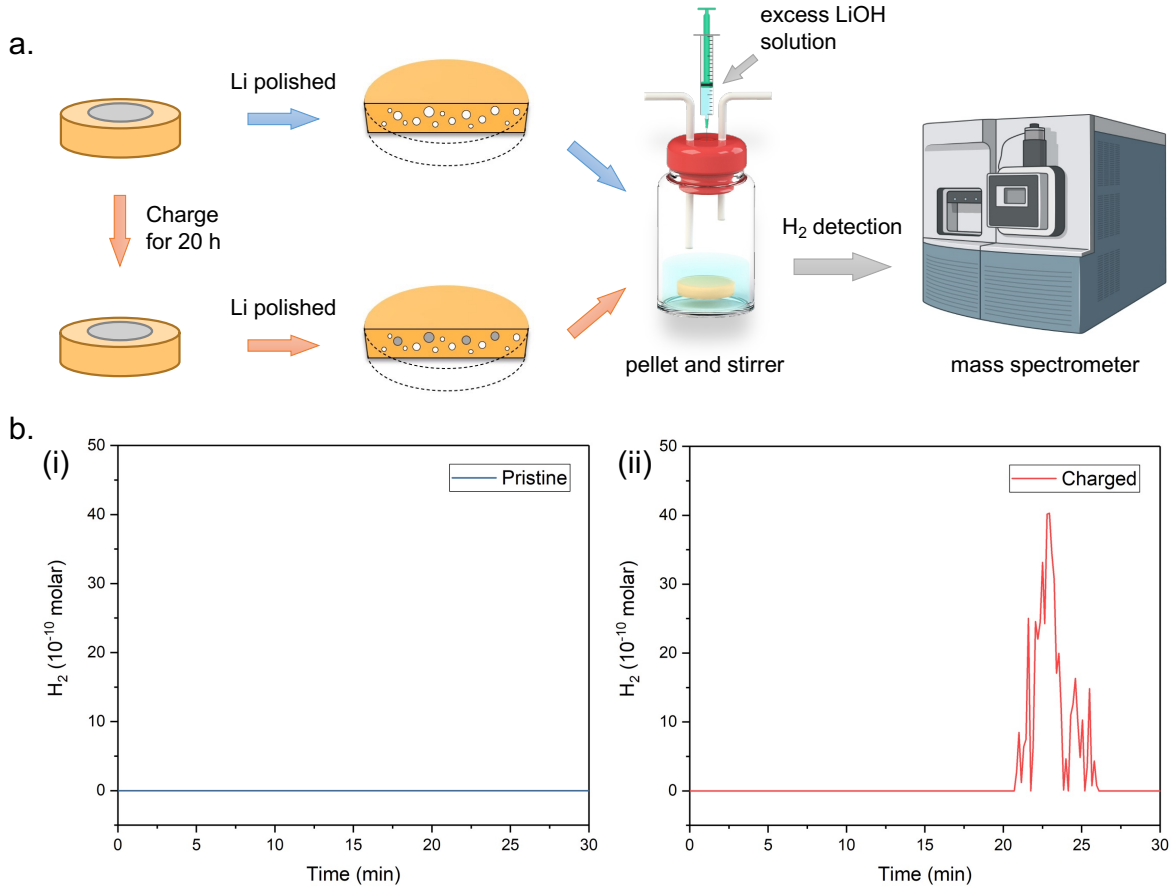



**Figure 3.4: a** A schematic illustrating the procedure. **b** Hydrogen gas concentration versus time during the etching of $Li_6PS_5Cl$ solid electrolyte discs with excess LiOH solution (i) pristine (ii) after charging at 0.05 mA/cm$^2$ for 2 mAh/cm$^2$. The data was collected using an on-line mass spectrometry set-up with assistance from Xiangwen Gao. Adapted from[292].

### 3.4.2.2 Conceptualisation of a pore filling initiation mechanism

Having established that sub-surface pores within the solid electrolyte can fill with Li metal during plating and having observed the key role this porosity plays in the formation of dendrite

cracks; a new model for the initiation of dendrite cracks through the pressurisation of sub-surface porosity was proposed. The easiest way for Li to fill such pores is by means of a direct connection to the solid electrolyte surface made possible due to the presence of pre-existing microcracks. A schematic of such a microcrack-pore system is presented in Figure 3.5. On plating, Li deposits first at the top surface of the microcrack, progressively filling it and the pore, Figure 3.5ai-iv. Further Li deposition occurs across the entire Li/electrolyte interface within the subsurface defect. Because the defect is already filled with Li, this deposition induces a strain within the defect structure, which is accompanied by a pressure build-up. The net effect of this pressure is Li extrusion back along the microcrack, to accommodate the freshly deposited Li. Because lithium metal undergoes creep at room-temperature it can be considered as a viscoplastic solid, and its flow through the narrower microcrack is primarily controlled by the current density in the subsurface pore. At sufficiently high plating rates, the high pressure drop associated with this viscoplastic flow is capable of inducing electrolyte fracture. Fracture near subsurface pores associated with creeping lithium flow through microcracks thus underpins the proposed initiation process.

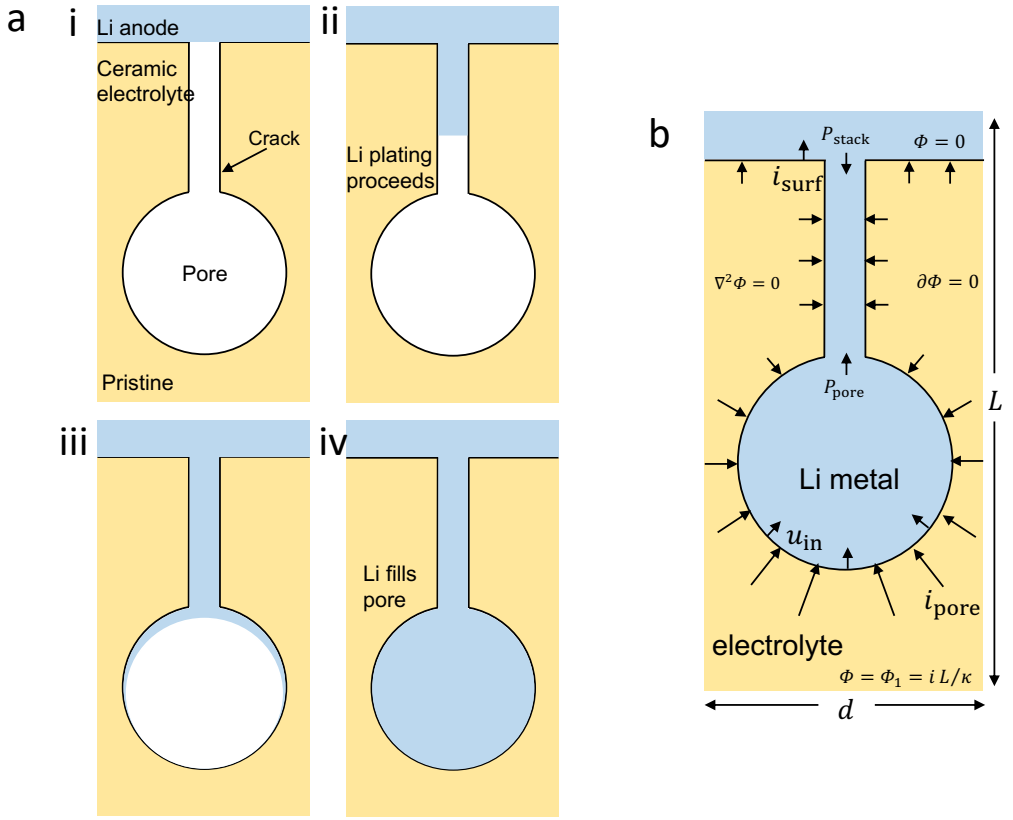



**Figure 3.5**: **a.** A schematic of a pore connected to the lithium/solid-electrolyte interface through a microcrack and being filled by Li deposition progressively from **i-iv**. **b.** A schematic of the filled subsurface pore/microcrack system, labelled with parameters relevant to the dendrite initiation model: $P_{stack}$ is the stack pressure on the cell. During constant-current charging, Li is plated with a current density of $i_{surf}$, while the pore interior experiences a different current density $i_{pore}$. Because the lithium is incompressible and ductile, $i_{pore}$ induces extrusion of lithium towards the surface. As a consequence of this current-induced lithium extrusion, a pressure, $P_{pore}$, builds up within the pore in excess of the stack pressure $P_{stack}$. The pore population density was used to calculate $i_{pore}$ and $i_{surf}$. Adapted from[292].

Having established a new crack initiation concept based on limited Li extrusion from sub-surface porosity, supporting calculations were provided by Guanchen Li to quantify the hydrodynamic pressure build-up under different operating conditions utilising the experimental characterisation from this Chapter as inputs. The calculations consider the case of the fully filled microcrack-pore system with the geometry illustrated in Figure 3.5b, and consist of three key stages: firstly the current distribution is determined to establish the rate of Li deposition across the Li/electrolyte interface, secondly the resultant Li flow within and extrusion out of the microcrack-pore system is determined and thirdly the corresponding hydrodynamic pressures

are compared to the fracture criterion of the solid electrolyte. If the pressure exceeds the fracture criterion, then a dendrite crack will initiate.

#### 3.4.2.3 Calculation of the electric field distribution

The current density distribution at the pores is established by first solving Laplace's equation (eq. 3.3) to determine the distribution of the electric potential, $\Phi$. Allowing the electric field, $\vec{E}$, to be solved via $\vec{E} = -\vec{\nabla}\Phi$ whereby the current density then follows from Ohm's law[294,295]. A Dirichlet boundary condition[†††] $\Phi = 0$ holds at the top (plating) electrode (and consequently all connected Li/electrolyte interfaces) and $\Phi = \Phi_1 = iL/\kappa$ at the more distant bottom electrode ($L$ = 1 mm). Where $i$ is the current density, $L$ is the electrolyte thickness ($L$ = 1 mm) and $\kappa$ is the conductivity of the electrolyte (1 mS/cm).

$$\nabla^2\Phi = 0 \tag{3.3}$$

Since the fully filled microcrack-pore will essentially act as a small protruding conductor within the electrolyte, a significant electric field enhancement at the pores will occur as result, see Figure 3.6b. This field enhancement on a given pore is spread across any neighbouring Li-filled defects. By applying a Neumann boundary condition[‡‡‡] of $\partial\Phi = 0$ to the edges of solid electrolyte domain (at $d/2$ away from the centre of the defect) the effect of neighbouring pores is considered. As a result, the pore separation distance is essentially made equivalent to $d$ and using XCT analysis the average pore separation in the near surface region of the electrolytes in this study could be experimentally determined. As shown in Figure 3.6a, the average pore separation was determined from XCT analysis to be $d$ = 10 μm.

[†††] Also known as a fixed boundary condition.
[‡‡‡] Also known as a 'second-type' boundary condition, meaning a derivative is applied at the boundary of the domain.

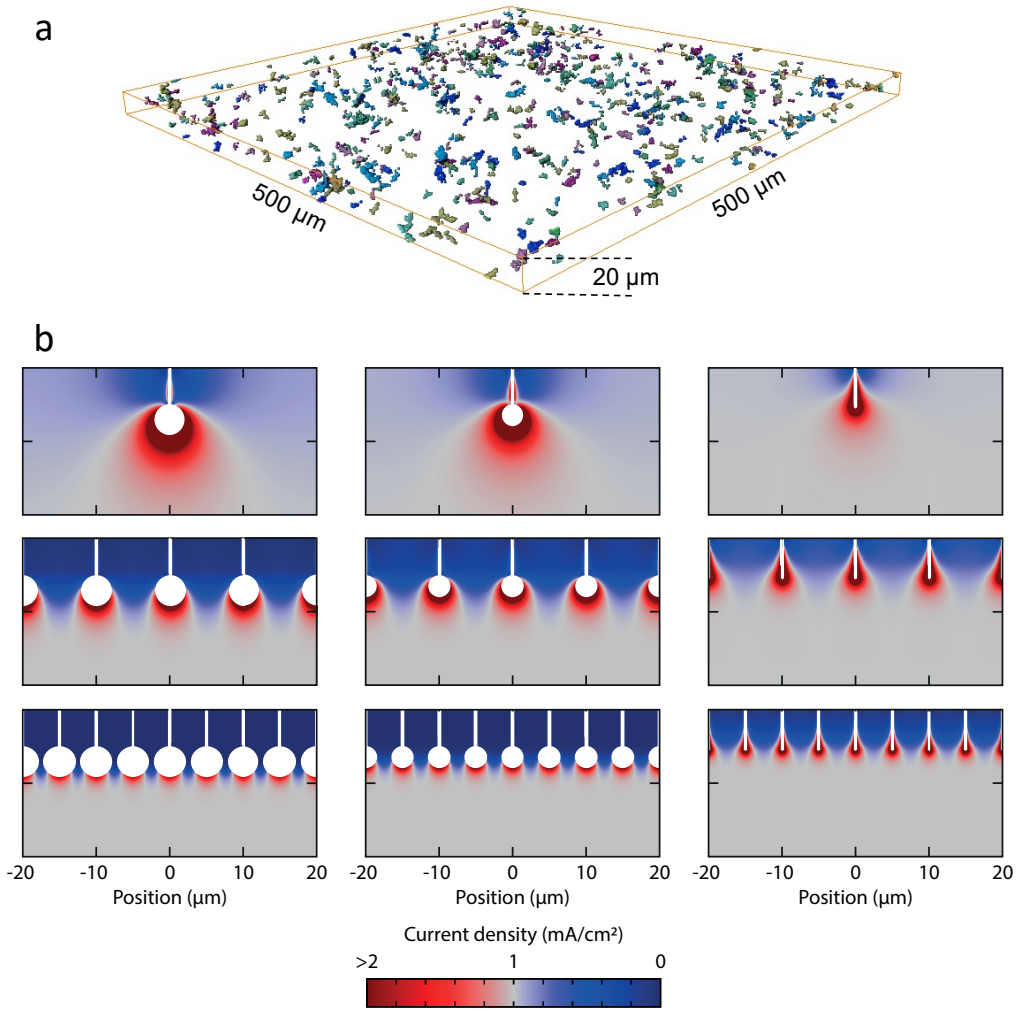



**Figure 3.6**: **a** 3D rendering of pores in a 500 × 500 × 20 µm$^3$ sub-volume of the solid electrolyte adjacent to the plated interface from the pristine XCT scan in Figure 3.1. The average distance from a pore to a nearest neighboured pore was then calculated to be 10 µm and this was used as the average distance between pores in the dendrite initiation modelling. **b** Current density distribution for different pore sizes 2.1 µm (left column), 1.5 µm (middle column), and 0.3 µm (right column) and different pore separations. 40 µm (top row), 10 µm (middle row), and 5 µm (bottom row). The applied current is 1 mA/cm$^2$. Without field enhancement and for pores that are far apart, $i_{surf}$ equals the applied current density, and $i_{pore}$ is lowered by the ratio of the interior pore surface area to that of the microcrack aperture at the surface of the anode. With field enhancement, and still assuming pores are far apart, $i_{pore}$ rises above this expected value and $i_{surf}$ falls, as demanded by charge continuity; when pores are close together, $i_{surf}$ falls to nearly zero and $i_{pore}$ spreads the current across the hemispherical tips of the pores.

#### 3.4.2.4 Calculation of the hydrodynamic pressure during Li plating

Once the electric field distribution across the system is fully evaluated, the flow of lithium across the surface of a fully filled pore and microcrack can be considered as simply the result of an electrochemical reaction whose rate is dependent on the electric field in the solid electrolyte by equation 3.4.[296]

$$u_{\text{in}} = \frac{\kappa M_{\text{Li}}}{F \rho_{\text{Li}}} E_{\perp} \tag{3.4}$$

where $u_{\text{in}}$ is the local velocity of lithium across the lithium-electrolyte interface (perpendicularly), $F$ = 96485 C/mol is the Faraday constant, the density and the molar mass of lithium are $\rho_{\text{Li}}$= 534 kg/m$^3$ and $M_{\text{Li}}$ = 7 g/mol, respectively.

Since Li metal is free to extrude from the microcrack-pore system, the pressure that builds during Li plating does so during an overall Li flow; that is to say the pressure is 'hydrodynamic'. To calculate the hydrodynamic pressure build-up during plating, Li was modelled as an incompressible fluid using, eq. 3.5, which is akin to a Navier-Stokes momentum equation.[297]

$$\rho_{\text{Li}}(\vec{u} \cdot \vec{\nabla})\vec{u} = \vec{\nabla} \cdot \vec{\vec{\sigma}}_{\text{Li}} \tag{3.5}$$

Whereby the stress tensor of the lithium metal, $\vec{\vec{\sigma}}_{\text{Li}}$, can be deconstructed as the sum of a deformation term (the deviatoric stress tensor, $\vec{\vec{\tau}}$) and a pressure term (the volumetric stress tensor, $-p\vec{\vec{I}}$), see eq. 3.6.[298]

$$\rho_{\text{Li}}(\vec{u} \cdot \vec{\nabla})\vec{u} = \vec{\nabla} \cdot \left(-p\vec{\vec{I}} + \vec{\vec{\tau}}\right) \tag{3.6}$$

As Li is being considered as a viscous fluid, the deviatoric stress tensor, $\vec{\vec{\tau}}$, can be expressed in terms of a pseudo-viscosity, $\eta$, and a plastic deformation-rate tensor, $\dot{\vec{\vec{\varepsilon}}}_{\text{p}} = \frac{1}{2}\left(\vec{\nabla}\vec{u} + \vec{\nabla}\vec{u}^{T}\right)$, see eq. 3.7.[299]

$$\vec{\vec{\tau}} = 2\eta \dot{\vec{\vec{\varepsilon}}}_{\text{p}} \tag{3.7}$$

Since Li metal readily undergoes creep at room temperature, a pseudo-viscosity of Li metal can be determined from experimentally reported creep tests. As reported in Maisa *et al.*[300], Li plastic creep follows a power-law plastic model with relation to shear rate, and thus a pseudo-viscosity can be approximated from eq. 3.8.

$$\eta = K \left(\frac{\dot{\bar{\varepsilon}}}{\dot{\bar{\varepsilon}}_{\text{ref}}}\right)^{n-1} \tag{3.8}$$

In this case, the shear rate is $\dot{\bar{\varepsilon}} = \sqrt{2\dot{\vec{\vec{\varepsilon}}}_{\text{p}} : \dot{\vec{\vec{\varepsilon}}}_{\text{p}}}$, and $n$ is the flow behaviour index. $\dot{\bar{\varepsilon}}_{\text{ref}}$ is a reference shear rate, and K is the effective viscocity at the reference shear rate $\dot{\bar{\varepsilon}}_{\text{ref}}$. For lithium, $n$ =

0.1524 according to Maisa *et al.*[300] and by selecting a reference shear rate of 2.828 × $10^{-7}$ $s^{-1}$ the effective viscosity can be determined from Maisa *et al.*[300] to be $K$ = $10^{12}$ Pa·s.

With these complete considerations, the deviatoric stress tensor, $\vec{\vec{\tau}}$, can be fully expressed in terms of $\vec{u}$ and equation 3.6 can be solved for $\vec{u}$ and $p$ using COMSOL Multiphysics®. Whereby $\left(-p\vec{\vec{I}} + \vec{\vec{\tau}}\right) \cdot \hat{n} = -p_{\text{stack}}\hat{n}$ is applied as a boundary condition at the base of the microcrack and the velocities from eq. 3.4 apply as a boundary condition at the Li/electrolyte interfaces.

#### 3.4.2.5 Local fracture strength as a crack initiation criterion

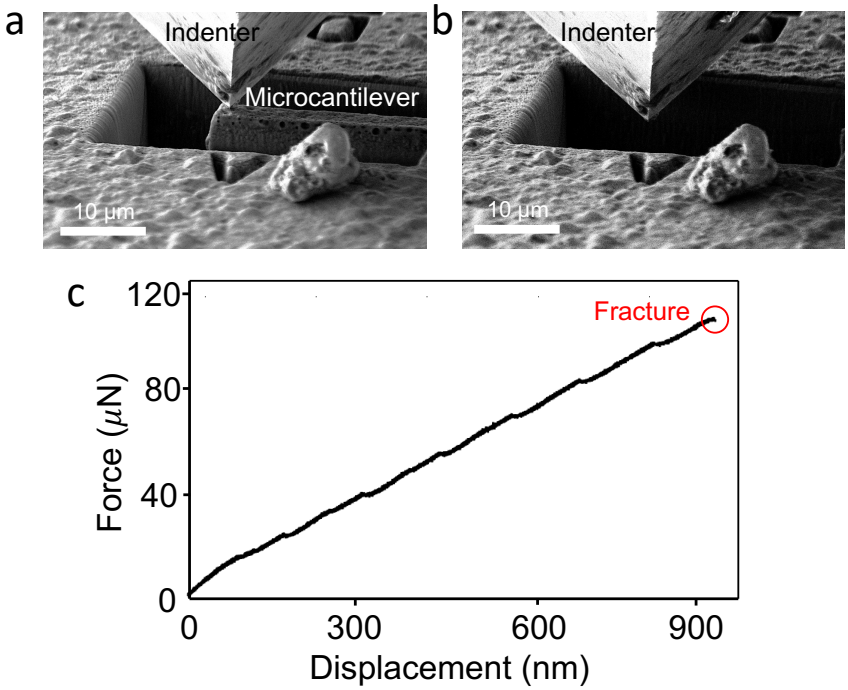



**Figure 3.7:** SEM image depicting the measurement of local fracture strength by microcantilever bend tests. (a) under stress before fracture (b) after fracture. (c) load curve during the test indicating the force at which fracture occurs.

To determine whether a dendrite crack will initiate, the hydrodynamic pressure build up $p$ (which exerts a hoop stress onto the pore surface) must be compared to a suitable fracture criterion for the electrolyte. Due to the highly air-sensitive nature of sulphide solid electrolytes, no experimentally determined mechanical properties of $Li_6PS_5Cl$ had ever been reported in the literature. As well as this, a suitable fracture criterion requires information about how the ceramic responds to microscopically applied stress. Such local fracture characteristics cannot

be accurately determined by standard methods, such as 3-point bend tests or indentation, which sample macroscopic properties averaged across multiple grains. With this considered, pioneering mechanical properties measurements were performed by Johann Perera who determined the local fracture strength of $Li_6PS_5Cl$ by microcantilever bending, as depicted in Figure 3.7. These measurements were performed without exposure to air and were used as direct input for the fracture criterion of the electrolyte in the model[§§§].

#### 3.4.2.6 Dendrite initiation is dependent on pore size, local fracture strength and the applied current density

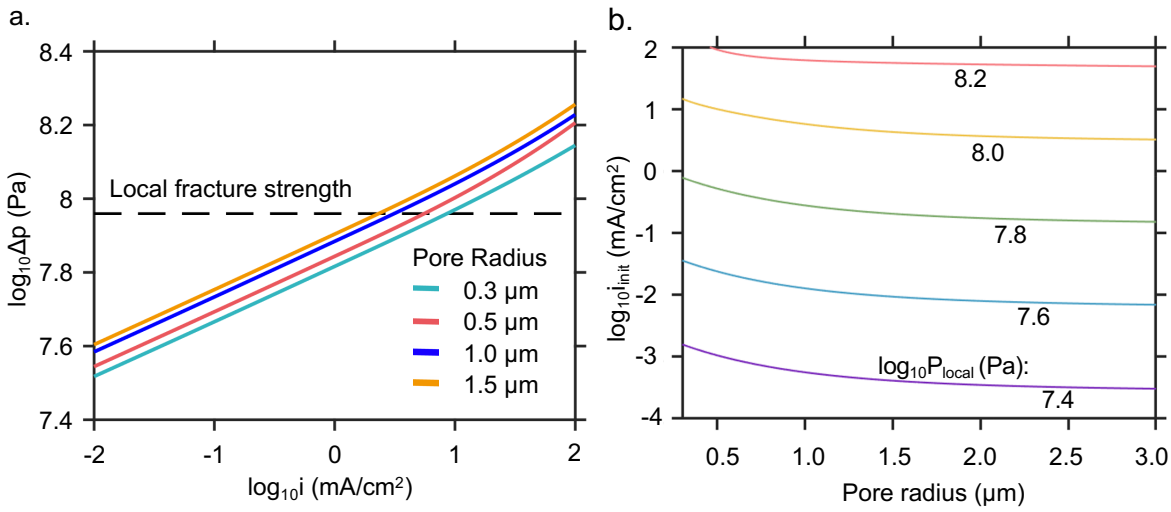



**Figure 3.8: a** The dependence of hydrodynamic pressure in the pore on current density, for various pore radii: 1.5 μm (orange), 1.0 μm (blue), 0.5 μm (red) and with no pore, i.e., a microcrack that terminates with a hemispherical tip, R = a, where a is 300 nm (turquoise). For simulations, the microcrack length L was 5 μm and the separation distance between pores was 10 μm (see Figure 3.1). The horizontal dashed line shows the local fracture strength of the electrolyte determined by the microcantilever experiments (see Figure 3.7). **b**. Plot showing how the critical current density for crack initiation varies with pore size for different local fracture strengths.

In this newly proposed model for dendrite initiation, greater applied current densities induce higher pressures. Therefore, by assessing the current required to induce fracture, an estimate of the critical current for the initiation of dendrite cracks ($CCD_{init}$) can be made. Based on the size, population density, and surface proximity of pores determined by XCT and SEM, and the

[§§§] A complete list of the newly determined mechanical properties is given in Table A.1.

local fracture strength determined for $Li_6PS_5Cl$ through microcantilever measurements, the model predicts a $CCD_{init}$ of ~1.0 mA/cm$^2$, which is in line with typical experimental values[****].[284] This close match with experimental observation indicates the overall feasibility of this kind of crack initiation mechanism for $Li_6PS_5Cl$ electrolytes.

As can be seen in Figure 3.6, the effect of pore geometry on the current distribution is significant. Greater pore sizes shield more current from the electrode interface, and this results in a greater total amount of current locally within the pore/crack system for a given total applied current density. Figure 3.8a shows the calculated dependence of the hydrodynamic pressure in the pore on current density, for various pore radii. The turquoise line in Figure 3.8a, represents a microcrack without a pore. The other lines in Figure 3.8a show how the presence of pores and their increasing size induces a higher extrusion rate of Li at a given applied current density, and hence higher pressure. This comparison helps to explain why subsurface pores are the weaknesses most likely to initiate cracks.

Considering the factors influencing dendrite initiation, an increase in critical currents may be provided either by microstructural or mechanical improvements. Two key parameters would be the size of near surface pores and the associated local fracture strength of the surrounding electrolyte. Figure 3.8b shows that either decreasing pore size or increasing the local fracture strength can have significant influence on the $CCD_{init}$ of a solid electrolyte.

### 3.4.3 Crack propagation based on wedge-opening

As well as enabling a new model for dendrite crack initiation, the results in Figure 3.1 give important insights into the subsequent crack propagation process. As the transverse crack propagates, there is significant widening of the crack as it extends. This widening also continues even once the crack has fully traversed the solid electrolyte and only ceases once the cell is short-circuited. This is consistent with a wedge-opening mechanism whereby propagating dendrite cracks are extended whilst only partially filled with Li metal. The extension of the crack is thereby driven by Li plating at the rear rather than at the crack tip. To

[****] Exact inputs are given in Table A.2.

provide a deeper understanding as to how such a mechanism is possible despite the low yield strength of Li, a model of the process was conceptualised, guided by calculations performed by Guanchen Li.

### 3.4.3.1 Conceptualisation of a wedge-opening propagation mechanism based on hydrodynamic pressure build-up

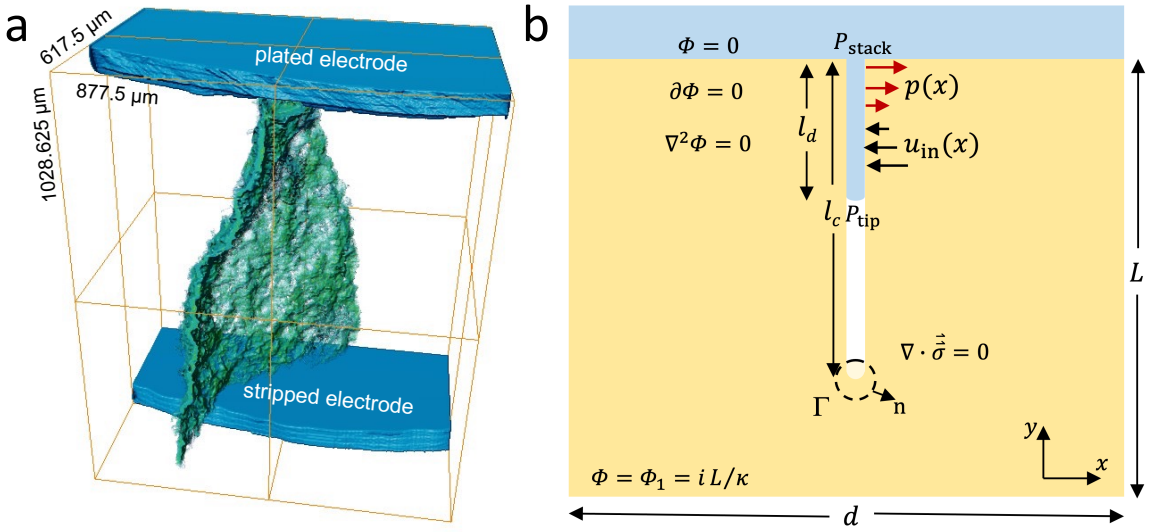



**Figure 3.9**: **a.** 3D rendering of the dendritic crack and Li electrode from the *operando* XCT scan of Figure 3.1b(vii). **b.** Schematic of a planar dendritic crack: length $l_c$ partially filled by a Li dendrite of length $l_d$, under a stack pressure of $P_{stack}$. Li plating takes place at all Li/electrolyte interfaces. Adapted from[292].

Figure 3.9a is a 3D reconstruction of the propagating transverse crack in Figure 3.1. It can be seen that dendrite propagation across the electrolyte occurs within an approximately planar crack, represented schematically in Figure 3.9b. Transverse cracks originating at the base of spallation cracks are those that lead to the failure of the cell and are therefore the most crucial to consider. After the initiation of the transverse dendrite crack a small amount of Li metal will immediately extrude into the crack, thus in the initial case a planar dendrite crack is considered perpendicular to the Li/electrolyte interface partially filled with a Li metal dendrite, Figure 3.9b. As plating proceeds, Li deposition occurs on regions of the crack interior in contact with the filling metal dendrite. Li deposition at the triple-junction of the Li, solid electrolyte, and free space, adjacent to the tip of the dendrite, will directly contribute to its lengthening as the lithium

can grow unimpeded into the free space of the crack. At the remaining areas of the Li/electrolyte interface within the filled region of the crack, Li deposition will cause a pressure build-up which in turn induces viscoplastic flow of the surrounding metal via creep. This plastic flow of Li within the dendrite both drives motion of the dendrite tip into the void space and Li extrusion back into the bulk Li anode (provided it can overcome the applied stack pressure). Whilst this plastic flow of the metal acts to release any pressure build-up within the dendrite crack, it is limited by the creep rate of lithium. As a result, if plating rates are sufficiently high a hydrodynamic pressure build-up will occur within the dendrite and exert a stress onto the solid electrolyte through the interior walls of the crack. By modelling the resultant stress field near the dry crack tip, one can calculate the strain energy release rate, i.e., the energy available to lengthen the crack, quantified by the J-integral. The criterion for fracture, and therefore crack propagation, is determined by comparing the calculated J-integral to the critical strain energy release rate required for crack propagation, a material property dependent on the electrolyte's fracture toughness, Young's modulus and Poisson's ratio.

#### 3.4.3.2 Calculation of the J-integral at the crack tip

As in the model for dendrite crack initiation, the stress exerted on the electrolyte is conceived as a result of limited extrusion of the plastically deforming Li metal. As a result, a similar procedure can be taken to evaluate the propagation criteria for the crack, whereby first the overall current distribution is used to determine Li flow within the crack, which in turns allows the calculation of any hydrodynamic stress build-up to be compared against a fracture criterion of the electrolyte. As in the initiation model, the Li injection rate into the crack is determined by solving Laplace's equation (eq. 3.3) with a combination of Dirichlet and Neumann boundary conditions and applying eq. 3.4 at the regions of contact between Li metal and the electrolyte. To solve the flow within the crack, the Li metal is again treated as an incompressible fluid with its flow properties taken from reported Li creep data. Unlike in the initiation model, the propagating crack is only partially filled, and so as well as extruding out of the base of the

crack the flow of Li can induce a lengthening of the dendrite. This balance between extrusion versus growth is governed by the implementation of two constant pressure conditions; a constant stack pressure, $p_{\mathrm{stack}}$, is applied at the base of the crack and a capillary pressure, $p_{\mathrm{tip}}$, is considered at the tip of the dendrite within the crack[††††]. Through an evaluation of the collective flow of Li metal within the crack, the magnitude of the hydrodynamic stress which applies perpendicularly to the interior walls of the crack can be determined. In contrast to crack initiation, the criterion for extension of an existing crack must be determined by evaluating the effect of these hydrodynamic stresses on the existing crack tip. To do this the total stress state of the solid electrolyte is evaluated by assuming linear elastic behaviour and using eq. 3.9[302]:

$$\nabla \cdot \vec{\vec{\sigma}}_{\mathrm{SE}} = 0 \tag{3.9}$$

The Li flow pressures are incorporated by applying eq. 3.10 to the interior surfaces of the crack,

$$\vec{\vec{\sigma}}_{\mathrm{SE}} \cdot \hat{n} = -p_{\mathrm{Li}} + \vec{\vec{\tau}}_{\mathrm{Li}} \cdot \hat{n} \tag{3.10}$$

where $\vec{\vec{\sigma}}_{\mathrm{SE}}$ is the stress tensor in the solid electrolyte and $\vec{\vec{\tau}}_{\mathrm{Li}}$ is the viscous stress tensor in the lithium, $\hat{n}$ is the normal unit vector at the lithium-electrolyte interface. Whilst the stack pressure applied to the cell is considered through the application of a fixed boundary condition ($\vec{\vec{\sigma}} \cdot \hat{n} = -p_{\mathrm{stack}}$) at the top and bottom surfaces, the other edges of the electrolyte are left free.

By solving equation 3.9, the strain energy release rate acting on the crack tip (expressed by the J-integral) can be determined using eq. 3.11.[303]

$$J = \int_{\Gamma} \left[ W(\mathrm{x},\mathrm{y}) d\mathrm{y} - \vec{t} \cdot \frac{\partial \vec{u}}{\partial \mathrm{x}} ds \right] \tag{3.11}$$

Where $\Gamma$ is the integral path, $\vec{t} = \vec{\vec{\sigma}} \cdot \hat{n}$ is the traction to the outer normal of the integral path, and $W$ is the strain energy density whereby $W = W(\mathrm{x},\mathrm{y}) = \int_0^{\vec{\vec{\epsilon}}} \sigma_{\mathrm{ij}} \mathrm{d}\epsilon_{\mathrm{ij}}$ .

The J-integral and stress intensity factor (SIF) are related by equation 3.12.[304]

[††††] $p_{\mathrm{tip}} = \frac{\gamma}{r}$, where the lithium surface energy is $\gamma$ = 0.45 J/m$^2$.[301] The radius of curvature at the tip is $r = \mathrm{a}/\cos\theta$, where $a$ is the half width of the crack and the contact angle is $\theta = \arccos(2/3) = 151°$.

$$\mathrm{SIF} = \sqrt{\frac{JE}{1-v^2}} \tag{3.12}$$

Whereby $E$ is the elastic modulus and $v$ the Poisson ratio of the electrolyte[‡‡‡‡]. When the SIF is greater than the fracture toughness, the crack will propagate through mode I fracture[§§§§]. As with all mechanical inputs in this thesis, the fracture toughness for $Li_6PS_5Cl$ was determined by indentation measurements performed by Johann Perera from samples made by the author.

### 3.4.3.3 Dendrite propagation is dependent on dendrite length, the electrolyte fracture toughness and the applied current density

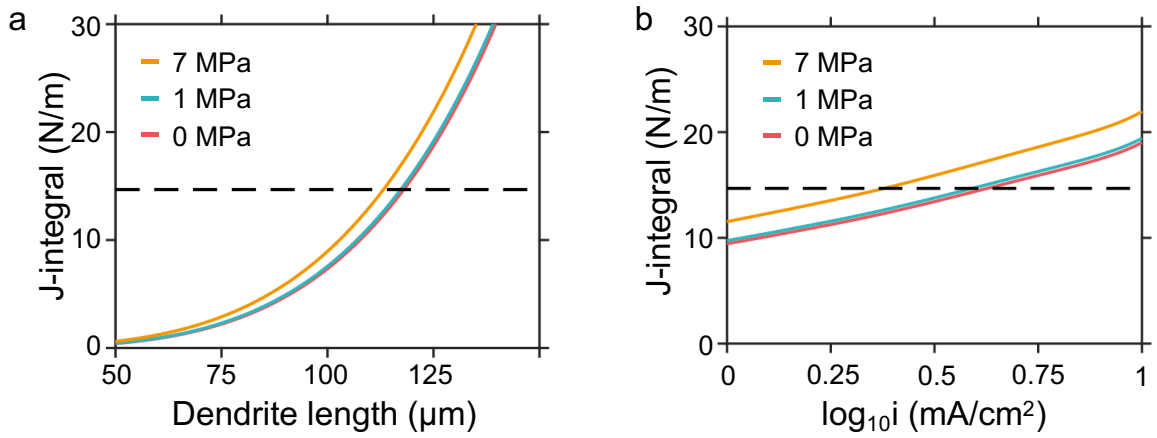



**Figure 3.10: a**. J-integral at the crack tip as a function of dendrite length. **b.** J-integral at the crack-tip as a function of the current density for Li plating (dendrite length $l_d$ = 115 μm). The critical J-integral for crack propagation in $Li_6PS_5Cl$ is shown by the black dashed lines in both **a** and **b**, and is determined using the experimentally measured fracture toughness.

The *operando* XCT micrograph in Figure 3.1b(vii) shows a crack in the process of propagation, which has initiated but not yet reached the counter electrode. From its approximate dimensions, 200 μm long and 2 μm wide, the stress field at the crack tip was modelled for a current density of 3.0 mA/cm$^2$ (typical of a practical charging rate and commensurate with the current used to collect the XCT in Figure 3.1). Since pressures are a result of restricted Li flow within the crack, the magnitude of the J-integral at the crack tip for a given dendrite length is

‡‡‡‡ $v$ = 0.37 is the Poisson's ratio of $Li_6PS_5Cl$ as reported by Deng *et al*.[305]

§§§§ Here Mode I fracture refers to cracks opening under extension, i.e., propagating as tension acts on all sides of a growing crack. Also known as "opening' mode. This Mode I-type fracture is not to be confused with Mode-I-type dendrites, the two are not necessarily equivalent.

greater for higher current densities, as shown for a fixed dendrite length of 115 μm in Figure 3.10b. As plating proceeds, the Li dendrite grows along the crack. As shown in Figure 3.10a, the strain energy release rate (J-integral) rises super-linearly with the Li dendrite length. This is a result of increasing Li/electrolyte contact area during the lengthening of the dendrite which increases both the flux of Li into the dendrite and the area of the electrolyte under stress from pressurised crack-filling Li.

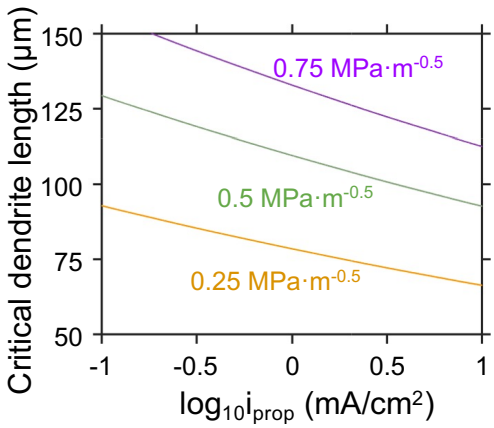



**Figure 3.11**: The effect of fracture toughness on applied current density and lithium dendrite length required to lengthen a dry crack (shown for a 200 μm long dry crack and zero stack pressure).

Stack pressure plays a key role in enhancing the stress at the crack tip by affecting the hydrodynamic pressure build-up within the crack by restricting Li extrusion. The different coloured lines in Figure 3.10a&b illustrate the major influence of stack pressure on dendrite crack propagation. The critical J-integral for crack propagation in $Li_6PS_5Cl$ is shown by the black dashed lines in Figure 3.10a & b. When stack pressure is reduced, dendrites must be longer to propagate the dry crack. For a dendrite length of 115 μm and stack pressure of 7 MPa, crack propagation occurs at 2.4 mA/cm$^2$, whereas removal of the stack pressure increases this significantly, to 4.2 mA/cm$^2$, Figure 3.10b. It is also worth noting that Figure 3.10b demonstrates that for a plating current density of 3.0 mA/cm$^2$ under 7 MPa stack pressure, the Li only needs to fill half the crack length (~115 μm) before the dry crack lengthens, which is consistent with the experimental observation that dendrite cracks propagate with a wedge-opening mechanism.

Crack propagation can be inhibited by toughening the electrolyte, Figure 3.11, since increasing fracture toughness increases the J-integral required for crack extension. With a higher fracture toughness, crack propagation requires higher current densities or longer Li dendrites, Figure 3.11.

### 3.4.4 When does propagation lead to a short-circuit?

The propagation of a dendrite crack is a function of applied current density, length of dendrite (amount of crack filling) and the applied stack pressure. For any given crack length under a fixed stack pressure and constant applied current density, a critical dendrite length exists which when reached will exert a pressure on the interior of the crack sufficient to extend it. During galvanostatic cycling of a cell, the capacity plated and stripped per half cycle will dictate the length of dendrite within the crack and consequently whether any crack extension occurs. As has already been described, Li plating will result in dendrite growth within the crack, but during stripping the dendrite will instead be depleted. This phenomenon has been observed during *operando* optical microscopy of Li dendrites previously, whereby dendrites were seen to recede back during the reverse application of the current[306]. A full consideration of the lengthening and shortening of the dendrite during galvanostatic cycling is therefore necessary to understand the consequential cycle life of solid-state cells.

### 3.4.4.1 The effect of stack pressure on lithium dendrite growth during cycling

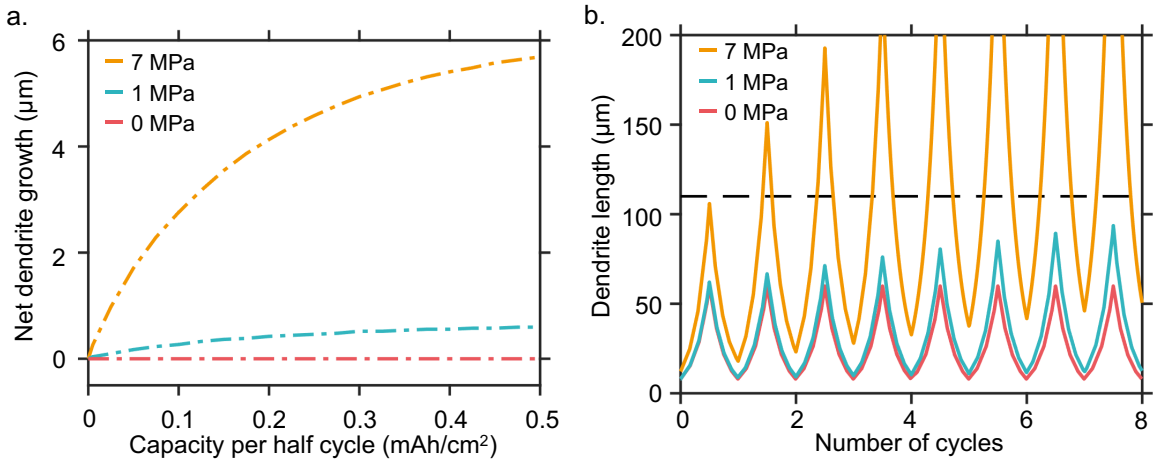



**Figure 3.12: a**. The net change in Li dendrite length within the crack on one charge–discharge cycle as a function of capacity under various stack pressures. **b**. Cumulative dendrite length during cell cycling under various stack pressures. As stack pressures reduce the net lengthening of the Li dendrite per cycle tends to zero, inhibiting both crack propagation and short-circuiting by the dendrite.

As discussed in section 3.4.2, stack pressure promotes Li flow towards the counter electrode and inhibits extrusion, resulting in greater net growth of the dendrite. To elucidate the magnitude of the effect of stack pressure during cycling, the net Li dendrite growth after a single cycle as a function of capacity was calculated for applied stack pressures of 7 MPa, 1 MPa, and 0 MPa, see Figure 3.12. Simulated dendrite length during repeated cycling is shown in Figure 3.12b. Cycling at a stack pressure of 7 MPa (orange) results in a substantial cumulative length change that soon drives crack propagation (dashed black line in Figure 3.12b), while lower stack pressures reduce the net growth markedly, Figure 3.12b. The net accumulation of Li metal in the electrolyte during cycling for different applied stack pressures was also demonstrated experimentally using the same mass spectrometry methodology as described in section 3.4.1. Removing the solid electrolyte from cells that had been cycled at a current density above the CCD for dendrite initiation, but not driven to failure allows for the amount of Li metal within the solid electrolyte to be quantified for a given cycle number. As shown in Figure 3.13, the amount of Li metal detected within the solid electrolyte was greatly affected by the applied stack pressure, as predicted by Figure 3.12.

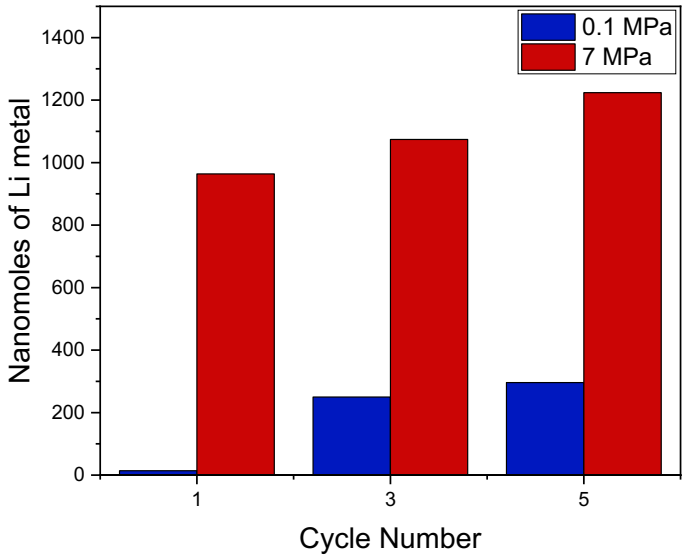



**Figure 3.13**: Quantification of Li metal within the solid electrolyte after stripping, determined through mass spectrometry. First, cells were cycled under 4 mA/cm$^2$ plating current and 0.05 mA/cm$^2$ stripping current for 0.5 mAh/cm$^2$ each half cycle, in accordance with the cells in Figure 3.14. After the final stripping step, cells were disassembled and the Li electrodes removed. After which the solid electrolyte is subjected to slow etching/dissolution while the gas is monitored by mass spectrometry. The amount of Li metal in the solid electrolyte cycled only once at 0.1 MPa was undetectable. The results demonstrate the effect of pressure in encouraging dendrite formation in solid electrolyte and how dendrites progressively grow over multiple cycles. Data collected with assistance from Xiangwen Gao.

#### 3.4.4.2 The effect of stack pressure on short-circuit

The short circuit of a solid-state cell occurs when Li metal physically reaches the counter electrode, creating an electrical pathway through the electrolyte. Although cells cycled above the $CCD_{init}$ will initiate dendrite cracks, even at low stack pressures, the propagation of the dendrite is predicted to be highly dependent on the applied stack pressure. As stack pressures tend to zero, very little net propagation occurs, Figure 3.12. The dendrite length oscillates during plating and stripping, indicating that the cell can be cycled more extensively before failure.

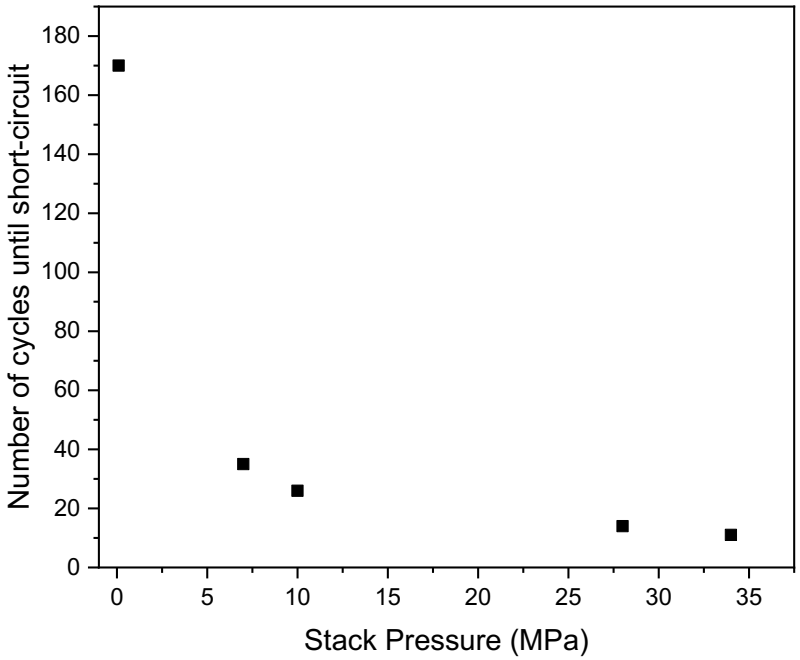



**Figure 3.14***:* Number of cycles to short-circuit vs applied stack pressure for Li/$Li_6PS_5Cl$ 3-electrode cells cycled under 4 mA $cm^{-2}$ plating current density, 0.05 mA $cm^{-2}$ stripping current density. Cells cycled at 0 MPa, 7MPa, 10 MPa, 28 MPa and 34 MPa failed at the 170$^{th}$, 35$^{th}$, 26$^{th}$, 14$^{th}$ and 11$^{th}$ cycle respectively.

To demonstrate this, three-electrode Li/$Li_6PS_5Cl$ cells were assembled, and plated at 4.0 mA/$cm^2$ under stack pressures of 0.1 MPa (ambient), 7 MPa, 10MPa, 28MPa and 34MPa, Figure 3.14. The cells were cycled until short-circuit. Examples of the voltage profiles for cycling at 0.1 MPa and 7MPa are shown in Figure 3.15. The remaining voltage profiles are presented in Figure A.1. Significantly, the cell under ambient pressure achieved a 5-fold increase in the number of cycles corresponding to 170 cycles, Figure 3.14, compared with the cell under 7 MPa stack pressure, which short-circuited on the 35th cycle.

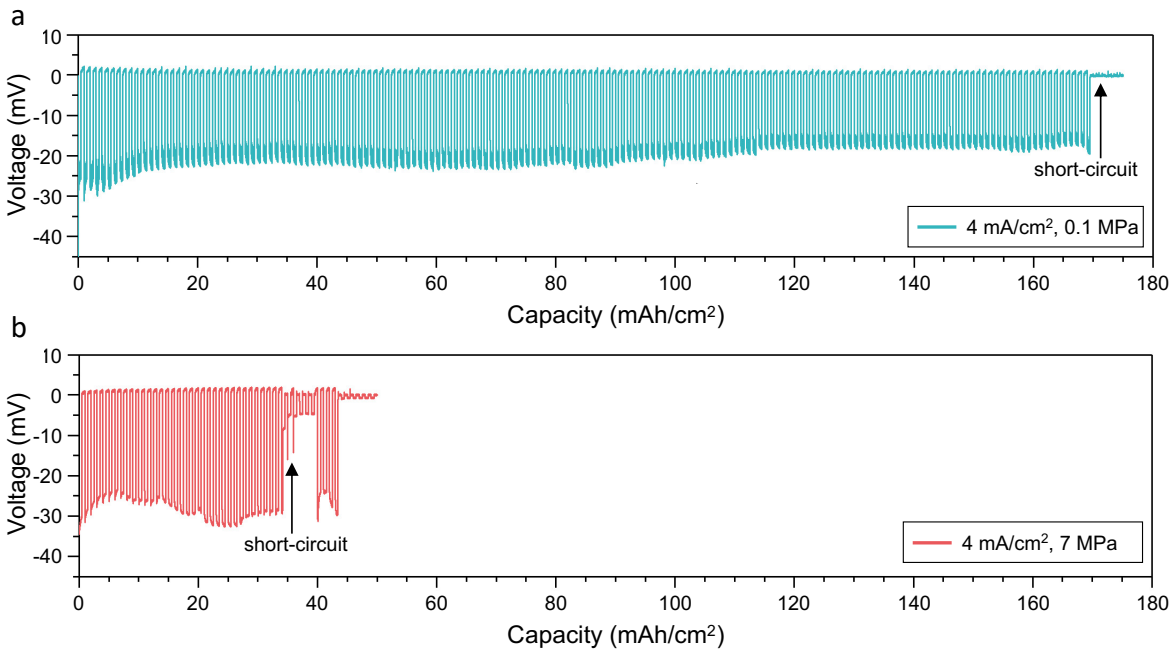



**Figure 3.15:** Voltage profiles corresponding to data points at **(a)** ambient pressure (0.1 MPa) and **(b)** 7 MPa in Figure 3.14. Cycling of employed Li/$Li_6PS_5Cl$ 3-electrode cells with current densities of 4.0 mA/cm$^2$ for plating, 0.05 mA/cm$^2$ for stripping (to avoid void formation), both for a capacity of 0.5 mAh/cm$^2$.

By performing single plating experiments any Li stripping effects are completely removed. Yet stack pressure will accelerate short-circuit by reducing the critical dendrite length and increasing the dendrite growth rate for a given applied current density. As predicted by the modelling, the key principle regarding the detrimental effect of stack pressure on dendrite failure is also seen during single plating experiments. As be seen in Figure 3.16, the amount of capacity passed (Li deposited) until a short circuit during single plating is reduced with greater applied stack pressures.

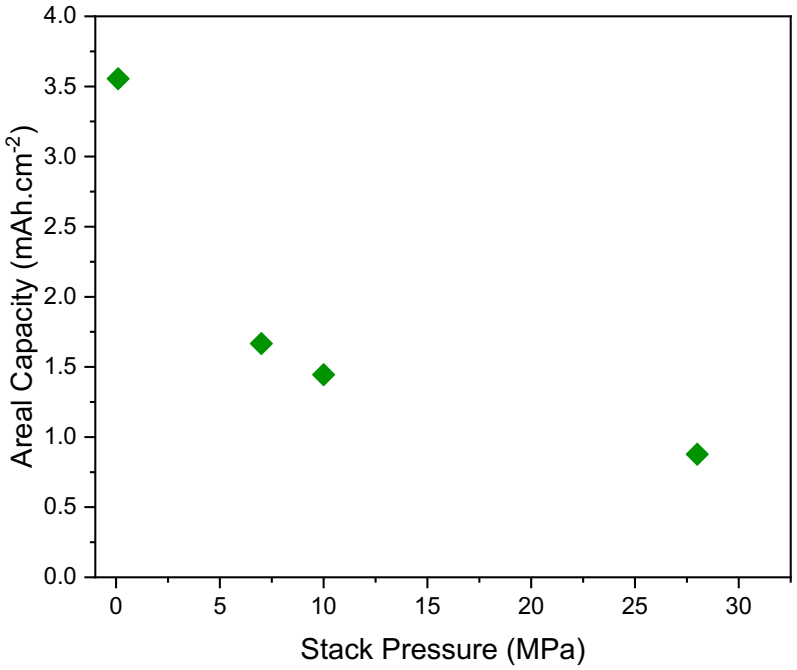



**Figure 3.16:** Capacity required to induce short-circuit versus stack pressure for Li/$Li_6PS_5Cl$ cells subject to single plating at 4 mA $cm^{-2}$ current density. Cells under 0.1 MPa (ambient pressure), 7 MPa, 10 MPa and 28 MPa short-circuited after plating 3.6 mAh $cm^{-2}$, 1.7 mAh $cm^{-2}$, 1.4 mAh $cm^{-2}$ and 0.9 mAh $cm^{-2}$ respectively.

#### 3.4.4.3 The dominant role of viscoplasticity

The overall coherence between imaging, modelling, and cycling presented in this chapter adds to the growing wider picture that it is the viscoplastic properties of the metal dendrite which are dominant in driving the formation and propagation of cracks. Similar insights have been made previously, for example Kinzer *et al.* reported critical currents of multiple hundreds of $mA/cm^2$ when using a molten Li anode due to the vastly improved viscoplasticity of the metal anode as well as a lack of applied stack pressure[307]. Significantly improved CCDs are also reported for sodium and potassium metal SSBs which inherently benefit from the enhanced creep of softer alkali metals[285,308,309]. In accordance with this, it was observed that low temperatures lead to early cell failure due to the reduced viscoplasticity of Li metal. As can be seen in Figure 3.17, the same experiment as in Figure 3.15b was carried out but at 0°C with the cell failing after only 17 cycles, almost half the number of cycles.

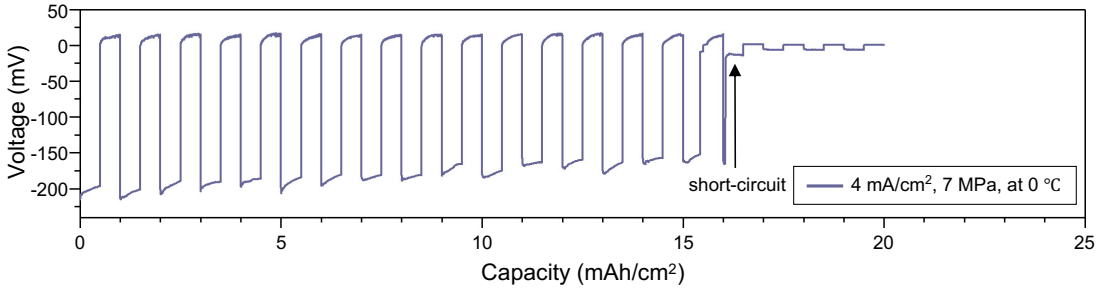



**Figure 3.17:** Cycling of Li/$Li_6PS_5Cl$ 3-electrode cell with current densities of 4.0 mA/cm$^2$ for plating, 0.05 mA/cm$^2$ for stripping, both for a capacity of 0.5 mAh/cm$^2$, under 7 MPa pressure at 0°C. Failure occurs on the 16$^{th}$ cycle, which is earlier than in Figure 3.14 (35 cycles), which was cycled at 30°C, this is due to the limited creep of Li at low temperature.

## 3.5 Conclusions

This chapter has explored the mechanistic underpinnings of Li dendrite failure of ceramic solid electrolytes. Through the use of *operando* XCT imaging with vastly improved time resolution the earliest developments of the dendrite cracks are seen to follow from the expansion of subsurface porosity. By contrast, larger dendrite cracks traverse the electrolyte without the presence of Li metal at the crack tip. Unlike in any previously proposed understanding, the process of Li dendrite penetration in ceramic electrolytes is described through two distinct stages, crack initiation and crack propagation. The initiation of the cracks is proposed to arise from the deposition of Li metal into subsurface pores, by means of microcracks that connect the pores to the surface. Once filled, further charging builds pressure in the pores owing to the slow extrusion of Li metal back to the surface, leading to cracking. Similarly, the limited creep of Li plated into transverse cracks is calculated to exert sufficient force on the crack walls to cause propagation through a purely hydrodynamic pressure build-up. Both processes are therefore fundamentally governed by flow stresses resulting from the restricted creep of Li metal. Using experimental inputs from XCT, FIB-SEM as well as novel mechanical testing, both the initiation and propagation processes were modelled. Whereas initiation of dendrite cracks is a function of the local microscopic fracture strength of the electrolyte, the pore size, pore population density and applied current density, propagation depends on the macroscopic fracture toughness of the ceramic, the length of the Li dendrite that partially occupies the dry

crack, current density, stack pressure and the charge capacity accessed during each cycle. The predicted differences in stack pressure sensitivity between the two processes were exploited in experimental cells to demonstrate a substantial extension in cycle life despite the initiation of dendritic cracks. The results both reinforce the new mechanistic understanding whilst also elucidating key design criteria needed to improve a ceramic electrolyte's tolerance to dendrite failure. Dendrite initiation can occur at low currents due to the presence of large subsurface pores in proximity to the electrolyte interface. Lower macroscopic fracture toughness enables the wedge-opened propagation of dendrite cracks at shorter dendrite lengths for a given applied current density. Strategies to improve the microstructural design of the argyrodite sulphide electrolyte, $Li_6PS_5Cl$, are the subject of Chapters 4 and 5.

# Chapter 4: The Effect of Microstructure on Dendrite Initiation

## 4.1 Aim

The work in this chapter builds on the new understanding made in Chapter 3 which added original insights into the growing picture of how microstructural defects influence dendrite formation in ceramic electrolytes. The aim of the chapter is to elucidate to what extent realistic changes in these microstructural defects can affect sustainable Li-anode charging rates. A variation in the $Li_6PS_5Cl$ microstructure is induced through sintering. By developing a new electrochemical testing protocol reinforced with micro-XCT characterisation, a trend in critical current densities is determined for each microstructure. Using FIB-SEM tomography the near-surface microstructural defects are imaged with improved spatial resolution and the overall change in defects across the sintering conditions is compared to the trend in critical current density.

## 4.2 Introduction

To match the 'fast' charging standards set by current state-of-the-art electric vehicles, SSBs capable of withstanding charging rates of between 1-3C[*****] have been targeted by automakers (equivalent to 5-15 mA $cm^{-2}$ assuming a cathode loading of 5 mAh $cm^{-2}$)[54,310]. Yet despite the wide range of fast $Li^+$ conducting solid electrolytes developed over the last decade, once combined with a lithium metal anode, all have suffered from the penetration of Li filaments (known as 'dendrites') and catastrophic short-circuit at charging rates of only a few mA $cm^{-2}$.[286,311] Consequently, the first generation of commercial SSBs look likely to avoid using Li anodes altogether, with the realisation of Li-SSBs seemingly perpetually delayed[312,313]. As detailed in Chapter 3, the initiation of dendrite cracks can be linked to the presence of pores

[*****] Whereby 1 C is defined as the rate at which it takes a battery 1 hour to fully charge.

and cracks in sulphide solid electrolytes. This raises the question as to what extent realistic changes in these microstructural defects can affect sustainable Li-anode charging rates.

As the first $Li^+$ conducting solids to exceed the ionic conductivities of liquid electrolytes, sulphide-based ceramics have garnered significant attention across the past decade globally[314–316]. Due to their inherent softness, these conductivities were achieved without sintering the powder together thermally, something that has proven impossible in stiffer oxide-based electrolytes whose conductivities decline orders of magnitude without optimised sintering regimes[317–319]. Consequently, sulphide electrolytes have generally been used as green bodies, that is to say, the powder has been bound together by cold pressing alone[320,321]. Sulphide electrolytes degrade when exposed to moisture and have limited thermal stability, and as a result, very few have been successfully thermally densified without severe degradation, with examples limited to a select few glasses[322,323]. Unfortunately, these sulphide glasses are often poorly conducting, brittle and undergo excessive interfacial reaction with Li metal[324,325]. As a result, limited improvement in performance has been reported when combining these dense sulphides with lithium anodes[322,326].

Argyrodite, $Li_6PS_5Cl$, has a high conductivity and although it reacts with lithium metal, it does so to form a solid electrolyte interphase that stabilises, preventing further reactivity[327]. In this chapter, the effect of sintering on the $Li_6PS_5Cl$ microstructure is investigated. It is found that $Li_6PS_5Cl$ can be densified to a very significant extent when heated at relatively low temperatures (several hundred degrees) for short durations using field assisted sintering. It is found that plating currents as high as 9 mA $cm^{-2}$ can be achieved without lithium dendrites in dense $Li_6PS_5Cl$ microstructures. Using the dendrite initiation model detailed in Chapter 3, the improvements in critical current density are rationalised with regards to the measured changes in the near-surface defects present in the electrolyte microstructure. While the decrease in crack widths and increase in pore separation acts to decrease the CCD, overall, this is outweighed by decreases in crack lengths and the size of pores.

## 4.3 Methods

### 4.3.1 Field assisted sintering and electrolyte preparation

All procedures were performed in an Ar-filled glovebox ($O_2$ and $H_2O$ levels < 1 ppm). $Li_6PS_5Cl$ powder was purchased from Ampcera and loaded into a graphite die set. The die set was then inserted into a spark plasma sintering system (FCT Systeme GmbH) within an Ar-filled glovebox and subject to 50 MPa uniaxial pressure at either 300, 350 or 400 °C for 5 minutes while under vacuum by passing a current through the die set. 5-mm diameter sintered electrolyte discs of identical thickness were then used for cell assembly. Cold pressed electrolyte discs were formed by loading the same pristine electrolyte powder into a 5-mm-diameter stainless-steel die set and pressing under a uniaxial pressure of 400 MPa. To determine the relative density of the electrolytes, discs were weighed, and their total volume measured using micro-XCT.

### 4.3.2 Three-electrode cells

For a three-electrode cell, two disc-shaped lithium electrodes of 1 mm diameter were pressed onto the same side of the electrolyte disc as the working and reference electrodes respectively. The remaining areas of the electrolyte surface were then covered by insulating polymer tape. A 5-mm lithium disc was pressed onto the opposite side as the counter electrode. The assembly was placed into a pouch cell and sealed under vacuum. A stack pressure of 7 MPa was applied to all cells in this study. For CCD determination, cells were subject to galvanostatic single plating for a capacity of 8 mAh $cm^{-2}$. For cycling studies, cells were cycled galvanostatically with a capacity on each half-cycle of 0.5 mAh $cm^{-2}$. Although the plating current on the working electrode was 9.0 mA $cm^{-2}$, a current density of 0.05 mA $cm^{-2}$ was used on stripping to avoid void formation at the working electrode–solid electrolyte interface. All galvanostatic measurements were performed using a Gamry Interface 1010 potentiostat.

### 4.3.3 *In-situ* X-ray tomography

X-ray tomograms were recorded at the I13-2 beamline at the Diamond Light Source and the TOMCAT beamline at the Swiss Light Source (Paul Scherrer Institute). For both experiments, the projections were collected with a PCO pco.edge 5.5 sCMOS camera combined with an optical microscope with a 4× magnification, resulting in a pixel size of 1.63 µm. For each tomogram, 1,801 equiangularly distributed projections were taken over 180°. Additionally, X-ray tomograms were collected using a Zeiss Xradia 610 Versa X-ray microscope and 3201 equiangularly distributed projections were taken over 360° for each tomogram, with a resultant pixel size of 1.63 µm. For the *in-situ* measurements, metallic lithium foil was punched into disc-shaped lithium electrodes and pressed onto both sides of the electrolyte disc, 1 mm diameter electrodes were used for the working electrode and 3 mm for the counter. X-ray tomograms were obtained at the pristine state and after charging in successive steps of 0.1 mAh $cm^{-2}$. During the experiment, 7 MPa of pressure was applied using a constantly applied spring force, which was measured and calibrated using a transducer.

### 4.3.4 Plasma FIB-SEM and microstructural analysis

Solid electrolyte discs were transferred into the chamber of a plasma FIB scanning electron microscope (Helios G4 PFIB DualBeam, Thermo Fisher Scientific) for FIB milling with an iLoad vacuum sample transfer system without exposure to air. The freshly milled cross-section was then imaged with the SEM to visualize the pores and cracks in proximity to the interface. Automated serial sectioning was used to obtain a three-dimensional depiction of the porosity. A 30 kV and 15 nA $Xe^{+}$ beam was used to mill the volume of interest and capture a stack of secondary electron cross-sectional images. Each slice had a thickness of 100 nm. To construct a three-dimensional view, the sequence of 2D secondary electron images were aligned using Avizo 3D (version 2021.2, ThermoFisher Scientific). Using the Avizo 3D software the images were subjected to a semi-automated segmentation process to differentiate between pores, cracks, and bulk electrolyte. The dimensions of the microstructural defects were then used as inputs for the modelling simulations.

### 4.3.5 Powder X-ray diffraction

The electrolyte discs were ground into powders using a pestle and mortar. XRD was carried out in a glovebox with a nitrogen atmosphere (< 1 ppm $O_2$ and $H_2O$) to prevent exposure of the sample to air. The sample was loaded onto a zero-background Si sample holder and the XRD pattern was collected with a Rigaku MiniFlex 600 diffractometer using Cu Kα radiation.

## 4.4 Results and Discussion

### 4.4.1 Densification of the $Li_6PS_5Cl$ microstructure

Initial explorations into the effect of heat treatment on the $Li_6PS_5Cl$ microstructure began with the use of a box furnace within an Ar filled glovebox. By compressing the electrolyte powder with a uniaxial press, green body discs could be formed. These discs were then subject to varying maximum temperatures and hold times to assess the effect on the porosity and phase purity. It was found that regardless of hold time, significant densification of the microstructure was not possible without subjecting the electrolyte to temperatures of at least 550 °C, see Figure 4.1.

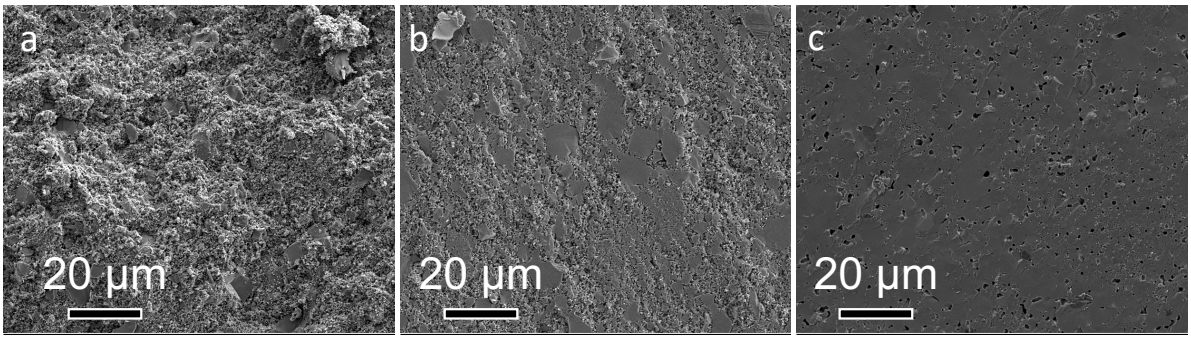



**Figure 4.1:** SEM images of $Li_6PS_5Cl$ fracture surfaces after **a** no heat treatment, **b** 450 °C, **c** 550 °C. 10 °C per min heating rate, 1 hour hold time.

Even after sintering at 550 °C, it can be seen that a large quantity of pores are still present in the electrolyte. These temperatures also seem to risk the thermal degradation of $Li_6PS_5Cl$, as significant quantities of new impurity phases were detected, this is shown in Figure 4.2, where the formation of LiCl within the bulk microstructure was observed during the collection of EDX maps on the fracture surfaces of the electrolyte. As well, the formation of phosphate layers at

the surface of the electrolyte was evident, likely resulting from a reaction with trace moisture in the atmosphere during heating. Consequently, only limited densification of $Li_6PS_5Cl$ electrolytes was possible through the use of conventional furnace sintering.

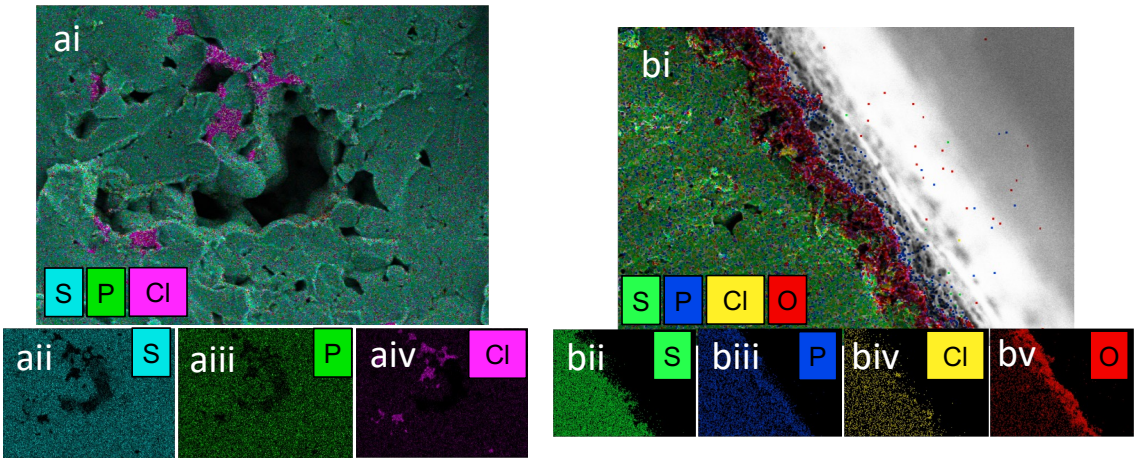



**Figure 4.2:** Sintering $Li_6PS_5Cl$ at 550 °C **ai** EDX maps overlaying on an SEM at the centre of a fracture surface, with individual EDX maps shown for S (turquoise), P (green) and Cl (pink) in **aii-iv**, respectively. **bi** EDX maps overlaying on an SEM at the edge of a fracture surface, with individual EDX maps shown for S (green), P (blue), Cl (yellow) and O (red) in **bii-v**, respectively.

In recent years, field assisted sintering, also known as spark plasma sintering, has been demonstrated as a highly effective method to densify oxide electrolytes in drastically shortened timeframes[328,329]. The process involves passing a current through the die and solid electrolyte disc during the application of uniaxial pressure, resulting in more homogeneous and rapid heating than conventional methods. Importantly, this combination of fast and efficient heating under vacuum meant lower maximum temperatures could be applied for shorter times in a more inert environment; all critical improvements in facilitating a significant densification of sulphide electrolytes without degradation. Figure 4.3 shows cross-sectional images of the $Li_6PS_5Cl$ microstructures across a range of field assisted sintering conditions as imaged by FIB-SEM. It can be seen that a not only is a dramatic densification of the electrolyte possible but also a systematic variation in microstructure could be achieved by control of the maximum temperature. As compared to a standard cold pressed microstructure, a significant change in microstructure was induced by heating for just 5 mins at 300 °C. Heating for 5 minutes at 350 and 400 °C resulted in microstructures with vastly increased density, and as a result with smaller pores and lower pore population densities.

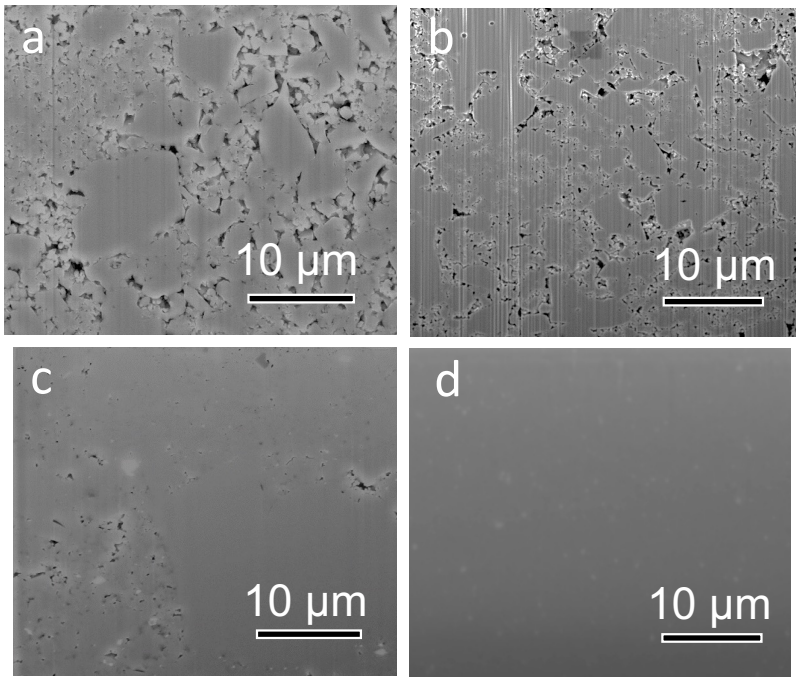



**Figure 4.3:** FIB-SEM cross-sections of $Li_6PS_5Cl$ **a** cold pressed **b** field assisted sintered at 300°C **c** field assisted sintered at 350°C **d** field assisted sintered at 400°C.

Due to the air sensitivity of $Li_6PS_5Cl$ and limited stability with most solvents, quantifying an overall change in porosity is challenging due to both a rarity in available air-sensitive equipment and the difficulty in performing Archimedes-type experiments without risking degradation. To overcome this, the total volume of electrolyte discs was determined by using micro-XCT to map the entire outer electrolyte surface. By measuring the weight of the electrolytes and comparing this to the total sample volume, the overall density of the electrolytes produced by each sintering condition could be calculated. Densities of 86, 95 and 99% were obtained by heating respectively at 300, 350 and 400 °C for just 5 mins. The standard cold pressed microstructure was determined to be only 83% dense. See also Table A.3.

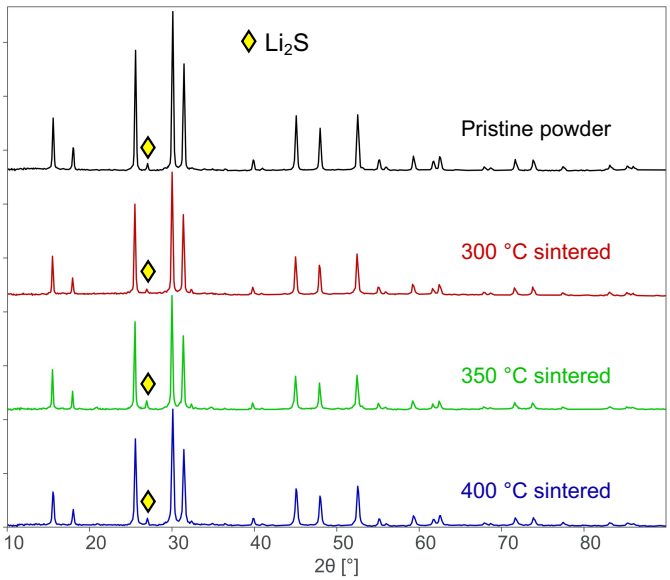



**Figure 4.4:** Powder X-ray diffraction patterns for the pristine $Li_6PS_5Cl$ powder, 300°C field assisted sintered, 350°C field assisted sintered, and 400°C field assisted sintered $Li_6PS_5Cl$.

In virtue of the short sintering durations made possible by field assisted sintering, the crystallinity and single-phase nature of the $Li_6PS_5Cl$ is retained. As confirmed by the powder X-ray diffraction patterns in Figure 4.4. It may be noted that small amounts of $Li_2S$ are present in all reported syntheses of $Li_6PS_5Cl$[330,331]. Similarly, $Li_2S$ is present in the as purchased $Li_6PS_5Cl$ used in this study, and comparable amounts were detected across all the field assisted sintering regimes used.

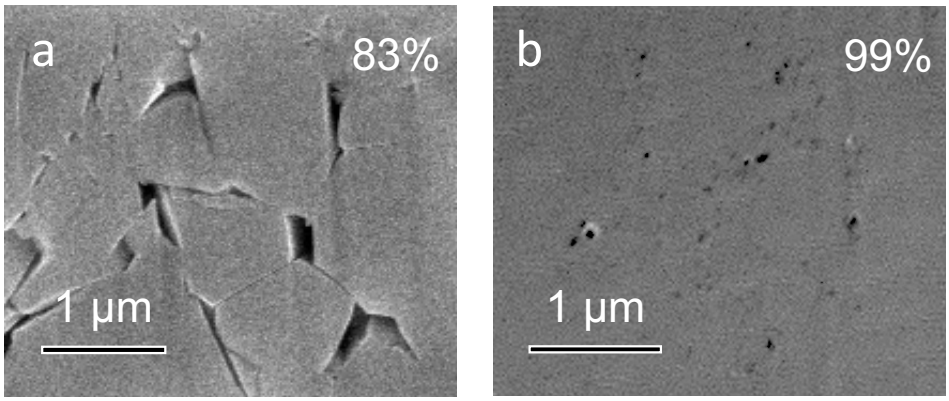



**Figure 4.5:** Magnified FIB-SEM cross-sections of the **a** 83% and **b** 99% dense $Li_6PS_5Cl$ electrolytes.

As well as the clear differences in porosity, a closer examination of the microstructure reveals further interesting developments during sintering. The SEM images in Figure 4.5 show the presence of grains in the 83% dense material whereas the 99% material exhibits greater

homogeneity, it is harder to identify individual grains. Sulphides are mechanically soft; their Young's moduli are typically in the range 10-30 GPa compared with oxides of 150-200 GPa[332–335]. Conventional thinking based on oxide ceramics may not be the best approach to understand these compliant materials, which densify to some extent even with cold pressing and to a very significant extent when heated at relatively low temperatures (several hundred degrees) for short durations.

### 4.4.2 Effect of $Li_6PS_5Cl$ microstructure on ionic conductivity

Interestingly, a significant improvement in the ionic conductivity of the $Li_6PS_5Cl$ discs occurs during the densification of the microstructure, see Figure 4.6a. Despite the vast literature aimed at improving the ionic conductivity of solid electrolytes through alterations in composition and crystal structure, there is a serious neglection of the impact of microstructure[336]. Although the improvements seen in Figure 4.6 can be rationalised solely in terms of a reduction in inactive volume and the tortuosity of the ionic pathways through the electrolyte disc, it is important to consider if any improvement derives from an alteration in the nature and/or number of inter particle/grain boundaries. The impedance of ions through the bulk crystal and across grain boundaries can in principle be resolved through analysis of PEIS spectra, but as can be seen in Figure 4.6b, the high conductivity of $Li_6PS_5Cl$ limits the observable contributions in the measurable frequency range at room temperature.

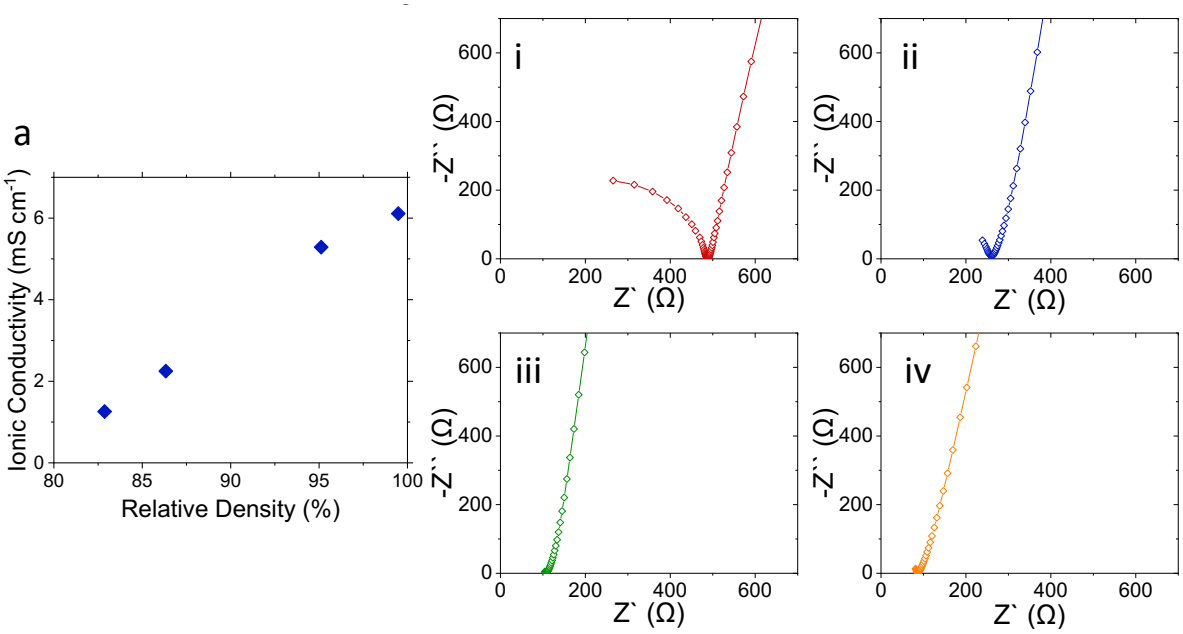



**Figure 4.6: a** Trend in ionic conductivity of $Li_6PS_5Cl$ with relative density **b** Nyquist plots from PEIS of $Li_6PS_5Cl$ with 4.5mm blocking electrodes for **i** cold pressed **ii** field assisted sintered at 300°C **iii** field assisted sintered at 350°C **iv** field assisted sintered at 400°C $Li_6PS_5Cl$.

To explore further, PEIS was performed at low temperatures (-40 °C) to see whether the impedance contributions from bulk crystal and grain boundaries could be resolved from one another.

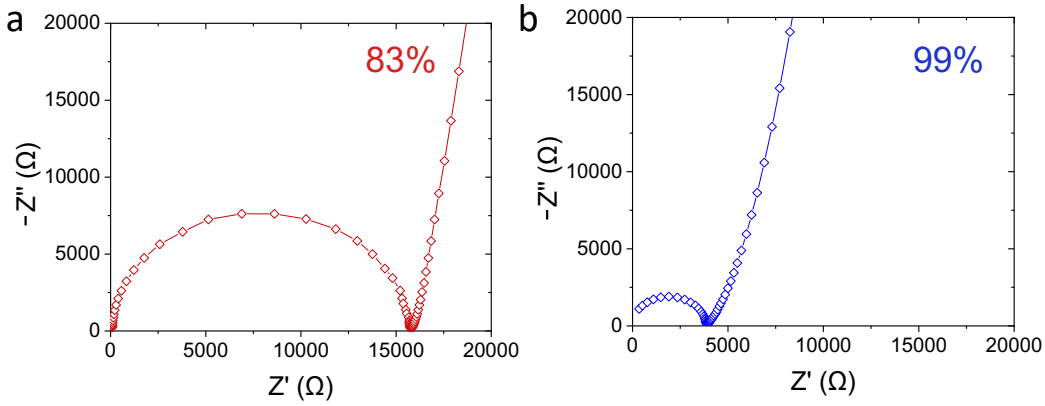



**Figure 4.7:** Nyquist plots from PEIS taken at -40°C for **a** cold pressed and **b** field assisted sintered at 400°C $Li_6PS_5Cl$ both with 4.5mm blocking electrodes.

Curiously, both the 83% and 99% dense $Li_6PS_5Cl$ electrolytes showed near-perfect semi-circular Nyquist plots, see Figure 4.7 and Table 4.1. When measuring the PEIS of an oxide solid electrolyte at low temperatures, two distinct semi-circular features are typically observed, corresponding to bulk crystal and grain boundary contributions[267]. That only one semi-circle is observed in either Figure 4.7a or b indicates that in $Li_6PS_5Cl$ the ionic conduction across the

grain boundaries is very similar to that through the bulk crystal, regardless of density. Similar observations have been reported in the literature previously for a multitude of sulphide electrolytes[116,117,337]. These results further add to the growing picture that conventional thinking based on oxide ceramics may be less applicable to understanding sulphides.

**Table 4.1:** Width and heights of the bulk/grain boundary semi-circular contribution to the Nyquist plots in Figure 4.7. Near perfect semi-circles are measured.

| Density (%) | Width (Ω) | Height (Ω) | Width:Height |
|---|---|---|---|
| 83 | 15775 | 7584 | 2.08:1 |
| 99 | 3910 | 1907 | 2.05:1 |

### 4.4.3 Determination of the critical current for dendrite initiation

As discussed in Chapter 3, changes in the microstructure of the solid electrolyte are expected to have a significant impact on Li dendrite failure. The initiation of Li dendrites in solid electrolytes occurs above a critical current density and it is this critical threshold that must be used first and foremost as a measure of any improved resistance to Li dendrites. In the literature, the most common methodology employed to determine the CCD of a given solid electrolyte is through galvanostatically cycling of a symmetric two-electrode cell with Li metal electrodes, stepping up the current density after each cycle[310,338]. This method was first introduced in 2016 by the Sakamoto group, whose pioneering work had established the current density dependence on dendrite failure in solid electrolytes and contributed significantly to the concept of a critical current density[339]. Since then, the use of the method throughout the literature has suffered from a lack of standardisation. Inconsistencies in the capacity per half cycle, number of cycles per current density, current density step sizes and a lack of consensus on what features in the voltage profile constitute dendrite failure have all lead to a frustrating scatter of reported CCDs[340,341]. Additionally, work published in 2019 by Kasemchainan *et al*. demonstrated that contact losses (known as 'voids') can occur at the Li/SE interface as stripping currents increase, leading to severe current focussing at the remaining areas of contact during subsequent plating[342]. Voiding on stripping therefore results

in the threshold for dendrite formation to be reached prematurely on subsequent plating. Since the critical current for void formation is generally lower than that of dendrite formation, this premature failure often dominates measured CCDs. As a result, many in the field have since advocated for protocols which avoid the complication of void formation during stripping, including Sakamoto himself[1,32].

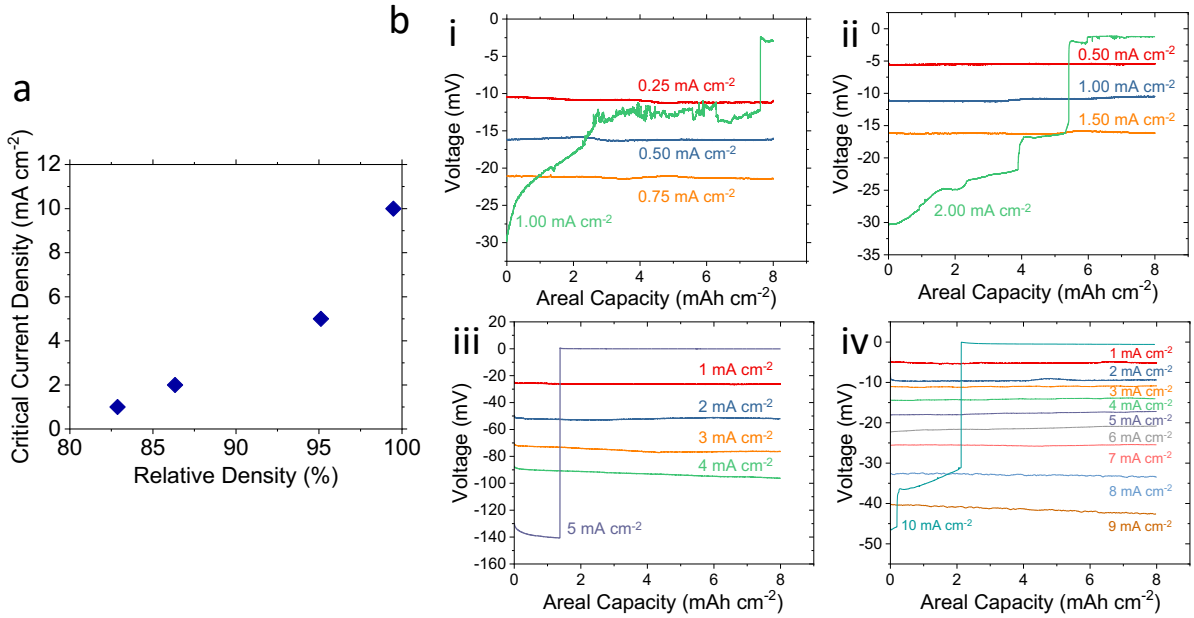



**Figure 4.8: a** Critical current for dendrite formation vs. relative density of $Li_6PS_5Cl$ **b** Voltage vs capacity plots for Li/$Li_6PS_5Cl$ 3-electrode cells, single plated for 8 mAh $cm^{-2}$ under 7 MPa stack pressure for **i** cold pressed, **ii** 300°C sintered, **iii** 350°C sintered, and **iv** 400°C sintered $Li_6PS_5Cl$ solid electrolytes.

To avoid any influence of void formation in this work when determining critical current densities, a single plating protocol was employed using 3-electrode cells. As detailed in Chapter 3, the process of dendrite propagation was shown to have a much higher sensitivity to the applied stack pressure and the areal capacity plated as compared to the initiation process. By applying a high stack pressure of 7 MPa and a high areal current density of 8 mAh $cm^{-2}$ (twice that typical of commercial cell loadings) a protocol was employed which would ensure any dendrite crack initiated would propagate until complete short circuit. This allows for the current density at which short circuit occurs to be used as an unambiguous measure of the critical current density for dendrite initiation. The voltage versus capacity plots for 3-electrode cells, single plated for 8 mAh $cm^{-2}$ under 7 MPa stack pressure for the differently

sintered $Li_6PS_5Cl$ are shown in Figure 4.8b, with the results summarised in Figure 4.8a. The CCD increases from 1 mA $cm^{-2}$ for the 83% dense solid electrolyte to 10 mA $cm^{-2}$ for the material with 99% relative density.

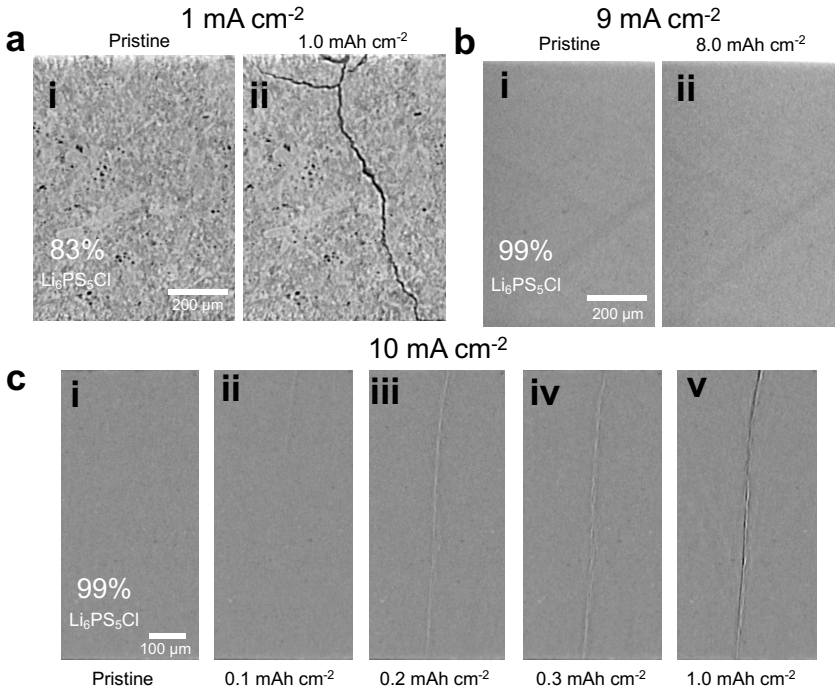



**Figure 4.9:** Virtual XCT cross-sections of Li/$Li_6PS_5Cl$/Li cells with plating at the top electrode **a** for a cold pressed $Li_6PS_5Cl$ electrolyte (83% dense) **i** pristine and **ii** after plating 1 mAh $cm^{-2}$ at 1 mA $cm^{-2}$. **b** for a 400°C sintered $Li_6PS_5Cl$ electrolyte (99% dense) **i** pristine and **ii** after plating 8 mAh $cm^{-2}$ at 9 mA $cm^{-2}$. **c** same electrolyte for plating at 10 mA $cm^{-2}$ **i** pristine, **ii** after plating 0.1 mAh $cm^{-2}$ **iii** 0.2 mAh $cm^{-2}$ **iv** 0.3 mAh $cm^{-2}$ **v** 1 mAh $cm^{-2}$. The Li electrodes have been removed from the images for clarity.

To support the results in Figure 4.8, *in-situ* micro X-ray computed tomography (XCT) experiments were performed to examine what happens when lithium is plated. XCT virtual cross-sections are presented in Figure 4.9. The data was collected from symmetric two electrode cells with lithium being plated at the electrode at the top of the images. Figure 4.9a shows the virtual cross-section of the cell with the 83% dense solid electrolyte before and after plating a capacity of 1 mAh $cm^{-2}$ at a rate of 1 mA $cm^{-2}$. The image after plating is very similar to those reported previously for lower density argyrodite, with a spalled-out piece of the ceramic and the transverse crack reaching the other electrode[286,311]. The current density at which this occurs is also consistent with previous work[286,311]. In contrast, the cell with the 99% solid electrolyte plated at a current density of 9 mA $cm^{-2}$ shows no evidence of a dendritic

crack, Figure 4.9b. This is also demonstrated in the 3D reconstructions of the XCT data in Figure 4.10bi. Repeating the experiment on the 99% dense solid electrolyte but increasing the current density to 10 mA $cm^{-2}$ does result in a dendritic crack, Figure 4.9c and Figure 4.10bii. The cracks are however different between the low and high-density ceramics. In the case of the dense solid electrolyte there is no evidence of spallation, and the transverse crack follows a very straight path to the other electrode. The XCT virtual cross-sectional images in Figure 4.9b and c for 99% dense solid electrolytes confirm that the CCD is between 9 and 10 mA $cm^{-2}$, in accord with the electrochemical measurements in Figure 4.8.

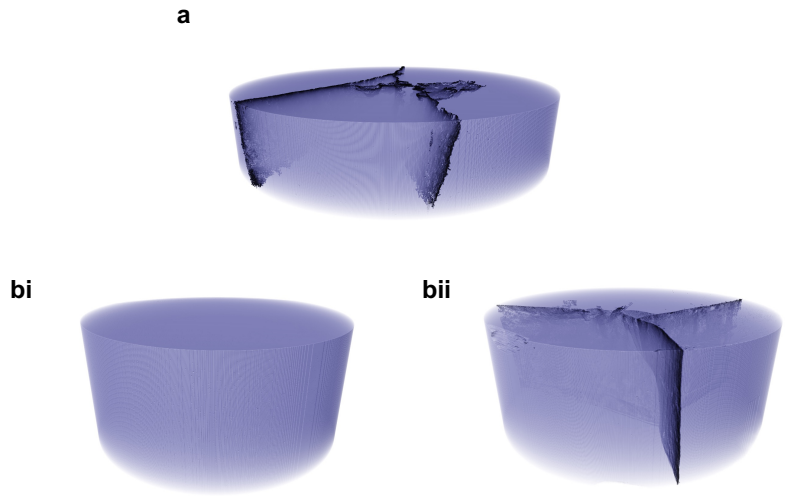



**Figure 4.10:** Three-dimensional renderings of the dendritic cracks in the electrolytes in Figure 4.9. **a** cold pressed $Li_6PS_5Cl$ (83% dense) after plating 1 mAh $cm^{-2}$ at 1 mA $cm^{-2}$ (corresponds to Figure 4.9a(ii)). **b** 400°C sintered $Li_6PS_5Cl$ (99% dense) after plating **i** 8 mAh $cm^{-2}$ at 9 mA $cm^{-2}$ (corresponds to Figure 4.9bii) and **ii** 1 mAh $cm^{-2}$ at 10 mA $cm^{-2}$ (corresponds to Figure 4.9cv).

To further demonstrate the resistance to dendrite failure of the 99% densified $Li_6PS_5Cl$, three-electrode cells with lithium working electrodes were subject to repeated fast charging at 9 mA $cm^{-2}$, see Figure 4.11. In the case of the 83% dense (cold pressed) $Li_6PS_5Cl$ solid electrolyte the cell short-circuits after 6 cycles. Whereas the 99% dense $Li_6PS_5Cl$ solid electrolyte cycles continuously until the cycling was stopped after 100 cycles. In both cases stripping was carried out at the lower current density of 0.05 mA $cm^{-2}$ to avoid voiding at the interface. The resistance to the initiation of any dendrite cracks in the dense $Li_6PS_5Cl$ electrolyte means the repeated fast charging is sustainable.

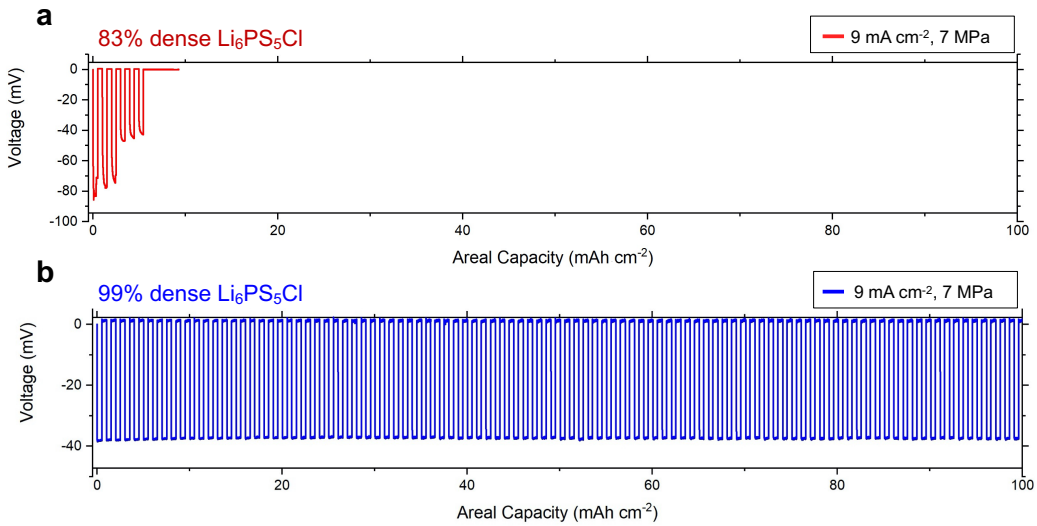



**Figure 4.11:** Cycling of Li/$Li_6PS_5Cl$ 3-electrode cells with current densities of 9 mA $cm^{-2}$ for plating, 0.05 mA $cm^{-2}$ for stripping (to avoid void formation), both for a capacity of 0.5 mAh $cm^{-2}$, under 7 MPa stack pressure, with **a** a cold pressed $Li_6PS_5Cl$ disc (83% dense) and **b** a 400°C sintered $Li_6PS_5Cl$ disc (99% dense).

### 4.4.4 The effect of microstructure on dendrite initiation

The single plating of differently sintered $Li_6PS_5Cl$ solid electrolytes shows a clear increase in CCD with increasing densification, and from the XCT results in Figure 4.9, the determined CCDs can be seen to correspond to the initiation of dendrites. As described in Chapter 3, the initiation of dendrite cracks is related to the microstructural defects in proximity to the anode surface, specifically pores and cracks. A CCD was rationalised as a direct result of the hydrodynamic nature of the pressure build up. When plating proceeds at low rates into filled pores and cracks connected to the interface, Li is able to continually extrude back to the surface through plastic deformation as it readily undergoes creep at room temperature. Only during high plating currents does the deposition of Li outpace the extrusion of Li metal and pressures build as a result. The critical currents needed to cause pressures capable of cracking the electrolyte are dependent on the size and proximity of the defects. Given the drastic overall microstructural differences, the question then became as to whether differences in the size and number of near surface defects were significant enough to explain the changes in CCD for the differently sintered $Li_6PS_5Cl$ solid electrolytes.

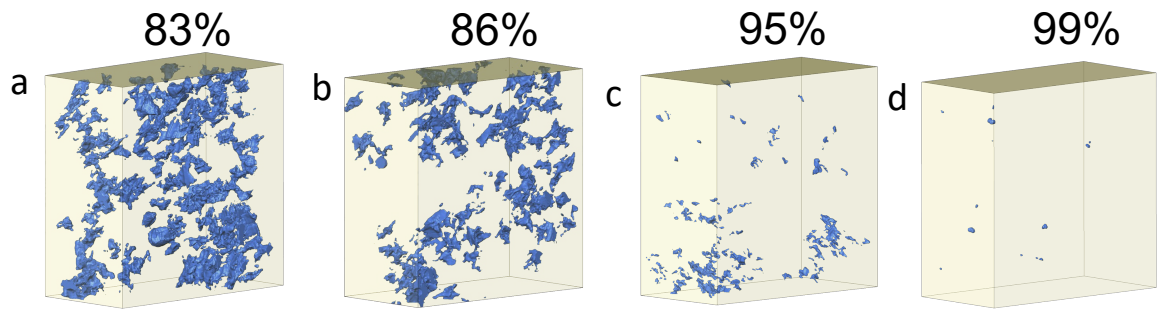



**Figure 4.12:** Tomographic FIB-SEM of near surface $Li_6PS_5Cl$ microstructures for **a** cold pressed, **b** field assisted sintered at 300°C, **c** field assisted sintered at 350°C, and **d** field assisted sintered at 400°C, obtained using FIB-SEM serial sectioning and imaging. Total volume of 20x20x10µm$^3$.

To measure the distributions of microstructural defects in the near subsurface region with high spatial resolution, tomographic FIB-SEM imaging was performed on the differently sintered $Li_6PS_5Cl$ solid electrolytes. Surface regions of the solid electrolytes were milled using a PFIB and the resultant cross-section was then imaged with the SEM to visualize the pores and cracks in proximity to the interface. Automated serial sectioning was then used to mill the volume of interest and capture a stack of secondary electron cross-sectional images which can be used to generate a three-dimensional depiction of the porosity, see Figure 4.12. The three-dimensional depictions were then subjected to a semi-automated segmentation process to differentiate between pores, cracks, and bulk electrolyte.

Taking the microstructure of a specific solid electrolyte and predicting its CCD is problematic, since the sizes of the microstructural features are distributed over a wide range, and we cannot assume that, for example, the average sizes of the microstructural features determine the CCD. Instead, the dimensions of critical defects within each microstructure must be rationalised through a consideration of the electrochemical processes during Li plating.

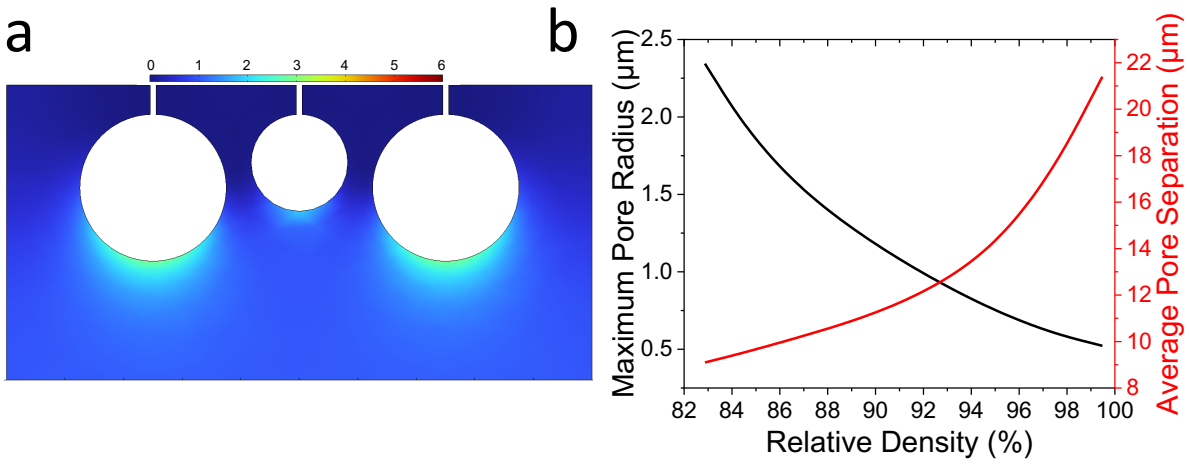



**Figure 4.13: a** The current distribution for multiple surface connected pores. Two pores of 2.5 μm radii (20 μm apart) are situated either side of a smaller pore (1.65 μm in radius). The colour bar indicates the amplification of the local current relative to the average. Less than 10% of the current is distributed across the smaller pore, therefore only pores within at least 1/3 of the radius of the large pore will significantly affect the current at the larger pore. **b** The changes in the largest pore sizes and their average separations with respect to the overall relative density of the $Li_6PS_5Cl$, as determined by FIB-SEM tomography.

As described in Chapter 3, it is the largest pores within the distribution of pore sizes that are primarily responsible for dendrite formation. This arises both because the current is focused on the larger pores and because the larger the pore surface area the greater the rate of Li build-up in the pores, such that the critical pressure for dendrite formation occurs first in the larger pores. Considering the four differently densified solid electrolytes, the largest pores in the near surface region of the electrolyte range from 0.5 (high density) to 2.3 μm (low density) in radii.

As well, the precise current at the pore is affected by the size and proximity of the neighbouring pores. This is because the neighbouring pores spread the current, reducing it at a given pore (as discussed in Chapter 3). This effect drops off rapidly with the size of the neighbouring pores. Whilst ultimately a distribution of pore sizes exists within a given microstructure, when solving Laplace's equation for a collection of pores whereby a smaller pore is considered in between two large pores, it was determined that there is only significant current spreading from the largest pores when neighbouring pores are of a comparable size (e.g., within a third of the radius). For pores less than 1/3 of the size, the effect is < 10%, see Figure 4.13a. Consequently, the average pore separation distances were calculated excluding pores of a

size less than 1/3 of the largest pores. Across the differently sintered electrolytes, the proximity between the large pores ranges from 10 (low density) to 22 µm (high density). Both the pore sizes and proximities from the microstructural analysis were used to define the ranges shown in Figure 4.13b.

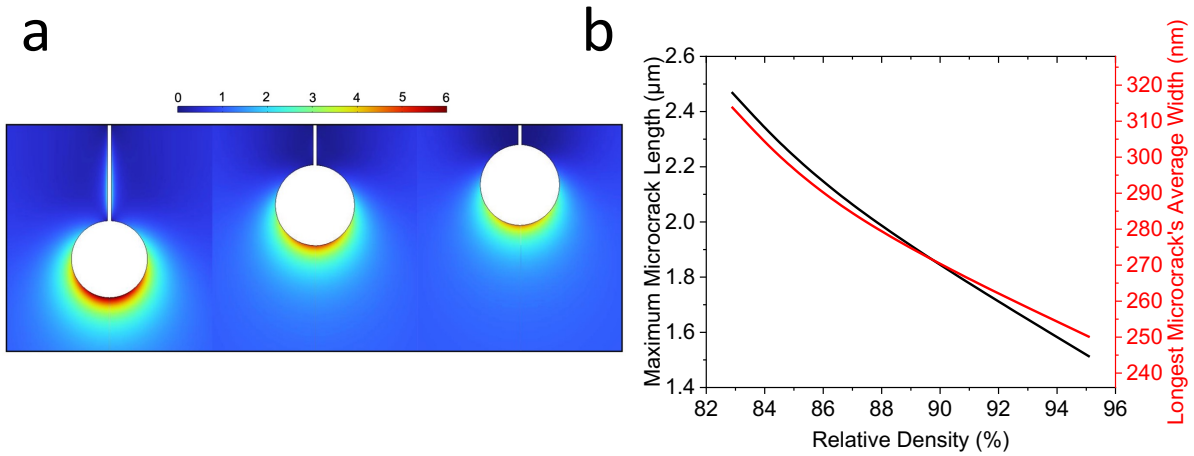



**Figure 4.14: a** The current distribution surrounding identical pores connected by three different crack lengths: 3.75, 1.5 and 0.75 µm. The colour indicates the local current from blue (low) to red (high). **b** The changes in the longest crack lengths and their associated widths with respect to the overall relative density of the $Li_6PS_5Cl$, as determined by FIB-SEM tomography.

As well as their size and vicinity to one another, the proximity of the pores to the surface also plays a key role in determining which are most critical regarding dendrite initiation. Pores very close to the surface cannot build pressures capable of cracking the ceramic as extrusion is too fast (easy). Instead, deeper pores are more likely to act as the critical defects. Not only is Li extrusion likely to be more difficult, but current focussing effects are also stronger for deeper pores. When solving Laplace's equation for pores at various depths from the surface, it can be seen that deeper pores attract more current, Figure 4.14a. Deeper pores will therefore build greater pressures during Li plating. Considering this, the longer cracks (deeper pores) and their associated widths were extracted for each density. The longest cracks measured within the differently densified solid electrolytes were found to range from 2.5 (low density) to 1.5 µm (high density). The average widths of the longest cracks (within 33% of the longest cracks) within each electrolyte was found to vary from 158 (low density) to 125 nm (high density). The crack lengths and widths were used to define the ranges in Figure 4.14b.

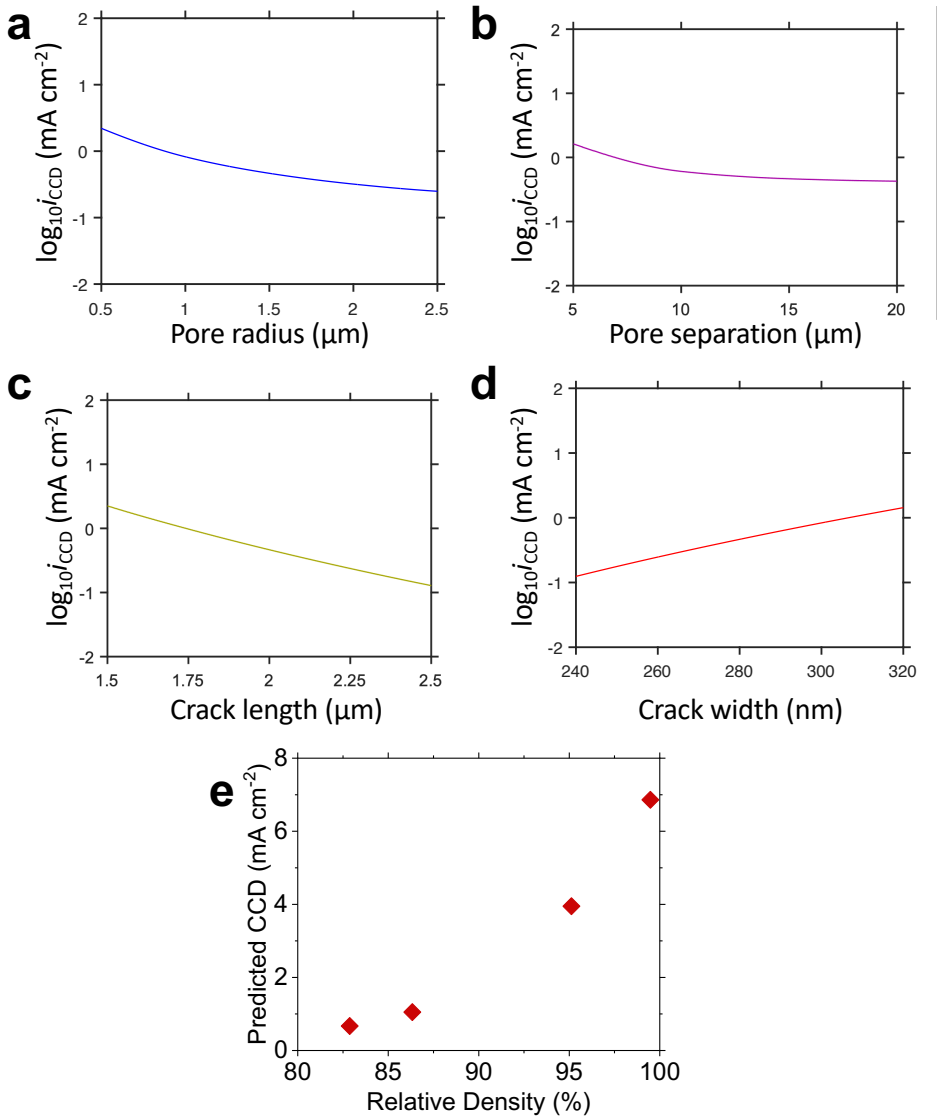



**Figure 4.15:** The effect on the critical current density for dendrite initiation of, **a,** pore radius, **b,** pore separation, **c,** crack length and **d** crack width. **e** Plot of predicted overall CCDs for each density of $Li_6PS_5Cl$.

Figure 4.15a-d illustrates how CCD will vary as a result of individual changes to pore size, pore separation, crack length and crack width. The ranges of the microstructural dimensions are obtained from Figures Figure 4.13b and Figure 4.14b, and thus represent typical values expected when densifying $Li_6PS_5Cl$. Looking at Figure 4.15a&b, we can see that CCD decreases with increasing pore size and separation, both due to their effect on the magnitude of current experienced by a given pore. As shown in Figure 4.15c&d, CCD increases with increasing crack width and decreases with increasing crack length, due to the effect of both on the rate of Li extrusion. The results in Figures 4.13b and 4.14b show that densifying

$Li_6PS_5Cl$ results in shorter and narrower cracks as well as smaller pores with greater separation. Therefore, not all changes in microstructure during the densification of $Li_6PS_5Cl$ act to increase CCD. While decreasing crack width and increasing pore separation acts to decrease CCD, at the same time the decreasing crack length and pore size act to increase it. The calculations show (Figure 4.15e) that the former outweigh the latter, predicting an overall increase in CCD as observed experimentally (Figure 4.8). While the trends in the predicted and experimental CCDs are the same (Figures 4.8a and 4.15e) a close match between the absolute values is not necessarily expected; for example, even the larger pores for a given density are not of identical size. Also, the microstructure model assumes a simple geometry for pores (spheres) and cracks (cylinders) whereas actual pores and cracks will have more complex shapes.

## 4.5 Conclusions

In this chapter, the effect of sintering conditions on the $Li_6PS_5Cl$ microstructure has been explored. It is found that plating currents as high as 9 mA $cm^{-2}$ can be achieved without lithium dendrites (and as a consequence without short-circuit) by sintering the solid electrolyte. Using the dendrite initiation model as detailed in Chapter 3, the improvements in critical current density are rationalised with regards to the measured changes in the solid electrolyte microstructure. Smaller pores and shorter cracks connecting the pores to the Li anode act to increase CCD, whereas narrower cracks and greater distance between pores (lower population density) act to reduce CCD. Increased sintering and densification of the $Li_6PS_5Cl$ solid electrolyte, from 83 to 99% relative density, results in a microstructure that has smaller pores with a lower population density and with cracks which trend to shorter and narrower dimensions. Therefore, not all the changes in microstructure with densification act to increase CCD. The reduction in pore size and the shorter crack lengths outweigh the narrower cracks and lower pore population density, achieving higher CCDs overall with densification. These

high plating currents are achieved without the need to form alloys with lithium and without the need to modify the solid electrolyte surface or introduce interlayers.

# Chapter 5: Transformation Toughening of $Li_6PS_5Cl$ Solid Electrolytes

## 5.1 Aim

In this thesis, the lithium dendrite failure of solid electrolytes and its relation to microstructural defects has been explored. This failure ultimately coincides with a mechanical failure of the electrolyte and accordingly the issue refreshes interest in the optimisation of the solid electrolyte's mechanical properties. Historically, ceramic electrolytes such as sodium β''-alumina have been toughened through the addition of metastablised zirconia particles as a secondary phase[343]. In this chapter, the effect of dispersing metastabilised zirconia particles within the microstructure of the sulphide electrolyte $Li_6PS_5Cl$ is investigated. The effect on fracture toughness is evaluated through mechanical indentation and the effect on ionic conductivity through PEIS. Using three-electrode cells, the question as to whether transformation toughening can stabilise propagating dendrite cracks is also considered.

## 5.2 Introduction

At the heart of the solid-state battery challenge is the exceptional difficulty in designing a single material which satisfies all solid electrolyte design criteria[47]. Aside from the obvious need for fast ion conduction, the electrolyte must be inherently safe, have both long-term chemical and electrochemical stability with high energy electrode materials, and all without sacrificing the prospects for cheap manufacture at scale[18,30]. Whilst there are continuous materials discovery efforts to offer a silver-bullet[102], many researchers have turned their attention to hybrid designs[99,344], interfacial layers[111,345] and the augmentation of the electrolyte layer itself through the introduction of secondary phases[346,347].

In this spirit, researchers have attempted to improve the dendrite resistance of solid electrolytes by including crack bridging fibres/platelets[217–219] or crack deflecting interior layers[52], overall, with mixed success. Composite solid electrolytes were also considered

during the commercialisation of Na-S batteries during the 1970s and 80s[343]. Na-S cells were produced using the fast $Na^+$ conducting β''-alumina ceramic electrolytes and to improve its mechanical reliability, metastable doped zirconia particles were incorporated into the microstructure as a finely dispersed second phase, with some reports indicating this led to an improvement in sustainable charging rates[225,226,348].

Although early investigations also ascribed the mechanical improvement to deflection toughening and improved grain size control, the main idea behind adding specifically metastable zirconia particles into the sodium β''-alumina matrix was to transformation toughen the electrolyte[221,222,224]. Transformation toughening is the increase in fracture toughness of a material due to a phase transformation occurring at the tip of an advancing crack[349]. Commonly, this has been achieved by dispersing small particles of zirconia within the microstructure which have been partially stabilised in the high temperature tetragonal phase[350,351]. The stress field in front of a propagating crack causes these metastably retained tetragonal particles to undergo a martensitic transformation to the stable monoclinic phase. Accompanying this transformation is a slight particle volume increase, and the net result is that compressive stresses are established on the crack surfaces near the crack tip that tend to pinch the crack shut, thereby arresting its growth (see Figure 5.1)[351].

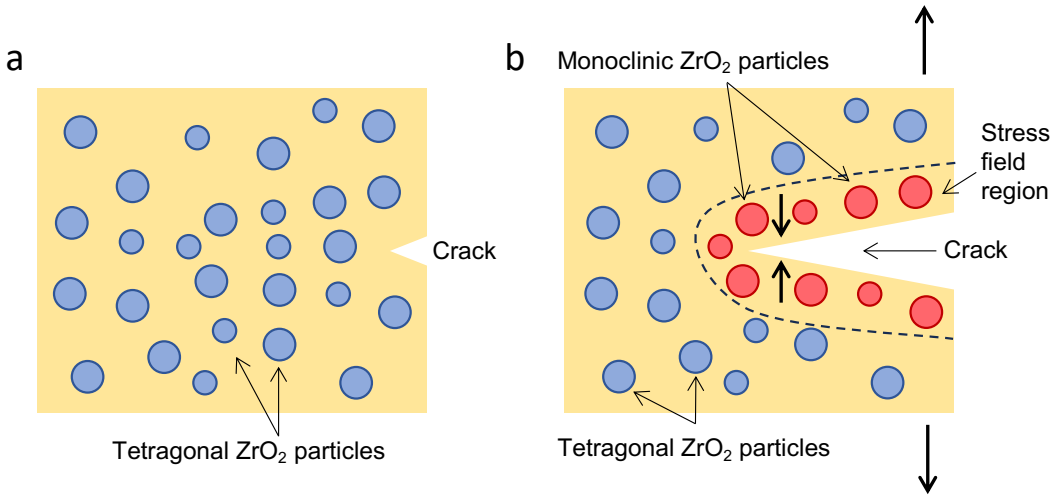



**Figure 5.1**: Schematic demonstration of transformation toughening **a** a crack prior to the inducement of $ZrO_2$ particle phase transformation **b** Crack arrestment due to the stress-induced phase transformation. Figure adapted from *Materials Science and Engineering: An Introduction, 8th Edition. (Wiley, 2009)*[349]. Reproduced with permission from John Wiley & Sons.

In Chapter 3, the propagation of dendrite cracks was significantly mitigated by lowering the applied stack pressure of the cell. But ultimately, the inevitable net growth of Li dendrites within the crack meant that at currents above the CCD, short circuit could only be prolonged rather than prevented completely. Transformation toughening can raise the fracture toughness of the material during the advancement of a crack, meaning cracks can be potentially stabilised during their propagation[349]. Therefore, transformation toughening may offer a route to preventing dendrite failure by stabilising propagating dendrite cracks.

No attempts to induce transformation toughening in $Li^+$ conducting solid electrolytes have so far succeeded. For example, when researchers attempted to include zirconia into $Li_7La_3Zr_2O_{12}$ (LLZO) electrolytes, a significant amount of LLZO had reacted with zirconia during sintering to form pyrochlore ($La_2Zr_2O_7$) and lithium zirconate ($Li_2ZrO_3$) phases[227]. In this chapter the effect of adding metastable zirconia particles into the sulphide electrolyte $Li_6PS_5Cl$ is investigated. A range of compositions are achieved by dry mixing the powders together with different ratios before using field assisted sintering to densify them into composite materials. The influence of the zirconia particles on the mechanical and electrochemical properties is then examined using a combination of indentation, PEIS and single plating experiments.

## 5.3 Experimental

### 5.3.1 Electrolyte preparation

All procedures were performed inside an Ar-filled glove box ($O_2$ and $H_2O$ levels < 1 ppm). $Li_6PS_5Cl$ solid electrolyte powder was purchased from *MSE Supplies* and 12 mol% $CeO_2$-$ZrO_2$ powder was purchased from *daiichi kigenso kagaku kogyo*. Before mixing, the 12 mol% $CeO_2$-$ZrO_2$ calcined in air at 900 °C for 1 hour, with a heating and cooling rate of 5 °C/min. This ensured that a sufficient amount of metastable tetragonal phase was present so to encourage transformation toughening in the final composite.

Powders were mixed using a combination of sieving (100 μm mesh) and using a pestle and mortar. In the optimised procedure, powders were first ground for 30 minutes after which the complete mixture was sieved to further mix the powder and break up any agglomerates. This

process was repeated three times. After mixing, the powders were loaded into a graphite die set. The die set was then inserted into a spark plasma sintering system (FCT systeme GmbH) within an Ar-filled glovebox and subject to 50 MPa uniaxial pressure 400 °C for 5 minutes while under vacuum by passing a current through the die set. 5-mm diameter sintered electrolyte discs of identical thickness were then used for cell assembly.

### 5.3.2 Potentiostatic electrochemical impedance spectroscopy (PEIS)

PEIS was taken using a 5 mV perturbation, collecting 10 points per decade across a frequency range of 1 MHz – 1 Hz. PEIS data were analysed and fitted to equivalent circuit models using the ZView software package.

### 5.3.3 Three-electrode cells

For a three-electrode cell, two disc-shaped lithium electrodes of 1 mm diameter were pressed onto the same side of the electrolyte disc as the working and reference electrodes. The working and reference electrodes were separated by a 1 mm-wide polymer insulating tape mask. A 5 mm lithium disc was pressed onto the other side as the counter electrode. The assembly was then placed into a pouch cell and sealed under vacuum (~ $10^{-3}$ bar). The cells were subject to 7 MPa stack pressure galvanostatic single plating at 10 mA $cm^{-2}$ until short circuit. All galvanostatic measurements were performed using a Gamry Interface 1010 potentiostat.

### 5.3.4 *In-situ* X-ray computed tomography

X-ray tomograms were recorded at the I13-2 beamline at the Diamond Light Source. For the experiments, the projections were collected with a PCO pco.edge 5.5 sCMOS camera combined with an optical microscope with a 4× magnification, resulting in a pixel size of 1.63 µm. For each tomogram, 1,801 equiangularly distributed projections were taken over 180°. For the *in-situ* measurements, metallic lithium foil was punched into disc-shaped lithium electrodes and pressed onto both sides of the electrolyte disc, 1 mm diameter electrodes were used for the working electrode and 3 mm for the counter. X-ray tomograms were obtained at

the pristine state and after charging. During the experiment, 7 MPa of pressure was applied using a constantly applied spring force, which was measured and calibrated using a transducer.

### 5.3.5 SEM/EDX and Plasma FIB-SEM

For SEM/EDX, powders were mounted on a plate using copper adhesive tape and the plate was sealed within an air-tight transfer holder which was used to move the samples to a Merlin SEM (Zeiss) without exposure to air. SEM was initially carried out using an acceleration voltage of 3 kV and a probe current of 200 µA. For SEM/EDX, data were collected at a higher voltage of 10 kV. The EDX was carried out within the Zeiss Merlin instrument using an X-Max 150 Silicon Drift detector (Oxford Instruments). Collection and analysis were carried out using the Aztec software package. For cross-sectional imaging, electrolyte discs were transferred into the chamber of the PFIB-SEM (Thermo Fisher Helios G4 Plasma-FIB Dualbeam) for FIB milling with an iLoad vacuum sample transfer system without exposure to air. The freshly milled cross-section was then imaged with SEM to visualise the distribution of $CeO_2$-$ZrO_2$ particles.

### 5.3.6 Nanoindentation: Elastic Modulus, Hardness and Fracture Toughness

*In-situ* indentation was performed using a (Hysitron PI 88) indenter within a TESCAN scanning electron microscope enabled the measurement of air sensitive $Li_6PS_5Cl$ discs without the need for mineral oil or other techniques that can affect the mechanical response. Samples were transferred to the SEM within an airtight transfer container. Indentation modulus and hardness were calculated using the Oliver-Pharr method on multiple indents made with a Berkovich tip. For the determination of fracture toughness, a cube corner tip was used to cause fracture of the electrolyte. Using the LEM equation (eq. 5.1) the fracture toughness, $K_{1C}$, was calculated for each of the multiple indents. The average across all indents was taken as the fracture toughness.

## 5.4 Results and Discussion

### 5.4.1 Development of $12CeO_2$-$ZrO_2$/$Li_6PS_5Cl$ composites

In this chapter, stabilised zirconia particles are mixed into $Li_6PS_5Cl$ solid electrolytes to investigate the effect on the mechanical and electrochemical properties. The inclusion of zirconia particles into the microstructure of a ceramic can benefit the fracture toughness through a combination of microcrack toughening, deflection toughening, grain pinning, but also through transformation toughening[343]. To maximise the magnitude of any transformation toughening effects, the size and distribution of the zirconia particles and crucially the volume fraction of the metastable phase must be optimised.

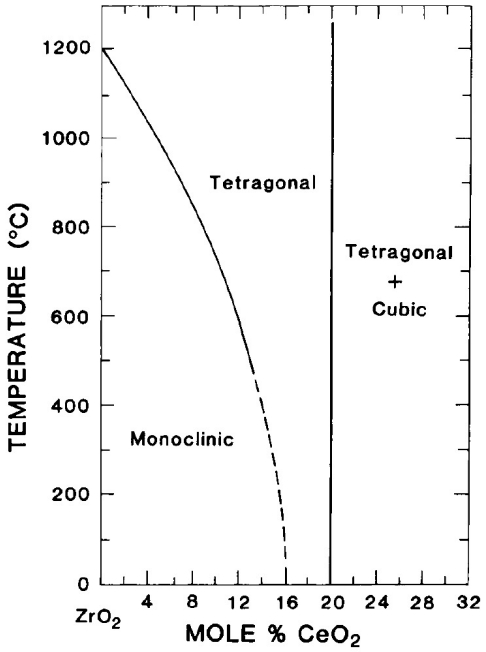



**Figure 5.2**: Zirconia-rich end of the $ZrO_2$-$CeO_2$ phase equilibrium diagram. *Reproduced from Transformation Toughening Of Ceramics. (CRC Press, 2017)*[351]. Reproduced with permission from CRC Press.

Pure zirconia is known to exhibit three polymorphs and which structural form exists will depend upon both temperature and pressure. At atmospheric pressure, zirconia exists as a cubic structure above 2360°C; below this temperature, it is tetragonal until approximately 1200°C, below which the transformation to a monoclinic structure begins. It is the martensitic transformation of zirconia particles from a metastable tetragonal phase to monoclinic which is invoked during transformation toughening. The driving force of this phase transformation is

dependent on the free energy of the crystal, the surface energy, the temperature, and the pressure[350,351]. It is the main aim of any fabrication process of transformation-toughened ceramics to develop the tetragonal zirconia phase into a metastable state, such that the nucleation barrier can be overcome by an applied stress, at or near room temperature[349,351].

The ease with which the tetragonal to monoclinic transformation can occur in zirconia will depend upon a number of physical and chemical factors, with one of the most important being the particle size[351]. Small particle sizes can stabilise the tetragonal phase by enhancing the relative influence of surface energy contributions to the transformation barrier. Critical particle sizes of 10nm or less are needed to stabilise unconstrained pure zirconia[352].

Doping the zirconia with small amounts of oxides such as Ceria ($CeO_2$) lowers the chemical free energy ($\Delta G_c$) and thereby the transformation temperature, meaning a higher fraction of larger particles can be stabilised in the tetragonal phase, see Figure 5.2 [351]. In this Chapter, 12 mol.% $CeO_2$-$ZrO_2$ (CSZ) is used as a secondary phase to maximise the fraction of the tetragonal phase at room temperature. Using SEM, the particles of the CSZ powder were imaged to ensure they were consistently sub-micron in size, see Figure 5.3. Aside from increasing the fraction of the tetragonal phase, the sub-micron particle sizes also enables a wider and more homogenous dispersion of CSZ particles throughout the $Li_6PS_5Cl$ matrix.

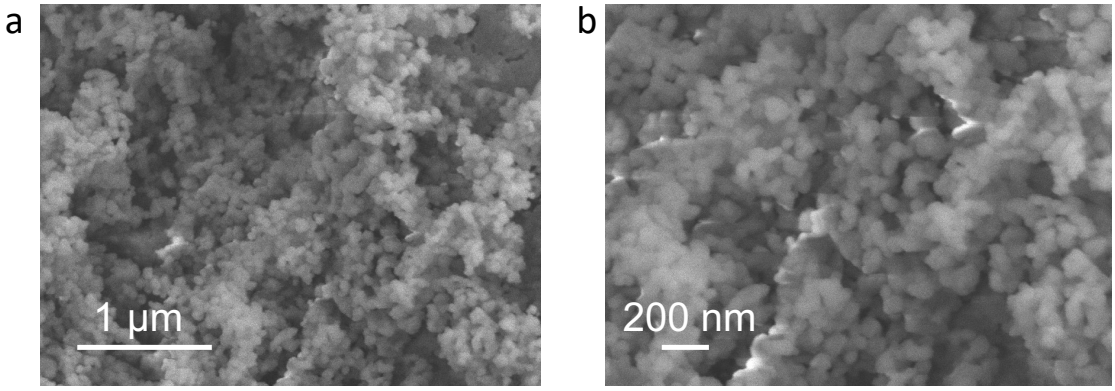



**Figure 5.3**: SEM images of 12 mol% $CeO_2$-$ZrO_2$ (CSZ) powder at **a** micrometre magnification and **b** nanometre magnification.

When stored for long durations, atmospheric moisture can adsorb to the surface of the particles and can prematurely induce the tetragonal to monoclinic phase transformation[353]. To ensure a high content of metastable tetragonal phase was present before incorporation into

the $Li_6PS_5Cl$ matrix a calcination step was performed in air at 900 °C for 1 hour, with a heating and cooling rate of 5 °C/min. Powder XRD patterns are shown in Figure 5.4 for CSZ before and after the calcination step. The relative volume percentages of the tetragonal and monoclinic phases can be estimated by comparison of the relative peak intensities of the monoclinic $(\bar{1}11)$ and $(111)$ (2θ = 28.2° and 31.5° respectively) and tetragonal $(110)$ (2θ = 30.2°) reflections, known as the Toraya method[354]. Using this method, the CSZ powder used in this work is estimated to contain 88 vol.% tetragonal phase after calcination.

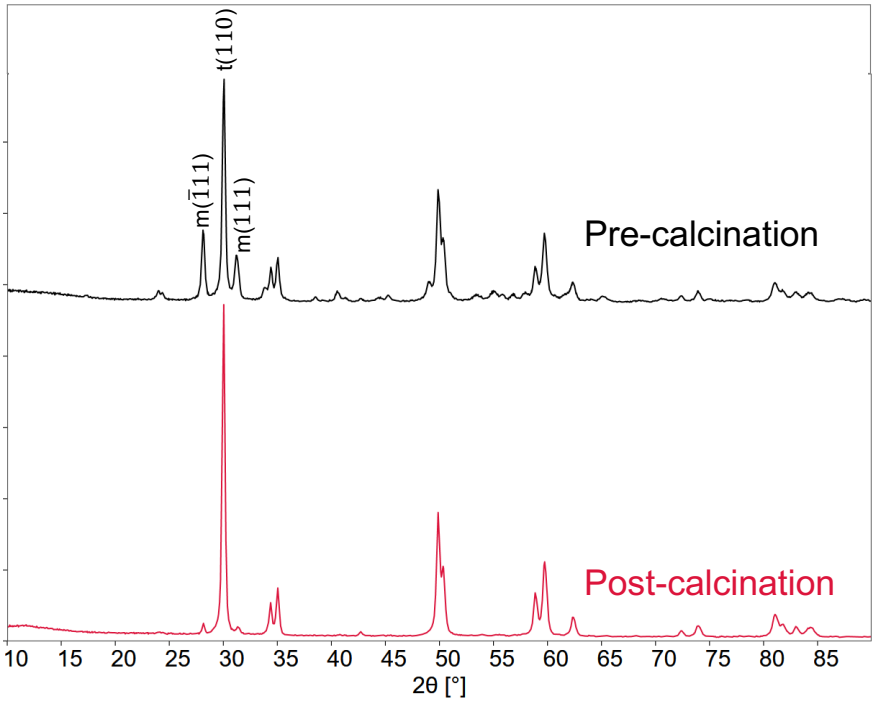



**Figure 5.4**: Powder X-ray diffraction patterns before (black) and after (red) 900°C calcination heat treatment.

Having established a high fraction of the tetragonal phase, it was then important to optimise the distribution of zirconia in the matrix. To ensure a homogeneous mixture of $Li_6PS_5Cl$ and CSZ particles, a combined procedure of sieving and hand milling was performed within an Ar-filled glovebox. As can be seen in Figure 5.5, the optimised mixing protocol was sufficient to ensure an effective coating of CSZ nanoparticles around individual $Li_6PS_5Cl$ particles. As well as maximising the distribution throughout the material, the mixing of the particles helps to minimise the number of CSZ agglomerates.

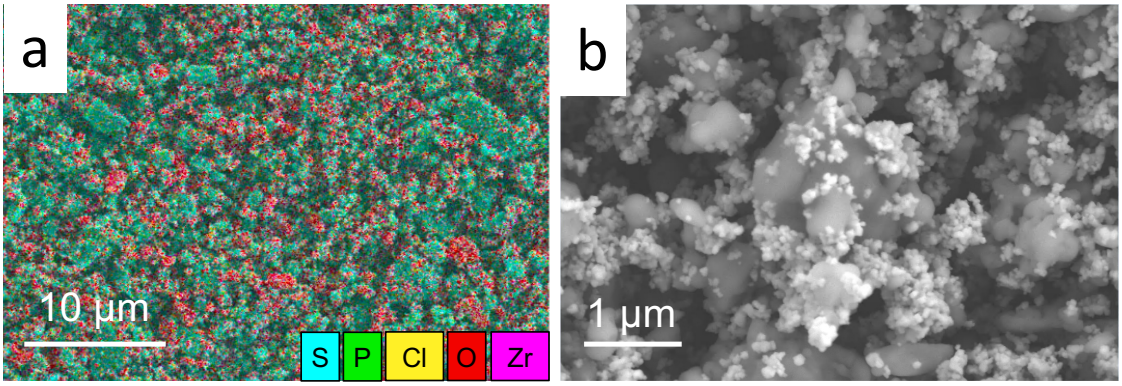



**Figure 5.5**: **a** EDX maps overlayed on an SEM image and **b** magnified SEM showing the mixed $Li_6PS_5Cl$ and CSZ powders.

The low sintering temperatures used for densifying $Li_6PS_5Cl$ mean any agglomerate will be retained as a loose cluster of nanoparticles in the densified material, potentially acting as points of weakness. In order to undergo a phase transformation during the fracture of the electrolyte, a CSZ particle must be put under strain by the advancing stress field at the crack tip[349]. As a result, the particles must be closely encapsulated by the fracturing matrix. Simply cold pressing a mixture of $Li_6PS_5Cl$ and CSZ particles will result in a porous final material, with only few CSZ particles likely to be trapped between grains of $Li_6PS_5Cl$ and many likely to sit in pre-existing pores and cracks unable to experience any strain during the fracture of the surrounding material. As described in the previous chapter, it is possible to densify $Li_6PS_5Cl$ to a considerable extent using an optimised field assisted sintering protocol. To maximise the encapsulation of CSZ particles throughout the material, the optimised sintering protocol was used to create high density CSZ-$Li_6PS_5Cl$ composites with a range in volume percentages of CSZ. Figure 5.6 shows the microstructures of five different compositions of CSZ-$Li_6PS_5Cl$ composites: 2%, 5%, 10%, 15% and 20% as compared to a pure $Li_6PS_5Cl$ electrolyte.

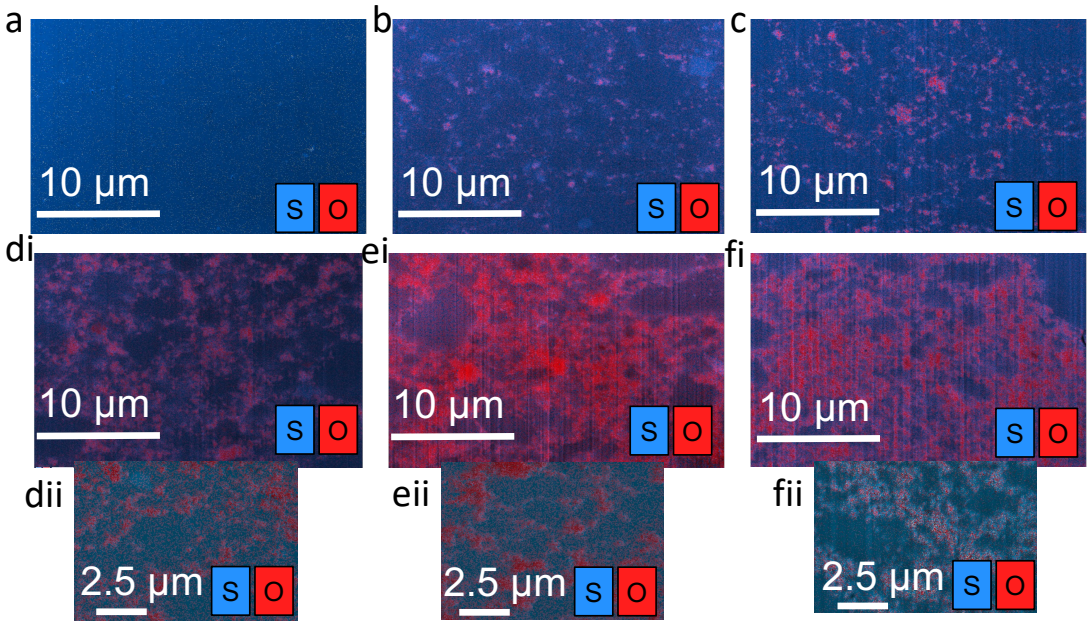



**Figure 5.6**: EDX maps overlayed on a FIB-SEM cross-section image illustrating the distribution of CSZ throughout the **a** pure $Li_6PS_5Cl$, **b** 2% CSZ, **c** 5% CSZ, **d** 10% CSZ, **e** 15% CSZ, **f** 20% CSZ CSZ-$Li_6PS_5Cl$ electrolytes. **dii**, **eii** and **fii** are magnified EDX maps for the 10% CSZ,15% CSZ and 20% CSZ composites respectively to illustrate the partial volume effects that occur in the low magnification maps. Such partial volume effects augment the apparent CSZ content in those composites.

### 5.4.2 Effect on mechanical properties

To evaluate the effect of CSZ additions on the fracture toughness of $Li_6PS_5Cl$, indentation tests were performed on the full range of compositions including the pure $Li_6PS_5Cl$ material. Due to their reactivity with moisture, sulphide solid electrolytes are highly air-sensitive making a large range of mechanical tests logistically challenging. As a result, there are a scarce number of articles in the literature reporting any mechanical property of any sulphide solid electrolytes, with the few that exist resorting to the use of mineral oil to avoid the sulphide's exposure to moisture[247,355]. No experimentally determined values for the mechanical properties of $Li_6PS_5Cl$ had ever been reported until my work in collaboration with Johann Perera[292].

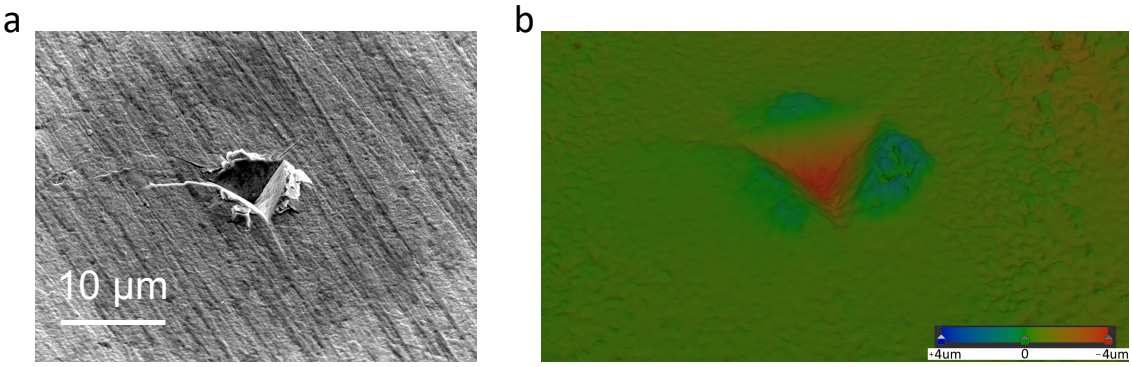



**Figure 5.7**: **a** SEM image and **b** 3D reconstructed height map of a $Li_6PS_5Cl$ ident.

Using an in-situ indenter within a scanning electron microscope, the mechanical measurement of air-sensitive solid electrolyte composites is enabled without the need for any mineral oil or other techniques that can affect the mechanical response. To determine the fracture toughness, a cube corner tip was used to indent the surface of the electrolyte and induce a crack. The toughness, $K_{1C}$, can then be calculated using the Lawn, Evans, and Marshall (LEM) equation (eq. 5.1) for each indent[273]. Where E is the modulus, H is the hardness, P is load, c is total crack length and α is a geometric constant for a cube corner tip. The average across all indents for a given composite was then taken as the fracture toughness. Since the calculation of fracture toughness using the LEM equation requires modulus and hardness values, the indentation modulus and hardness for each composite were calculated using the Oliver-Pharr method[271] on multiple indents made with a Berkovich tip.

$$K_{1C} = \alpha \left(\frac{E}{H}\right)^{1/2} \left(\frac{P}{c^{3/2}}\right) \tag{5.1}$$

Due to the soft nature of sulphide electrolytes, some spallation (pile-up) around the indent edges is inevitable, even with the addition of CSZ nanoparticles. For corner crack lengths to be considered valid, pileups on the indent edges must be minimal[356]. To ensure meaningful values of fracture toughness were collected from the indentation methodology used in this work, the amount of pile-up surrounding the indents was examined. As can be seen in Figure 5.7, the pile-up at the indentation edges was seen to be minimal and much smaller than the size of the indent itself. Figure 5.7b shows a 3D reconstruction of the indent and compares it with the SEM image from Figure 5.7a. From this we see the radial cracks emanating from the

corners of the indent that are significantly larger than the complex cracks occurring in the piled-up regions of compressive stress around the indent, which incorporates some plastic deformation as well as some secondary radial cracks. As described in work done by Kruzic *et al*.[356] the degree of cracking present should allow a fracture toughness within 10% of the value when measured using standard fracture mechanics experiments, e.g., notched three-point bending.

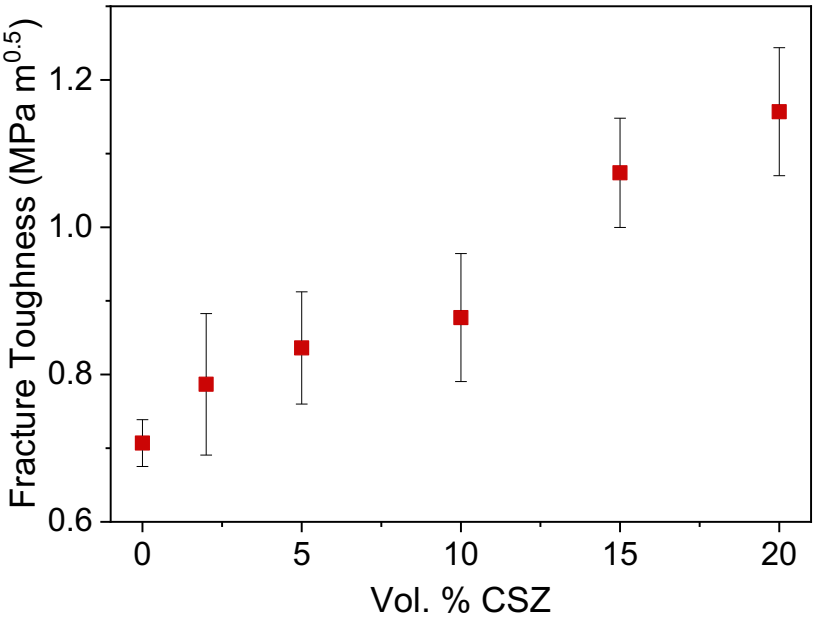



**Figure 5.8**: Trend in fracture toughness measured by indentation with increasing amounts of 12 mol% $CeO_2$-$ZrO_2$ (CSZ) powder. Error bars indicate the standard deviation between repeat measurements.

The fracture toughnesses determined for a range of CSZ-$Li_6PS_5Cl$ composites are plotted in Figure 5.8. Increasing the amount of CSZ within the material has a positive impact on the mechanical properties, almost doubling the measured fracture toughness. The inclusion of 20 vol.% CSZ raises the fracture toughness to 1.16 MPa $m^{1/2}$ as compared to 0.71 MPa $m^{1/2}$ measured for the pure $Li_6PS_5Cl$.

### 5.4.3 Effect on ionic conductivity

Although the inclusion of CSZ particles can have a positive impact on the mechanical properties of $Li_6PS_5Cl$ electrolyte, since they do not contribute to the transportation of $Li^+$, higher volume fractions will detrimentally impact the total ionic conductivity of the composite

materials. Through the use of physical vapour deposition (PVD), Ni metal layers of several hundreds of nm in thickness are deposited through a mask onto the composite electrolyte's surface. These layers act as a blocking electrode for potentiostatic electrochemical impedance spectroscopy (PEIS), allowing the transport of $Li^+$ through the composite materials to be isolated in the measurement. The Nyquist plots produced by PEIS on each of the composite materials are shown in Figure 5.9. The partial semi-circular shape produced at high frequencies corresponds to the bulk crystal and grain boundary conduction through the composite electrolytes, and the sharp tail at low frequencies corresponds to the eventual convergence to ideal capacitive behaviour due to the use of blocking electrodes.

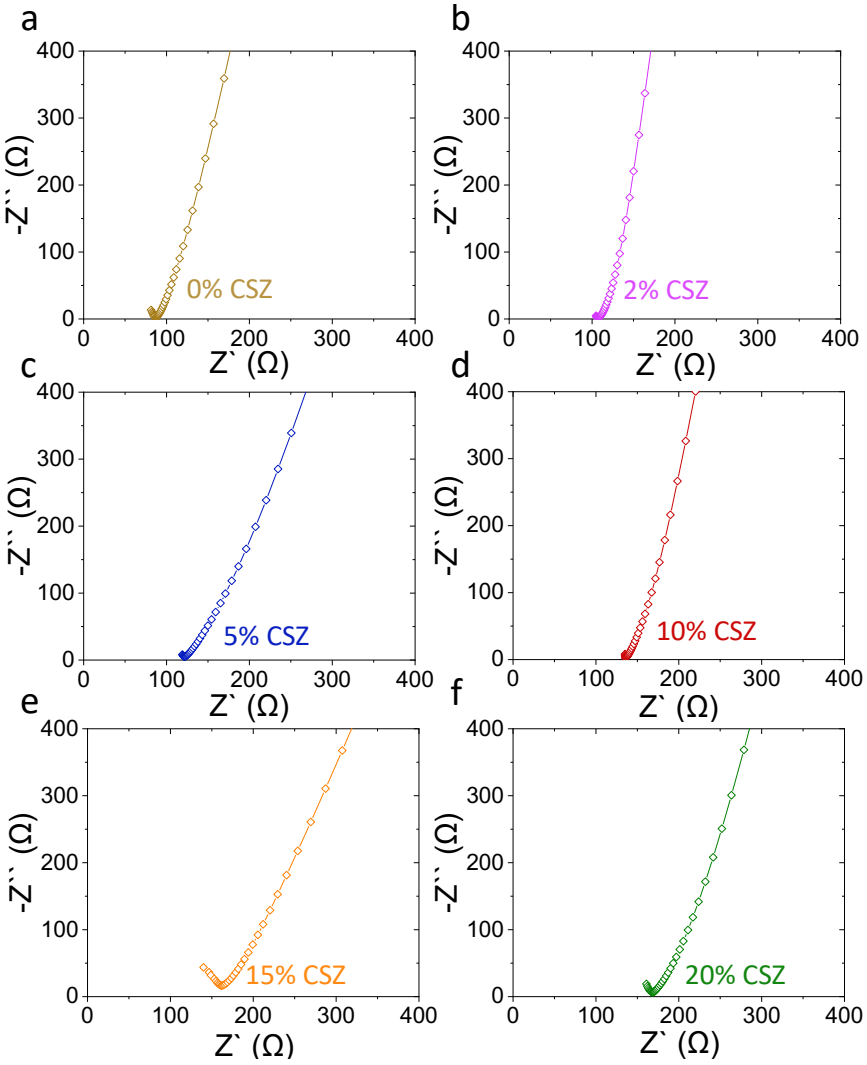



**Figure 5.9**: Nyquist plots from PEIS of CSZ-$Li_6PS_5Cl$ composites with 4.5mm blocking electrodes for **a** pure $Li_6PS_5Cl$, **b** 2% CSZ, **c** 5% CSZ, **d** 10% CSZ, **e** 15% CSZ, **f** 20% CSZ.

High ionic conductivities are needed in electrolyte materials to minimise the internal resistance of the cell, which would ultimately avoid unnecessarily limiting the utilised capacity during cycling. Liquid electrolytes have $Li^+$ conductivities of the order $10^{-3}$ S $cm^{-1}$, with typical Li-ion separator thicknesses ranging from 20-30 μm[76,357]. If solid electrolyte separator layers can be manufactured at similar thicknesses, a similar order of magnitude in ionic conductivity would be seen as acceptable[30]. By fitting an equivalent circuit model to the PEIS data shown in Figure 5.9, the bulk/grain boundary conductivity for each of the composite materials can be determined, see Figure 5.10.

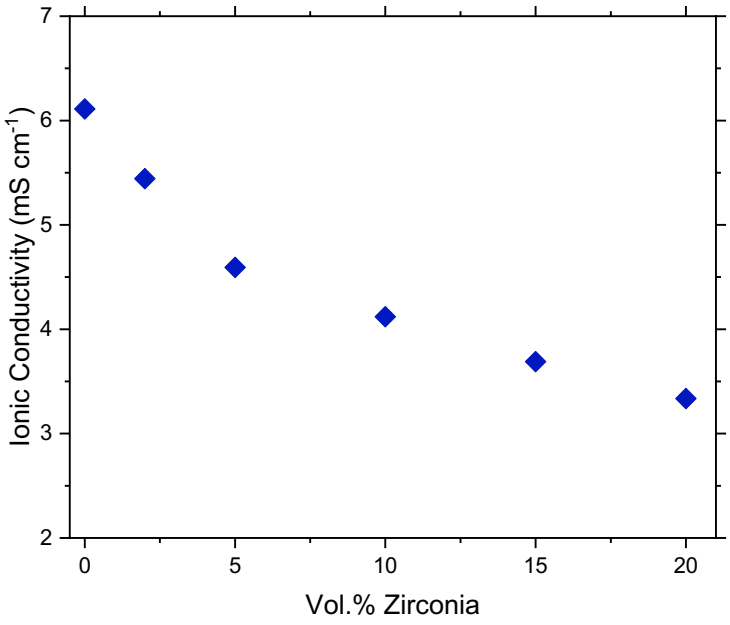



**Figure 5.10**: Trend in ionic conductivity with increasing 12 mol% $CeO_2$-$ZrO_2$ (CSZ) in CSZ-$Li_6PS_5Cl$ composites.

As a result of the addition of CSZ particles, the measured ionic conductivity decreases, almost halving upon the addition of 20 vol.%. The ionic conductivity of the pure $Li_6PS_5Cl$ electrolyte was measured as 6.1 mS $cm^{-1}$ and this fell to 3.2 mS $cm^{-1}$ upon the addition of 20 vol.% CSZ. The high densities achieved through the field assisted sintering of $Li_6PS_5Cl$ mean that its conductivity sits comfortably within the needed order of magnitude[18,30,77]. As a result, despite the detrimental effects of adding CSZ, the drop in conductivity is theoretically acceptable, at least up to 20 vol.%.

### 5.4.4 Effect on Li dendrite propagation

As described in Chapter 3, dendrite cracks initiate as a result of Li plating pressurising subsurface porosity within the solid electrolyte. The then initiated transverse cracks propagate across the entire electrolyte, allowing Li metal to plate through and reach the counter electrode, causing a short circuit. Using *operando* XCT imaging, it was determined that dendrite cracks propagate whilst only partially filled with Li metal, driven by a wedge-opening mechanism as Li plates at the inner surfaces of the crack. Through a basic model of the process, the magnitude of the total force applied on the inner walls during the wedge-opening was shown to be highly dependent on the amount of Li filling (e.g., the length of the Li dendrite within the crack). By evaluating how the strain energy release rate of the crack develops during the pressurisation of the inner walls during dendrite lengthening, a dendrite length criterion for crack propagation could be identified at the point at which the strain energy release rate reaches a critical value determined by the fracture toughness of the electrolyte. In short, for a given current density and stack pressure, the amount of crack filling necessary to propagate a crack can be directly related to the toughness of the electrolyte. Figure 5.11 shows the amount of crack filling (dendrite length) needed to propagate a 200 μm long, 2 μm wide dendrite crack at an applied current density of 10 mA $cm^{-2}$ and a stack pressure of 7 MPa. If the electrolyte toughness is increased from 0.71 MPa $m^{1/2}$ to 1.16 MPa $m^{1/2}$, the Li dendrite must be over a third longer to propagate the dendrite crack. As a result, more capacity may be needed during plating to cause failure of the cell, i.e., the cell will take longer to fail.

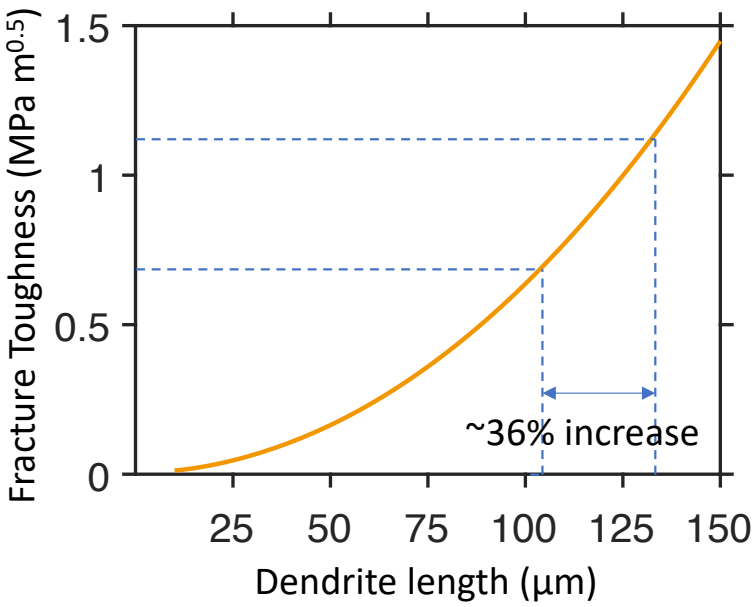



**Figure 5.11**: Dendrite length required to extend a 200 µm long, 2µm wide crack for an applied current density of 10 mA $cm^{-2}$ and a stack pressure of 7 MPa, calculated using the dendrite crack propagation model detailed in Chapter 3. For the increase in fracture toughness seen in Figure 5.8, around a 36% increase in dendrite length is required to propagate the same dendrite crack further.

To investigate the effect of CSZ on dendrite propagation, three-electrode cells were assembled with Li electrodes, and plated at 10 mA $cm^{-2}$ under a stack pressure of 7 MPa. The areal capacity required to induce a short-circuit was compared between cells made with pure $Li_6PS_5Cl$ electrolytes and 20 vol.% CSZ-$Li_6PS_5Cl$ electrolytes. By performing single plating experiments any Li stripping effects are completely removed. A similar protocol was used in Chapter 3 to determine the effect of stack pressure on dendrite propagation. Figure 5.12 presents typical voltage profiles for the single plating experiment, the areal capacity at which short circuit occurs can be identified at the point at which the voltage of the cell falls to zero.

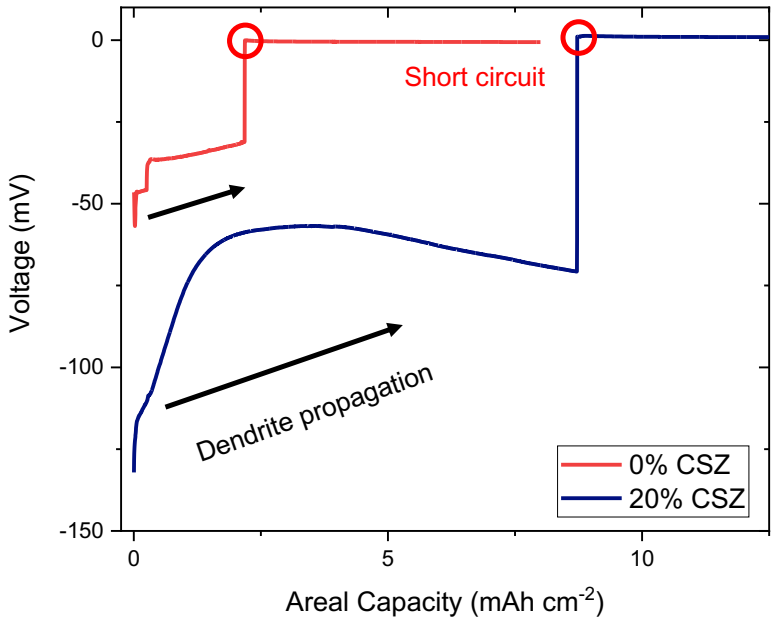



**Figure 5.12**: Voltage profiles for 3-electrode single plating experiments under 10 mA $cm^{-2}$ under a stack pressure of 7 MPa for pure $Li_6PS_5Cl$ (red) and 20 vol.% CSZ-$Li_6PS_5Cl$ (blue) electrolytes. Cells were run until complete short-circuit (indicated with red circles).

When a ceramic fractures as a result of pre-existing defects, as is the case in Li dendrite failure, the process is inherently statistical and this will be somewhat reflected in the plated capacity needed to cause the short-circuit of a given cell. Consequently, a number of single plating experiments are necessary in order to assess a distribution. An identical single plating protocol was applied to five cells composed of pure $Li_6PS_5Cl$ electrolytes and five cells composed of 20 vol.% CSZ-$Li_6PS_5Cl$ electrolytes. The areal capacity required to induce short circuit across the ten experiments is presented in Figure 5.13. The distribution of results indicates that the 20 vol.% CSZ-$Li_6PS_5Cl$ electrolytes fail only after greater plating capacities are applied to the cell. On average, pure $Li_6PS_5Cl$ electrolytes sustained 3.8 mAh $cm^{-2}$ before short circuit whereas 20 vol.% CSZ-$Li_6PS_5Cl$ composite electrolytes sustained 7.2 mAh $cm^{-2}$; almost twice as much capacity.

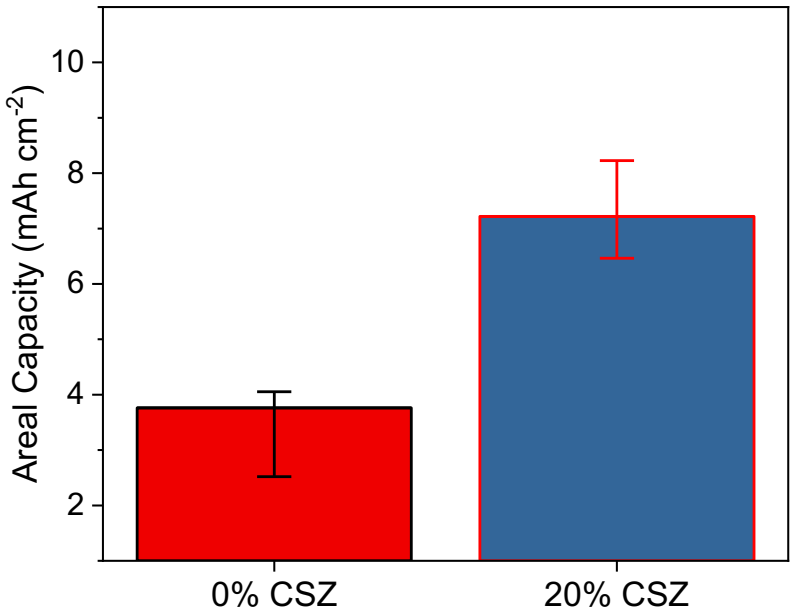



**Figure 5.13**: Average areal capacity required to short circuit three-electrode cells subject to 10 mA $cm^{-2}$ under a stack pressure of 7 MPa for pure $Li_6PS_5Cl$ (red) 20 vol.% CSZ-$Li_6PS_5Cl$ (blue) electrolytes. Error bars indicate the standard deviation of the repeat experiments.

Although effective in demonstrating the feasibility of a wedge-opening crack mechanism based on the hydrodynamic pressures resulting from lithium plating, the propagation model presented in Chapter 3 is a simplification of the true situation within the electrolyte. In reality, specific crack geometries are unpredictable and their morphological development during their propagation can be even more so. Therefore, it is not possible to use the proposed crack propagation model to predict the total areal capacity required to short-circuit an electrolyte.

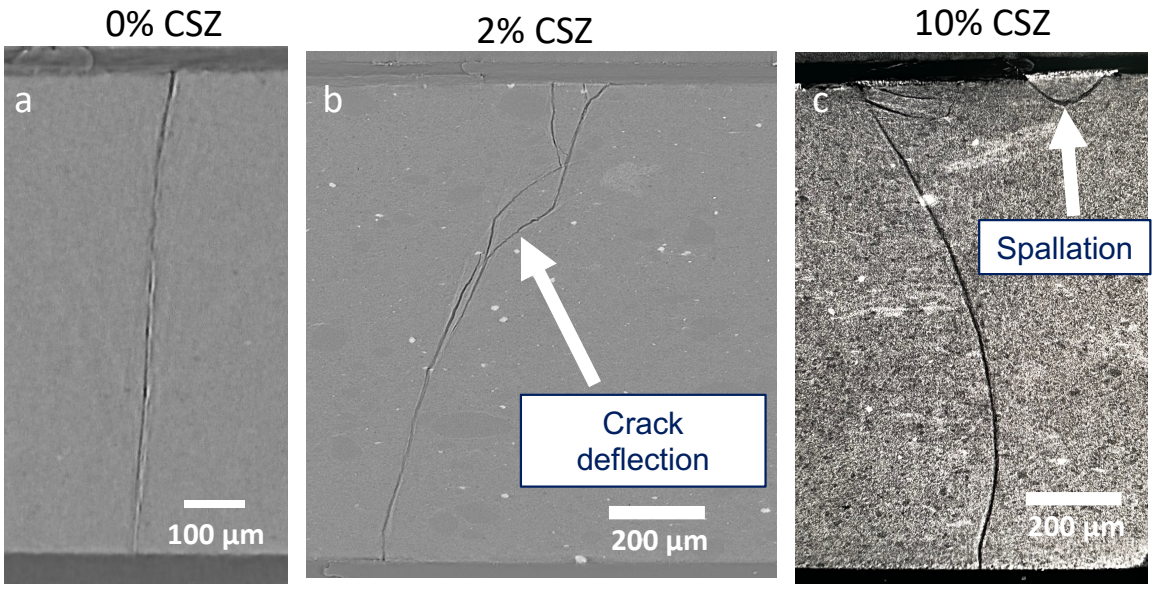



**Figure 5.14**: *In-situ* X-ray computed tomography virtual cross-sectional image slices reveal the morphonology of dendrite cracks for **a** pure $Li_6PS_5Cl$, **b** 2 vol.% CSZ-$Li_6PS_5Cl$ and **c** 10 vol.% CSZ-$Li_6PS_5Cl$ electrolytes.

Through the use of *in-situ* X-ray computed tomography, we can see that the effect of CSZ content on dendrite crack morphology is significant. As discussed in Chapter 4, the crack geometries observed within pure $Li_6PS_5Cl$ electrolytes densified using field assisted sintering are straight and occur without the formation of spallations, see Figure 5.14a. Even adding only a small percentage of CSZ is enough to cause a noticeable deflection of the transverse dendrite crack, Figure 5.14b. Upon the addition of 10 vol.% CSZ, a return of spallation features is seen in Figure 5.14c. This observation may provide further insights into the origin of spallation cracking during Li dendrite failure of solid electrolytes. Unfortunately, due to the high X-ray attenuation of zirconium and cerium the in-situ XCT imaging of dendrite cracks in 20 vol.% CSZ-$Li_6PS_5Cl$ electrolytes was not possible. Overall, the XCT results collected across a range of CSZ contents indicate that the addition of CSZ nanoparticles significantly alters Li dendrite crack morphologies, resulting in a return of spallation cracks and more convoluted transverse cracks. Both of these can be expected to prolong the short circuit of the electrolyte. As a result, a combination of raising the inherent toughness, $K_{1C}$, of the material and the significant effects on crack morphologies can explain the rise in areal capacity needed to

propagate dendrite cracks and cause short circuit with the addition of transformation toughening CSZ nanoparticles.

### 5.4.5 Feasibility of dendrite crack stabilisation

As is shown in Figure 5.8, the addition of metastable zirconia particles into $Li_6PS_5Cl$ electrolytes brings an increase in the measured fracture toughness. Whilst this was seen to affect the propagation of dendrite cracks, no observed increase in the current densities required to initiate dendrites was observed. Any associated improvement in the local mechanical properties at the Li/SE interface was likely mitigated by worsened current focusing caused by the addition of the insulating secondary phase.

To constitute a meaningful improvement in performance, dendrite cracks must be completely stabilised rather than temporarily delayed during propagation. During the experiments in Figure 5.13, all cells eventually short circuited, implying that any stabilisation of dendrite cracks during propagation was ultimately temporary. The dynamic relationship between fracture toughness and crack extension is characterised by the crack growth resistance curve (R-curve)[350]. Rising R-curves mean that the extension of a crack can potentially be stabilised to such an extent that it can no longer propagate. The results shown in Figure 5.13, imply that any rising R-curve behaviour caused by the inclusion of zirconia is ultimately not steep enough to stabilise dendrite cracks completely. Given that separators will ultimately have to be thinner than 50 μm[18,30], the feasibility of stabilising dendrite cracks as a practical solution to the dendrite problem should be re-evaluated.

## 5.5 Conclusions

This chapter has explored the effect of adding metastable $CeO_2$-$ZrO_2$ (CSZ) nanoparticles into $Li_6PS_5Cl$ solid electrolytes. Guided by iterative XRD and SEM characterisation, a mixing procedure to distribute the CSZ particles evenly throughout a dense $Li_6PS_5Cl$ microstructure was optimised. Using an *in-situ* indenter within a scanning electron microscope, the

mechanical measurement of the composites is enabled without the need for any mineral oil or other techniques that can affect the mechanical response. Fracture toughnesses determined through indentation indicate an almost doubling in the toughness of $Li_6PS_5Cl$ solid electrolytes through the addition of 20 vol.% CSZ. The zirconia particles do not contribute to the transport of $Li^+$ and so limit the active volume of the electrolyte, increasing the tortuosity of ionic pathways. As a result, the conductivity of the electrolyte is reduced upon the addition of CSZ, with 20 vol.% CSZ enough to almost half the conductivity. Despite this, due to the high conductivity of pure $Li_6PS_5Cl$ solid electrolytes densified by field assisted sintering, the conductivity of 20 vol.% CSZ-$Li_6PS_5Cl$ composites may still be seen as acceptable. In Chapter 3, the propagation of dendrite cracks was shown to depend on the fracture toughness of the electrolyte. 3-electrode single plating experiments demonstrate an increase in plated capacity needed to propagate dendrite cracks and cause short circuit with the addition of transformation toughening CSZ nanoparticles. Using *in-situ* XCT imaging, a combination of an increase in inherent toughness, $K_{1C}$, and significant effects on crack morphologies is proposed to explain the greater capacities required to fail cells. Whilst the improvement in fracture toughness can act to benefit future manufacturing and handleability, the use of CSZ nanoparticles does not appear a practical route to solving the SSB dendrite problem, merely delaying rather than preventing failure. Ultimately, the eventual short-circuit of toughened CSZ-$Li_6PS_5Cl$ composites means that any anticipated R-curve toughening was not sufficient to stabilise the dendrite crack during its propagation, even in thick electrolytes. Whilst interesting from a mechanistic perspective, by only delaying an inevitable cell failure once dendrites have initiated, the added resistance to dendrite propagation does not constitute a meaningful improvement in performance. Given that separators will ultimately have to be thinner than 50 μm, future work should re-consider pursuing the stabilisation of propagating dendrite cracks as a feasible route to overcoming the SSB dendrite problem.

# Chapter 6: Conclusions and outlook

Following the discovery of fast $Li^+$ conducting ceramics, significant efforts have been placed into realising high-energy lithium metal anode solid-state batteries (Li-SSBs). Yet despite considerable research, the charging times of these cells have been slower than what is needed for applications such as electric vehicles due to the formation of Li dendrites.

In Chapter 3 of this thesis, the mechanistic underpinnings of Li dendrite failure have been investigated in argyrodite-type $Li_6PS_5Cl$ solid electrolytes. *Operando* XCT observations indicated that the processes governing the initiation of dendrite cracks is distinct from the mechanism by which the cracks later propagate. Dendrite cracks are suggested to initiate due to excessive Li plating within subsurface pores, which are filled with Li due to their connection to the surface via pre-existing microcracks. In contrast, dendrite cracks are proposed to propagate whilst only partially filled with Li, through a wedge-opening-type mechanism.

In Chapter 4, the effect of microstructure on dendrite crack initiation is explored within $Li_6PS_5Cl$ electrolytes. Using field-assisted sintering, a range of different $Li_6PS_5Cl$ microstructures were produced of varying overall density (porosity), between which a considerable variation in the size and number of pre-existing microcracks and pores was shown to exist. During the densification of $Li_6PS_5Cl$, microcracks are shown to narrow and shorten whilst the size and number of pores is shown to be reduced (hence their proximity from one another increases). Consequently, not all the changes in the microstructure which occur during densification necessarily act to increase critical currents. In $Li_6PS_5Cl$, the reduction in pore size and crack length is predicted to outweigh crack narrowing and increases in separation, giving an overall increase in critical current density. Accordingly, improvements in critical plating currents are measured experimentally for highly dense $Li_6PS_5Cl$ electrolytes using a combination of imaging and electrochemical cell testing.

Chapter 5 considered the effects of incorporating metastabilised zirconia nanoparticles within the microstructures of densified $Li_6PS_5Cl$ electrolytes. Even though their addition lowers the

overall ionic conductivity, materials containing zirconia particles demonstrated considerably improved fracture toughnesses. Whilst the use of zirconia nanoparticles alone does not appear to be a practical route to solving the SSB dendrite problem, merely delaying rather than preventing failure, their toughening effects could still potentially benefit future manufacturing and handleability.

If Li-SSBs are to be used to power electric vehicles, industry charging standards of at least 1 C will need to be met[54,140]. Additionally, to meet the ~1,000 Wh/l and ~400 Wh/kg required to justify a transition to a non-Li-ion system, Li-SSB cells may require cathode loadings greater than 4 mAh/cm$^2$.[358] Consequently, charging currents of at least 5 mA cm$^{-2}$ may be considered as necessary for practical EV application. In Chapter 4, highly dense $Li_6PS_5Cl$ electrolytes manufactured using field-assisted sintering enabled sustainable plating currents as high as 9 mA cm$^{-2}$. The results validate that in some solid electrolyte systems, the size and number of microstructural defects can be controlled such to enable practical charging currents across entire electrode interfaces. Still, future work is needed to investigate whether similar $Li_6PS_5Cl$ microstructures can be achieved in the scalable production of thin film electrolytes (< 50 μm thickness).

Whilst the work in this thesis has focused on argyrodite-type sulphide electrolytes, further work is needed to unify the understanding of dendrites in these materials with other classes of ceramic electrolytes. Numerous studies have been conducted on LLZO-type oxide electrolytes in which simply densifying the electrolyte has not enabled significantly higher plating currents[155,186,270]. In the light of the new insights made in this thesis regarding the effect of microstructure on dendrites in $Li_6PS_5Cl$ electrolytes, further comparative work is necessary to expand a general understanding which applies to all ceramic electrolytes.

Additionally, future ambitions regarding $Li_6PS_5Cl$ electrolytes will still need to marry any achievable high plating currents with practically relevant stripping currents. Throughout this thesis, both impractically low stripping currents and impractically high stack pressures (>2 MPa is impractical for large format cells[54]) are used to minimise any interfacial voiding in cycled cells. Future work should assess the influence of densification on Li stripping to assess

whether further interfacial patterning or thin interlayers would still be needed for a commercial application.

# References


1. Tarascon, J.-M. & Armand, M. Issues and challenges facing rechargeable lithium batteries. *Nature* **414**, 359–367 (2001).
2. Goodenough, J. B. & Park, K.-S. The Li-Ion Rechargeable Battery: A Perspective. *J. Am. Chem. Soc.* **135**, 1167–1176 (2013).
3. Larcher, D. & Tarascon, J.-M. Towards greener and more sustainable batteries for electrical energy storage. *Nat. Chem.* **7**, 19–29 (2015).
4. Levin, T. *et al.* Energy storage solutions to decarbonize electricity through enhanced capacity expansion modelling. *Nat. Energy* **8**, 1199–1208 (2023).
5. Li, M., Lu, J., Chen, Z. & Amine, K. 30 Years of Lithium-Ion Batteries. *Adv. Mater.* **30**, 1800561 (2018).
6. Crabtree, G. The coming electric vehicle transformation. *Science* **366**, 422–424 (2019).
7. Tian, Y. *et al.* Promises and Challenges of Next-Generation "Beyond Li-ion" Batteries for Electric Vehicles and Grid Decarbonization. *Chem. Rev.* **121**, 1623–1669 (2021).
8. Albertus, P. *et al.* Challenges for and Pathways toward Li-Metal-Based All-Solid-State Batteries. *ACS Energy Lett.* **6**, 1399–1404 (2021).
9. Winter, M. & Brodd, R.J., What Are Batteries, Fuel Cells, and Supercapacitors? Chemical Reviews 104 (10), 4245-4270 (2004).
10. Huggins, R. A. Advanced Batteries: Materials Science Aspects 474 (Springer, 2008)
11. Armand, M. & Tarascon, J.-M. Building better batteries. *Nature* **451**, 652–657 (2008).
12. Mizushima, K., Jones, P. C., Wiseman, P. J. & Goodenough, J. B. LixCoO2 (0<x<-1): A new cathode material for batteries of high energy density. *Mater. Res. Bull.* **15**, 783–789 (1980).
13. Mohri, M. *et al.* Rechargeable lithium battery based on pyrolytic carbon as a negative electrode. *J. Power Sources* **26**, 545–551 (1989).
14. Goodenough, J. B. How we made the Li-ion rechargeable battery. *Nat. Electron.* **1**, 204–204 (2018).
15. Korthauer, R., *Handbuch Lithium-Ionen-Batterien*. (Springer, Berlin, Heidelberg, 2013). doi:10.1007/978-3-642-30653-2.
16. Trends in batteries – Global EV Outlook 2023 – Analysis. *IEA* https://www.iea.org/reports/global-ev-outlook-2023/trends-in-batteries.
17. Broussely, M. & Archdale, G. Li-ion batteries and portable power source prospects for the next 5–10 years. *J. Power Sources* **136**, 386–394 (2004).
18. Janek, J. & Zeier, W. G. Challenges in speeding up solid-state battery development. *Nat. Energy* **8**, 230–240 (2023).
19. Edström, K., Herstedt, M. & Abraham, D. P. A new look at the solid electrolyte interphase on graphite anodes in Li-ion batteries. *J. Power Sources* **153**, 380–384 (2006).
20. Verma, P., Maire, P. & Novák, P. A review of the features and analyses of the solid electrolyte interphase in Li-ion batteries. *Electrochimica Acta* **55**, 6332–6341 (2010).

21. Broussely, M. *et al.* Main aging mechanisms in Li ion batteries. *J. Power Sources* **146**, 90–96 (2005).
22. Booth, S. G. *et al.* Perspectives for next generation lithium-ion battery cathode materials. *APL Mater.* **9**, 109201 (2021).
23. Li, T. *et al.* Degradation Mechanisms and Mitigation Strategies of Nickel-Rich NMC-Based Lithium-Ion Batteries. *Electrochem. Energy Rev.* **3**, 43–80 (2020).
24. Ruff, Z., Xu, C. & Grey, C. P. Transition Metal Dissolution and Degradation in NMC811-Graphite Electrochemical Cells. *J. Electrochem. Soc.* **168**, 060518 (2021).
25. Shen, C. *et al.* Direct Observation of the Growth of Lithium Dendrites on Graphite Anodes by Operando EC-AFM. *Small Methods* **2**, 1700298 (2018).
26. Liu, X. *et al.* In situ observation of thermal-driven degradation and safety concerns of lithiated graphite anode. *Nat. Commun.* **12**, 4235 (2021).
27. Wise, M. S. *et al.* Calculating Heat Release Rates from Lithium-Ion Battery Fires: A Methodology Using Digital Imaging. *Fire Technol.* **59**, 3565–3587 (2023).
28. Finegan, D. P. *et al.* Tracking Internal Temperature and Structural Dynamics during Nail Penetration of Lithium-Ion Cells. *J. Electrochem. Soc.* **164**, A3285 (2017).
29. Hynynen, J., Willstrand, O., Blomqvist, P. & Andersson, P. Analysis of combustion gases from large-scale electric vehicle fire tests. *Fire Saf. J.* **139**, 103829 (2023).
30. Janek, J. & Zeier, W. G. A solid future for battery development. *Nat. Energy* **1**, 1–4 (2016).
31. Tarascon, J.-M. Is lithium the new gold? *Nat. Chem.* **2**, 510–510 (2010).
32. Brandt, K. Historical development of secondary lithium batteries. *Solid State Ion.* **69**, 173–183 (1994).
33. Jasinski, R. High-energy batteries. [Book with 377 publications references and 427 patent references]. (1967).
34. Kozawa, A. Manganese dioxide symposium : vol.1, Cleveland, 1975. *No Title*.
35. Schneider, A. A. & Moser, J. R. Primary cells and iodine containing cathodes therefor. (1972).
36. Xu, W. *et al.* Lithium metal anodes for rechargeable batteries. *Energy Environ. Sci.* **7**, 513–537 (2014).
37. Lin, D., Liu, Y. & Cui, Y. Reviving the lithium metal anode for high-energy batteries. *Nat. Nanotechnol.* **12**, 194–206 (2017).
38. Aurbach, D. Review of selected electrode–solution interactions which determine the performance of Li and Li ion batteries. *J. Power Sources* **89**, 206–218 (2000).
39. Cheng, X.-B., Zhang, R., Zhao, C.-Z. & Zhang, Q. Toward Safe Lithium Metal Anode in Rechargeable Batteries: A Review. *Chem. Rev.* **117**, 10403–10473 (2017).
40. Laman, F. C. & Brandt, K. Effect of discharge current on cycle life of a rechargeable lithium battery. *J. Power Sources* **24**, 195–206 (1988).
41. Whittingham, M. S. Electrical Energy Storage and Intercalation Chemistry. *Science* **192**, 1126–1127 (1976).
42. Blomgren, G. E. The Development and Future of Lithium Ion Batteries. *J. Electrochem. Soc.* **164**, A5019 (2016).

43. Li, W. *et al.* The synergetic effect of lithium polysulfide and lithium nitrate to prevent lithium dendrite growth. *Nat. Commun.* **6**, 7436 (2015).
44. Gong, C. *et al.* Revealing the Role of Fluoride-Rich Battery Electrode Interphases by Operando Transmission Electron Microscopy. *Adv. Energy Mater.* **11**, 2003118 (2021).
45. Camacho-Forero, L. E., Smith, T. W. & Balbuena, P. B. Effects of High and Low Salt Concentration in Electrolytes at Lithium–Metal Anode Surfaces. *J. Phys. Chem. C* **121**, 182–194 (2017).
46. Jeong, S.-K. *et al.* Suppression of dendritic lithium formation by using concentrated electrolyte solutions. *Electrochem. Commun.* **10**, 635–638 (2008).
47. Banerjee, A., Wang, X., Fang, C., Wu, E. A. & Meng, Y. S. Interfaces and Interphases in All-Solid-State Batteries with Inorganic Solid Electrolytes. *Chem. Rev.* **120**, 6878–6933 (2020).
48. Xiao, Y. *et al.* Understanding interface stability in solid-state batteries. *Nat. Rev. Mater.* **5**, 105–126 (2020).
49. Famprikis, T., Canepa, P., Dawson, J. A., Islam, M. S. & Masquelier, C. Fundamentals of inorganic solid-state electrolytes for batteries. *Nat. Mater.* **18**, 1278–1291 (2019).
50. Pervez, S. A., Cambaz, M. A., Thangadurai, V. & Fichtner, M. Interface in Solid-State Lithium Battery: Challenges, Progress, and Outlook. *ACS Appl. Mater. Interfaces* **11**, 22029–22050 (2019).
51. Krauskopf, T., Richter, F. H., Zeier, W. G. & Janek, J. Physicochemical Concepts of the Lithium Metal Anode in Solid-State Batteries. *Chem. Rev.* **120**, 7745–7794 (2020).
52. Ye, L. & Li, X. A dynamic stability design strategy for lithium metal solid state batteries. *Nature* **593**, 218–222 (2021).
53. Balaish, M. *et al.* Processing thin but robust electrolytes for solid-state batteries. *Nat. Energy* **6**, 227–239 (2021).
54. Wang, M. J., Kazyak, E., Dasgupta, N. P. & Sakamoto, J. Transitioning solid-state batteries from lab to market: Linking electro-chemo-mechanics with practical considerations. *Joule* **5**, 1371–1390 (2021).
55. Minnmann, P., Quillman, L., Burkhardt, S., Richter, F. H. & Janek, J. Editors' Choice—Quantifying the Impact of Charge Transport Bottlenecks in Composite Cathodes of All-Solid-State Batteries. *J. Electrochem. Soc.* **168**, 040537 (2021).
56. Liu, B. *et al.* The effect of volume change and stack pressure on solid-state battery cathodes. *SusMat* **3**, 721–728 (2023).
57. Gao, X. *et al.* Solid-state lithium battery cathodes operating at low pressures. *Joule* **6**, 636–646 (2022).
58. Experimental researches in electricity. *Library of Congress, Washington, D.C. 20540 USA* https://www.loc.gov/item/03006832/.
59. Nernst, W. *Z Elektrochem* **6**, (1900).
60. Alkire, R.C., Kolb, D.M., Advances in Electrochemical Science and Engineering, Volume 8 (2006).
61. Kummer, J. T. & Weber, N. Thermo-electric generator. (1969).

62. Goodenough, J. B., Hong, H. Y.-P. & Kafalas, J. A. Fast Na+-ion transport in skeleton structures. *Mater. Res. Bull.* **11**, 203–220 (1976).
63. Bruce, P.G., *Solid State Electrochemistry*. (Cambridge University Press, Cambridge, 1994). doi:10.1017/CBO9780511524790.
64. Owens, B. B. Solid state electrolytes: overview of materials and applications during the last third of the Twentieth Century. *J. Power Sources* **90**, 2–8 (2000).
65. Manthiram, A. & Yu, X. Ambient Temperature Sodium–Sulfur Batteries. *Small* **11**, 2108–2114 (2015).
66. Bates, J. B., Dudney, N. J., Neudecker, B., Ueda, A. & Evans, C. D. Thin-film lithium and lithium-ion batteries. *Solid State Ion.* **135**, 33–45 (2000).
67. Trask, J. *et al.* Optimization of 10-μm, sputtered, LiCoO2 cathodes to enable higher energy density solid state batteries. *J. Power Sources* **350**, 56–64 (2017).
68. Chen, R., Li, Q., Yu, X., Chen, L. & Li, H. Approaching Practically Accessible Solid-State Batteries: Stability Issues Related to Solid Electrolytes and Interfaces. *Chem. Rev.* **120**, 6820–6877 (2020).
69. Nie, X., Hu, J. & Li, C. Halide-based solid electrolytes: The history, progress, and challenges. *Interdiscip. Mater.* **2**, 365–389 (2023).
70. Mizuno, F., Hayashi, A., Tadanaga, K. & Tatsumisago, M. New, Highly Ion-Conductive Crystals Precipitated from Li2S–P2S5 Glasses. *Adv. Mater.* **17**, 918–921 (2005).
71. Kamaya, N. *et al.* A lithium superionic conductor. *Nat. Mater.* **10**, 682–686 (2011).
72. Kato, Y. *et al.* High-power all-solid-state batteries using sulfide superionic conductors. *Nat. Energy* **1**, 1–7 (2016).
73. Murugan, R., Thangadurai, V. & Weppner, W. Fast Lithium Ion Conduction in Garnet-Type Li7La3Zr2O12. *Angew. Chem. Int. Ed.* **46**, 7778–7781 (2007).
74. Thompson, T. *et al.* A Tale of Two Sites: On Defining the Carrier Concentration in Garnet-Based Ionic Conductors for Advanced Li Batteries. *Adv. Energy Mater.* **5**, 1500096 (2015).
75. Asano, T. *et al.* Solid Halide Electrolytes with High Lithium-Ion Conductivity for Application in 4 V Class Bulk-Type All-Solid-State Batteries. *Adv. Mater.* **30**, 1803075 (2018).
76. Dahbi, M., Ghamouss, F., Tran-Van, F., Lemordant, D. & Anouti, M. Comparative study of EC/DMC LiTFSI and LiPF6 electrolytes for electrochemical storage. *J. Power Sources* **196**, 9743–9750 (2011).
77. Ohno, S. *et al.* Materials design of ionic conductors for solid state batteries. *Prog. Energy* **2**, 022001 (2020).
78. Bielefeld, A., Weber, D. A. & Janek, J. Modeling Effective Ionic Conductivity and Binder Influence in Composite Cathodes for All-Solid-State Batteries. *ACS Appl. Mater. Interfaces* **12**, 12821–12833 (2020).
79. Han, F. *et al.* High electronic conductivity as the origin of lithium dendrite formation within solid electrolytes. *Nat. Energy* **4**, 187–196 (2019).

80. Zhang, W. *et al.* Interfacial Processes and Influence of Composite Cathode Microstructure Controlling the Performance of All-Solid-State Lithium Batteries. *ACS Appl. Mater. Interfaces* **9**, 17835–17845 (2017).
81. IEC 62660-2:2018 RLV | IEC Webstore. https://webstore.iec.ch/publication/64367.
82. Singh, D. K. *et al.* Li6PS5Cl microstructure and influence on dendrite growth in solid-state batteries with lithium metal anode. *Cell Rep. Phys. Sci.* **3**, 101043 (2022).
83. Ning, Z. *et al.* Visualizing plating-induced cracking in lithium-anode solid-electrolyte cells. *Nat. Mater.* **20**, 1121–1129 (2021).
84. Wenzel, S., Leichtweiss, T., Krüger, D., Sann, J. & Janek, J. Interphase formation on lithium solid electrolytes—An in situ approach to study interfacial reactions by photoelectron spectroscopy. *Solid State Ion.* **278**, 98–105 (2015).
85. He, Y., Lu, C., Liu, S., Zheng, W. & Luo, J. Interfacial Incompatibility and Internal Stresses in All-Solid-State Lithium Ion Batteries. *Adv. Energy Mater.* **9**, 1901810 (2019).
86. Cui, C. *et al.* In Situ Visualizing the Interfacial Failure Mechanism and Modification Promotion of LAGP Solid Electrolyte toward Li Metal Anode. *Adv. Energy Mater.* **12**, 2202250 (2022).
87. Connell, J. G. *et al.* Kinetic versus Thermodynamic Stability of LLZO in Contact with Lithium Metal. *Chem. Mater.* **32**, 10207–10215 (2020).
88. Sharafi, A. *et al.* Impact of air exposure and surface chemistry on Li–Li 7 La 3 Zr 2 O 12 interfacial resistance. *J. Mater. Chem. A* **5**, 13475–13487 (2017).
89. Brugge, R. H. *et al.* Garnet Electrolytes for Solid State Batteries: Visualization of Moisture-Induced Chemical Degradation and Revealing Its Impact on the Li-Ion Dynamics. *Chem. Mater.* **30**, 3704–3713 (2018).
90. H. Brugge, R. *et al.* The origin of chemical inhomogeneity in garnet electrolytes and its impact on the electrochemical performance. *J. Mater. Chem. A* **8**, 14265–14276 (2020).
91. Yu, H.-C. *et al.* Deformation and stresses in solid-state composite battery cathodes. *J. Power Sources* **440**, 227116 (2019).
92. Ren, Y. *et al.* Oxide-Based Solid-State Batteries: A Perspective on Composite Cathode Architecture. *Adv. Energy Mater.* **13**, 2201939 (2023).
93. Weiss, M. *et al.* From Liquid- to Solid-State Batteries: Ion Transfer Kinetics of Heteroionic Interfaces. *Electrochem. Energy Rev.* **3**, 221–238 (2020).
94. Schmaltz, T. *et al.* A Roadmap for Solid-State Batteries. *Adv. Energy Mater.* **13**, 2301886 (2023).
95. Wang, S. *et al.* Lithium Chlorides and Bromides as Promising Solid-State Chemistries for Fast Ion Conductors with Good Electrochemical Stability. *Angew. Chem. Int. Ed.* **58**, 8039–8043 (2019).
96. Li, X. *et al.* Water-Mediated Synthesis of a Superionic Halide Solid Electrolyte. *Angew. Chem.* **131**, 16579–16584 (2019).
97. Zhang, H., Zeng, Z., Shi, X., Wang, C.-H. & Du, Y. Doping engineering of scandium-based solid-state electrolytes toward superior ionic conductivity. *EcoMat* **5**, e12315 (2023).
98. Bahmani, F., Rodmyre, C. & Smirnova, A. Li3InCl6 Electrolyte with High Voltage Compatibility for All-Solid-State Batteries. *ECS Meet. Abstr.* **MA2023-01**, 1017 (2023).

99. Zhou, L. *et al.* High areal capacity, long cycle life 4 V ceramic all-solid-state Li-ion batteries enabled by chloride solid electrolytes. *Nat. Energy* **7**, 83–93 (2022).
100. Li, X. *et al.* Origin of Superionic Li3Y1–xInxCl6 Halide Solid Electrolytes with High Humidity Tolerance. *Nano Lett.* **20**, 4384–4392 (2020).
101. Riegger, L. M., Schlem, R., Sann, J., Zeier, W. G. & Janek, J. Lithium-Metal Anode Instability of the Superionic Halide Solid Electrolytes and the Implications for Solid-State Batteries. *Angew. Chem. Int. Ed.* **60**, 6718–6723 (2021).
102. Yin, Y.-C. *et al.* A LaCl3-based lithium superionic conductor compatible with lithium metal. *Nature* **616**, 77–83 (2023).
103. Ong, S. P. *et al.* Phase stability, electrochemical stability and ionic conductivity of the Li10±1MP2X12 (M = Ge, Si, Sn, Al or P, and X = O, S or Se) family of superionic conductors. *Energy Environ. Sci.* **6**, 148–156 (2012).
104. Deiseroth, H.-J. *et al.* Li6PS5X: A Class of Crystalline Li-Rich Solids With an Unusually High Li+ Mobility. *Angew. Chem. Int. Ed.* **47**, 755–758 (2008).
105. Sakuda, A., Hayashi, A. & Tatsumisago, M. Sulfide Solid Electrolyte with Favorable Mechanical Property for All-Solid-State Lithium Battery. *Sci. Rep.* **3**, 2261 (2013).
106. Culver, S. P., Koerver, R., Zeier, W. G. & Janek, J. On the Functionality of Coatings for Cathode Active Materials in Thiophosphate-Based All-Solid-State Batteries. *Adv. Energy Mater.* **9**, 1900626 (2019).
107. Wu, E. A. *et al.* A Facile, Dry-Processed Lithium Borate-Based Cathode Coating for Improved All-Solid-State Battery Performance. *J. Electrochem. Soc.* **167**, 130516 (2020).
108. Chen, Y.-T. *et al.* Investigating dry room compatibility of sulfide solid-state electrolytes for scalable manufacturing. *J. Mater. Chem. A* **10**, 7155–7164 (2022).
109. Miura, A. *et al.* Liquid-phase syntheses of sulfide electrolytes for all-solid-state lithium battery. *Nat. Rev. Chem.* **3**, 189–198 (2019).
110. Wenzel, S., Sedlmaier, S. J., Dietrich, C., Zeier, W. G. & Janek, J. Interfacial reactivity and interphase growth of argyrodite solid electrolytes at lithium metal electrodes. *Solid State Ion.* **318**, 102–112 (2018).
111. Lee, Y.-G. *et al.* High-energy long-cycling all-solid-state lithium metal batteries enabled by silver–carbon composite anodes. *Nat. Energy* **5**, 299–308 (2020).
112. Hahn, H., Schulze, H. & Sechser, L. Über einige ternäre Chalkogenide vom Argyrodit-Typ. *Naturwissenschaften* **52**, 451–451 (1965).
113. Deiseroth, H.-J. *et al.* Li7PS6 and Li6PS5X (X: Cl, Br, I): Possible Three-dimensional Diffusion Pathways for Lithium Ions and Temperature Dependence of the Ionic Conductivity by Impedance Measurements. *Z. Für Anorg. Allg. Chem.* **637**, 1287–1294 (2011).
114. Zhou, L., Minafra, N., Zeier, W. G. & Nazar, L. F. Innovative Approaches to Li-Argyrodite Solid Electrolytes for All-Solid-State Lithium Batteries. *Acc. Chem. Res.* **54**, 2717–2728 (2021).
115. Morgan, B. J. Mechanistic Origin of Superionic Lithium Diffusion in Anion-Disordered Li6PS5X Argyrodites. *Chem. Mater.* **33**, 2004–2018 (2021).

116. Kraft, M. A. *et al.* Influence of Lattice Polarizability on the Ionic Conductivity in the Lithium Superionic Argyrodites Li6PS5X (X = Cl, Br, I). *J. Am. Chem. Soc.* **139**, 10909–10918 (2017).
117. Kraft, M. A. *et al.* Inducing High Ionic Conductivity in the Lithium Superionic Argyrodites Li6+xP1–xGexS5I for All-Solid-State Batteries. *J. Am. Chem. Soc.* **140**, 16330–16339 (2018).
118. Ohno, S. *et al.* Further Evidence for Energy Landscape Flattening in the Superionic Argyrodites Li6+xP1–xMxS5I (M = Si, Ge, Sn). *Chem. Mater.* **31**, 4936–4944 (2019).
119. Patel, S. V. *et al.* Tunable Lithium-Ion Transport in Mixed-Halide Argyrodites Li6–xPS5–xClBrx: An Unusual Compositional Space. *Chem. Mater.* **33**, 1435–1443 (2021).
120. Adeli, P. *et al.* Boosting Solid-State Diffusivity and Conductivity in Lithium Superionic Argyrodites by Halide Substitution. *Angew. Chem. Int. Ed.* **58**, 8681–8686 (2019).
121. Wenzel, S., Sedlmaier, S. J., Dietrich, C., Zeier, W. G. & Janek, J. Interfacial reactivity and interphase growth of argyrodite solid electrolytes at lithium metal electrodes. *Solid State Ion. Gener. Batter.* **318**, 102–112 (2018).
122. Otto, S.-K. *et al.* In Situ Investigation of Lithium Metal–Solid Electrolyte Anode Interfaces with ToF-SIMS. *Adv. Mater. Interfaces* **9**, 2102387 (2022).
123. Narayanan, S. *et al.* Effect of current density on the solid electrolyte interphase formation at the lithium|Li6PS5Cl interface. *Nat. Commun.* **13**, 7237 (2022).
124. Lewis, J. A. *et al.* Linking void and interphase evolution to electrochemistry in solid-state batteries using operando X-ray tomography. *Nat. Mater.* **20**, 503–510 (2021).
125. Engineering of solid state ionic devices | Ionics. https://link.springer.com/article/10.1007/BF02376599.
126. Peljo, P. & Girault, H. H. Electrochemical potential window of battery electrolytes: the HOMO–LUMO misconception. *Energy Environ. Sci.* **11**, 2306–2309 (2018).
127. Wagner, C. Beitrag zur Theorie des Anlaufvorgangs. *Z. Für Phys. Chem.* **21B**, 25–41 (1933).
128. Wenzel, S. *et al.* Interphase formation and degradation of charge transfer kinetics between a lithium metal anode and highly crystalline Li7P3S11 solid electrolyte. *Solid State Ion.* **286**, 24–33 (2016).
129. Cheng, D. *et al.* Unveiling the Stable Nature of the Solid Electrolyte Interphase between Lithium Metal and LiPON via Cryogenic Electron Microscopy. *Joule* **4**, 2484–2500 (2020).
130. Schmalzried, H. & Janek, J. Chemical kinetics of phase boundaries in solids. *Berichte Bunsenges. Für Phys. Chem.* **102**, 127–143 (1998).
131. Frank, W., Breier, U., Elsässer, C. & Fähnle, M. First-Principles Calculations of Absolute Concentrations and Self-Diffusion Constants of Vacancies in Lithium. *Phys. Rev. Lett.* **77**, 518–521 (1996).
132. Krauskopf, T., Hartmann, H., Zeier, W. G. & Janek, J. Toward a Fundamental Understanding of the Lithium Metal Anode in Solid-State Batteries—An Electrochemo-Mechanical Study on the Garnet-Type Solid Electrolyte Li6.25Al0.25La3Zr2O12. *ACS Appl. Mater. Interfaces* **11**, 14463–14477 (2019).
133. Meyer, M., Rickert, H. & Schwaitzer, U. Investigations on the kinetics of the anodic dissolution of lithium at the interface Li/Li3N. *Solid State Ion.* **9–10**, 689–693 (1983).

134. Jow, T. R. & Liang, C. C. Interface Between Solid Electrode and Solid Electrolyte—A Study of the Li / LiI ( Al2 O 3 ) Solid-Electrolyte System. *J. Electrochem. Soc.* **130**, 737 (1983).
135. Kasemchainan, J. *et al.* Critical stripping current leads to dendrite formation on plating in lithium anode solid electrolyte cells. *Nat. Mater.* **18**, 1105–1111 (2019).
136. Spencer Jolly, D. *et al.* Sodium/Na β″ Alumina Interface: Effect of Pressure on Voids. *ACS Appl. Mater. Interfaces* **12**, 678–685 (2020).
137. Spencer Jolly, D. *et al.* Temperature Dependence of Lithium Anode Voiding in Argyrodite Solid-State Batteries. *ACS Appl. Mater. Interfaces* **13**, 22708–22716 (2021).
138. Cao, D. *et al.* Lithium Dendrite in All-Solid-State Batteries: Growth Mechanisms, Suppression Strategies, and Characterizations. *Matter* **3**, 57–94 (2020).
139. Liu, H. *et al.* Controlling Dendrite Growth in Solid-State Electrolytes. *ACS Energy Lett.* **5**, 833–843 (2020).
140. Lu, Y. *et al.* Critical Current Density in Solid-State Lithium Metal Batteries: Mechanism, Influences, and Strategies. *Adv. Funct. Mater.* **31**, 2009925 (2021).
141. Buschmann, H. *et al.* Structure and dynamics of the fast lithium ion conductor “Li7La3Zr2O12”. *Phys. Chem. Chem. Phys.* **13**, 19378–19392 (2011).
142. Cheng, L. *et al.* The origin of high electrolyte–electrode interfacial resistances in lithium cells containing garnet type solid electrolytes. *Phys. Chem. Chem. Phys.* **16**, 18294–18300 (2014).
143. Cheng, L. *et al.* Effect of Surface Microstructure on Electrochemical Performance of Garnet Solid Electrolytes. *ACS Appl. Mater. Interfaces* **7**, 2073–2081 (2015).
144. Ren, Y., Shen, Y., Lin, Y. & Nan, C.-W. Direct observation of lithium dendrites inside garnet-type lithium-ion solid electrolyte. *Electrochem. Commun.* **57**, 27–30 (2015).
145. Cheng, E. J., Sharafi, A. & Sakamoto, J. Intergranular Li metal propagation through polycrystalline Li6.25Al0.25La3Zr2O12 ceramic electrolyte. *Electrochimica Acta* **223**, 85–91 (2017).
146. Aguesse, F. *et al.* Investigating the Dendritic Growth during Full Cell Cycling of Garnet Electrolyte in Direct Contact with Li Metal. *ACS Appl. Mater. Interfaces* **9**, 3808–3816 (2017).
147. Pesci, F. M. *et al.* Elucidating the role of dopants in the critical current density for dendrite formation in garnet electrolytes. *J. Mater. Chem. A* **6**, 19817–19827 (2018).
148. Porz, L. *et al.* Mechanism of Lithium Metal Penetration through Inorganic Solid Electrolytes. *Adv. Energy Mater.* **7**, 1701003 (2017).
149. Krauskopf, T. *et al.* The Fast Charge Transfer Kinetics of the Lithium Metal Anode on the Garnet-Type Solid Electrolyte Li6.25Al0.25La3Zr2O12. *Adv. Energy Mater.* **10**, 2000945 (2020).
150. Singh, D. K., Fuchs, T., Krempaszky, C., Mogwitz, B. & Janek, J. Non-Linear Kinetics of The Lithium Metal Anode on Li6PS5Cl at High Current Density: Dendrite Growth and the Role of Lithium Microstructure on Creep. *Adv. Sci.* **10**, 2302521 (2023).
151. Fincher, C. D. *et al.* Controlling dendrite propagation in solid-state batteries with engineered stress. *Joule* **6**, 2794–2809 (2022).
152. McConohy, G. *et al.* Mechanical regulation of lithium intrusion probability in garnet solid electrolytes. *Nat. Energy* **8**, 241–250 (2023).

153. Kazyak, E. *et al.* Li Penetration in Ceramic Solid Electrolytes: Operando Microscopy Analysis of Morphology, Propagation, and Reversibility. *Matter* **2**, 1025–1048 (2020).

154. De Jonghe, L. C., Feldman, L. & Beuchele, A. Slow degradation and electron conduction in sodium/beta-aluminas. *J. Mater. Sci.* **16**, 780–786 (1981).

155. Shen, F., Dixit, M. B., Xiao, X. & Hatzell, K. B. Effect of Pore Connectivity on Li Dendrite Propagation within LLZO Electrolytes Observed with Synchrotron X-ray Tomography. *ACS Energy Lett.* **3**, 1056–1061 (2018).

156. Seitzman, N. *et al.* Toward All-Solid-State Lithium Batteries: Three-Dimensional Visualization of Lithium Migration in β-Li3PS4 Ceramic Electrolyte. *J. Electrochem. Soc.* **165**, A3732 (2018).

157. Doux, J.-M. *et al.* Stack Pressure Considerations for Room-Temperature All-Solid-State Lithium Metal Batteries. *Adv. Energy Mater.* **10**, 1903253 (2020).

158. Zhao, J. *et al.* In situ Observation of Li Deposition-Induced Cracking in Garnet Solid Electrolytes. *ENERGY Environ. Mater.* **5**, 524–532 (2022).

159. Siniscalchi, M. *et al.* Initiation of dendritic failure of LLZTO via sub-surface lithium deposition. *Energy Environ. Sci.* (2024) doi:10.1039/D3EE03916A.

160. Wang, M., Wolfenstine, J. B. & Sakamoto, J. Temperature dependent flux balance of the Li/Li7La3Zr2O12 interface. *Electrochimica Acta* **296**, 842–847 (2019).

161. Masias, A., Felten, N., Garcia-Mendez, R., Wolfenstine, J. & Sakamoto, J. Elastic, plastic, and creep mechanical properties of lithium metal. *J. Mater. Sci.* **54**, 2585–2600 (2019).

162. LePage, W. S. *et al.* Lithium Mechanics: Roles of Strain Rate and Temperature and Implications for Lithium Metal Batteries. *J. Electrochem. Soc.* **166**, A89 (2019).

163. Fricker, H. S. Why does charge concentrate on points? *Phys. Educ.* **24**, 157 (1989).

164. Armstrong, R. D., Dickinson, T. & Turner, J. The breakdown of β-alumina ceramic electrolyte. *Electrochimica Acta* **19**, 187–192 (1974).

165. Barroso-Luque, L., Tu, Q. & Ceder, G. An Analysis of Solid-State Electrodeposition-Induced Metal Plastic Flow and Predictions of Stress States in Solid Ionic Conductor Defects. *J. Electrochem. Soc.* **167**, 020534 (2020).

166. Hitchcock, D. C. & De Jonghe, L. C. Fracture Toughness Anisotropy of Sodium β- Alumina. *J. Am. Ceram. Soc.* **66**, c204–c205 (1983).

167. Virkar, A. V., Viswanathan, L. & Biswas, D. R. On the deterioration of ß″-alumina ceramics under electrolytic conditions. *J. Mater. Sci.* **15**, 302–308 (1980).

168. Virkar, A. V. On some aspects of breakdown of β″-alumina solid electrolyte. *J. Mater. Sci.* **16**, 1142–1150 (1981).

169. Ansell, R. 0. The chemical and electrochemical stability of beta-alumina. *J. Mater. Sci.* **21**, 365–379 (1986).

170. Brennan, M. P. J. The failure of beta-alumina electrolyte by a dendritic penetration mechanism. *Electrochimica Acta* **25**, 621–627 (1980).

171. Feldman, L. A. & De Jonghe, L. C. Initiation of mode I degradation in sodium-beta alumina electrolytes. *J. Mater. Sci.* **17**, 517–524 (1982).

172. Virkar, A. V. & Viswanathan, L. A three-dimensional approach to the electrolytic degradation of solid electrolytes. *J. Mater. Sci.* **18**, 1202–1212 (1983).
173. Klinsmann, M., Hildebrand, F. E., Ganser, M. & McMeeking, R. M. Dendritic cracking in solid electrolytes driven by lithium insertion. *J. Power Sources* **442**, 227226 (2019).
174. Perzyna, P. Fundamental Problems in Viscoplasticity. in *Advances in Applied Mechanics* (eds. Chernyi, G. G. et al.) vol. 9 243–377 (Elsevier, 1966).
175. Xu, C., Ahmad, Z., Aryanfar, A., Viswanathan, V. & Greer, J. R. Enhanced strength and temperature dependence of mechanical properties of Li at small scales and its implications for Li metal anodes. *Proc. Natl. Acad. Sci.* **114**, 57–61 (2017).
176. Darnbrough, E., Aspinall, J., Pasta, M. & Armstrong, D. E. J. Elastic and plastic mechanical properties of lithium measured by nanoindentation. *Mater. Des.* **233**, 112200 (2023).
177. Bucci, G. & Christensen, J. Modeling of lithium electrodeposition at the lithium/ceramic electrolyte interface: The role of interfacial resistance and surface defects. *J. Power Sources* **441**, 227186 (2019).
178. Doux, J.-M. *et al.* Pressure effects on sulfide electrolytes for all solid-state batteries. *J. Mater. Chem. A* **8**, 5049–5055 (2020).
179. Kinzer, B. *et al.* Operando analysis of the molten Li|LLZO interface: Understanding how the physical properties of Li affect the critical current density. *Matter* **4**, 1947–1961 (2021).
180. Spencer Jolly, D. *et al.* High critical currents for dendrite penetration and voiding in potassium metal anode solid-state batteries. *J. Solid State Electrochem.* **26**, 1961–1968 (2022).
181. Park, R. J.-Y. *et al.* Semi-solid alkali metal electrodes enabling high critical current densities in solid electrolyte batteries. *Nat. Energy* **6**, 314–322 (2021).
182. Qi, Y., Ban, C. & Harris, S. J. A New General Paradigm for Understanding and Preventing Li Metal Penetration through Solid Electrolytes. *Joule* **4**, 2599–2608 (2020).
183. Rao, A. C. U., Vasu, V., Govindaraju, M. & Srinadh, K. V. S. Stress corrosion cracking behaviour of 7xxx aluminum alloys: A literature review. *Trans. Nonferrous Met. Soc. China* **26**, 1447–1471 (2016).
184. Richman, R. H. & Tennenhouse, G. J. A Model for Degradation of Ceramic Electrolytes in Na-S Batteries. *J. Am. Ceram. Soc.* **58**, 63–67 (1975).
185. DAVIDGE, R., G, T., JR, M. & GJ, M. STRENGTH AND DELAYED FRACTURE BAHAVIOR OF BETA ALUMINA. *Amer Ceram Soc Bull* **58**, (1979).
186. Reisecker, V. *et al.* Effect of pulse-current-based protocols on the lithium dendrite formation and evolution in all-solid-state batteries. *Nat. Commun.* **14**, 2432 (2023).
187. Zhang, Y., Dong, Y. & Li, J. Electrochemical shock and transverse cracking in solid electrolytes. *Acta Mater.* **265**, 119620 (2024).
188. Zhu, C. *et al.* Understanding the evolution of lithium dendrites at Li6.25Al0.25La3Zr2O12 grain boundaries via operando microscopy techniques. *Nat. Commun.* **14**, 1300 (2023).
189. Liu, X. *et al.* Local electronic structure variation resulting in Li 'filament' formation within solid electrolytes. *Nat. Mater.* **20**, 1485–1490 (2021).

190. Li, G. & W. Monroe, C. Dendrite nucleation in lithium-conductive ceramics. *Phys. Chem. Chem. Phys.* **21**, 20354–20359 (2019).
191. Gu, Z. *et al.* Insights into the Anode-Initiated and Grain Boundary-Initiated Mechanisms for Dendrite Formation in All-Solid-State Lithium Metal Batteries. *Adv. Energy Mater.* **13**, 2302945 (2023).
192. Tu, Q., Shi, T., Chakravarthy, S. & Ceder, G. Understanding metal propagation in solid electrolytes due to mixed ionic-electronic conduction. *Matter* **4**, 3248–3268 (2021).
193. Weppner, W. Fundamental Aspects of Electrochemical, Chemical and Electrostatic Potentials in Lithium Batteries. in *Materials for Lithium-Ion Batteries* (eds. Julien, C. & Stoynov, Z.) 401–412 (Springer Netherlands, Dordrecht, 2000). doi:10.1007/978-94-011-4333-2_20.
194. Jonghe, L. C. D. Transport Number Gradients and Solid Electrolyte Degradation. *J. Electrochem. Soc.* **129**, 752 (1982).
195. Raj, R. & Wolfenstine, J. Current limit diagrams for dendrite formation in solid-state electrolytes for Li-ion batteries. *J. Power Sources* **343**, 119–126 (2017).
196. Kuribayashi, K. & Nicholson, P. S. The deterioration of sodium ion conductors under applied stress. *J. Mater. Sci.* **18**, 1590–1596 (1983).
197. Sharafi, A. *et al.* Surface Chemistry Mechanism of Ultra-Low Interfacial Resistance in the Solid-State Electrolyte Li7La3Zr2O12. *Chem. Mater.* **29**, 7961–7968 (2017).
198. Chen, L. *et al.* Nanosecond Laser Cleaning Method to Reduce the Surface Inert Layer and Activate the Garnet Electrolyte for a Solid-State Li Metal Battery. *ACS Appl. Mater. Interfaces* **13**, 37082–37090 (2021).
199. Huo, H. *et al.* In-situ formed Li2CO3-free garnet/Li interface by rapid acid treatment for dendrite-free solid-state batteries. *Nano Energy* **61**, 119–125 (2019).
200. Kun (Kelvin) Fu *et al.* Three-dimensional bilayer garnet solid electrolyte based high energy density lithium metal–sulfur batteries. *Energy Environ. Sci.* **10**, 1568–1575 (2017).
201. Hitz, G. T. *et al.* High-rate lithium cycling in a scalable trilayer Li-garnet-electrolyte architecture. *Mater. Today* **22**, 50–57 (2019).
202. Xu, R. *et al.* A Morphologically Stable Li/Electrolyte Interface for All-Solid-State Batteries Enabled by 3D-Micropatterned Garnet. *Adv. Mater.* **33**, 2104009 (2021).
203. McOwen, D. W. *et al.* 3D-Printing Electrolytes for Solid-State Batteries. *Adv. Mater.* **30**, 1707132 (2018).
204. Zhang, S. *et al.* Influence of contouring the lithium metal/solid electrolyte interface on the critical current for dendrites. *Energy Environ. Sci.* **17**, 1448–1456 (2024).
205. Han, X. *et al.* Negating interfacial impedance in garnet-based solid-state Li metal batteries. *Nat. Mater.* **16**, 572–579 (2017).
206. Alexander, G. V., Shi, C., O'Neill, J. & Wachsman, E. D. Extreme lithium-metal cycling enabled by a mixed ion- and electron-conducting garnet three-dimensional architecture. *Nat. Mater.* **22**, 1136–1143 (2023).
207. Kim, S. *et al.* The Role of Interlayer Chemistry in Li-Metal Growth through a Garnet-Type Solid Electrolyte. *Adv. Energy Mater.* **10**, 1903993 (2020).

208. Fu, K. (Kelvin) *et al.* Transient Behavior of the Metal Interface in Lithium Metal–Garnet Batteries. *Angew. Chem. Int. Ed.* **56**, 14942–14947 (2017).
209. Lu, Y. *et al.* An in situ element permeation constructed high endurance Li–LLZO interface at high current densities. *J. Mater. Chem. A* **6**, 18853–18858 (2018).
210. Aspinall, J. *et al.* Effect of Microstructure on the Cycling Behavior of Li–In Alloy Anodes for Solid-State Batteries. *ACS Energy Lett.* **9**, 578–585 (2024).
211. Obrovac, M. N. & Chevrier, V. L. Alloy Negative Electrodes for Li-Ion Batteries. *Chem. Rev.* **114**, 11444–11502 (2014).
212. Spencer-Jolly, D. *et al.* Structural changes in the silver-carbon composite anode interlayer of solid-state batteries. *Joule* **7**, 503–514 (2023).
213. Xie, F., Diallo, M. S., Kim, H., Tu, Q. H. & Ceder, G. The Microscopic Mechanism of Lithiation and Delithiation in the Ag/C Buffer Layer for Anode-Free Solid-State Batteries. *Adv. Energy Mater.* **n/a**, 2302960.
214. Kodama, M., Takashima, K. & Hirai, S. Improvement of lithium-metal electrode performance of all-solid-state batteries by shot peening on solid-electrolyte surface. *J. Power Sources* **537**, 231556 (2022).
215. Flatscher, F. *et al.* Deflecting Dendrites by Introducing Compressive Stress in Li7La3Zr2O12 Using Ion Implantation. *Small* **n/a**, 2307515.
216. Jagad, H. D., Harris, S. J., Sheldon, B. W. & Qi, Y. Tradeoff between the Ion Exchange-Induced Residual Stress and Ion Transport in Solid Electrolytes. *Chem. Mater.* **34**, 8694–8704 (2022).
217. Duan, J. *et al.* Solid electrolyte cracking due to lithium filament growth and concept of mechanical reinforcement – An operando study. *Mater. Today* (2023) doi:10.1016/j.mattod.2023.10.003.
218. Athanasiou, C. E., Jin, M. Y., Ramirez, C., Padture, N. P. & Sheldon, B. W. High-Toughness Inorganic Solid Electrolytes via the Use of Reduced Graphene Oxide. *Matter* **3**, 212–229 (2020).
219. Yersak, T., Salvador, J. R., Schmidt, R. D. & Cai, M. Hot Pressed, Fiber-Reinforced (Li2S)70(P2S5)30 Solid-State Electrolyte Separators for Li Metal Batteries. *ACS Appl. Energy Mater.* **2**, 3523–3531 (2019).
220. El-Shinawi, H. *et al.* Liquid-Phase Approach to Glass-Microfiber-Reinforced Sulfide Solid Electrolytes for All-Solid-State Batteries. *ACS Appl. Mater. Interfaces* **15**, 36512–36518 (2023).
221. Heavens, S. N. Strength improvement in beta″ alumina by incorporation of zirconia. *J. Mater. Sci.* **23**, 3515–3518 (1988).
222. Green, D. J. Transformation toughening and grain size control inβ″-Al2O3/ZrO2 composites. *J. Mater. Sci.* **20**, 2639–2646 (1985).
223. Viswanathan, L., Ikuma, Y. & Virkar, A. V. Transfomation toughening of β″-alumina by incorporation of zirconia. *J. Mater. Sci.* **18**, 109–113 (1983).
224. Binner, J. G. P. & Stevens, R. Improvement in the mechanical properties of polycrystalline beta-alumina via the use of zirconia particles containing stabilizing oxide additions. *J. Mater. Sci.* **20**, 3119–3124 (1985).

225. Olson, D. & De Jonghe, L. C. Zirconia-toughened sodium beta″-alumina solid electrolyte. *J. Mater. Sci.* **21**, 4221–4226 (1986).

226. Sheng, Y., Sarkar, P. & Nicholson, P. S. The mechanical and electrical properties of ZrO2-Naβ″-Al2O3 composites. *J. Mater. Sci.* **23**, 958–967 (1988).

227. Wolfenstine, J., Allen, J. L., Sakamoto, J., Siegel, D. J. & Choe, H. Mechanical behavior of Li-ion-conducting crystalline oxide-based solid electrolytes: a brief review. *Ionics* **24**, 1271–1276 (2018).

228. Jia, Z. *et al.* Solid Electrolyte Bimodal Grain Structures for Improved Cycling Performance. *Adv. Mater.* **n/a**, 2309019.

229. Hong, M. *et al.* Tailoring grain growth and densification toward a high-performance solid-state electrolyte membrane. *Mater. Today* **42**, 41–48 (2021).

230. Sharafi, A., Haslam, C. G., Kerns, R. D., Wolfenstine, J. & Sakamoto, J. Controlling and correlating the effect of grain size with the mechanical and electrochemical properties of Li7La3Zr2O12 solid-state electrolyte. *J. Mater. Chem. A* **5**, 21491–21504 (2017).

231. Sato, M., Garcia-Mendez, R. & Sakamoto, J. Mapping hot-pressed Li6.25Al0.25La3Zr2O12 (LLZO) grains and grain boundaries through a simple thermal grooving technique. *J. Asian Ceram. Soc.* **8**, 793–803 (2020).

232. Okur, F. *et al.* Intermediate-Stage Sintered LLZO Scaffolds for Li-Garnet Solid-State Batteries. *Adv. Energy Mater.* **13**, 2203509 (2023).

233. Ren, Y., Shen, Y., Lin, Y. & Nan, C.-W. Microstructure Manipulation for Enhancing the Resistance of Garnet-Type Solid Electrolytes to “Short Circuit” by Li Metal Anodes. *ACS Appl. Mater. Interfaces* **11**, 5928–5937 (2019).

234. Swamy, T. *et al.* Lithium Metal Penetration Induced by Electrodeposition through Solid Electrolytes: Example in Single-Crystal Li6La3ZrTaO12 Garnet. *J. Electrochem. Soc.* **165**, A3648 (2018).

235. Zheng, C. *et al.* Grain boundary modification in garnet electrolyte to suppress lithium dendrite growth. *Chem. Eng. J.* **411**, 128508 (2021).

236. Hongahally Basappa, R. *et al.* Grain boundary modification to suppress lithium penetration through garnet-type solid electrolyte. *J. Power Sources* **363**, 145–152 (2017).

237. Zheng, C. *et al.* Grain Boundary Engineering Enabled High-Performance Garnet-Type Electrolyte for Lithium Dendrite Free Lithium Metal Batteries. *Small Methods* **6**, 2200667 (2022).

238. Qin, Z. *et al.* Grain Boundary Engineering in Ta-Doped Garnet-Type Electrolyte for Lithium Dendrite Suppression. *ACS Appl. Mater. Interfaces* **14**, 40959–40966 (2022).

239. Hoinkis, N. *et al.* Amorphous Phase Induced Lithium Dendrite Suppression in Glass-Ceramic Garnet-Type Solid Electrolytes. *ACS Appl. Mater. Interfaces* **15**, 28692–28704 (2023).

240. Lewis, J. A. *et al.* Role of Areal Capacity in Determining Short Circuiting of Sulfide-Based Solid-State Batteries. *ACS Appl. Mater. Interfaces* **14**, 4051–4060 (2022).

241. Li, J., Li, Y., Zhang, S., Li, D. & Ci, L. Two-step sintering of sulfide solid electrolyte with improved electrochemical properties for all-solid-state lithium batteries. *eTransportation* **16**, 100236 (2023).

242. Zhao, C. *et al.* Synthesis of high ionic conductivity Li6PS5Cl solid electrolyte by second sintering process. *Results Chem.* **4**, 100468 (2022).

243. Diallo, M. S. *et al.* Effect of solid-electrolyte pellet density on failure of solid-state batteries. *Nat. Commun.* **15**, 858 (2024).

244. Garcia-Mendez, R., Smith, J. G., Neuefeind, J. C., Siegel, D. J. & Sakamoto, J. Correlating Macro and Atomic Structure with Elastic Properties and Ionic Transport of Glassy Li2S-P2S5 (LPS) Solid Electrolyte for Solid-State Li Metal Batteries. *Adv. Energy Mater.* **10**, 2000335 (2020).

245. Yersak, T. A., Salvador, J. R., Pieczonka, N. P. W. & Cai, M. Dense, Melt Cast Sulfide Glass Electrolyte Separators for Li Metal Batteries. *J. Electrochem. Soc.* **166**, A1535 (2019).

246. Garcia-Mendez, R., Mizuno, F., Zhang, R., Arthur, T. S. & Sakamoto, J. Effect of Processing Conditions of 75Li2S-25P2S5 Solid Electrolyte on its DC Electrochemical Behavior. *Electrochimica Acta* **237**, 144–151 (2017).

247. McGrogan, F. P. *et al.* Compliant Yet Brittle Mechanical Behavior of Li2S–P2S5 Lithium-Ion-Conducting Solid Electrolyte. *Adv. Energy Mater.* **7**, 1602011 (2017).

248. Carter, C. B. & Norton, M. G. *Ceramic Materials: Science and Engineering*. (Springer, New York, NY, 2013). doi:10.1007/978-1-4614-3523-5.

249. Processing of Materials. in *An Introduction to Materials Engineering and Science* 681–813 (John Wiley & Sons, Ltd, 2003). doi:10.1002/0471473359.ch7.

250. Lee, W. E. & Rainforth, M. *Ceramic Microstructures: Property Control by Processing*. (Springer Science & Business Media, 1994).

251. Guillon, O. *et al.* Field-Assisted Sintering Technology/Spark Plasma Sintering: Mechanisms, Materials, and Technology Developments. *Adv. Eng. Mater.* **16**, 830–849 (2014).

252. Hulbert, D. M. *et al.* The absence of plasma in “spark plasma sintering”. *J. Appl. Phys.* **104**, 033305 (2008).

253. Klug, H. P. & Alexander, L. E. *X-Ray Diffraction Procedures: For Polycrystalline and Amorphous Materials* (1974).

254. Bragg, W. H. & Bragg, W. L. The reflection of X-rays by crystals. *Proc. R. Soc. Lond. Ser. Contain. Pap. Math. Phys. Character* **88**, 428–438 (1997).

255. Köhler, H. On Abbe’s Theory of Image Formation in the Microscope. *Opt. Acta Int. J. Opt.* **28**, 1691–1701 (1981).

256. Egerton, R. F. *Physical Principles of Electron Microscopy*. (Springer International Publishing, Cham, 2016). doi:10.1007/978-3-319-39877-8.

257. Orloff, J., Swanson, L. & Utlaut, M. *High Resolution Focused Ion Beams: FIB and Its Applications: Fib and Its Applications : The Physics of Liquid Metal Ion Sources and Ion Optics and Their Application to Focused Ion Beam Technology*. (Springer Science & Business Media, 2003).

258. Ul-Hamid, A. *A Beginners’ Guide to Scanning Electron Microscopy*. (Springer International Publishing, Cham, 2018). doi:10.1007/978-3-319-98482-7.

259. Joo, S. & Liang, H. Secondary Ion Mass Spectroscopy (SIMS). in *Encyclopedia of Tribology* (eds. Wang, Q. J. & Chung, Y.-W.) 2989–2994 (Springer US, Boston, MA, 2013). doi:10.1007/978-0-387-92897-5_1218.

260. Stock, S. R. Recent advances in X-ray microtomography applied to materials. *Int. Mater. Rev.* **53**, 129–181 (2008).
261. Pietsch, P. & Wood, V. X-Ray Tomography for Lithium Ion Battery Research: A Practical Guide. *Annu. Rev. Mater. Res.* **47**, 451–479 (2017).
262. Als-Nielsen, J. & McMorrow, D. *Elements of Modern X-Ray Physics*. (John Wiley & Sons, 2011).
263. Bech, M. X-ray imaging with a grating interferometer PhD thesis. *Univ. Cph. Den.* (2009).
264. Paganin, D., Mayo, S. C., Gureyev, T. E., Miller, P. R. & Wilkins, S. W. Simultaneous phase and amplitude extraction from a single defocused image of a homogeneous object. *J. Microsc.* **206**, 33–40 (2002).
265. Gross, J. H. *Mass Spectrometry*. (Springer International Publishing, Cham, 2017). doi:10.1007/978-3-319-54398-7.
266. Wang, S. *et al.* Electrochemical impedance spectroscopy. *Nat. Rev. Methods Primer* **1**, 1–21 (2021).
267. Irvine, J. T. S., Sinclair, D. C. & West, A. R. Electroceramics: Characterization by Impedance Spectroscopy. *Adv. Mater.* **2**, 132–138 (1990).
268. Browne, W. R. & Browne, W. R. *Electrochemistry*. (Oxford University Press, Oxford, New York, 2018).
269. Mo, F. *et al.* Inside or Outside: Origin of Lithium Dendrite Formation of All Solid-State Electrolytes. *Adv. Energy Mater.* **9**, 1902123 (2019).
270. Fuchs, T., Haslam, C. G., Richter, F. H., Sakamoto, J. & Janek, J. Evaluating the Use of Critical Current Density Tests of Symmetric Lithium Transference Cells with Solid Electrolytes. *Adv. Energy Mater.* **13**, 2302383 (2023).
271. Oliver, W. C. & Pharr, G. M. An improved technique for determining hardness and elastic modulus using load and displacement sensing indentation experiments. *J. Mater. Res.* **7**, 1564–1583 (1992).
272. Oliver, W. C. & Pharr, G. M. Measurement of hardness and elastic modulus by instrumented indentation: Advances in understanding and refinements to methodology. *J. Mater. Res.* **19**, 3–20 (2004).
273. Lawn, B. R., Evans, A. G. & Marshall, D. B. Elastic/Plastic Indentation Damage in Ceramics: The Median/Radial Crack System. *J. Am. Ceram. Soc.* **63**, 574–581 (1980).
274. Di Maio, D. & Roberts, S. G. Measuring fracture toughness of coatings using focused-ion-beam-machined microbeams. *J. Mater. Res.* **20**, 299–302 (2005).
275. Chen, Y. *et al.* Measurements of elastic modulus and fracture toughness of an air plasma sprayed thermal barrier coating using micro-cantilever bending. *Surf. Coat. Technol.* **374**, 12–20 (2019).
276. Krauskopf, T., Richter, F. H., Zeier, W. G. & Janek, J. Physicochemical Concepts of the Lithium Metal Anode in Solid-State Batteries. *Chem. Rev.* **120**, 7745–7794 (2020).
277. Monroe, C. & Newman, J. The Impact of Elastic Deformation on Deposition Kinetics at Lithium/Polymer Interfaces. *J. Electrochem. Soc.* **152**, A396 (2005).

278. Dixit, M. B., Park, J.-S., Kenesei, P., Almer, J. & Hatzell, K. B. Status and prospect of in situ and operando characterization of solid-state batteries. *Energy Environ. Sci.* **14**, 4672–4711 (2021).
279. Scharf, J. *et al.* Bridging nano- and microscale X-ray tomography for battery research by leveraging artificial intelligence. *Nat. Nanotechnol.* **17**, 446–459 (2022).
280. Porz, L. *et al.* Mechanism of Lithium Metal Penetration through Inorganic Solid Electrolytes. *Adv. Energy Mater.* **7**, 1–12 (2017).
281. Bucci, G. & Christensen, J. Modeling of lithium electrodeposition at the lithium/ceramic electrolyte interface: The role of interfacial resistance and surface defects. *J. Power Sources* **441**, 227186 (2019).
282. Klinsmann, M., Hildebrand, F. E., Ganser, M. & McMeeking, R. M. Dendritic cracking in solid electrolytes driven by lithium insertion. *J. Power Sources* **442**, 227226 (2019).
283. Barroso-Luque, L., Tu, Q. & Ceder, G. An Analysis of Solid-State Electrodeposition-Induced Metal Plastic Flow and Predictions of Stress States in Solid Ionic Conductor Defects. *J. Electrochem. Soc.* **167**, 020534 (2020).
284. Kasemchainan, J. *et al.* Critical stripping current leads to dendrite formation on plating in lithium anode solid electrolyte cells. *Nat. Mater.* **18**, (2019).
285. Spencer Jolly, D. *et al.* Sodium/Na β″ Alumina Interface: Effect of Pressure on Voids. *ACS Appl. Mater. Interfaces* **12**, 678–685 (2020).
286. Ning, Z. *et al.* Visualizing plating-induced cracking in lithium-anode solid-electrolyte cells. *Nat. Mater.* **20**, 1121–1129 (2021).
287. Gong, C. *et al.* Revealing the Role of Fluoride-Rich Battery Electrode Interphases by Operando Transmission Electron Microscopy. *Adv. Energy Mater.* **11**, 2003118 (2021).
288. Peng, Z., Freunberger, S. A., Chen, Y. & Bruce, P. G. A Reversible and Higher-Rate Li-O2 Battery. *Science* **337**, 563–566 (2012).
289. Oliver, W. C. & Pharr, G. M. Measurement of hardness and elastic modulus by instrumented indentation: Advances in understanding and refinements to methodology. *J. Mater. Res.* **19**, 3 (2004).
290. Di Maio, D. & Roberts, S. G. Measuring fracture toughness of coatings using focused-ion-beam-machined microbeams. *J. Mater. Res.* **20**, 299–302 (2005).
291. Chen, Y. *et al.* Measurements of elastic modulus and fracture toughness of an air plasma sprayed thermal barrier coating using micro-cantilever bending. *Surf. Coat. Technol.* **374**, 12–20 (2019).
292. Ning, Z. *et al.* Dendrite initiation and propagation in lithium metal solid-state batteries. *Nature* **618**, 287–293 (2023).
293. H S Fricker. Why does charge concentrate on points? *Phys. Educ.* **24**, 157 (1989).
294. Feynman, R. P. (Richard P., 1918-1988. *The Feynman Lectures on Physics*. (Reading, Mass. : Addison-Wesley Pub. Co., c1963-1965., 1965).
295. Luo, Y. F. Differential equations for the ultra-fast transient migration in electrolytic dissolution. *Electrochem. Commun.* **8**, 353–358 (2006).
296. Wilcox, G. D. & Gabe, D. R. Faraday's Laws of Electrolysis. *Trans. IMF* (1992).

297. Łukaszewicz, G. & Kalita, P. *Navier–Stokes Equations*. (Springer International Publishing, Cham, 2016). doi:10.1007/978-3-319-27760-8.

298. Irgens, F. *Tensor Analysis*. (Springer International Publishing, Cham, 2019). doi:10.1007/978-3-030-03412-2.

299. William Rider & Drikakis, D. *High-Resolution Methods for Incompressible and Low-Speed Flows*. (Springer-Verlag, Berlin/Heidelberg, 2005). doi:10.1007/b137615.

300. Masias, A., Felten, N., Garcia-Mendez, R., Wolfenstine, J. & Sakamoto, J. Elastic, plastic, and creep mechanical properties of lithium metal. *J. Mater. Sci.* **54**, 2585–2600 (2019).

301. Sharafi, A. *et al.* Surface Chemistry Mechanism of Ultra-Low Interfacial Resistance in the Solid-State Electrolyte Li7La3Zr2O12. *Chem. Mater.* **29**, 7961–7968 (2017).

302. Brebbia, C. A., Telles, J. C. F. & Wrobel, L. C. *Boundary Element Techniques*. (Springer, Berlin, Heidelberg, 1984). doi:10.1007/978-3-642-48860-3.

303. Rice, J. R. A Path Independent Integral and the Approximate Analysis of Strain Concentration by Notches and Cracks. *J. Appl. Mech.* **35**, 379–386 (1968).

304. Sih, G. C. *Mechanics of Fracture Initiation and Propagation*. (Springer Netherlands, Dordrecht, 1991). doi:10.1007/978-94-011-3734-8.

305. Deng, Z., Wang, Z., Chu, I.-H., Luo, J. & Ong, S. P. Elastic Properties of Alkali Superionic Conductor Electrolytes from First Principles Calculations. *J. Electrochem. Soc.* **163**, A67–A74 (2015).

306. Kazyak, E. *et al.* Li Penetration in Ceramic Solid Electrolytes: Operando Microscopy Analysis of Morphology, Propagation, and Reversibility. *Matter* **2**, 1025–1048 (2020).

307. Kinzer, B. *et al.* Operando analysis of the molten Li|LLZO interface: Understanding how the physical properties of Li affect the critical current density. *Matter* **4**, 1947–1961 (2021).

308. Spencer Jolly, D. *et al.* High critical currents for dendrite penetration and voiding in potassium metal anode solid-state batteries. *J. Solid State Electrochem.* **26**, 1961–1968 (2022).

309. Park, R. J.-Y. *et al.* Semi-solid alkali metal electrodes enabling high critical current densities in solid electrolyte batteries. *Nat. Energy* **6**, 314–322 (2021).

310. Lu, Y. *et al.* Critical Current Density in Solid-State Lithium Metal Batteries: Mechanism, Influences, and Strategies. *Adv. Funct. Mater.* **2009925**, 1–33 (2021).

311. Ning, Z. *et al.* Dendrite initiation and propagation in lithium metal solid-state batteries. *Nature* **618**, 287–293 (2023).

312. Schmaltz, T. *et al. Solid-State Battery Roadmap 2035*+. (2022) doi:10.24406/publica-68.

313. The Battery Report 2022. https://www.volta.foundation/annual-battery-report (2023).

314. Kato, Y. *et al.* High-power all-solid-state batteries using sulfide superionic conductors. *Nat. Energy* **1**, 1–7 (2016).

315. Janek, J. & Zeier, W. G. Challenges in speeding up solid-state battery development. *Nat. Energy* **8**, 230–240 (2023).

316. Kamaya, N. *et al.* A lithium superionic conductor. *Nat. Mater.* **10**, 682–686 (2011).

317. Ping, X. Y. *et al.* Influence of sintering atmosphere on the phase, microstructure, and lithium-ion conductivity of the Al-doped $Li_7La_3Zr_2O_{12}$ solid electrolyte. *Ceram. Int.* **48**, 25689–25695 (2022).

318. Huang, X. *et al.* Manipulating $Li_2O$ atmosphere for sintering dense $Li_7La_3Zr_2O_{12}$ solid electrolyte. *ENERGY STORAGE Mater.* **22**, 207–217 (2019).

319. Xia, W. H. *et al.* Ionic Conductivity and Air Stability of Al-Doped $Li_7La_3Zr_2O_{12}$ Sintered in Alumina and Pt Crucibles. *ACS Appl. Mater. INTERFACES* **8**, 5335–5342 (2016).

320. Zhou, L., Assoud, A., Zhang, Q., Wu, X. & Nazar, L. F. New Family of Argyrodite Thioantimonate Lithium Superionic Conductors. *J. Am. Chem. Soc.* **141**, 19002–19013 (2019).

321. Kraft, M. A. *et al.* Inducing High Ionic Conductivity in the Lithium Superionic Argyrodites Li6+xP1–xGexS5I for All-Solid-State Batteries. *J. Am. Chem. Soc.* **140**, 16330–16339 (2018).

322. Garcia-Mendez, R., Smith, J. G., Neuefeind, J. C., Siegel, D. J. & Sakamoto, J. Correlating Macro and Atomic Structure with Elastic Properties and Ionic Transport of Glassy Li 2 S-P 2 S 5 (LPS) Solid Electrolyte for Solid-State Li Metal Batteries . *Adv. Energy Mater.* **5**, 2000335 (2020).

323. Garcia-Mendez, R., Mizuno, F., Zhang, R., Arthur, T. S. & Sakamoto, J. Effect of Processing Conditions of 75Li2S-25P2S5 Solid Electrolyte on its DC Electrochemical Behavior. *Electrochimica Acta* **237**, 144–151 (2017).

324. Wood, K. N. *et al.* Operando X-ray photoelectron spectroscopy of solid electrolyte interphase formation and evolution in Li2S-P2S5 solid-state electrolytes. *Nat. Commun.* **9**, 2490 (2018).

325. McGrogan, F. P. *et al.* Compliant Yet Brittle Mechanical Behavior of Li2S–P2S5 Lithium-Ion-Conducting Solid Electrolyte. *Adv. Energy Mater.* **7**, 1602011 (2017).

326. Yersak, T. A., Salvador, J. R., Pieczonka, N. P. W. & Cai, M. Dense, Melt Cast Sulfide Glass Electrolyte Separators for Li Metal Batteries. *J. Electrochem. Soc.* **166**, A1535 (2019).

327. Otto, S.-K. *et al.* In Situ Investigation of Lithium Metal–Solid Electrolyte Anode Interfaces with ToF-SIMS. *Adv. Mater. Interfaces* **9**, 2102387 (2022).

328. Zhang, Y., Chen, F., Tu, R., Shen, Q. & Zhang, L. Field assisted sintering of dense Al-substituted cubic phase Li7La3Zr2O12 solid electrolytes. *J. Power Sources* **268**, 960–964 (2014).

329. Yang, L. *et al.* Rapid sintering method for highly conductive Li7La3Zr2O12 ceramic electrolyte. *Ceram. Int.* **46**, 10917–10924 (2020).

330. Wang, S. *et al.* High-Conductivity Argyrodite Li6PS5Cl Solid Electrolytes Prepared via Optimized Sintering Processes for All-Solid-State Lithium–Sulfur Batteries. *ACS Appl. Mater. Interfaces* **10**, 42279–42285 (2018).

331. Yu, C. *et al.* Facile Synthesis toward the Optimal Structure-Conductivity Characteristics of the Argyrodite Li6PS5Cl Solid-State Electrolyte. *ACS Appl. Mater. Interfaces* **10**, 33296–33306 (2018).

332. Kato, A., Yamamoto, M., Sakuda, A., Hayashi, A. & Tatsumisago, M. Mechanical Properties of Li2S–P2S5 Glasses with Lithium Halides and Application in All-Solid-State Batteries. *ACS Appl. Energy Mater.* **1**, 1002–1007 (2018).

333. Hikima, K., Totani, M., Obokata, S., Muto, H. & Matsuda, A. Mechanical Properties of Sulfide-Type Solid Electrolytes Analyzed by Indentation Methods. *ACS Appl. Energy Mater.* **5**, 2349–2355 (2022).

334. Cho, Y.-H. *et al.* Mechanical properties of the solid Li-ion conducting electrolyte: Li0.33La0.57TiO3. *J. Mater. Sci.* **47**, 5970–5977 (2012).

335. Ni, J. E., Case, E. D., Sakamoto, J. S., Rangasamy, E. & Wolfenstine, J. B. Room temperature elastic moduli and Vickers hardness of hot-pressed LLZO cubic garnet. *J. Mater. Sci.* **47**, 7978–7985 (2012).

336. Banik, A. *et al.* On the underestimated influence of synthetic conditions in solid ionic conductors. *Chem. Sci.* **12**, 6238–6263 (2021).

337. Gautam, A. *et al.* Rapid Crystallization and Kinetic Freezing of Site-Disorder in the Lithium Superionic Argyrodite Li6PS5Br. *Chem. Mater.* **31**, 10178–10185 (2019).

338. Sarkar, S. & Thangadurai, V. Critical Current Densities for High-Performance All-Solid-State Li-Metal Batteries: Fundamentals, Mechanisms, Interfaces, Materials, and Applications. *ACS Energy Lett.* **7**, 1492–1527 (2022).

339. Sharafi, A., Meyer, H. M., Nanda, J., Wolfenstine, J. & Sakamoto, J. Characterizing the Li–Li7La3Zr2O12 interface stability and kinetics as a function of temperature and current density. *J. Power Sources* **302**, 135–139 (2016).

340. Fuchs, T., Haslam, C. G., Richter, F. H., Sakamoto, J. & Janek, J. Evaluating the Use of Critical Current Density Tests of Symmetric Lithium Transference Cells with Solid Electrolytes. *Adv. Energy Mater.* **n/a**, 2302383 (2023).

341. Wan, H., Wang, Z., Zhang, W., He, X. & Wang, C. Interface design for all-solid-state lithium batteries. *Nature* (2023) doi:10.1038/s41586-023-06653-w.

342. Kasemchainan, J. *et al.* Critical stripping current leads to dendrite formation on plating in lithium anode solid electrolyte cells. *Nat. Mater.* **18**, 1105–1111 (2019).

343. Lu, X., Xia, G., Lemmon, J. P. & Yang, Z. Advanced materials for sodium-beta alumina batteries: Status, challenges and perspectives. *J. Power Sources* **195**, 2431–2442 (2010).

344. Spencer Jolly, D. *et al.* Interfaces between Ceramic and Polymer Electrolytes: A Comparison of Oxide and Sulfide Solid Electrolytes for Hybrid Solid-State Batteries. *Inorganics* **10**, 60 (2022).

345. Wan, H., Wang, Z., Zhang, W., He, X. & Wang, C. Interface design for all-solid-state lithium batteries. *Nature* 1–6 (2023) doi:10.1038/s41586-023-06653-w.

346. Kim, D. H. *et al.* Thin and Flexible Solid Electrolyte Membranes with Ultrahigh Thermal Stability Derived from Solution-Processable Li Argyrodites for All-Solid-State Li-Ion Batteries. *ACS Energy Lett.* **5**, 718–727 (2020).

347. Simon, F. J., Hanauer, M., Richter, F. H. & Janek, J. Interphase Formation of PEO20:LiTFSI–Li6PS5Cl Composite Electrolytes with Lithium Metal. *ACS Appl. Mater. Interfaces* **12**, 11713–11723 (2020).

348. Inwang, I. B., McColm, I. J. & Wronski, A. Zirconia infiltration toughening of Na-β-alumina. *J. Mater. Sci.* **36**, 1823–1832 (2001).

349. Callister, W. D. & Rethwisch, D. G. *Materials Science and Engineering: An Introduction, 8th Edition*. (Wiley, 2009).

350. Hannink, R. H. J., Kelly, P. M. & Muddle, B. C. Transformation Toughening in Zirconia-Containing Ceramics. *J. Am. Ceram. Soc.* **83**, 461–487 (2000).

351. Green, D. J. *Transformation Toughening Of Ceramics*. (CRC Press, Boca Raton, 2017). doi:10.1201/9781351077408.

352. Bailey, J. Phase transformations in milled zirconia. *Trans J Br Ceram Soc* **71**, 25–30 (1972).

353. Chevalier, J., Gremillard, L., Virkar, A. V. & Clarke, D. R. The Tetragonal-Monoclinic Transformation in Zirconia: Lessons Learned and Future Trends. *J. Am. Ceram. Soc.* **92**, 1901–1920 (2009).

354. Toraya, H., Yoshimura, M. & Somiya, S. Calibration Curve for Quantitative Analysis of the Monoclinic-Tetragonal ZrO2 System by X-Ray Diffraction. *J. Am. Ceram. Soc.* **67**, C-119-C–121 (1984).

355. Baranowski, L. L., Heveran, C. M., Ferguson, V. L. & Stoldt, C. R. Multi-Scale Mechanical Behavior of the Li3PS4 Solid-Phase Electrolyte. *ACS Appl. Mater. Interfaces* **8**, 29573–29579 (2016).

356. Kruzic, J. J. & Ritchie, R. O. Determining the Toughness of Ceramics from Vickers Indentations Using the Crack-Opening Displacements: An Experimental Study. *J. Am. Ceram. Soc.* **86**, 1433–1436 (2003).

357. Zhang, S. S. A review on the separators of liquid electrolyte Li-ion batteries. *J. Power Sources* **164**, 351–364 (2007).

358. Kim, K. J., Balaish, M., Wadaguchi, M., Kong, L. & Rupp, J. L. M. Solid-State Li–Metal Batteries: Challenges and Horizons of Oxide and Sulfide Solid Electrolytes and Their Interfaces. *Adv. Energy Mater.* **11**, 2002689 (2021).

# Appendix

**Table A.1:** List of $Li_6PS_5Cl$ mechanical properties determined in this work and used as input for the modelling in Chapter 3.

| Name | Symbol | Unit | Method | Value ± s.d |
|---|---|---|---|---|
| Elastic Modulus | E | GPa | Nanoindentation | 28.0 ± 1.8 |
| Hardness | H | MPa | Nanoindentation | 921 ± 196 |
| Fracture Toughness | $K_{IC}$ | MPa $m^{1/2}$ | Nanoindentation | 0.69 ± 0.12 |
| Local Fracture Strength | $\sigma_c$ | MPa | Microcantilever bending | 91.1 ± 14.5 |

**Table A.2:** List of simulation inputs used to estimate a $CCD_{init}$ ~ 1 $mA/cm^2$ in Chapter 3.

| Input | Value |
|---|---|
| Pore radius | 1.5 µm |
| Pore separation | 10 µm |
| Crack length | 5 µm |
| Crack radius | 300 nm |

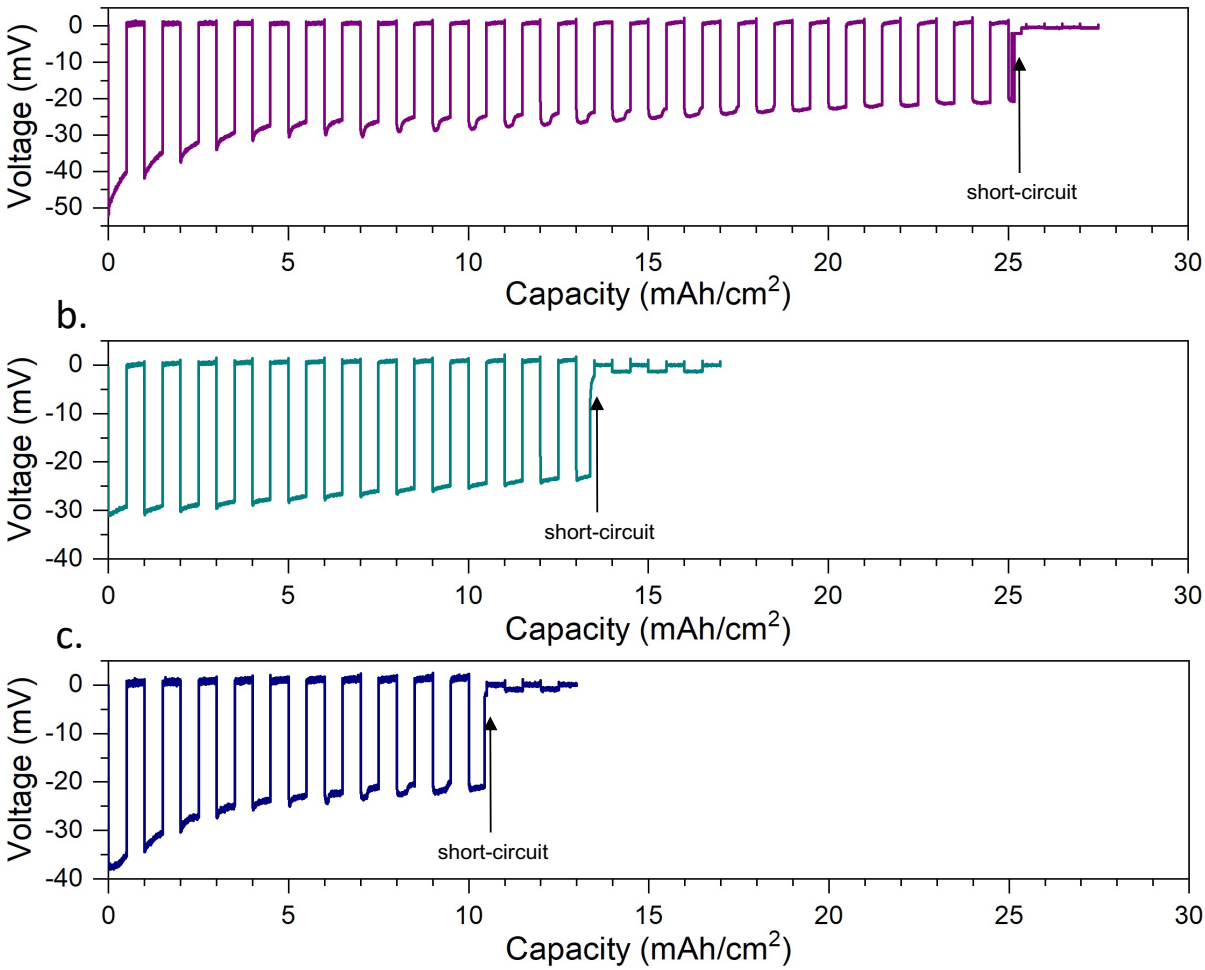



**Figure A.1:** Voltage profiles corresponding to data points at **(a)** 10 MPa **(b)** 28 MPa and **(c)** 34 MPa in Figure 3.14. Cycling of employed Li/$Li_6PS_5Cl$ 3-electrode cells with current densities of 4.0 mA/cm$^2$ for plating, 0.05 mA/cm$^2$ for stripping (to avoid void formation), both for a capacity of 0.5 mAh/cm$^2$.

**Table A.3**: Relative density measurements for differently sintered solid electrolytes used in Chapter 4. Calculated by imaging the outer surface using XCT to give the total volume, measuring their weight, and then comparing the result to the theoretical density of $Li_6PS_5Cl$.

| Sintering conditions | Sample 1 Relative Density (%) | Sample 2 Relative Density (%) | Sample 3 Relative Density (%) | Average relative density ± s.d (%) |
|---|---|---|---|---|
| Cold Pressed | 83.61 | 82.95 | 82.67 | 82.67 ± 0.48 |
| 300 °C | 86.72 | 86.11 | 86.38 | 86.40 ± 0.31 |
| 350 °C | 95.08 | 95.45 | 95.19 | 95.24 ± 0.19 |
| 400 °C | 99.10 | 99.28 | 99.45 | 99.28 ± 0.18 |